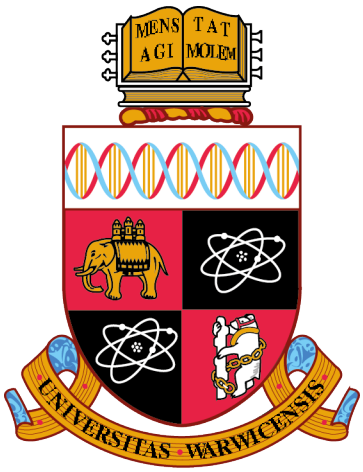

Approaches to ab-initio GIPAW-DFT calculations of NMR parameters in disordered materials

By

Stephen Paul Day

Thesis

Submitted to the University of Warwick

for the degree of

Doctor of Philosophy

Supervised by Dr. John Hanna & Dr. David Quigley

Department of Physics

September 2015

THE UNIVERSITY OF WARWICK

CONTENTS

LIST OF TABLES

LIST OF FIGURES

ACKNOWLEDGEMENTS

The completion of this PhD has only been made possible through the invaluable contributions of a number of important people. Principally I would like to offer my special thanks to my supervisors John Hanna and Dr. David Quigley. John has given me the opportunity to study a rich variety of systems during my time at Warwick (many of which have not been recorded in this thesis) that have greatly aided my development as a scientist, while this thesis could not have been completed without Dave's valuable and constructive suggestions during the development of this research work. I also wish to acknowledge the assistance of Dr. Dinu Iuga, Dr. Andy Howes and Dr. Gregory Rees for their frequent methodological advice and help handling the NMR spectrometers. Furthermore I would like to thank Prof. Jonathan Yates for his constant willingness to help with the computational side of my work.

I am particularly grateful to Prof. Dr. David Bryce, Dr. Kevin Burgess, Patrick Szell and Dr. Victor Terskikh for their help during my time at the University of Ottawa. Their kindness and excellent knowledge made this collaborative project a highlight of my PhD. Likewise I am indebted to Dr. Zhe Liu who patiently guided me through the SQS structure generation. Moreover I would like to express my very great appreciation to Dr. Thibault Charpentier for his vital contributions to both the vaterite and KNN work.

I would like to acknowledge the EPSRC, the Warwick-Monash Alliance and the 850 MHz Solid-State NMR Facility for their generous grants that have given me the opportunity to not only take part in interesting scientific research, but to travel and share my research with a global audience.

Finally, I would like to offer a special thanks to my friends for offering support, encouragement and a vital source of escapism. In particular my ex-band mates who had to suffer my perpetual late arrivals due to magnet time, the NMR football team for the perfect excuse to play the greatest sport on the planet and to the cake club for making one of life's great pleasures a weekly feature. To Drake, Sarah, Richard and Steven for their ability make me laugh even when science wasn't fun, Jamie and John for their infectious sense of adventure, Charles, Bridget and Nina for being interested (or at least pretending to be) in my PhD and making me feel like I was driving towards something worthwhile, to my brother and sister for the endless lifts and the generous accommodation, to Jonny for being the nicest guy I've ever met and to Lizzie for being the nicest lady I've ever met and a constant support.

DECLARATIONS

This thesis, **Approaches to ab-initio GIPAW-DFT calculations of NMR parameters in disordered materials**, is original work based on my research at the University of Warwick under the supervision of Dr. David Quigley and Dr John Hanna, and no part of it has been submitted for any degree at any other university.

A number of the results presented in this work were obtained in collaboration with others. All DFT calculations and solid-state NMR spectra, measurements, spectral assignments and data analyses were recorded or carried out by myself, except for the following: the spectrum shown in **Figure 4.3** was recorded by Dr Gregory Rees and all NMR measurements in Chapter 5 were recorded by Dr John Hanna and the inversion datasets were created by Dr. Thibault Charpentier. In Chapter 6 Dr. Thibault Charpentier was responsible for the 3Q-MAS inversion data and produced **Figure 6.9** and **Figure 6.10**.

Results from other authors' publications, where quoted, are referenced in the text.

ABSTRACT

The use of *ab initio* Density Functional Theory (DFT) to calculate key Nuclear Magnetic Resonance (NMR) parameters has been shown to be very successful in a variety of cases. These calculations allow one to extract meaningful data from NMR measurements by providing a foundation for spectral peak assignment. However, first principle calculations for disordered systems, typically based on a single realisation of the disorder, are inadequate if the NMR parameters depend sensitively on the location of the disordered species. In this thesis, a number of different approaches for characterising disorder in solids are presented. The aim of which is to overcome current challenges regarding the computational cost of conventional supercell approaches that make it difficult to perform a direct study of the complete configurational ensemble for any supercell with a sufficient simulation cell.

A case study is presented for the Ge-based apatite $La_{7.5}Ca_{2.5}Ge_6O_{25.75}$ that shows that the number of configurations one needs to consider can be vastly reduced by exploiting the symmetry of the system over a wholly enumerative approach, although exhaustive statistical averaging of the atomic positions required to reproduce the atomic resolution afforded by the solid-state NMR (ssNMR) measurement makes this problem intractable via this methodology.

The sodium potassium niobate system ($Na_xK_{1-x}NbO_3$) is studied across a series of compositions between the ordered $KNbO_3$ and $NaNbO_3$ end-members. This novel material exhibits purely atomic position / permutation disorder that is reflected in initial ^{23}Na and ^{93}Nb MAS NMR studies, but the true explanation of the disorder described by this data is not well understood. The Special Quasi-random Structure (SQS) approach to studying this disorder is presented as a computationally cheaper alternative to the supercell approach. It is noted that further studies are required to assess whether this is an adequate description of the $Na_xK_{1-x}NbO_3$ system due the complications of modelling the complex tilting patterns exhibited by these structures.

A combined ssNMR and GIPAW-DFT approach is reported to resolve the complex disorder within the vaterite polymorph of calcium carbonate. The computational data for the various structural candidates in the literature is utilised to simulate the highly sensitive DOR data, thereby elevating the predictive capability of this complementary approach to substantiate the stacking model of vaterite that views the material as a dynamic system under ambient conditions.

ABBREVIATIONS

2D	Two-Dimensional
CASTEP	Cambridge Serial Total Energy Package
CSA	Chemical Shift Anisotropy
DFT	Density Functional Theory
DOR	Double Orientation Rotation
FID	Free Induction Decay
FT	Fourier Transform
GGA	Generalised Gradient Approximation
GIPAW	Gauge Including Projector Augmented Waves
IUPAC	International Union of Pure and Applied Chemistry
ICSD	Inorganic Crystal Structure Database
MAS	Magic Angle Spinning
MQMAS	Multiple Quantum Magic Angle Spinning
NMR	Nuclear Magnetic Resonance
PAF	Principle Axis Frame
PAW	Projector Augmented Waves
PBE	Perdew-Burke-Ernzerhof
PBEsol	Perdew-Burke-Ernzerhof Solids
ppm	Parts Per Million
r.f.	Radio Frequency
S/N	Signal to Noise
SSNMR	Solid-State Nuclear Magnetic Resonance
SOD	Site-Occupancy Disorder
SQS	Special Quasi-random Structures
TMS	Tetramethylsilane
TPPI	Time-Proportional Phase Incrementation

1

INTRODUCTION

Nuclear Magnetic Resonance (NMR) is a spectroscopic technique used to probe the local chemical and crystallographic environments of isotopic nuclei with a magnetic moment. Rather than being used directly for the complete solution of a crystal structure it is generally employed in conjunction with diffraction based studies to constrain structural models.[1] Indeed NMR is considered a natural complement to diffraction measurements that investigate long-range periodic order of a structure because it is able to probe the ensemble of local environments for a given NMR-active nuclei. In this capacity it has been used to establish space groups, the number of species in the asymmetric unit cell, occupancies, probe dynamics and disorder. [2,3,4]

NMR was initially developed for the study of liquids (or gases) where fast molecular tumbling meant that an NMR spectrum is usually characterized by a set of narrow lines whose positions corresponding to the isotropic chemical shift. In the solid-state NMR there are a number of interactions that cause the broadening of resonance peaks that smears structural detail. However, there now exists a large number of solid-state NMR experiments that can not only remove these broadening contributions but are able to measure these additional interactions. Thus solid-state NMR can provide information on the local chemical and structural environment of a nucleus through the isotropic chemical shift and the corresponding chemical shift anisotropy (CSA), quadrupolar and *J*-coupling parameters.

This becomes a particularly powerful approach if these experimental parameters are coupled with quantum-mechanical calculations of the NMR parameters for a given structure. [5,6,7] Though the theoretical framework for the calculation of NMR parameters was outlined in the early 1950s[8,9,10] it wasn't until the ground-breaking work of Pickard and Mauri[11], which introduced the Gauge Including Projector Augmented Wave (GIPAW) method, that such calculations became a common approach. This allowed the

computation of NMR tensors at the density functional level of theory using a plane-wave basis set for extended systems to an all-electron level of accuracy.

The ability to relate calculated NMR parameters of atoms in the unit cell to crystallographic locations and therefore aid spectral assignment has extended the scope of solid-state NMR such that in the last decade NMR crystallography has emerged. Indeed there are an increasing number of cases where NMR is used as the primary technique for 3D crystal structure solutions as opposed to diffraction. [12,13] The importance of NMR as a crystallographic technique is only emphasized by the prediction that in the future crystal structures maybe established by simultaneously fitting both diffraction patterns and NMR spectra.[1]

High-resolution solid-state NMR is now recognized as a vital method of investigation for inorganic crystal structures.[14] Increasingly there is interest in complex inorganic materials where single crystals cannot be obtained. Larger cell volumes and the potential lack of atomic contrast make the process of structure solution from powder diffraction techniques difficult and in the worst cases intractable. The combined NMR and GIPAW-DFT approach can excel in such circumstances.

Diffraction based techniques extract the long-range periodic order from a crystal structure. If a crystal contains point defects (vacancies, interstitials and substitutions) the periodic nature of the lattice is disrupted. In these cases a diffraction-based investigation will report average information on these non-periodic properties that is mapped onto small crystal unit cells using fractional site-occupancy configurations. Such site-occupancy disorder is ubiquitous in solid-state chemistry across many classes of material including metallic alloys, mineral solid solutions and synthetic non-stoichiometric compounds.

In the context of periodic solid-state calculations a common approach to defective structures is by creating supercells where the size of the supercell should be sufficient to minimize the interaction of the defect and its periodic image.[15] The major disadvantage of this tactic is that it is computationally expensive, both in the sense that the calculation of the property of interest is expensive, and that the number of configurations increases dramatically with the supercell size so that it is impractical to characterize a complete configurational ensemble for any supercell. A single realisation of the disorder is inadequate if the NMR parameters depend sensitively on the location of the disordered species so that a compromise between both these methodologies would be of great use to NMR crystallography.

In this thesis we will consider computational approaches to calculating NMR parameters for materials exhibiting partial occupancy type disorder for germanium and silicon based apatites and $K_xNa_{1-x}NbO_3$ (KNN).

In the apatites aliovalent doping is used to induce charge-compensating vacancies. We begin by enumerating the configurational ensemble based on an approximation to the fractional occupancies described in the unit cell before showing that the problem can be vastly simplified by taking into account symmetry equivalent configurations as outlined by Grau-Crespo *et al.*[16] However it is shown that rounding fractional occupancies to convenient numbers from a modelling perspective can remove detail in the lineshape that is highly computationally expensive to recover using an enumerative approach due to the combinatorics. Indeed when a crystal structure exhibits multiple sites with fractional occupancies it is shown the configurational space grows to become intractable very quickly if *ab initio* techniques are to be employed.

As such we investigated the use of special quasi-random structures (SQS)[17] as a further alternative approach to characterizing disorder in the context of NMR calculations within the crystal structure of KNN at room temperature across numerous key points in its phase diagram. Existing diffraction based structures for KNN display both atomic and positional disorder, however this is shown to correlate strongly with the concentration of sodium in the KNN system. These differences are reflected in the ssNMR results that show for the sodium-rich compositions there exist highly correlated ^{23}Na chemical shifts and quadrupolar parameter behaviour and distinctive trends in ^{93}Nb quadrupolar coupling constant and isotropic chemical shifts, thus making it an ideal case study for such an approach.

The cluster expansion method [18,19,20] was first introduced to characterise binary metal alloys exhibiting partial occupancy disorder, but has been extended to a host of chemically diverse materials in recent times. Using special quasi-random Structures (SQS) it has been shown that one can avoid having to complete the highly intensive and computationally expensive cluster expansion method by generating structures that mimic 'randomness'.

Finally an extensive investigation into the calcium carbonate polymorph vaterite is reported. This complicated system exhibits multiple forms of potential crystallographic disorder that are still poorly resolved. It was postulated in the 1960's that the vaterite crystal exhibited a disorder in the carbonate positions orientated along the c-axis of the

unit cell[21], but more recent considerations suggest that this carbonate partial occupancy is actually a simplification of the interconversion between multiple structures that co-exist within domains defined by superbasins of multiple structures which is manifest as stacking faults in the crystal system.[22] We show that a combined ssNMR and GIPAW-DFT approach is sufficient to finally resolve the disorder within this system.

2

TECHNIQUES

2.1 NMR Interactions

In principle the only prerequisite for an element to be studied via nuclear magnetic resonance (NMR) is that it has a magnetically active isotope with a non-zero nuclear spin, a characteristic that only two nuclei in the periodic table lack: Ar and Ce.[23,24] For such NMR-active nuclear isotopes the technique offers a non-destructive method to determine quantitative information on chemical environments. In the liquid state rapid molecular tumbling motion averages anisotropic components of the internal NMR interactions so that narrow lines define the corresponding NMR spectra.[25] The absence of such motion in solids means that the anisotropic components of the internal interaction Hamiltonian broaden the spectral detail, compromising ones ability to interpret the features. The ability to acquire high-resolution isotropic spectra, free from anisotropic broadening, has been, and still is, a major impetus behind experimental developments in solid-state NMR and the past two decades there have been major instrumental advances so that ultrafast magic angle spinning (MAS) of rotor frequencies up to 100 kHz can be achieved at ultrahigh magnetic fields (23.3T)[26] while high-resolution spectra for spin-$\frac{1}{2}$ nuclei mean the anisotropy of NMR interactions can now be probed by the appropriate recoupling experiments[27] and quadrupolar nuclei have been made accessible by techniques like double orientation rotation (DOR), dynamic angle spinning (DAS), multiple-quantum magic-angle spinning (MQMAS) and satellite-transition magic-angle spinning (STMAS).[28]

These developments have lead to the emergence of the NMR crystallography movement in the past few years that posits the technique as an integral component in a standard template process of structural elucidation by the complementary diffraction, computational chemistry and NMR approaches.[1] In this modern paradigm solid-state NMR presents a versatile spectroscopic technique capable of providing isotope-specific information on key structural details like the connectivity, stereochemistry, spatial

proximity and dynamics within materials.

In the periodic table the chemical elements are arranged in a tabular framework according to their atomic number. Conversely in the field of NMR elements are described in terms of their intrinsic nuclear spin (I). Within this model the periodic table is split into two broad classes of NMR-active nuclei; nuclei with a nuclear spin $I = \frac{1}{2}$ and those $I > \frac{1}{2}$. This dichotomy reflects the electric quadrupole moment $I > \frac{1}{2}$ nuclei possess in addition to the magnetic dipole that all NMR-active nuclei have. For such nuclei in non-cubic crystallographic environments the electric quadrupole moment couples with the electric field gradients generated by other charges in the system to produce the 'quadrupole interaction' that generally dominates all other interactions and therefore the NMR spectra in solids. As ~75% of NMR-active nuclei are quadrupolar this interaction is seen to define many of the materials that we may wish to study.

In this chapter, the author focuses on the experimental implementations for enhancing the resolution of quadrupolar NMR spectra. The theoretical foundation of the quadrupolar interaction in NMR has already been well defined [29,30,31,32,33,28] and therefore only a very brief overview of the necessary theoretical background is given here. Additionally some of the fundamental principles of solid-state NMR relevant to the subsequent results chapters are outlined including the chemical shift interaction that interplays with the quadrupolar interaction to define the experimental line position on an NMR spectrum.

2.1.1 Zeeman Interaction

In the presence of an external magnetic field $(\boldsymbol{B_0})$ the degeneracy of the intrinsic nuclear spin states is broken so that they lie on different energies such that the projection along the field of the different states of angular momentum is dependent on the quantum number (m_I) as shown by equation (2.1).

$$\boldsymbol{E|m_I\rangle = -\mu.B_0 = -\gamma m_I \hbar B_0 = -\omega_0 \hbar \hat{I}_z} \tag{2.1}$$

where γ is the gyromagnetic ratio, $\boldsymbol{B_0}$ is the external magnetic field chosen to be aligned with the z-axis, $\boldsymbol{\mu}$ is the nuclear magnetic moment, $\hbar\hat{I}_z$ is the angular momentum along the z-axis.[34]

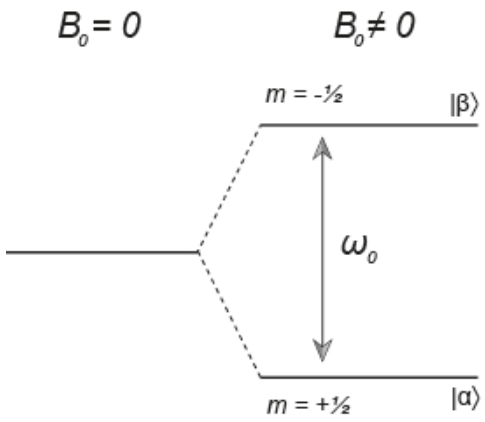

Figure 2.1, schematic representation of the energy levels splitting for a spin-1/2 nucleus due to an applied magnetic field, $\mathbf{B_0}$. The energy difference of states **α** and **β** is equivalent to the Larmor frequency (in rads^{-1}), which is proportional to the magnitude of the applied magnetic field.

Thus the Zeeman splitting produces a series of energy levels ($2I + 1$ levels for a nucleus of spin number I) that are separated by an energy difference equivalent to the Larmor frequency (ω_0) in the presence of a magnetic field (see Figure 2.1). At equilibrium the Boltzmann distribution dictates that a small population difference exists between the spin-states and hence a net magnetization exists. Transitions between different energy levels of a nuclear spin system can be simulated by radiofrequency (r.f) irradiation and therefore the induced net magnetization can be manipulated. In this manner NMR spectroscopy probes the small perturbations of the resonance away from the Larmor frequency (ω_0) defined by the Zeeman interaction.

2.1.2 Chemical Shift

Chemical shielding denotes the change in the magnetic field experienced by a nuclear spin due an induced local magnetic field in the electron orbitals surrounding the nucleus by an externally applied magnetic field (B_0). This effect is described by the magnetic shielding tensor σ. The perturbation of the Zeeman interaction due to the response of the electron density surrounding the nuclear site in a magnetic field $\boldsymbol{B_0}$ can be described formally as:[35]

$$\hat{H}_{CS} = \gamma \boldsymbol{I}.\boldsymbol{\sigma}.\boldsymbol{B_0} \tag{2.2}$$

where σ is a second-rank tensor.

By diagonalising σ so that it describes the magnetic shielding in its principal axis system (PAS), it is possible to identify the isotropic and anistropic components of the chemical shift interaction. This distinction is important because the anisotropic components are the origin of lineshape broadening for the chemical shift interaction. This motivates the parametrisation of the chemical shielding lineshape according to three parameters using the Haeberlen convention[36]; the isotropic magnetic shielding (σ_{iso}), the anisotropy (Δ) and the asymmetry (η) that are related to the diagonal components $\sigma_{11}^{PAS}, \sigma_{22}^{PAS}$ and σ_{33}^{PAS} of the magnetic shielding tensor according to the following definitions:

$$\sigma_{iso} = \frac{\sigma_{11}^{PAS}+\sigma_{22}^{PAS}+\sigma_{33}^{PAS}}{3} \tag{2.3}$$

$$\Delta = \sigma_{33}^{PAS} - \sigma_{iso} \tag{2.4}$$

$$\eta = \frac{\sigma_{22}^{PAS}-\sigma_{11}^{PAS}}{\Delta}, -1 \leq \eta \leq 1 \tag{2.5}$$

As the strength of the chemical shift interaction is proportional to the external magnetic field a universal field-independent chemical shift parameter (δ) is introduced to allow the comparison of magnetic shielding acquired under different external magnetic fields. Thus the magnetic shielding is quoted against a given standard resonance σ_{REF}. Thus σ_{iso} is converted to the isotropic chemical shift parameter δ_{iso}, which corresponds to the centre of gravity of the observed resonance for a spin-$\frac{1}{2}$ nuclei.

$$\delta_{iso} = \frac{(\sigma_{REF}-\sigma_{iso})}{(1-\sigma_{REF})} \tag{2.6}$$

The International Union of Pure and Applied Chemistry (IUPAC) have outlined a catalogue of standard reference samples for each nucleus. [37,38]

Local increases or decreases in the magnetic field at the nuclear site lead to the nucleus appearing shielded or deshielded relative to a bare nucleus. Under classical chemical shift theory the magnetic shield tensor can be conveniently split into a diamagnetic (σ^{dia}) term that opposes the applied magnetic field and a paramagnetic contribution that augments the applied field (σ^{para}) as shown in eq. (2.7) .

$$\boldsymbol{\sigma = \sigma^{dia} + \sigma^{para} + \sum_{B \neq A} \sigma_{AB}} \tag{2.7}$$

where σ_{AB} is the contribution from other atoms, B.

Generally trends in chemical shifts arise primarily from changes in the paramagnetic (deshielding) contribution to the shift that correlates with increasing occupancy of the excited states (it depends on the expectation value of the electron-nuclear distance (r) as $\frac{1}{r^3}$) and therefore increasing covalent character in the bond. [39,40] The corresponding change of a resonance position δ_{iso} with an increasingly shielded or deshielded nuclear environment is summarized in Figure 2.2.

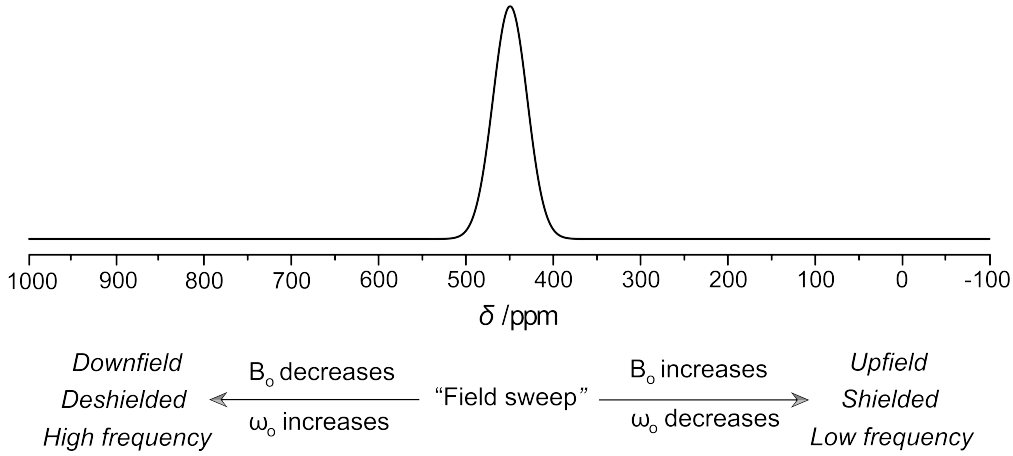

Figure 2.2, General chemical shift scale showing the change in line position due to changes in electronic shielding of the nuclear environment.

2.1.3 The Quadrupolar Interaction

For analysis of the quadrupolar spectra in this thesis it is sufficient to consider the quadrupolar Hamiltonian $\hat{H}_Q$ in terms of standard perturbation theory of the Zeeman Hamiltonian $(\hat{H}_Z)$ with an expansion up to the second-order level of detail.

$$\hat{\boldsymbol{H}}_{\boldsymbol{Z}} = \omega_0 \hat{\boldsymbol{I}}_{\boldsymbol{z}} \tag{2.8}$$

$$\hat{\boldsymbol{H}} = \hat{\boldsymbol{H}}_{\boldsymbol{Z}} + \hat{\boldsymbol{H}}_{\boldsymbol{Q}} \tag{2.9}$$

$$\hat{\boldsymbol{H}}_{\boldsymbol{Q}} = \hat{\boldsymbol{H}}_{\boldsymbol{Q}}^{(\boldsymbol{1})} + \hat{\boldsymbol{H}}_{\boldsymbol{Q}}^{(\boldsymbol{2})} \tag{2.10}$$

For illustrative purposes a schematic of the Zeeman levels and the corresponding perturbations to these states due to the first and second-order quadrupolar interaction for a $I = \frac{3}{2}$ spin system is shown in **Figure 2.3**.

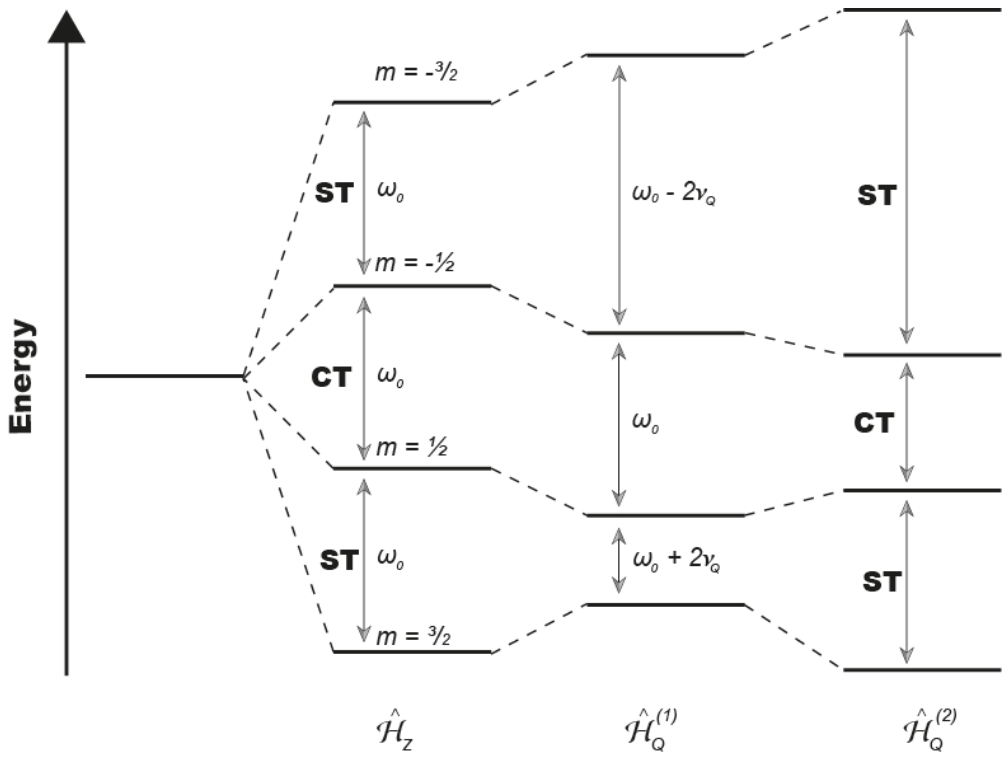

Figure 2.3, Perturbation of the Zeeman energy levels arising from the quadrupolar interaction to the first- and second-order approximation for a spin $\mathbf{I} = \frac{3}{2}$ system. Note that the central and triple quantum transitions are unaffected to the first order, but are perturbed to the second-order.

The shifts the eigenvalues of the Zeeman Hamiltonian due to the quadrupolar interaction split the NMR spectrum into $2I$ peaks. The vocabulary of NMR the single-quantum $|1/2\rangle \leftrightarrow |-1/2\rangle$ transition is called the central transition while the transitions $m \leftrightarrow m \pm 1$ where $|m|$ takes on the values $\frac{1}{2}, \frac{3}{2}, \frac{5}{2}, \cdots$ are the satellite transitions. Though the satellite transitions are observable in the NMR experiment (see **Figure 2.4**) their transitions are shift by orientation-dependent components of $\widehat{H}_Q^{(1)}$, which imposes extensive broadening to these transitions. In contrast the symmetric $|m\rangle \leftrightarrow |-m\rangle$ central transition is not broadened to the first order by the quadrupolar interaction, but is broadened by the second-order interaction ($\widehat{H}_Q^{(2)}$). Thus the $|1/2\rangle \leftrightarrow |-1/2\rangle$ transition is key for half-integer quadrupole nuclei as it provides a relatively narrow powder lineshape compared to the satellite transitions by which the quadrupolar environment can be characterized. The deviations from ω_0, which defines the energy of the transition, due to the second-order quadrupolar component of the interaction complicates NMR spectra in two ways; it imposes a field-dependent shift of the chemical shift from the

centre of the spectral width due to an isotropic term (zero-rank) and a broadening of the spectral features due to orientation-dependent terms (second and forth rank tensors).

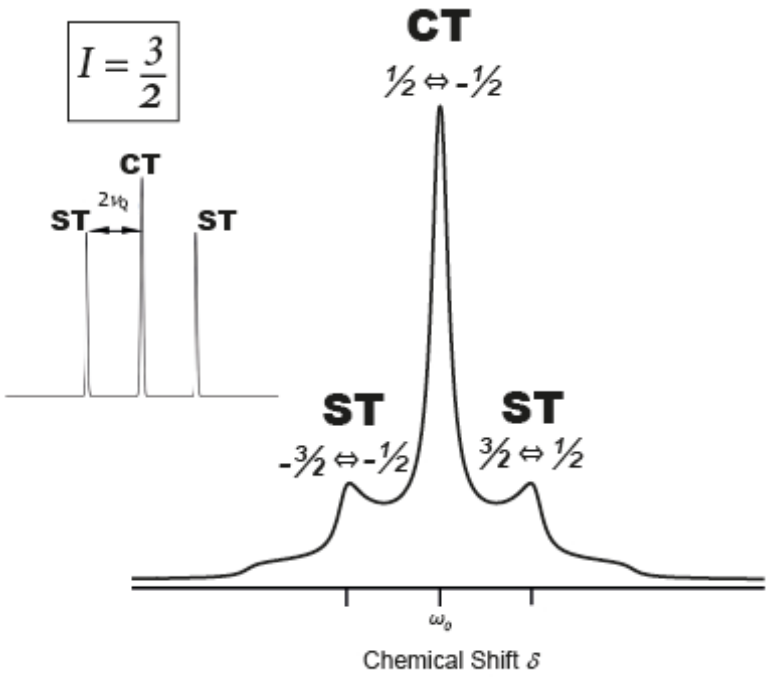

Figure 2.4, an example of a spectrum for a powder distribution of $\boldsymbol{\omega_Q}$ due to the first-order perturbation of the Zeeman energy levels by the quadrupolar interaction for an $\mathbf{I} = \frac{3}{2}$ system. The resulting spectrum has contributions from each of the $\mathbf{2I}$ non-degenerate transitions separated by $\mathbf{2\nu_Q}$. Figure is adapted from Donna L. Carrol's thesis[41]

The centre of gravity $(\delta_{CG})$of the experimental lineshape is used to denote the quadrupolar-induced shift (δ_{QIS}) from the isotropic chemical shift (δ_{iso}) and are related by eq. (2.11).[42]

$$\delta_{iso} = \delta_{CG} - \frac{1}{30}\left(1 + \frac{\eta^2}{3}\right) X \left[I(I+1) - \frac{3}{4}\right] \left[\frac{3C_Q}{2I(2I-1)\omega_0}\right]^2 \qquad (2.11)$$

$$\delta_{QIS} = \frac{1}{30}\left(1 + \frac{\eta^2}{3}\right) X \left[I(I+1) - \frac{3}{4}\right] \left[\frac{3C_Q}{2I(2I-1)\omega_0}\right]^2 \qquad (2.12)$$

For powdered samples, which is the case for all samples under investigation in this thesis, the chemical environment of a quadrupolar nuclei is generally described in terms of three parameter; the isotropic chemical shift (δ_{iso}), the quadrupolar coupling constant (C_Q) and the asymmetry parameter (η_Q). Indeed the powder pattern of the central line $(|1/2\rangle \leftrightarrow |-1/2\rangle)$ can be parameterized by these three parameters. It is therefore useful to briefly review the origins and meaning of these parameters.

The electric field gradients (EFG) surrounding a quadrupole nucleus can be described by a second-rank symmetrical tensor $(V_{\alpha\beta})$ where U is the electrostatic potential at the origin (inside the nucleus) generated by external charges.

$$V_{\alpha\beta} = \left.\frac{\partial^2 U}{\partial\alpha\partial\beta}\right|_{r=0} \tag{2.13}$$

In the principal axis system (PAS) the EFG tensor is diagonal and is a property of the molecular structure. In Cartesian coordinates the diagonal components of the EFG tensor are $V_{xx}^{PAS}, V_{yy}^{PAS}, V_{zz}^{PAS}$ where convention dictates that $|V_{zz}^{PAS}| \geq |V_{yy}^{PAS}| \geq |V_{xx}^{PAS}|$.

$$V^{PAS} = \begin{bmatrix} V_{xx}^{PAS} & 0 & 0 \\ 0 & V_{yy}^{PAS} & 0 \\ 0 & 0 & V_{zz}^{PAS} \end{bmatrix} \tag{2.14}$$

For the perspective of the EFG, the nucleus is a charge-free region of space as it is created by external nuclear charges and therefore LaPlace's equation is true.

$$\nabla^2 V = V_{xx} + V_{yy} + V_{zz} = 0 \tag{2.15}$$

It follows that the EFG can be parameterized by two independent variables; the anisotropy which is defined as the largest value of V^{PAS} and the asymmetry (η_Q).

$$eq = {V_{zz}}^{PAS} \tag{2.16}$$

$$\eta_Q = \frac{V_{xx}^{PAS} - V_{yy}^{PAS}}{V_{zz}^{PAS}} \tag{2.17}$$

where $0 \leq \eta_Q \leq 1$

Insight into the crystal symmetry can be inferred from the dependence of the quadrupolar coupling parameters on the EFG tensor. In fact for cubic point symmetry $V_{xx}^{PAS} = V_{yy}^{PAS} = V_{zz}^{PAS}$ therefore it follows from the Laplace equation that the electric field gradient vanishes at the nucleus. This is the case for perfect fourfold tetrahedral, sixfold octahedral and eightfold cubic coordination environments. Practically the quadrupolar coupling is rarely zero because of defects: generally distortions or deviations of bond angles and/or bond lengths from their ideal values lead to small quadrupolar

broadening. Additionally if $\eta_Q = 0$ then the nuclear site has axial symmetry $V_{xx}^{PAS} = V_{yy}^{PAS}$ which can only occur when the nucleus in question lies on an *n*-fold rotation axis where *n*=3,4,5 or 6.[43] The quadrupolar Hamiltonian in the PAS can be written as shown in eq (2.18) where Q denotes the electric quadrupole moment. [44]

$$\widehat{\boldsymbol{H}}_{\boldsymbol{Q}} = \frac{e^2qQ}{4I(2I-1)\hbar}\left\{3\boldsymbol{I}_{\boldsymbol{z}}^{\boldsymbol{2}} - \boldsymbol{I}(\boldsymbol{I}+1) + \eta_Q\left(\boldsymbol{I}_{\boldsymbol{x}}^{\boldsymbol{2}} - \boldsymbol{I}_{\boldsymbol{y}}^{\boldsymbol{2}}\right)\right\} \tag{2.18}$$

The coefficients of eq. (2.18) contain the interaction of the nuclear quadrupole moment eQ and the principal field gradient eq. This defines the quadrupole coupling constant (C_Q), which is used as a gauge of the magnitude of the quadrupolar interaction.

$$C_Q = \frac{e^2qQ}{h} \tag{2.19}$$

The quadrupolar frequency υ_Q^{PAS} defined in eq. (2.20) is actually a better representation of the strength of the quadrupolar interaction for a given nuclear spin I and is frequently observed in discussions on quadrupolar nuclei due to its ability to simplify expressions.

$$\upsilon_Q^{PAS} = \frac{\omega_Q^{PAS}}{2\pi} = \frac{3C_Q}{2I(2I-1)} \tag{2.20}$$

2.2 NMR Spectroscopy

2.2.1 Magic Angle Spinning

The first experimental implementation of Magic Angle Spinning (MAS) was published in 1958[45] and since then has evolved to become one of the most fundamental techniques to enhance spectral resolution in solid-state NMR spectroscopy. The sample under investigation is packed into a container, which in NMR nomenclature is called a rotor, and is rapidly spun about its axis of symmetry. This imposes a time-dependence on the Hamiltonian such that if the timescale of the averaging is fast compared to the decay time caused by the interaction then some of these broadening components may be averaged. If the rotor axis is aligned at 54.7° (the 'magic' angle) with respect to the externally applied magnetic field then the average interaction is projected along this axis. This alignment coincides with common orientation dependence for many of the NMR

interactions at which their contributions are reduced to zero and therefore their contribution to the lineshape is removed.

The rotor speeds achievable in present day (up to ~100 kHz though 40-65 kHz are more routine)[26] mean that in principle chemical shift anisotropy, heteronuclear dipolar coupling, homonuclear dipolar coupling and first order quadrupolar coupling can be averaged via MAS. Practically this fact cannot always be utilized due to the necessary reduction in rotor size, and therefore sample size, for greater rotor frequencies making spectral acquisition unfeasible on realistic timescales.

For some quadrupolar nuclei the interaction is weak enough to be described by quadrupolar coupling to the first order. In these cases, such as observed for ^{133}Cs or ^{2}H, MAS is sufficient to remove the broadening effects of the quadrupolar interaction.[46,47] However when the magnitude of quadrupolar frequency, υ_Q^{PAS}, is comparable to that of the Larmor frequency, ω_0 the second-order approximation is necessary. The average second-order quadrupolar frequency shift for a half-integer quadrupolar spin, I, due to an integral number of sample spinning periods at an angle χ between the spinning-axis and the z-axis of the laboratory frame is given by eq. (2.21).[48]

$$\langle E_{|m\rangle}^{(2)} - E_{|-m\rangle}^{(2)} \rangle = \frac{\left(\omega_Q^{PAS}\right)^2}{\omega_0}\left\{A_{I,m}^{(0)} Q^0(\eta) + B_{I,m}^{(2)} d_{0,0}^2(\chi) Q^2(\alpha,\beta,\eta) + C_{I,m}^{(4)} d_{0,0}^4(\chi) Q^4(\alpha,\beta,\eta)\right\} \tag{2.21}$$

$$Q^0(\eta) = \left(1 + \frac{\eta^2}{3}\right) \tag{2.22}$$

$$Q^2(\alpha,\beta,\eta) = \left(1 - \frac{\eta^2}{3}\right) d_{0,0}^2(\chi) - \frac{\sqrt{8}}{\sqrt{3}} \eta d_{2,0}^2(\chi) cos2\alpha \tag{2.23}$$

$$Q^4(\alpha,\beta,\eta) = \left(1 + \frac{\eta^2}{18}\right) d_{0,0}^4(\chi) + \frac{\sqrt{10}}{3} \eta d_{2,0}^4(\chi) cos2\alpha + \frac{35}{9\sqrt{70}} \eta^2 d_{4,0}^4(\chi) cos4\alpha \tag{2.24}$$

where η is the asymmetry parameter and the angles α and β describe the rotation of the principal axis frame of the quadrupolar interaction onto the sample frame and the $d_{m',m}^l(\chi)$ terms are reduced Wigner matrix elements.[49] The isotropic frequency shift of the central transition that was alluded to earlier in the chapter can be seen to originate from the $\frac{\left(\omega_Q^{PAS}\right)^2}{\omega_0} A_{I,m_I}^{(0)} Q^0(\eta)$ terms, while the inhomogeneous broadening of the spectral lineshape derives from the rank $l = 2$ and 4 anisotropic shifts that will preferentially

weight some crystallite orientations over others in a powder average. For nuclear spins $I = 3/2$ and $5/2$ the coefficients $A^{(0)}_{I,m_I}$, $B^{(2)}_{I,m_I}$ and $C^{(4)}_{I,m_I}$ are summarized in Table 2-1.

Table 2-1. Coefficients of the zero-, second-, and fourth-rank contributions of the second-order frequency shift given in eq.(2.21)

I	m_I	$A^{(0)}_{I,m_I}$	$B^{(2)}_{I,m_I}$	$C^{(4)}_{I,m_I}$
3/2	1/2	-2/5	-8/7	54/35
3/2	3/2	6/5	0	-6/5
5/2	1/2	-16/15	-64/21	144/35
5/2	3/2	-4/5	-40/7	228/35
5/2	5/2	20/3	40/21	-60/7

The terms $d^2_{0,0}(\chi)$ and $d^4_{0,0}(\chi)$ modulate the magnitude of the quadrupolar interaction anisotropy. These terms actually correspond to the second and fourth-rank polynomials given in the following:

$$d^2_{0,0}(\chi) = P_2(cos\chi) = \frac{1}{2}(3cos^2\chi - 1) \tag{2.25}$$

$$d^4_{0,0}(\chi) = P_4(cos\chi) = \frac{1}{8}(35cos^4\chi - 30cos^2\chi + 3) \tag{2.26}$$

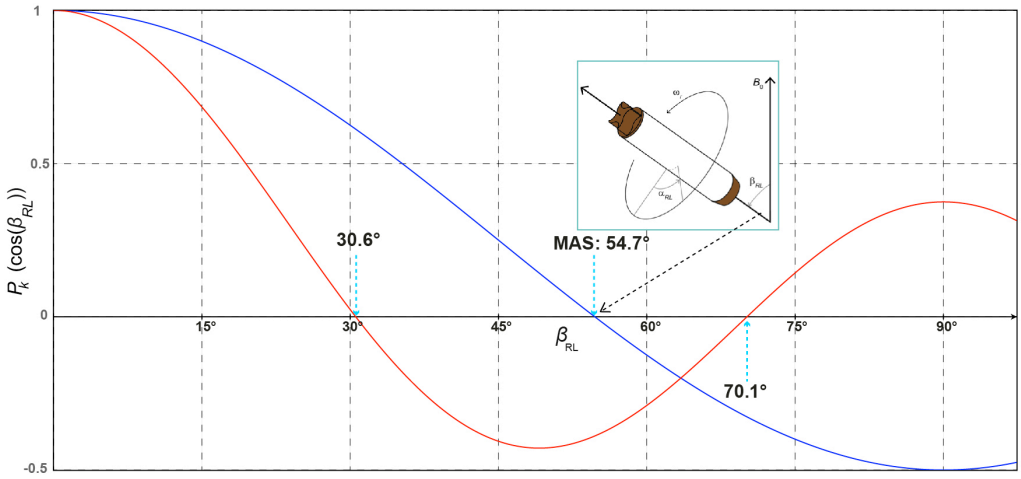

Figure 2.5, plot of the $\mathbf{P_2(cos\chi)}$ (blue) and $\mathbf{P_4(cos\chi)}$ (red) Legendre polynomials with their corresponding roots. The two angles used in DOR are chosen to match the roots of these functions.

As illustrated in **Figure 2.5** there are no common roots to the second and fourth rank Legendre polynomials. The magic angle is a solution to the second rank polynomial ($\chi_{MA} = arctan\left(\frac{1}{\sqrt{2}}\right)$), however leaves behind a contribution from the fourth-order Legendre polynomial. Consequently a central transition lineshape acquired under MAS

experiences a partial broadening due to the incomplete averaging of the second-order quadrupolar interaction.

Nonetheless the second-order quadrupolar broadening can be reduced between 3 and 4 times the line width of the equivalent static case by employing MAS. The orientation-dependence of the lineshapes gives rise to a set of second-order quadrupolar lineshapes, a sample of which are given in **Figure 2.6**.

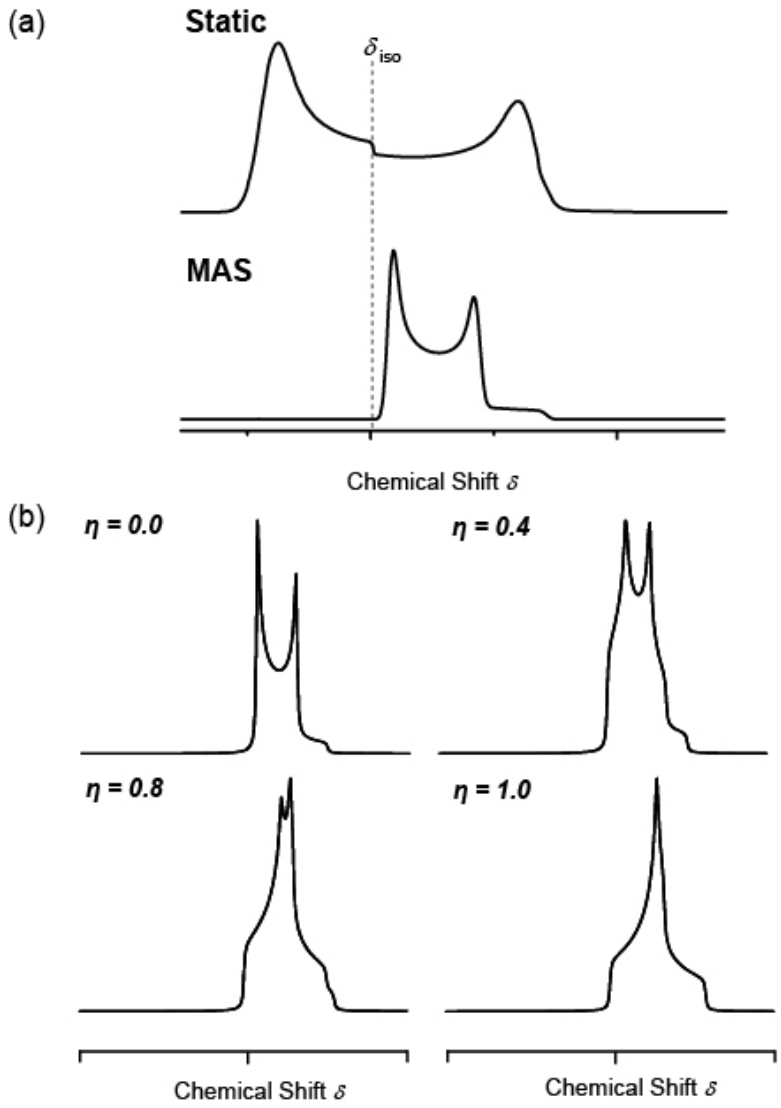

Figure 2.6, a) the narrowing effects of MAS upon the NMR signal for a quadrupolar nucleus. Adapted from Donna L. Carroll's thesis[41] b) Variation in the second-order broadened central-transition MAS powder patterns for a $\mathbf{I} = \frac{3}{2}$ spin system for various asymmetry parameters. Adapted from Sharon Ashbrook's thesis[50].

2.2.2 Interaction with Radiofrequency Fields

As an aside it is useful to clarify some of the practical considerations in acquiring central-transition quadrupolar lineshapes as these recur in other resolution enhancement experimental techniques that will be discussed later in the chapter. For quadrupolar nuclei the excitation profile of a nuclear spin is modulated by the size of the quadrupolar interaction and requires one to account for the existences of satellite transitions in addition to the central transition.

The response of a nuclear spin system to rf-pulse(s) is dictated by the relative magnitude of three parameters[32];

1. The amplitude of the rf-pulse $\omega_1 = \gamma B_1 = 2\pi\nu_1$ where B_1 is the strength of the rotating magnetic component of the rf-field.
2. The first-order quadrupolar splitting $\Delta\omega_Q = 2\pi\Delta\upsilon_Q$
3. The offset of the resonant frequency of the nuclear spins from the carrier frequency of the rf-pulse $\Delta\omega_0 = \omega_0 - \omega_{rf} = \Delta\nu_0$

Key to this discussion is the concept of nutation, which is easiest to introduce in the context of spin-$\frac{1}{2}$ nuclei. The offset is a major factor in dictating whether a rf-pulse causes nutation and is accounted for by the use of a rotating frame: an axes system that rotates with the frequency of the rf-carrier frequency so that the rf-field can be reduced to a constant vector ν_1, of magnitude $\boldsymbol{\nu_1}$ that for convenience is generally chosen to align with the x-axis (see **Figure 2.7**).

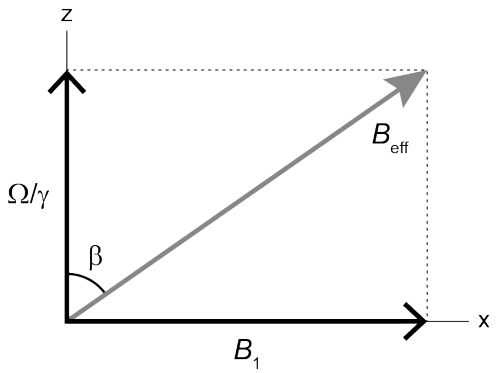

Figure 2.7, Graphic illustration of the effective field, $\mathbf{B_{eff}}$, which in the rotating frame is equal to $\sqrt{\mathbf{B_1}^2 + (\boldsymbol{\Omega}/\boldsymbol{\gamma})^2}$. Figure is taken from Jonathan M. Lamley's thesis.[51]

This exercise makes the Zeeman interaction (external field $\boldsymbol{B_0}$ is chosen to be along the z-axis) an offset vector $\Delta\boldsymbol{\nu_0}$ along the z-axis so that in the rotating frame the magnetization precesses about an effective field $\boldsymbol{\nu_{eff}}$. In NMR terminology if the rf-

pulse is close to resonance $(\Delta\nu_0 \ll \nu_1)$ the rf irradiation causes a precession of nuclear spin in the (y, z) plane. This is termed nutation where the nutation frequency is equal to the rf-amplitude $(\nu_1 = \nu_{nut})$. If the irradiation is far-off resonance $\Delta\nu_0 \gg \nu_1$ then no nutation is observed.

For quadrupolar nuclei the response of the spins to the rf irradiation depends on the position of the carrier frequency and the relative strengths of the rf-field strength $(\omega_1 = \gamma B_1)$ with respect to the quadrupolar interaction $\Delta\upsilon_Q$. In contrast in the weak rf-field regime $\nu_1 < \Delta\nu_Q$ a pulse applied with an rf profile that overlaps with the central transition will selectively excite the central transition. In this case the central transition will nutate with a frequency given by $\nu_{nut} = \left(I + \frac{1}{2}\right)\nu_1$.

For these two cases the observed magnetization displays a simple sinusoidal oscillations at ν_1 and $\nu_{nut} = \left(I + \frac{1}{2}\right)\nu_1$ respectively. Thus an on-resonances pulse of duration T_p causes a coherent oscillation of the magnetization such that it is tipped by an angle θ_p away from the direction of B_0 according to eq (2.27).[31]

$$\theta_p = \nu_1 \, T_p = \gamma B_1 T_p \tag{2.27}$$

However, for intermediate rf-fields that falls between these limiting cases $\left(\nu_1 \approx \nu_Q\right)$ the nutation behavior of the central transition is more complex and is dependent on ν_Q. This nutation effect means that for samples containing sites that have widely differing quadrupolar coupling constants long rf-pulses can distort the lineshape. Thus, for accurate quantitative spectra small angle pulses $\nu_{nut} = \left(I + \frac{1}{2}\right)\nu_1 T_p \leq \frac{\pi}{6}$ are used to ensure uniform excitation.

2.2.3 Simple Echo experiments

In the simplest NMR experiment the spin-system is excited by the application of an rf-pulse and the free induction decay (FID) of the spin-system is detected as the system returns to thermal equilibrium. This process is shown schematically in **Figure 2.8**.

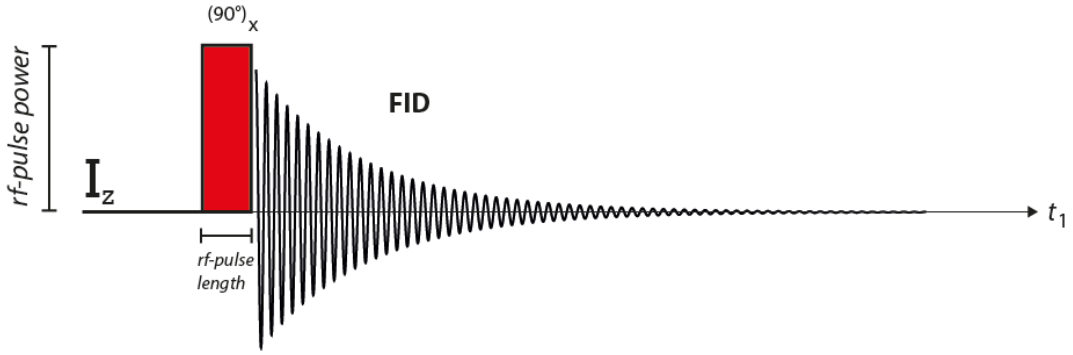

Figure 2.8, Pictorial representation of a single-pulse experiment. A 90° rf-pulse perturbs the spin system from thermal equilibrium and is allowed to evolve under the applied magnetic field. The evolution of the spin system is acquired as an FID. The experiment is repeated after the system has relaxed back to thermal equilibrium.

For a single quantum transition $(m+1, m)$ its corresponding FID, $F(t_1, \tau_2)$, is Fourier transformed to obtain its associated absorption spectrum $S(\omega, t_1)$ according to the expression shown in eq.(2.28) where t_1 is the pulse length and τ_2 is the acquisition time.

$$F(t_1, \tau_2) = \int_{-\infty}^{\infty} S(\omega, t_1) e^{-i\omega\tau_2} d\omega \qquad (2.28)$$

However, experimentally τ_2 is never actually zero as the first few digitized points of the FID are lost in the dead time of the receiver. This loss of signal intensity can cause significant lineshape distortions; however can be compensated for by the use of an echo-based experiment. Such spin-echo sequences refocus the magnetization lost in the dead time of the receiver so that the effective time zero point occurs outside the dead time allowing the complete acquisition of the FID.

There are two widely adopted pulse sequences for this purpose that exploit T_2 relaxation of the spin system to refocus the signal; the Hahn-echo and the solid-echo. The Hahn-echo sequence (see **Figure 2.9**) consists of a $\frac{\pi}{2}$-τ-π that produces a refocusing at τ after the second pulse. In the solid-echo the second pulse is the same length as the first pulse but has an additional 90° phase shift. The solid-echo is advantageous for larger C_Q's where the shorter second pulse has a large bandwidth of excitation.

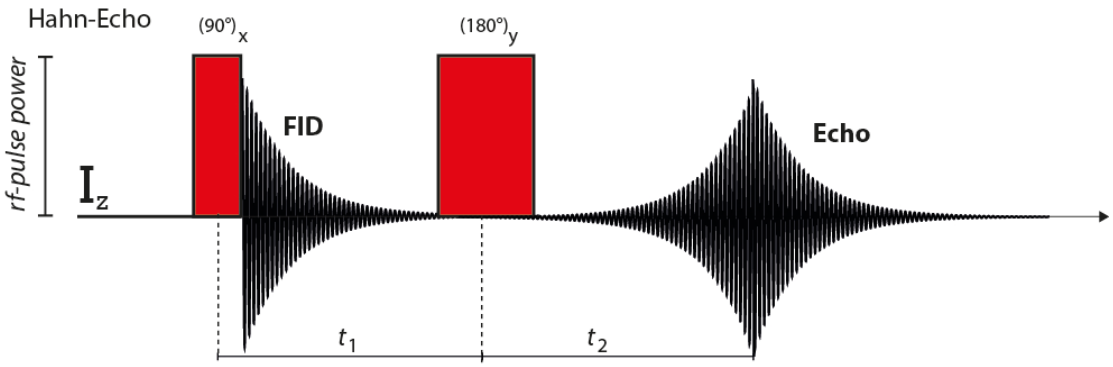

Figure 2.9, a Hahn-Echo pulse-sequence where the dephasing of the magnetisation after the 90° rf-pulse is refocused by a 180° pulse such that it reaches a maximum at a time t_2.

The echo formation for quadrupolar nuclei has been extensively investigated [52,53,54], as the evolution is dependent on the strength of the quadrupolar interaction, rf-strength and duration. The general conclusions of these investigations suggest that echoes will be formed for most conditions but that to acquire useful quantitative information it is safest to use weak $(\nu_1 < \Delta\nu_Q)$ rf-excitation of only the central transition.

2.2.4 Multiple Quantum Magic Angle Spinning

In the previous discussion the second-order quadupolar interaction was shown to possess higher-order orientational terms of significant magnitude that are not averaged by MAS alone. In 1995 Frydman *et al*[55] proposed and demonstrated that by correlating multiple and single quantum coherences under MAS it is possible to obtain a high-resolution NMR spectrum. Fundamentally the multiple-quantum magic angle spinning (MQ-MAS) technique enables the observation of a purely isotropic echo from which the second-order broadening has been removed. This is recorded as a 2D experiment with a high-resolution isotropic indirect dimension and a MAS spectrum in the detection or direct dimension.

An expression for the average second-order frequency shift of the $|m_I = +m\rangle \leftrightarrow |m_I = -m\rangle$ transition for a half-integer quadrupolar spin $\boldsymbol{I}$ was given in eq.(2.21). It can be seen that the expression is a function of the second- and fourth-order Legendre polynomials so that at the magic angle $(\chi = 54.736°)$ the second-rank elements of the second-order quadrupolar interaction are removed. In MQMAS rf-pulse induces multiple quantum transitions after which the coherence freely precesses during an evolution period. In the vocabulary of NMR pulse sequences a p-quantum coherence

is a convenient mechanism to define the echo pathway in the pulse sequence. Formally it is defined as the superposition of the $|m\rangle$ and $|m'\rangle$ states with a multiplicity defined by $p = m - m'$. Using eq.(2.21) it is then possible to define the evolution undergone by a p-quantum coherence $(\frac{p}{2}, -\frac{p}{2})$ in terms of its accumulated phase (ϕ) as defined in eq.(2.29).[48]

$$\phi(p, \chi, \alpha, \beta, t) = \left\{\nu^{CS} p + A_I^{(0)}(p) Q^0(\eta) + C_I^{(4)}(p) P_4(cos\chi) Q^4(\alpha, \beta, \eta)\right\} t \tag{2.29}$$

where ν^{CS} is associated with the isotropic chemical shift.

After the spins have evolved over a period t_1 the spin system is transferred back to the $(-\frac{1}{2}, \frac{1}{2})$ central transition coherence and allowed to evolve over a second period t_2 that can be correlated to form the 2D experiment. The key factor in obtaining an isotropic echo signal is that under correlation the anisotropic part of the phase ϕ should be set to zero.

$$C_I^{(4)}(p) P_4(cos\chi) Q^4(\alpha, \beta, \eta) t_1 + C_I^{(4)}(-1) P_4(cos\chi) Q^4(\alpha, \beta, \eta) t_2 = 0 \tag{2.30}$$

From which it follows that if the multiple quantum $(\mp\frac{p}{2}, \pm\frac{p}{2})$ coherence is correlated with the $(-\frac{1}{2}, \frac{1}{2})$ central transition an isotropic echo will be observed at

$$t_2 = -\frac{C_I^{(4)}(p)}{C_I^{(4)}(-1)} t_1 \tag{2.31}$$

Therefore the unique feature of the MQ-MAS sequence is that it selectively averages the remaining anisotropic term (last term in eq.(2.21)) of the spin system by forcing it to evolve outside the central transition. Note that the ratio of $C_I^{(4)}(p)$ terms defined in terms of p-quantum coherences is able to change sign according to changing the sign of a p.[56]

$$R(I, p) = \frac{C_m^I}{C_{1/2}^I} = \frac{p[36I(I+1) - 17p^2 - 10]}{36I(I+1) - 27} \tag{2.32}$$

During the MQ-MAS experiment there are two possible echo pathways that can be described using the notation of the changes in p-quantum coherence: $0 \rightarrow p \rightarrow -1$ and $0 \rightarrow -p \rightarrow -1$. A distinction is made between a signal arising from a positive value of $R(I, p)$, which is called an echo, and that arising from a negative value that is called an

antiecho. How these echoes are dealt with in the pulse sequences in order to achieve purely absorptive lineshapes distinguishes between the two different MQMAS approaches; amplitude modulation during t_1 (z-filter) and phase-modulated during t_1 (shifted echo and antiecho). Specifically these strategies are used to remove the presence of dispersive components in the MQMAS that lower the resolution of the corresponding spectrum. The modifications to the original two pulse MQMAS sequence that these techniques employ to obtain a purely absorption 2D lineshape are shown in **Figure 2.10**.

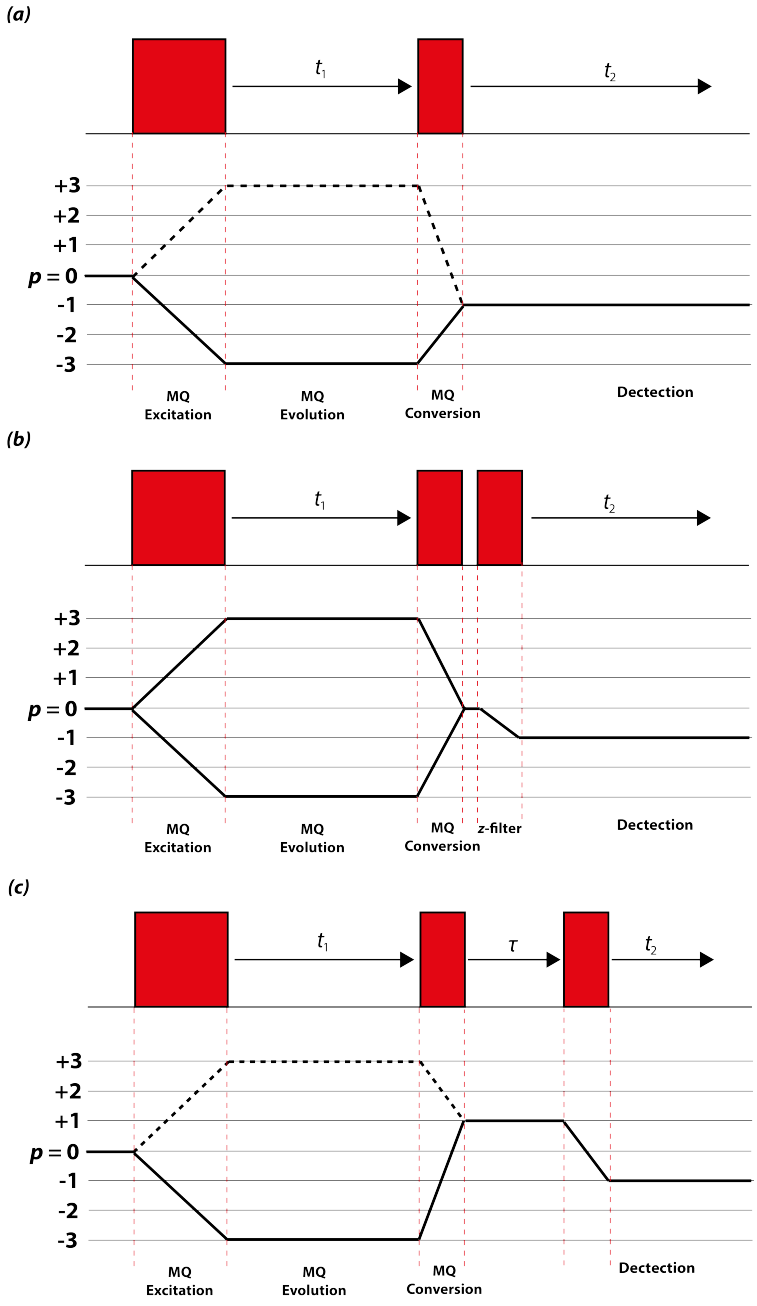

Figure 2.10, pulse sequence and coherence transfer pathway diagrams for a) Simple two-pulse amplitude modulated MQMAS b) Amplitude-modulated z-filter triple quantum experiment c) phase-modulated shifted-echo (solid line) and shifted-anti-echo (dotted line).

2.2.5 z-Filter Experiments

The z-filter experiment shown in figure 10 was introduced by Amoureux *et al*[57]. In contrast to the original MQMAS sequence[55] that used strong continuous wave rf-pulses for preparation of the multiple quantum excitation and mixing to the single quantum coherence $(0 \rightarrow \pm p \rightarrow -1)$ the z-filter breaks this process into a three-pulse sequence $(0 \rightarrow \pm p \rightarrow 0 \rightarrow -1)$. The z-filter is a hard pulse that transfers the multiple quantum coherence to a zero quantum coherence (magnetization is stored along $\boldsymbol{B_0}$) from which a soft central transition $\frac{\pi}{2}$ pulse transfers the signal into the observable single quantum coherence. This is significant because it makes the coherence pathway symmetric so that the echo and anti-echo intensities are equal so the resulting time domain signal is amplitude modulated: a pure cosine modulation along the indirect dimension, t_1. Spectra acquired using the amplitude-modulated method will present two resonances in the p-quantum dimension based symmetrically around $F_1 = 0$ positioned at $F_1 = \pm \nu_p$. To restore sign discrimination in F_1 the time-proportional phase incrementation (TPPI)[58] or the hypercomplex (*states*)[59] approach can be employed.

A 2D Fourier transform of the time domain signal will display a correlation spectrum where the resonances are aligned along a direction defined by

$$F_1 = R(I,p)F_2 \tag{2.33}$$

where F_2 and F_1 are frequencies in the single and multiple-quantum dimensions respectively. In order to obtain a purely isotropic Fourier transformed spectrum a shearing transformation in the form of a linear phase correction in the mixed (t_1, ν_2) domain is applied so that F_1 becomes an isotropic dimension F_{iso}. This means that the orthogonal projection of the MQMAS onto the F_{iso} does not include the anisotropic contributions from the quadrupole and chemical shift interactions. After the shearing transformation the new axis F_{iso} can be expressed as a linear combination of F_1 and F_2.

$$F_{iso} = F_1 + R(I,p)F_2 \tag{2.34}$$

The MQMAS spectrum can then be referenced such that a peak position along the multiple-quantum dimension accounts for the quadrupolar induced shift (eq. (2.12)) to the overall line position.

$$\delta_{MQ} = \delta_{iso} - \frac{10}{17}\delta_{QIS} \tag{2.35}$$

Hence for any given spin-system this axis becomes independent of the coherence pathway.

2.2.6 Phase modulated split t_1 whole echo

For suitably phased symmetrical whole NMR echoes the Fourier transform will yield a spectrum that is purely absorptive[60]. Massiot *et al*[61] adapted this principle for MQMAS, which is an echo-based experiment, as an alternate method of removing the dispersive component from MQMAS spectra. In order to ensure that the entire signal is detected in the t_2 domain a refocusing π pulse ($\pm 1Q \leftrightarrow \mp 1Q$) is applied at the end of the sequence.

This can be combined with the split-t_1 method of data acquisition proposed by Brown *et al*[49] to remove the need for the post-processing shear transformation. The namesake split-t_1 refers to the fact that the time t_1 is split into single-quantum and multiple quantum evolution periods in proportion to the ratio $R(I,p)$ so that the fourth-rank anisotropic term can always be refocused at the end of the t_1 period.

An example of the split-t_1 whole-echo pulse sequence is shown schematically in figure 10. The coherence transfer pathway $(0 \rightarrow \pm p \rightarrow 1 \rightarrow -1)$ is achieved via three pulses: a multiple-quantum excitation pulse, a conversion pulse and a soft π pulse.

2.2.7 Interpretation

The chemical shift axis for a sheared MQMAS experiments has a constant slope of 1. As has already been discussed in the presence of a significant quadrupolar interaction the observed chemical shift is displaced from the chemical shift axis. This displacement in the MQMAS experiment is called the quadrupolar-induced shift (QIS) and the direction of the displacement forms the QIS-axis that has a constant slope of $-10/17$ regardless of the values of I and p. Additionally there is an anisotropic axis (A) that aligns itself parallel to the F_2 axis. These axes are plotted on a MQMAS spectrum for $Sr_2Sc_{1.5}P_{0.5}O_{5.5}$ in **Figure 2.11**. They are useful for spectral interpretation. Narrow ridge-like alignment of the resonances parallel to the F_2 axis (along the A-axis) indicates a well-defined quadrupolar dominated environment. The strength of the interaction dictates the

distance of the resonances from the chemical shift axis. Broadening of the resonance along the chemical shift axis represents a dispersion of chemical shift environments.

The QIS-axis can be used to obtain the isotropic chemical shift : The axis can be shifted so that it intersects with the spectral lines centre of gravity, then the corresponding intersection point of the QIS-axis and the chemical shift axis along $F_1$is the position of the isotropic chemical shift.

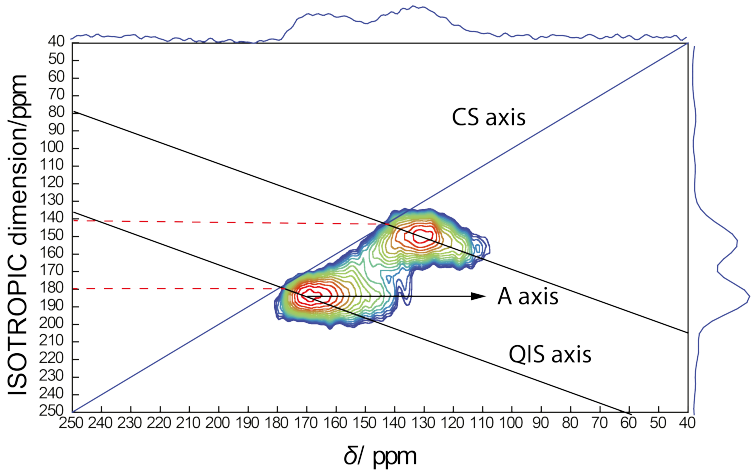

Figure 2.11, ^{45}Sc 3Q-MAS spectrum for $Sr_2Sc_{1.5}P_{0.5}O_{5.5}$ showing the quadrupolar-induced shift, chemical shift and A axes used for spectral interpretation.

2.2.8 MQ-MAS Inversion

A spectrum-inversion approach can be used to extract information from MQ-MAS NMR by reconstructing the underlying two-dimensional distribution of the isotropic chemical shift correlated to the quadrupolar interaction. As has previously been discussed a sheared MQMAS spectrum shows a correlation of the isotropic spectrum to the anisotropic spectrum. If one assumes homogeneous coherence transfer the projection of the MQMAS spectrum onto the anisotropic dimension is identical to the MAS spectrum. For an MAS spectrum the observed position of the resonance (δ_{cg}) is shifted according to the δ_{iso} due to the quadrupolar interaction as defined by eq (2.11).

While the position of the resonance on the isotropic 3Q-MAS dimension (δ_{MQ}) is a weighted average of the triple quantum and single quantum frequencies consistent with the conditions that insure the average fourth-rank anisotropic frequencies are all zero defined by the ratio R.[61]

$$\delta_{MQ} = \frac{1}{R+1}\delta_{MQ}^{\pm p} + \frac{R}{R+1}\delta_{MQ}^{-1} \tag{2.36}$$

$$\delta_{MQ}^{\pm p} = \mp p\delta_{iso} - \frac{\nu_Q^2.10^6}{\omega_0^2} A_I^{(0)}(p)\left(\frac{\eta^2}{3}\right).\left(\frac{1}{6\sqrt{5}}\right) \tag{2.37}$$

$$\delta_{MQ}^{-1} = \delta_{iso} - \frac{\nu_Q^2.10^6}{\omega_0^2} A_I^{(0)}(-1)\left(\frac{\eta^2}{3}\right).\left(\frac{1}{6\sqrt{5}}\right) \tag{2.38}$$

Hence for a spin $I = \frac{5}{2}$ δ_{CG} and δ_{MQ} become:

$$\delta_{CG} = \delta_{iso} - \frac{8\times10^6}{30}\frac{\nu_Q^2}{\omega_0^2} \tag{2.39}$$

$$\delta_{MQ} = -\frac{17}{31}\delta_{iso} - \frac{8\times10^6}{93}\frac{\nu_Q^2}{\omega_0^2}\left(\frac{\eta^2}{3} + 1\right) \tag{2.40}$$

The MQ-MAS experiment allows the measurement of δ_{CG} and δ_{MQ} directly. Therefore by an inversion procedure it is possible to separately determine δ_{iso} and ν_Q.

Zwanziger[62] has outlined two approaches for this purpose: the first option solves the forward problem where an initial guess is made of the distribution and iteratively adjusted by minimizing the sum of the squared deviation of the simulated spectrum with the experimental one, whereas the second approach solves the inverse problem by computing the distribution from the experimental data. Generally the second approach is favoured as the first method involves fitting to a model and therefore involves an inherent bias.

Any quadrupolar environment can be characterized by three parameters: δ_{iso}, ν_Q and η. For well-defined crystalline environments the asymmetry parameter η is well defined, however for a distribution of sites the two-dimensional MQ-MAS spectrum is featureless and an assumption must be made about η. If $I(\omega_{iso}, \omega_{MAS})$ denotes the frequency domain of the experimental MQ-MAS-spectrum then the theoretical MQ-MAS spectrum based on a calculation using (δ_{iso}, ν_Q) for a given MQ-MAS pulse sequence can be denoted by $I(\omega_{iso}, \omega_{MAS}; \delta_{iso}, \nu_Q)$.

$$I(\omega_{iso}, \omega_{MAS}) = \int_0^{+\infty} d\nu_Q \int_{-\infty}^{+\infty} d\delta_{iso}\pi(\nu_Q, \delta_{iso}) I(\delta_{iso}, \nu_Q; \omega_{iso}, \omega_{MAS})\delta\left(\delta_{iso} - \frac{(\omega_{iso} - \beta\nu_Q^2)}{\alpha}\right) \tag{2.41}$$

The constraint by the delta-function arises from the fact that the following can specify the position of the resonance on the isotropic dimension of the MQ-MAS spectrum:

$$\omega_{iso} = \alpha\delta_{iso} + \beta\nu_Q^2 \tag{2.42}$$

where α and β are numerical coefficients as shown previously.

This reduces the problem to a set of uncoupled one-dimensional equations that can be solved for ν_Q and δ_{iso}.

$$I(\omega_{iso}, \omega_{MAS}) = \int_0^{+\infty} d\nu_Q \, \pi(\nu_Q, \frac{-\omega_{iso} + \beta\nu_Q^2}{\alpha}) I\left(\nu_Q, \frac{-\omega_{iso} + \beta\nu_Q^2}{\alpha}; \omega_{iso}, \omega_{MAS}\right) \tag{2.43}$$

It is possible solve this equation for every slice of the MQMAS by a numerical procedure (generally the singular value decomposition (SVD)[62,57]) along curves $\tilde{\pi}(\nu_Q, \frac{-\omega_{iso}+\beta\nu_Q^2}{\alpha})$ in the two-dimensional parameter space where two dimensional interpolation leads to the original distribution $\pi(\nu_Q, \delta_{iso})$.

The major advantage of technique is that it readily reveals possible correlations between the δ_{iso}/ν_Q distributions. It has been employed extensively by Charpentier *et al* on various quadrupolar nuclei (^{27}Al, ^{23}Na and ^{17}O) in amorphous systems. [63,64,65,66] The compositional changes of sodium potassium niobate exemplify the potential of the method for identifying correlated behaviour as shown in **Figure 2.12**. For the potassium rich $K_{0.9}Na_{0.1}NbO_3$ there is little dispersion in the ^{23}Na NMR parameters, however for the sodium rich $K_{0.26}Na_{0.74}NbO_3$ there is a range in ^{23}Na environments orientated such the isotropic chemical shift and the quadrupolar parameters are strongly correlated.

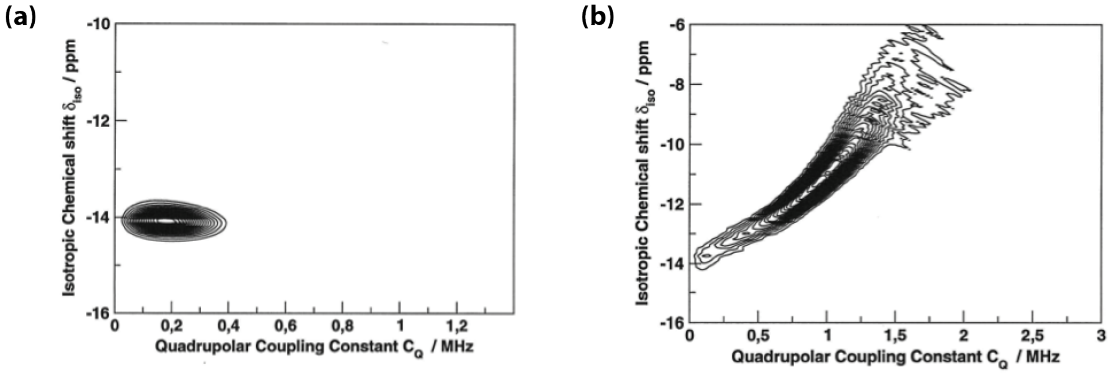

Figure 2.12, Inversion data for a) $K_{0.9}Na_{0.1}NbO_3$ and b) $K_{0.26}Na_{0.74}NbO_3$

2.2.9 Double Orientation Rotation

It was shown in section 2.2.1 that the second-order quadrupolar interaction possess second and fourth-rank terms that are proportional to the Legendre polynomials $P_2(cos\chi)$ and $P_4(cos\chi)$. As these share no common root it is impossible to completely remove the corresponding anisotropic terms using MAS alone. Double orientation rotation (DOR) was proposed independently by two groups in 1988[67,68] as a method to practically solve this problem by the use of two rotors simultaneously. Samoson e*t al*[68] first implemented the scheme where an outer rotor is spun at the conventional magic angle $P_2(cos\chi_{magic}) = 0$ while an inner rotor is spun at $\chi_2 = 30.56°$ with respect to $\boldsymbol{B_0}$ so that $P_4(cos\chi_2)$=0 as shown schematically in **Figure 2.13**.

In a modern setup of the technique the inner rotor can rotate with a frequency between 5-12 kHz while the much larger outer rotor can be expected to spin between 0.8-2 kHz where the spinning speeds are largely dictated by the torque exerted by the inner rotor upon the host rotor. The perfect spinning conditions are under zero torque that occurs is the following equation is satisfied:

$$\frac{\nu_{IR}}{\nu_{OR}} = cos\beta_{IR}\left(\frac{I_{tr}-I_{ax}}{I_{ax}}\right) \tag{2.44}$$

where β_{IR} is the angle between the inner and outer rotors, ν_{IR} and ν_{OR} are the angular frequencies of the inner and outer rotor respectively and I_{tr} and I_{ax} are the transverse and axial moments of inertia of the inner rotor.

Both ν_{IR} and ν_{OR} are measured experimentally so that the $\frac{\nu_{IR}}{\nu_{OR}}$ ratio is used as a guide for stable spinning conditions. The torque free value can be altered according to the dimensions of the inner rotor, but are generally chosen so that this value is ~5 and that the ratio is ideally between 5 and 6 during experimental implementation – below the torque free condition the inner rotor is liable to enter a downward spiral due to the torque becoming stronger, which can cause the rotor to slow down and stop abruptly.

In MAS it was shown that in order to average out an interaction then you must spin the sample at a rate comparable to or greater than the size of the interaction in Hz. However, this causes rotational echoes in the FID that create a manifold of spinning sidebands in the NMR spectrum after Fourier transform. The spinning sidebands are spaced at integer multiples of the rotor frequency from the isotropic line. For DOR the outer rotor is limited to the slow rotor frequency regime, which can complicate the DOR

spectrum. Samoson e*t al*[69] proposed odd-order sideband suppression to compensate for this limitation. By recognizing that the sample is effectively axially orientated relative to the outer rotor due to the outer rotors rotation the modulation in the FID is dependent on the position of the internal rotor with respect to the outer rotor, which is described by a phase γ_{IROR} shown schematically in **Figure 2.13**. Data acquisition is synchronized with the outer rotor positions $\gamma_{IROR'} = 0°$ and $\gamma_{IROR''} = 180°$ while the phase cycling is kept fixed for two acquisitions rather than one.

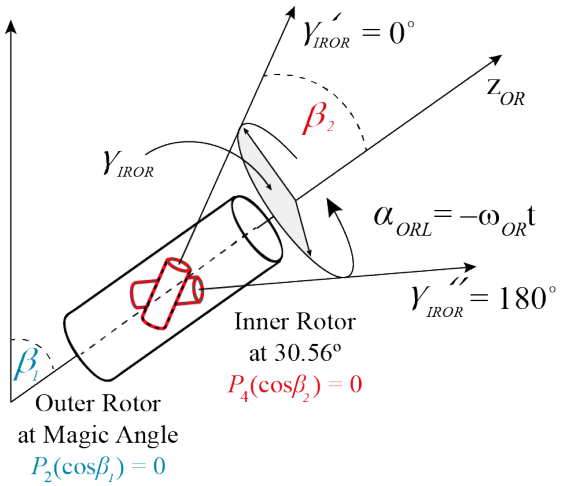

Figure 2.13, schematic of a DOR rotor and the angles at which the inner and outer rotor spin adapted from review[70]. The outer larger rotor spins at the magic angle of 54.74° with the smaller inner rotor spinning to narrow the $\mathbf{P_4}$ terms of the Legendre polynomials at 30.56° or 72.19°.

One-dimensional DOR spectra can be used to extract the isotropic chemical shift (δ_{iso}) and the quadrupolar product (P_Q) for a nuclear environment as the parameters are related to the centre of gravity of the DOR peak (δ_{DOR}) according to eq. ((2.45)

$$\delta_{DOR} = \delta_{iso} - \frac{3}{40} f(I) \frac{P_Q^2}{\omega_0^2} \tag{2.45}$$

$$P_Q = C_Q \left(1 + \frac{\eta_Q^2}{3}\right)^{\frac{1}{2}} \tag{2.46}$$

$$f(I) = \frac{\left[I(I+1) - \frac{3}{4}\right]}{I^2(2I-1)^2} \tag{2.47}$$

However, this requires DOR measurements at multiple fields in order to establish the magnitude of the quadrupolar-induced shift. By plotting the observed shift (δ_{DOR}) against $\frac{1}{\omega_0^2}$ as shown in **Figure 2.14** the quadrupolar induced shift can be extrapolated to

the infinite external magnetic field condition at which it is zero ($\delta_{DOR} = \delta_{iso}$). The gradient of the corresponding linear fit allows the extraction of P_Q.

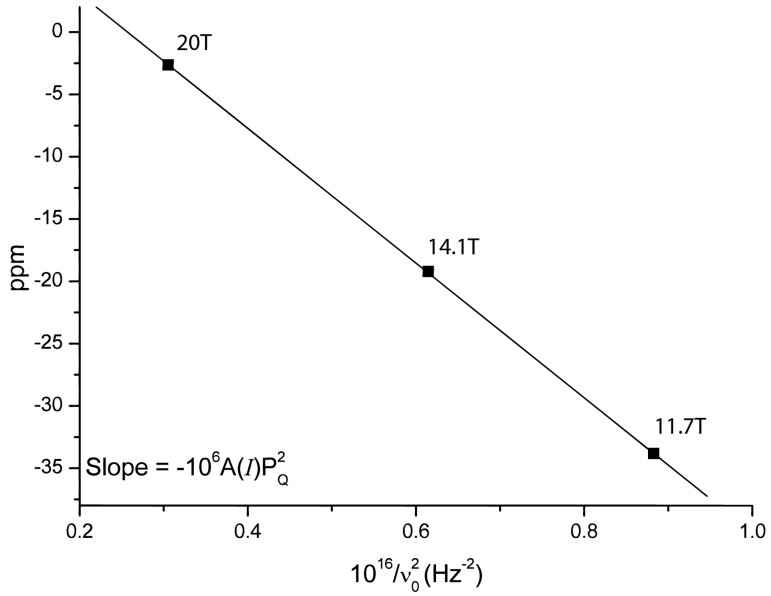

Figure 2.14, Plot of the DOR line position at three different magnetic fields against $\mathbf{1/\omega_0^2}$ adapted from James MacDonald's thesis[71]. The intercept gives the isotropic chemical shift $\boldsymbol{\delta_{iso}}$ and the slope $\mathbf{P_Q}$.

Under DOR the NMR spectrum is pseudo spin-$\frac{1}{2}$, that is with the removal of the quadrupolar broadening the lineshape is dictated by the same NMR interactions as for a spin-$\frac{1}{2}$ nuclei. For spin-$\frac{1}{2}$ nuclei it is possible in the slow MAS spinning regime the manifold of spinning sidebands approximates the shape of the NMR resonances in the absence of MAS. Under such conditions it is possible to fit the sideband intensities to obtain the chemical shift anisotropy (CSA). DOR can be used in an analogous manner for quadrupolar nuclei except that the sideband intensity depends on all the anisotropic interactions present in the sample and the relative orientation of the interactions respective tensors as described by Euler angles.[72]

This is particularly well illustrated by the ^{17}O DOR spectrum for [40%-^{17}O]OPPh$_3$ that is shown in **Figure 2.15** along with simulations based on the inclusion of various interactions including the quadrupolar interaction QI, CSA, J-coupling and the dipolar interaction. In this case the linewidths of the DOR spectrum are narrow enough to observe ^{17}O-^{31}P J-coupling, but the difference in the relative intensities of the two components of the line can only be accounted for by the inclusion of the entire set of corresponding NMR interactions.

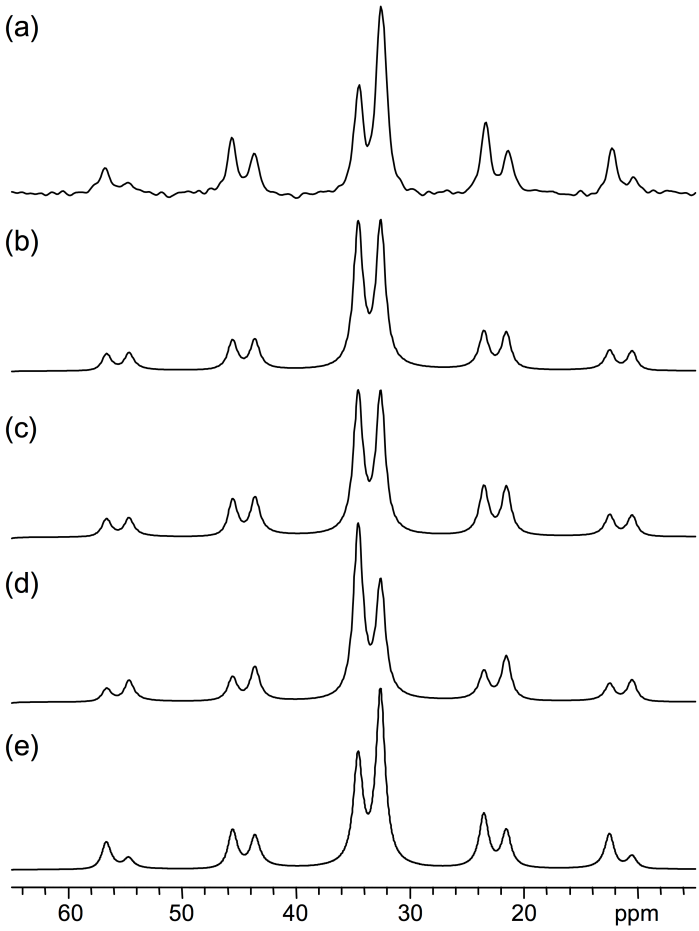

Figure 2.15, ^{17}O DOR spectra experimental (a) and simulations without ssb suppression of $OPPh_3$ at $\mathbf{B_0}$= 14.1 T, $\boldsymbol{\nu_{OR}}$= 900 Hz, $\boldsymbol{\nu_{IR}/\nu_{OR}}$~ 4.7 taken from a review on DOR[70] b) J-coupling (J) and Quadrupolar Interaction (QI) c) J + QI + Chemical Shift Anisotropy (CSA) d) J + QI + Dipolar Coupling (D) e) J + QI + CSA + D

2.3 Electronic Structure Calculations

First-principle calculations refer to the practical application of quantum-mechanical theory to calculate the cohesive properties of solids. There are two major schemes within the quantum chemistry community used for such calculations: those employing the Hartree-Fock (HF) theory and those employing density functional theory (DFT) that uses the electron density as the fundamental variable. In this work DFT is adopted primarily as a means to calculating NMR parameters. In this section electronic structure calculations at the DFT level of theory are briefly outlined before discussing the calculation of NMR parameters.

2.3.1 Density Functional Theory

The DFT approach begins by considering Schrödinger's equation under the Born-Oppenheimer approximation[73] where the electronic Hamiltonian $H(\boldsymbol{R})$ depends parametrically on the nuclear positions $\boldsymbol{R}$ so that for a system of electrons and nuclei:

$$\boldsymbol{H(R)\Psi(r;R)} = E(\boldsymbol{R})\boldsymbol{\Psi(r;R)} \tag{2.48}$$

where $\Psi(\boldsymbol{r};\boldsymbol{R})$ is the many-body wave-function of the coordinates of the electrons $\boldsymbol{r}$ and nuclei $\boldsymbol{R}$.

Hohenberg and Kohn proposed the fundamental theorems of DFT in 1964[74] where they developed an exact formal variational principle for the ground state energy formulated in terms of the electron density $\rho(\boldsymbol{r})$ as opposed to the full many body wave function used in Schrödinger's equation. Kohn and Sham[75] applied the variational theorem for the energy functional rendering the Schrödinger many-body problem in terms of a set of noninteracting fictitious particles. In this formalism the charge density is decomposed into a summation of one-particle orbtials $\psi_i(r)$ whose charge density is identical to that of the true system.

$$\rho(\boldsymbol{r}) = \sum_i \boldsymbol{n_i}|\boldsymbol{\psi_i(r)}|^2 \tag{2.49}$$

where n_i is the occupation number of the eigenstate that is represented by the one-particle wave function $\psi_i(r)$. The corresponding set of Kohn-Sham equations for the electronic eigenstate energy ε_i are defined in the following:

$$\left[-\frac{\hbar}{2m}\boldsymbol{\nabla^2} + V_{eff}(\boldsymbol{r})\right]\boldsymbol{\psi_i(r)} = \varepsilon_i\boldsymbol{\psi_i(r)} \tag{2.50}$$

$$V_{eff}(\boldsymbol{r}) = V_{nuc} + V_{hartree}[\boldsymbol{\rho}] + V_{xc}[\boldsymbol{\rho}] \tag{2.51}$$

$$V_{eff}(\boldsymbol{r}) = -e^2\sum_{\alpha}\frac{Z_\alpha}{|\boldsymbol{r}-\boldsymbol{R_\alpha}|} + e^2\int\frac{\rho(\boldsymbol{r})}{|\boldsymbol{r}-\boldsymbol{r'}|}\boldsymbol{dr'} + \frac{\delta E_{xc}[\rho(\boldsymbol{r})]}{\delta\rho(\boldsymbol{r})} \tag{2.52}$$

where e is the elementary positive charge, m is the mass of an electron, Z_α is the atomic number of atom α, r denotes the coordinates of a point in real space, R_α are the coordinates of each atom α.

The kinetic energy of the non-interacting electrons, the electrostatic interaction with nuclei (V_{nuc}) and the electrostatic repulsion due to the electron charge density generated by the other electrons in the system ($V_{hartree}[\rho]$) can all be computed directly. However, the true functional form of exchange-correlation $V_{xc}[\rho]$, which corresponds to the remaining many-body interaction, is unknown. To compensate for this deficiency assumptions must be made based on known physical constraints. The local density approximation (LDA)[75] is the crudest estimate of the exchange-correlation functional where the exchange-correlation contribution is considered equivalent to that of a uniform electron gas with the equivalent density to the point of interest. The LDA approximation has well-documented drawbacks: it generally overestimates the binding energy by 5-20%[76], while underestimating the lattice constant by ~1-3%. The generalized gradient approximation (GGA) improves results[77] for many properties by including the gradient of the charge density into the functional with the charge density at each point in space, although there remain complications with regards to 3d transition metals. In the context of GIPAW NMR calculations the GGA functional proposed by Perdew, Burke and Ernzerhof (PBE)[78] and an adaptation of this functional specifically for densely packed solids (PBEsol)[79] have been most widely applied.

2.3.2 DFT of Solid Materials

In a crystalline solid, the translational symmetry means that it can be reduced to a unit cell with periodic boundary condition. The reciprocal unit cell is defined by convention as the Brillouin zone (BZ) that can be mapped out by a series of continuous *k*-points. At each *k*-point only the occupied states contribute to the electronic density so that for a continuous distribution of k-points, in principle, an infinite number of calculations would be required to calculate the electronic potential. However, for macroscopic solids most properties vary smoothly across the BZ. Thus, for a small enough BZ, it can be assumed that a single *k*-point can be used to describe the electronic wavefunction for that region of space. For a larger BS, *k*-space is discretized into a set of regularly spaced points in the BZ and the electronic potential can be evaluated. The practical implementation for the evaluation of the density and electronic potential requires a consideration for the optimal method for integrating over *k*-space in the Brillouin zone. While there are a number of strategies for performing integrations numerically from a finite number of representative *k*-points[80,81,82] a common choice is the Monkhorst-Pack scheme.[81] Convergence tests to establish and reduce the error due to finite *k*-point sampling can be

completed by considering denser *k*-point grid.

2.3.3 Basis Set

In quantum chemistry codes the basis set is chosen so that the Kohn-Sham equations can be implemented in a computer program, therefore they are generally chosen to be linear combinations of simple mathematical functions that can be truncated to achieve an appropriate level of accuracy. Localized atomic centered orbitals [83,77] like Gaussian-type orbitals are well suited to expanding the electronic wave function and have been implemented in periodic simulations. However, the GIPAW method[11] has been implemented using a set of planewaves as the basis function and therefore this defines the focus of the rest of this chapter.

Bloch's theorem[84] states that the energy eigenstates for an electron in a periodically repeating environment can be written as Bloch waves, and therefore its electronic wavefunction $\psi_n^k(\boldsymbol{r})$ can be expanded in terms of a discrete plane wave basis set for each *k*-point k, and band/orbital n

$$\psi_n^k(\boldsymbol{r}) = e^{\boldsymbol{ik.r}} u_n^k(\boldsymbol{r}) \tag{2.53}$$

where $u_n^k(\boldsymbol{r})$ is a periodic function of the unit cell such that $u_n^k(\boldsymbol{r}) = u_n^k(\boldsymbol{r} + \boldsymbol{R})$.

If $\boldsymbol{G}$ are the set of reciprocal lattice vectors defined by $\boldsymbol{G}.\boldsymbol{l} = 2\pi m$ where $\boldsymbol{l}$ is a lattice vector of the crystal and m is an integer the periodic function can be expanded to give:

$$u_n^k(\boldsymbol{r}) = \sum_{\boldsymbol{G}} c_n^G(\boldsymbol{G}) e^{\boldsymbol{iG.r}} \tag{2.54}$$

Then planewave functions automatically satisfy the periodic boundary conditions.

$$\boldsymbol{\Psi_n^k}(\boldsymbol{r}) = \sum_{\boldsymbol{G}} \boldsymbol{c_n^{k+G}}(\boldsymbol{G}) \boldsymbol{e^{i(k+G).r}} \tag{2.55}$$

In order to exactly reproduce the spatial dependence of the wavefunction an infinite number of planewaves should be employed. However, the coefficients $c_n^{\boldsymbol{G}}$ of the plane waves with higher wave vectors $\boldsymbol{G}$ become increasingly insignificant, therefore a cut-off

wave vector is defined G_{cut} that truncates the basis set. This can be defined by the maximum kinetic energy of the waves it contains.

$$E_{cut} = \frac{\hbar G_{cut}^2}{2m} \tag{2.56}$$

Significant errors introduced by the basis set truncation can be avoided by converging the parameter of interest with respect to the cut-off energy E_{cut}, which is systematically controllable. The value of E_{cut} is atomic dependent as it relies upon the both the atomic species and the form of pseudopotential employed for each atomic species as will be discussed in the following section. Thus the optimization of the electronic structure reduces to locating the expansion coefficients that minimize the total energy using conjugate gradient methods[85].

Planewaves are less suited to the representation of the electronic wavefunction in contrast to Gaussian-type orbitals. Therefore a calculation using planewaves will require significantly more basis functions than the equivalent Gaussian-type orbital representation. For an all-electron description of a nucleus the tightly bound core electrons and the rapid oscillation of the valence electron function close to the nucleus require a vast number of planewaves to model accurately, which make such a description computationally expensive.

2.3.4 Pseudopotentials

The pseudo-potential approximation can be introduced to simplify the wavefunction so that it can be expanded in terms of a smaller number of planewaves.[86] This approximation arises from two distinct observations with regards to the core electrons and the oscillations of the valence wavefunction close to the nucleus. Indeed it is the valence electrons that generally dictate the cohesive properties of a solid where the "core" electrons are essentially chemically inert and unchanged by different chemical environments. In considering the valence electrons it is additionally observed that the computationally expensive oscillations of the valence function close to the nucleus do not directly contribute to bonding.

Under such circumstances the calculation of the core electron wavefunctions are unnecessary and can therefore be removed. Assuming that the core electrons do not take part in chemical bonding is called the frozen core approximation.[87] This approximation is

complicated by the presence of semicore states where the definition of valence and core states is less well-defined such as is observed for the 3p states in 3d transition metals[88]and the 1s states in Li[89]. In these cases the "valence" electrons are re-defined to include some of the filled atomic shells.

Nonetheless the idea of the pseudopotential is to remove the core electrons, the strong ionic potential and the interaction between the valence and core electrons with a smooth effective potential. As such this effective potential or pseudo-potential acts on a set of pseudo-wavefunctions rather than the true valence wavefunctions. Outside the core region the pseudo-wavefunction matches the all-electron wavefunction. Additionally the pseudopotential must contain 'projectors' which act on the valence electrons to remove any overlap with core states, enforcing orthogonality.

The pseudopotential is not a unique construction and numerous schemes have been developed to define optimal pseudopotentials for example [90,91,92,93]. In this thesis "ultrasoft pseudo-potentials" scheme developed by Vanderbilt[93] is implemented in conjunction with the CASTEP[94] quantum mechanical planewave code.

Pseudopotentials are constructed to minimize the number of planewaves needed to represent a wavefunction without significantly diminishing the predictive power of the method. With this in mind the pseudo-potential construction is completed under the requirement that the pseudo-wavefunction is smoothly varying in the core region. Under the Vanderbilt method[93] 'smoother' pseudo-wavefunctions can be generated by relaxing the condition that the norm of the wave function should give the charge density, which allows for the potential to be softer.

The projector-augmented wave (PAW) method[95] allows one to reintroduce the core electron density. This is important for the calculation of properties that rely on the electronic structure in the core region such as NMR-related properties. In this approach a linear transformation $(\boldsymbol{T})$ maps the valence pseudo-wavefunctions $\left(\left|\tilde{\Psi}\right\rangle\right)$ onto the all-electron wavefunctions $|\Psi\rangle$.

$$|\boldsymbol{\Psi}\rangle = \boldsymbol{T}\left|\tilde{\boldsymbol{\Psi}}\right\rangle \tag{2.57}$$

$$\boldsymbol{T} = \mathbf{1} + \sum_{\boldsymbol{R},\boldsymbol{n}} \left[\left|\boldsymbol{\phi}_{\boldsymbol{R},\boldsymbol{n}}\right\rangle - \left|\tilde{\boldsymbol{\phi}}_{\boldsymbol{R},\boldsymbol{n}}\right\rangle\right] \left\langle\tilde{\boldsymbol{p}}_{\boldsymbol{R},\boldsymbol{n}}\right| \tag{2.58}$$

where $\boldsymbol{\phi}_{\boldsymbol{R},\boldsymbol{n}}$ and $\tilde{\boldsymbol{\phi}}_{\boldsymbol{R},\boldsymbol{n}}$are the all-electron and pseudo partial waves derived from isolated

atomic calculations centered on an atomic site $\boldsymbol{R}$, n is an angular momentum quantum number and $\langle\tilde{p}_{\boldsymbol{R},n}|$ are a set of projectors such that

$$\langle\tilde{\boldsymbol{p}}_{\boldsymbol{R}',n}|\tilde{\boldsymbol{\phi}}_{\boldsymbol{R},m}\rangle = \boldsymbol{\delta}_{\boldsymbol{R},\boldsymbol{R}'}\boldsymbol{\delta}_{\boldsymbol{n},\boldsymbol{m}} \tag{2.59}$$

The atomic states provide a good basis for the re-construction of the wavefunction in the core region and by this method the all-electron form replaces the component of a given atomic-like states in the pseudo-wavefunction form.

2.3.5 Geometry Optimization

For a typical GIPAW-DFT based NMR calculation one starts from an initial guess at the crystal structure sourced either from diffraction based investigations or computational prediction. This structure is generally geometry optimized to allow the positions of the atoms to vary under a specified level of constraint (restricting the point symmetry and lattice dimensions are common practice) so that the forces within the system are minimized.

Geometry optimization forms an iterative process whereby the user specifies the initial starting geometry. The total energy is then used to establish the forces on the ions, (F_I), according to:

$$\boldsymbol{F_I} = -\boldsymbol{\nabla_R}\langle E\rangle \tag{2.60}$$

where I denotes the ion of interest, E is the energy of the system and $\boldsymbol{R_I}$ is the position of the ion. Ions are moved to a new position using a standard minimisation algorithm [96,97,98], typically the Broyden-Fletcher-Goldfarb-Shanno[97] scheme for calculations reported in this thesis. At each minimization step the electronic configuration is re-optimized. The total energy for the new configuration is then calculated and compared with the previous configurations and the forces are tested against tolerance limits. If the structure is not 'optimised' the process continues and a new set of ionic positions is generated. This cycle continues until the forces are within the tolerance limit and the resulting configuration should correspond to the local energy minimum. The outputted geometry is used as an input for the GIPAW calculation of the NMR tensors. It should be emphasized here that these are static calculations that neglect temperature effects. As such they are frequently described as being undertaken at 0K, though a true 0K

calculation should account for zero point energy.

As NMR experiments are commonly completed under ambient conditions the corresponding NMR parameters can be influenced by thermal motion. Two methods have been proposed for incorporating motional effects by generating a set of configurations from which average NMR parameters can be calculated. The first employs molecular dynamic simulations over a relevant timeframe, while the second method uses vibrational modes to generate a set of configurations.[99]

2.3.6 Calculating the Electric Field Gradient

As was discussed in section 2.1.3 the electric field gradient tensor can be expressed by a traceless tensor that can be denoted $G_{\alpha\beta}(\boldsymbol{r})$:

$$G_{\alpha\beta}(r) = \frac{\partial E_\alpha(r)}{\partial r_\beta} - \frac{1}{3}\delta_{\alpha\beta}\sum_\gamma \frac{\partial E_\gamma(r)}{\partial r_\gamma} \tag{2.61}$$

where α, β, γ denote the Cartesian coordinates x, y, z and $E_\alpha(\boldsymbol{r})$ is the local electric field at the position **r**. The local electric field can be calculated from the total charge density $n(\boldsymbol{r})$, which corresponds to the sum of the ionic and electronic charge distributions.

$$E_\alpha(\boldsymbol{r}) = \int \boldsymbol{d^3 r'} \frac{n(\boldsymbol{r'})}{|\boldsymbol{r} - \boldsymbol{r'}|^3}(\boldsymbol{r_\alpha} - \boldsymbol{r'_\alpha}) \tag{2.62}$$

Then the EFG tensor is equal to:

$$G_{\alpha\beta}(\boldsymbol{r}) = \int \boldsymbol{d^3 r'} \frac{n(\boldsymbol{r'})}{|\boldsymbol{r} - \boldsymbol{r'}|^3}\left[\delta_{\alpha\beta} - \boldsymbol{3}\frac{(\boldsymbol{r_\alpha} - \boldsymbol{r'_\alpha})(\boldsymbol{r_\beta} - \boldsymbol{r'_\beta})}{|\boldsymbol{r} - \boldsymbol{r'}|^2}\right] \tag{2.63}$$

Therefore the calculation of the EFG tensor only requires knowledge of the ground-state charge density. While this can be directly obtained from all-electron approaches, in the context of the pseudopotenital approach it can be calculated using the PAW or GIPAW methodologies to re-construct the all-electron charge. Both the PAW and GIPAW approaches have been shown to reliably predict the EFG tensor in solids[100]. Indeed the GIPAW method has been directly compared to the all-electron Linear Augmented Planewave method (LAPW)[101] method and shown to be in very good agreement.[102,103]

To obtain the all-electron electronic charge distribution from the ground-state pseudo-

wavefunction the density is 'corrected' such that:

$$n^{El}(\boldsymbol{r}) = n^{El,PS}(\boldsymbol{r'}) + n^{El,corr}(\boldsymbol{r}) \tag{2.64}$$

where $n^{El,PS}(\boldsymbol{r'})$ is the electronic density calculated from the ground-state pseudo-wavefunction and $n^{El,corr}(\boldsymbol{r})$ is the correction term to the density unique to either the PAW or GIPAW approach. Here we outline the PAW approach to the reconstruction of the all-electron charge[100].

For the ground-state density from the pseudized wavefunction its contribution to the EFG tensor $G_{\alpha\beta}^{El,PS}(\boldsymbol{r})$ can be calculated in reciprocal space using the eq. where $n(\boldsymbol{r}) = n^{El}(\boldsymbol{r'}) = \mathbf{2}\sum_o \left\langle \tilde{\psi}_o^{(\mathbf{0})} \middle| \boldsymbol{r'} \right\rangle \left\langle \boldsymbol{r'} \middle| \tilde{\psi}_o^{(\mathbf{0})} \right\rangle$. Likewise the eq. can be used to establish the contribution $G_{\alpha\beta}^{El,corr}(\boldsymbol{r})$ setting $n(\boldsymbol{r}) = n^{El,cor}(\boldsymbol{r'})$.

$$\begin{aligned} \boldsymbol{n^{El,corr}(r)} = \mathbf{2} \sum_{\boldsymbol{R,o,J,J'}} & \left\langle \tilde{\psi}_o^{(\mathbf{0})} \middle| \tilde{p}_{RJ} \right\rangle \left[\langle \phi_{RJ} | r \rangle \langle r | \phi_{RJ'} \rangle \right. \\ & \left. - \langle \tilde{\phi}_{RJ} | r \rangle \langle r | \tilde{\phi}_{RJ'} \rangle \right] \left\langle p_{RJ'} \middle| \tilde{\psi}_o^{(\mathbf{0})} \right\rangle \end{aligned} \tag{2.65}$$

where $|\phi_{R,J}\rangle$ and $|\tilde{\phi}_{R,J}\rangle$ are the all-electron and pseudopartial-waves of the atomic site $\boldsymbol{R}$, the index $J(J')$ refer to the angular moment $l(l')$, its projection on the z-axis $m(m')$. $|\tilde{p}_{R,J}\rangle$ are the projectors as defined in eq. (2.63).

For ultrasoft pseudopotentials the contribution due to the density from atomic sites other than $\boldsymbol{R}$ must be included, however for norm-conserving pseudopotentials these correction terms can be ignored greatly simplifying the expression for $G_{\alpha\beta}^{El,corr}(\boldsymbol{r})$:

$$\begin{aligned} \boldsymbol{G_{\alpha\beta}^{El,corr}(R)} = \mathbf{2} \sum_{\boldsymbol{o,J,J'}} & \left\langle \tilde{\psi}_o^{(\mathbf{0})} \middle| \tilde{p}_{RJ} \right\rangle \left[\left\langle \phi_{RJ} \middle| \frac{\mathbf{1}}{\boldsymbol{r^3}} \left[\delta_{\alpha\beta} - \mathbf{3} \frac{\boldsymbol{r_\alpha r_\beta}}{\boldsymbol{r^2}} \right] \middle| \phi_{RJ'} \right\rangle \right. \\ & \left. - \left\langle \tilde{\phi}_{RJ} \middle| \delta_{\alpha\beta} - \mathbf{3} \frac{\boldsymbol{r_\alpha r_\beta}}{\boldsymbol{r^2}} \middle| \tilde{\phi}_{RJ'} \right\rangle \right] \left\langle p_{RJ'} \middle| \tilde{\psi}_o^{(\mathbf{0})} \right\rangle \end{aligned} \tag{2.66}$$

Finally the contribution to the total charge density distribution from the ionic charges Z_R from atomic sites at positions $\boldsymbol{R}$ can also be calculated according to eq. (2.63).

$$G_{\alpha\beta}^{ION}(r) = \sum_{R} \frac{Z_R}{|r-R|^3}\left[\delta_{\alpha\beta} - 3\frac{(r_\alpha - R_\alpha)(r_\beta - R_\beta)}{|r-R|^2}\right] \tag{2.67}$$

2.3.7 Calculating the Chemical Shift

Magnetic shielding was introduced in section 2.1.2. Here it was shown that the magnetic shielding (σ) describes the induced field (B_{in}) experienced by a nuclear spin due to the electronic response to an applied field (B_0).

$$B_{in} = -\sigma B_0 \tag{2.68}$$

The induced field $\left(B_{in}(r)\right)$ arises solely from orbital currents $j(r)$ due to the applied field:

$$B_{in}(r) = \frac{1}{c}\int d^3\, r' j(r') \times \frac{r-r'}{|r-r'|^3} \tag{2.69}$$

Then the calculation of the magnetic shield relies on being able to compute the electronic current induced by the applied field. This is completed quantum mechanically using first-order perturbation theory where the electronic wave function (ψ) in the presence of an applied external field is expanded as the ground-state wavefunction in the absence of the field $\left(\psi^{(0)}\right)$ with a first-order change described by the wavefunction $\psi^{(1)}$.

$$\psi(r) = \psi^{(0)}(r) + \psi^{(1)}(r) + O(B^2) \tag{2.70}$$

The quantum mechanical probability current can be written as the sum or the diamagnetic and paramagnetic terms:

$$J(r') = J^d(r') + J^p(r') \tag{2.71}$$

$$J^d(r') = \frac{1}{c}A(r')|r'\rangle\langle r'| \tag{2.72}$$

$$J^p(r') = -\frac{|r'\rangle\langle r'| + |r'\rangle\langle r'|p}{2} \tag{2.73}$$

Then the first-order term of the induced orbital current $j^{(1)}(r)$ is:

$$j^{(1)}(r') = 4\sum_{o} Re\left[\left\langle \Psi_o^{(0)} \middle| J^p(r') \middle| \Psi_o^{(1)} \right\rangle\right] + 2\sum_{0} \left\langle \Psi_o^{(0)} \middle| J^d(r') \middle| \Psi_o^{(0)} \right\rangle \quad (2.74)$$

The first-order change in the wavefunction and $\left|\Psi_o^{(1)}\right\rangle$ is given by:

$$\left|\Psi_o^{(1)}\right\rangle = \sum_{e} \frac{\left|\Psi_e^{(0)}\right\rangle\left\langle\Psi_e^{(0)}\right|}{\varepsilon_o - \varepsilon_e} H^{(1)} \left|\Psi_o^{(0)}\right\rangle = \mathcal{G}(\varepsilon_o^{(0)}) H^{(1)} \left|\Psi_o^{(0)}\right\rangle \quad (2.75)$$

where $H^{(1)} = \frac{1}{2c}(p.A + A.p)$.

Then the induced current can be expressed as:

$$j^{(1)}(r') = 4\frac{1}{2c}\sum_{o} Re\left[\left\langle \Psi_o^{(0)} \middle| J^p(r') \mathcal{G}(\varepsilon_o^{(0)}) r' \times p \middle| \Psi_o^{(0)} \right\rangle\right] - \frac{1}{2c}\rho(r') B \times r' \quad (2.76)$$

by using the symmetric gauge for the vector potential, $A(r) = \frac{1}{2} B \times r$ and simplifying the expression by using the fact that $\rho(r') = 2\sum_o \left\langle \Psi_o^{(0)} \middle| r' \right\rangle \left\langle r' \middle| \Psi_o^{(0)} \right\rangle$.

For finite basis sets this highlights a practical complication with regards to calculating the chemical shielding for identical chemical environments known as the gauge origin problem. The definition of the symmetric gauge is not unique and as the derivation relies upon the choice of $A(r)$ can change the balance between paramagnetic and diamagnetic currents, though the total current is well defined. So two identical chemical sites at different distances from the gauge origin will have the same shielding, but different diamagnetic and paramagnetic terms. However, the diamagnetic and paramagnetic terms do not converge with respect to the atomic orbital basis set at the same rate so that for two identical sites there is a possibility that they will have different computed shieldings.

For planewave basis sets the gauge-origin problem arises from the introduction of the localized atomic states via the PAW transformation[95]. The pioneering work of Pickard and Mauri[11] introduced the Gauge Including Projector Augmented Wave (GIPAW)

method to address this problem. In this approach a field-dependent transformation operator (T_B) imposes translational invariance exactly:

$$\boldsymbol{T_B = 1 + \sum_{R,n} e^{\left(\frac{i}{2c}\right)r.R\times B}\left[\left|\phi_{R,n}\right\rangle - \left|\widetilde{\phi}_{R,n}\right\rangle\right]\left\langle\widetilde{p}_{R,n}\right|e^{-\left(\frac{i}{2c}\right)r.R\times B}} \tag{2.77}$$

Practically eq. (2.76) is not used for extended systems. In the GIPAW method to calculate the shielding tensor in crystal the current description is re-worked such that the cell-periodic function part of the Bloch function can be exploited. This is completed by considering the response to a magnetic field with a finite wavelength $\boldsymbol{B = \sin(q.r)\hat{q}}$ in the limit $q \to 0$ that corresponds to the uniform field. For a full derivation the reader is referred to references [104,11]. In this formalism calculating the induced current at a *k*-point in the BZ requires an additional consideration of the wavefunction at $\boldsymbol{k \pm q}$ where the current is defined as:

$$\boldsymbol{j^{(1)}(r') = \lim_{q\to 0}\frac{1}{2q}[S(r',q) - S(r',-q)]} \tag{2.78}$$

$$\boldsymbol{S(r',q) = \frac{2}{cN_k}\sum_{i=x,y,z}\sum_{o,k} Re\left[\frac{1}{i}\left\langle u^{(0)}_{o,k}\middle|J^{p}_{k,k+q}(r')\mathcal{G}_{k+q}(\varepsilon_{o.k})B\times u_i.(p+k)\middle|\bar{u}^{(0)}_{o,k}\right\rangle\right]} \tag{2.79}$$

$$\boldsymbol{J^{p}_{k,k+q_i} = -\frac{(p+k)|r'\rangle\langle r'| + |r'\rangle\langle r'|(p+k+q_i)}{2}} \tag{2.80}$$

where $\boldsymbol{q_i = qu_i}$, N_k is the number of *k*-points included in the BZ summation.

2.4 Theoretical Approaches to Modelling Disorder in Solids

2.4.1 Site-Occupancy Disorder

The Site-Occupancy Disorder (SOD) software[16] implements a methodology to reduce the number of configurations that need to be considered when modelling partial occupancy disorder in solids by exploiting the fact that many configurations are symmetry related and therefore identical.

An isometric transformation is a geometric operation (e.g. reflections, rotations and translations) that leaves the object and its image unchanged. For crystals, the

symmetry operations that map the structures onto itself are isometric[105]. In the context of different realisations of a crystal considered by SOD, two configurations are considered equivalent if there is one isometric transformation that converts one in to the other (see **Figure 2.16**).

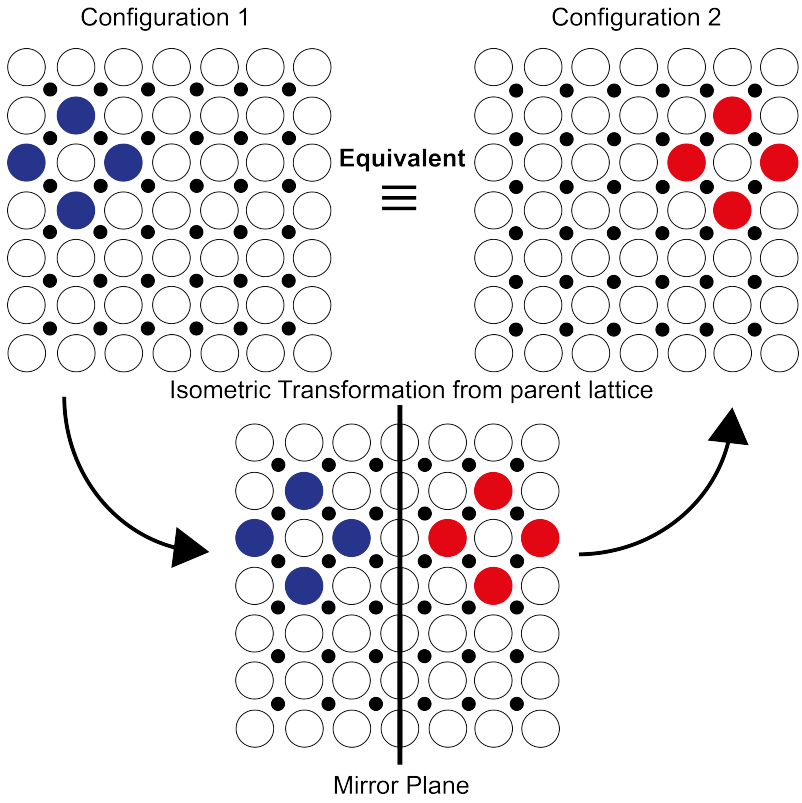

Figure 2.16, illustration of equivalent configurations related by an isometric transformation. Figure is adapted from Crespo et al.[16]

Given that the parent structure of a crystal lattice defines the lattice from which *all* configurations can be derived, the symmetry operator that converts one configuration into another has to be a symmetry operator of the parent lattice.

Therefore to establish whether configurations derived by effecting certain site substitutions are equivalent, it is sufficient to establish if any of the symmetry operators of the parent structure map one configuration into the other. In general a substitution will break the symmetry of the parent lattice so that the symmetry operator that transforms one configuration into another is not necessarily a symmetry operator of the two equivalent structures, but has to be of the parent structure. In this manner it is possible to limit the configurational space to a set of symmetrically inequivalent configurations.

In general it is necessary to create a supercell from the small crystal unit cell with fractional sites occupancies to describe the aperiodic crystal generated by the site-

occupancy disorder. Then the complete SOD approach involves establishing the symmetry operators of the supercell. The symmetry operators are the pool of isometric transformations that can be used to establish all the equivalent configurations within the complete space of N configurations. This defines a reduced configurational space of M independent configurations where in general $M \ll N$. Each independent configuration $m \in M$ is attributed a degeneracy corresponding to the number of configurations in the complete space that are equivalent to the independent configuration m.

The SOD approach is limited by the size of the supercell one can afford, both due to the expense of a larger cell and the fact that larger cells have more permutations. Ideally one increases the supercell size, considering all permutations, until the quantity of interest converges i.e. no new environments are sampled which are not just repeats of those generated with smaller supercells. However, in general this is rarely practiced because it is too computationally expensive.

2.4.2 Special Quasi-random Structures

The Special Quasi-random Structure (SQS)[17] method was proposed as an extension of structural techniques such as the cluster expansion technique[18,106] used in the calculation of the properties of substitutionally random binary $A_{1-x}B_x$ alloys. The cluster expansion is a generalization of the Ising Hamiltonian that can be used to expand any configuration-dependent physical quantity as a weighted series of multi-site cluster functions.

The Ising model for magnetic materials labels each lattice site as -1 for spin down or +1 for spin up so that a Hamiltonian can be constructed that describes the system in terms of the spin of each lattice site. Thus a given configuration can be denoted by a vector $\boldsymbol{\sigma}$ consisting of spin σ_i variables describing the type of spin on the parent lattice. Then the nearest-neighbour Ising model can be represented by eq. ((2.81)

$$\boldsymbol{E(\sigma_1, \sigma_2, \sigma_3, \ldots, \sigma_N) = J_0 + J_1 \sum_{j}^{N} \sigma_j + J_{ij} \sum_{<i,j>} \sigma_i \sigma_j} \tag{2.81}$$

where $< i, j >$ is the summation over all nearest neighbor pairs, J_{ij} are the nearest-neighbour interaction energies between lattice sites i and j and N is the number of occupied lattice sites.

This formalism is adopted in the cluster expansion technique to denote the occupation of a lattice site by either an element A or and element B: each lattice site is labelled by -1 for the presence of an element A or +1 for the presence of an element B (see Figure 2.17).

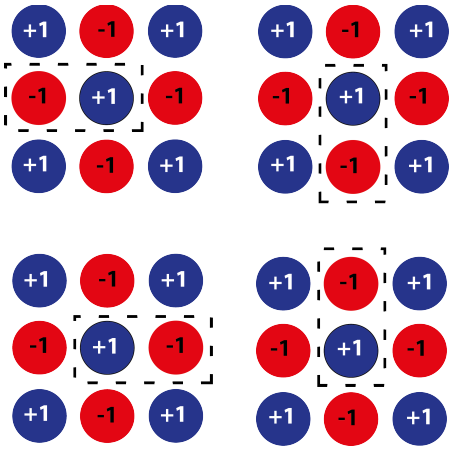

Figure 2.17, the unique orientations of a nearest neighbour (pair) cluster

Analogously a given configuration is denoted by a vector $\boldsymbol{\sigma}$ consisting of spin-like σ_i variables describing the occupation of each site on the parent lattice. For a configuration of N lattice sites this is denoted:

$$\boldsymbol{\sigma} = (\boldsymbol{\sigma_1}, \boldsymbol{\sigma_2}, \boldsymbol{\sigma_3}, \ldots, \boldsymbol{\sigma_N}) \tag{2.82}$$

where $\sigma_i = \pm 1$.

The cluster expansion refers to the fact that Hamiltonian is expanded to include interactions from additional groups of atoms or "clusters" such as multiple pair interactions, triplet and quadruplet interactions etc. (see **Figure 2.18**).

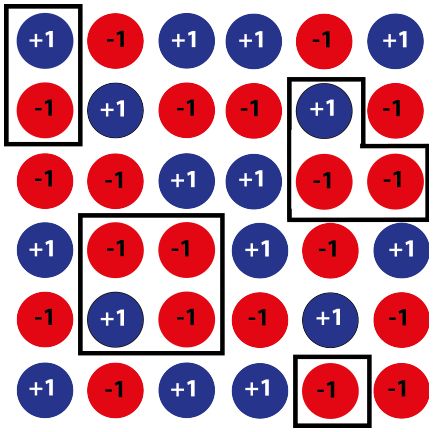

Figure 2.18, examples of orientations that would contribute to single, pair, triplet and quadruplet clusters

The clusters are discretized into "figures" $f = (k, m)$ where k denotes a group of atoms e.g. pair $k = 2$, triplet $k = 3$, quadruplet $k = 4$ etc and m denotes the mth-neighbour distance. In fact the Hamiltonian is exact if *all* possible figures (f) that can be found among the lattice sites, that is all inequivalent clusters up to the *M*-body interaction are included in the expansion. In the basic formalism of the cluster expansion $\Pi_f(\boldsymbol{l}, \boldsymbol{\sigma})$ is defined as the product $\Pi\sigma_i$ of spin variables for figure f positioned in the lattice at location $\boldsymbol{l}$. If there are D_f figures per site then this allows one to represent a lattice average of the spin product over all locations of symmetry-related figures of type f:[17]

$$\overline{\boldsymbol{\Pi}}_{\boldsymbol{f}}(\boldsymbol{\sigma}) = \frac{\mathbf{1}}{\boldsymbol{N}\boldsymbol{D}_{\boldsymbol{f}}} \sum_{\boldsymbol{l}} \boldsymbol{\Pi}_{\boldsymbol{f}}(\boldsymbol{l}, \boldsymbol{\sigma}) \tag{2.83}$$

Then for this method the configuration-dependent ensemble of a physical quantity P over configurations can be expanded as:[18]

$$\langle \boldsymbol{P} \rangle = \sum_{\boldsymbol{k},\boldsymbol{m}} \boldsymbol{D}_{\boldsymbol{k},\boldsymbol{m}} \langle \overline{\boldsymbol{\Pi}}_{\boldsymbol{k},\boldsymbol{m}} \rangle \boldsymbol{p}_{\boldsymbol{k},\boldsymbol{m}} \tag{2.84}$$

Where k is the cluster size and m is the mth-neighbour distance $p_{k,m}$ are the interaction parameters of figures $f = (k, m)$ and $\langle \overline{\Pi}_{k,m} \rangle$ are the correlation functions.

In the cluster expansion method the interaction coefficients are calculated from an independent set of calculations for the property of interest, which are subsequently used to fit the model. The models accuracy is appraised against known experimental values and if considered inaccurate the fitting set is expanded and the process repeated. Accordingly the interaction coefficients approach those of a perfectly random $A_{1-x}B_x$ structure. However, the many-body correlation functions for a completely random binary alloy can be expressed according to:

$$\langle \overline{\boldsymbol{\Pi}}_{\boldsymbol{k},\boldsymbol{m}} \rangle = (\mathbf{2}\boldsymbol{x} - \mathbf{1})^{\boldsymbol{k}} \tag{2.85}$$

The simple analytic expression for the correlation functions of a perfectly random alloy is the basis for the SQS methods. Rather than converging upon the expression by traditional statistical sampling methods like the cluster expansion technique, the SQS

approach simply designs *N*-atom periodic structures whose distinct correlation functions $\overline{\Pi}_{k,m}$ best match the random ensemble averages of a random alloy.

While the SQS approach was initially proposed in the context of random alloys it can be can be generalized to any lattice types where the distribution of species upon the parent lattice is approximately random. Indeed there are now numerous cases where the method has been applied to cation partial occupancy problems in perovskite systems. It should be emphasized that in the latter case not all sites in the crystal are subject to the disorder, i.e. the Ising-like spin analogues are occupancies of just some of the crystallographic sites. The major limitation of the SQS approach is that it is implemented under the rather severe approximation that there exists purely random occupancy for a given lattice site, which neglects short-ranged ordering. For many materials, such as the apatites investigated in chapter 4 where the lattice favours configurations with larger Ca sites separations, this approximation is violated.

3

LITERATURE REVIEW

3.1 General computational approaches to characterizing disorder for GIPAW calculations

The introduction of the GIPAW[11] method for the calculation of chemical shifts in extended periodic solids has enabled numerous experimental NMR and GIPAW-DFT approaches to structural characterization. The sensitivity of NMR spectrometry to the local nuclear environment has already opened up new opportunities for the sophisticated characterization of slight thermal disorder; Cadar *et al*[107] has proposed a general approach to sample local disorder from a study on bisphosphinoamine that used the statistical analysis of 2D ^{31}P-^{31}P through-space correlation NMR lineshapes to provide information on the maximum range of the dynamic distortions. The thermally motivated dynamic motion is subsequently sampled by generating structures within the constraints of the NMR data by using the low energy vibrational modes of the proposed crystal structure to inform possible distortions. The GIPAW-DFT calculated isotropic shifts of the generated structures were used to predict the 2D crosspeak positions in NMR correlation spectra to refine the possible dynamics.

However, in general the characterization of disorder by the combined approach remains in its infancy and existing studies reflect this by the variation in approaches reported in the literature. Perhaps the one exception to this situation is in glass that has been extensively characterized by theoretical modelling techniques. In this case the well-defined general approach to studying these materials has simply been adapted to accommodate GIPAW-DFT calculations; employ molecular dynamics (MD) simulations to generate an ensemble of model glass structures, refine these models using a DFT-based geometry optimization and finally calculate the NMR parameters. For bulk properties like NMR observables the experimental results are compared to a Boltzmann weighted value and the interpretation of NMR spectra through comparison with GIPAW-DFT calculations has proved to be highly successfully to a wide range of

glasses. [108,109,65, 108] Although this methodology is limited by the quality of the MD potential: if there isn't a close match between the DFT energy landscape then the MD might not visit structures that would be strongly weighted by the DFT energetics.

Broadly speaking computational approaches to disorder can generally be divided into two subsets based on whether they are considering static positional type disorder (see **Figure 3.1**) or local dynamics. As this thesis is largely concerned with the former this forms the focus of this review.

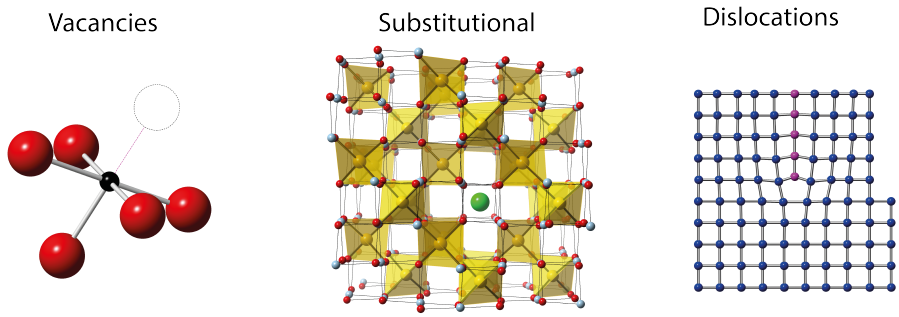

Figure 3.1, pictorial representation of various types of static disorder

There are a number of ad-hoc investigations in the literature on the subject of positional disorder that generally attempt to extract a correlation between possible realizations of disorder and one or more of the NMR parameters to aid the rationalization of the experimental NMR data. An investigations into cationic disorder in the $Y_2Ti_{2-x}Sn_xO_7$ pyrochlores where the Sn/Tn disorder was studied by combining ^{89}Y and ^{119}Sn NMR with the computation of NMR parameters by GIPAW-DFT is a particularly good example of this.[110] Here the possible arrangements of the six next nearest neighbours of Sn^{4+}/Tn^{4+} to the yittrium occupied A-site and Sn/Ti occupied B-site were manually generated. Subsequently the structures were relaxed before the NMR parameters were calculated allowing the identification of a strong correlation between the number of Sn nearest neighbours and ^{89}Y isotropic chemical shifts.

In general, the characterization of point defect type disorder in solids by quantum mechanical studies adopts either the cluster or supercell approach. The supercell approach is more suited to the study of defects in the context of bulk properties as the cluster method is prone to spurious perturbations arising from the truncation of the infinite lattice. The supercell approach exploits the implementation of *ab initio* programs designed to characterize periodic perfect crystals for the study of local defects. As the GIPAW method allows the calculation for NMR chemical shift for extended systems,

where the three-dimensional structure is recreated from a single unit cell the supercell approach would seem highly suitable for defect-related investigations.

It is useful at this juncture to briefly describe the supercell approach before reviewing existing literature on the method in the context of ssNMR. For a completely ordered solid the three dimensional crystal structure can be constructed from a unit cell that is repeated along each lattice dimension. For disordered solids containing substitutional defects the crystal structure is aperiodic, but can be approximated to a crystal composed of periodically repeating 'supercells' that contain the local defect(s) (see **Figure 3.2**). The supercell size is generally picked to contain the defective zone, which generally translates to the use of a larger or 'super' cell of $O(10^2)$ atoms. However as the unit cell size is increased so does the computational cost as not only are bigger cells more expensive to simulation but as the cell size increases the number of permutations of defective or substitutional sites also increases, which highlights the first and major disadvantage of the supercell approach.

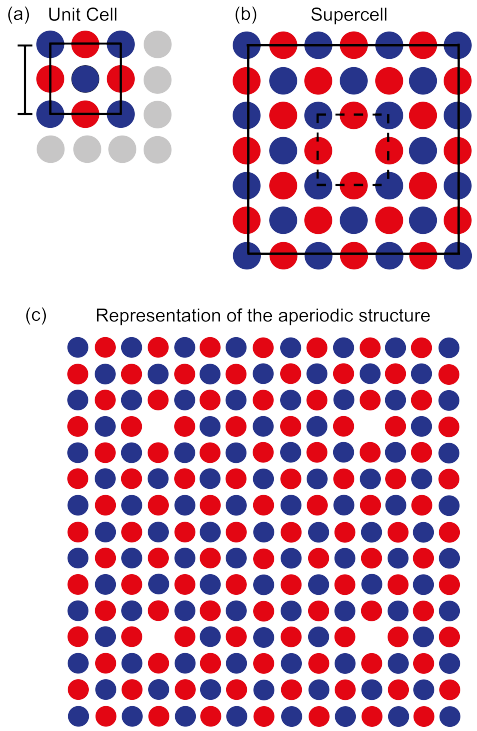

Figure 3.2, a) unit cell of a crystal lattice b) supercell containing vacancy defect c) the aperiodic structure as modelled by the supercell.

The supercell approach is generally used to calculate the defect formation energy from which key quantities for characterizing point defects can be derived such as their concentration or induced volume changes. However the formation energy of an isolated defect is complicated by the possible interaction of defects with its periodic image, which can occur via three mechanisms; electronic interaction due to the overlap of the defect wave function, elastic interactions induced by atomic relaxation around the defect and if the defect is charged there will be a corresponding electrostatic interactions between defects in periodic images.[111] Therefore practically the size of the supercell should minimize the contribution due to the interaction between periodic images. Practical limitations on the size of supercell mean that this isn't always possible and correction schemes for the aforementioned defect interactions have been proposed to adjust the formation energy of defects in modest supercells so that they approximate a defect in an infinitely large supercell. [112,113,114]

Though this is a widely used approach in the modelling of solids, it hasn't been widely exploited for NMR calculations using GIPAW electronic structure methods, which must be partially due to the fact that it is prohibitively computationally expensive. There are examples where it is employed for the calculation of NMR parameters of an isolated molecule[115] and in the context of modelling thermal disorder of L-alanine by molecular dynamics (MD) where the size of the supercell can restrict the dynamics.[116] In the context of point defects in crystalline solids Pruneda *et al*[117] have used supercells to investigate disorder in irradiated zircons ($ZrSiO_4$). In this case a catalogue of neutral charge combinations of interstitials and vacancies supercells were created. *Ab initio* DFT methods were used to relax the structures to inform structural arguments but due to the computational demand of the chemical shift calculation only unit cells (and not supercells) were amenable for such an NMR treatment. Another combined GIPAW-DFT and experimental NMR approach was used to study the fluorine and hydrogen positions of clinohumite $(Mg,Fe)_9(SiO_4)_4(F,OH)_2$ that are difficult to determine by diffraction alone.[110] Supercells of the proposed unit cell were created with differing levels and positions of F substitution. The NMR calculations of the structures revealed four ranges of chemical shifts that allowed the assignment of the four ^{19}F NMR signals observed in a 50% fluorine-substituted deuterated hydrous magnesium silicate ($4Mg_2SiO_4 \cdot Mg(OD_{1-x}F_x)_2$ with x = 0.5) sample.

The site-occupancy disorder (SOD)[16] program has been designed for crystal structures that exhibit a non-periodic occupation of lattice sites according to the 'average'

configuration reported by long-range techniques such as diffraction. Such a description leaves local distortions due to point defects and the distribution of ions over the sublattices ill defined. In these cases the crystal structure simply defines a configurational space of all possible structures consistent with such a fractional occupancy. In order to establish the underlying detail of such a description these configurations must be evaluated. Modelling such a configurational space can be complicated by the fact that fractional occupancies are mapped onto a small crystal unit cell that does not possess enough lattice sites to accommodate the proposed site occupancies. Thus the unit cell size must be increased such that the configurational space is actually composed of a series of supercells, for which the set of commensurate structures with the specified partial occupancy can increase dramatically. In order to make the assessment of the configurational space tractable by computational modelling techniques there have been a number of strategies proposed to reduce the size of the set of structures that need to be evaluated. The Monte Carlo method constructs a smaller representative set of configurations for the total configurational space by randomly generating structures before accepting or rejecting structures according to the Metropolis algorithm. [118, 119,120,121]

However the SOD programs uses a symmetry-based approach to identify symmetrically equivalent configurations, that is configurations related by an isometric transformation defined by a symmetry operator of the parent lattice. In contrast to the selective sampling of structures via the Monte Carlo method this approach exhaustively enumerates all possibilities within a given supercell size. The SOD program reduces the total configurational space to a set of symmetry inequivalent configurations with a degeneracy corresponding to the number of times the configuration is 'repeated'. This additional symmetry based degeneracy is included in the Boltzmann statistics such that the probability of an occurrence of a given independent configuration m, with energy E_m and degeneracy Ω_m for the symmetry-adapted Boltzmann ensemble can be described by eq.1 where Z is the partition function, R is the gas constant and T is the equilibrium temperature for the configuration.

$$\boldsymbol{P_m = \frac{\Omega_m}{Z} e^{-\frac{E_m}{RT}}} \qquad \textbf{(3.1)}$$

Since the methodology developed by Grau-Crespo et al[16] was formally introduced in 2007 the symmetry-adapted Boltzmann ensemble has been successfully applied to a range of important families of material.[122,123,124,125] Whilst there have been no publications

that solely focus on the application of SOD (or an equivalent code) for the reproduction of ssNMR parameters, in the last couple of years there have been a couple of complementary experimental and theoretical approaches that have included both GIPAW-DFT calculations and experimental ssNMR as part of the structural elucidation process.

Laurencin *et al*[126] used a more sophisticated supercell approach to investigate cationic disorder due to the incorporation of magnesium into hydroxyapatite. In the hydroxyapatite system magnesium had been postulated to occupy either of two calcium crystallographic positions (Ca(I) or Ca(II)). The structures were generated with different concentrations of magnesium to additionally investigate the possibility of clustering. In order to incorporate increasing concentrations of magnesium into the base structure supercells were created using the Site Occupancy Disorder (SOD)[16] program and optimized using the classical General Utility Lattice Program (GULP)[127] before the NMR parameters for the corresponding structures were calculated using the GIPAW-DFT approach. This approach seemed successful and by comparison with ^{25}Mg and ^{43}Ca NMR measurements it was shown that Mg substitutes preferentially into the Ca(II) positions, though the author acknowledges that the steep escalation in the size of the configurational space with supercell size mean that the problem became computationally prohibitive to run geometry optimizations for substituted structures so that a random five candidates were picked out of the thousands of possibilities for DFT treatment. However, the utility of this is limited by how well the classical potential in GULP matches the *ab initio* energy surface.

An extensive study into the most effective aliovalent substitution to introduce lithium vacancies into the olivine ($LiMgPO_4$) structure in order to generate Li ion conductivity used an 'in-house' code similar to SOD (SimDope.py) to generate symmetrically unique supercells for a given composition. A single aliovalent substitution was performed on a 2x2x2 supercell of $LiMgPO_4$ such that Li^+ ions were removed to charge balance the structure.[128] The structures were relaxed in the DFT code VASP and used to estimate the doping enthalpy and doping free energy. These results suggested that doping the olivine structure with In^{3+} was the most promising strategy. It is unclear exactly how many configurations were considered for each nuclei, however given the size of the supercell and that numerous concentrations of the aliovalent dopants were considered the number must have been substantial (>1000 per concentration per nuclei) and highly computationally expensive given that the structures were additionally relaxed

using the quantum mechanical VASP[129] code. NMR calculations and MD simulations were undertaken on the undoped and lowest-energy $Li_{31/32}Mg_{31/32}In_{1/32}PO_4$ relaxed structure of the 1000 supercells in which a random distribution of 19 Mg^{2+} (15%) had been substituted for In^{3+}, and 19 random Li^+ ions have been removed.

This subsequent exercise show that the while the In^{3+} dopants are effective at introducing vacancies the Li vacancies are more strongly bound to the dopant thereby partially inhibiting the conductivity of the lithium, consequently future applications of this material should work on mechanisms to separate the defects and dopant.

The olivine-type $LiCoPO_4$ structure is the basis for another multi-faceted experimental and computational investigation. The study shows that $LiCoPO_4$, which is a strong candidate for use as a cathode battery material, undergoes phase changes during charging and discharging.[130]

In this study the NMR and XRD measurements suggest that the unit cell of the Li_xCoPO_4 intermediate phase must be an expansion of the original $LiCoPO_4$ unit cell. Six supercells (2x1x1, 1x2x1, 1x1x2, 3x1x1, 1x3x1, 1x1x3) of this structure are generated and on the basis of the quantitative 2:1 ratio of the two resonances in the ^{31}P spectrum it is concluded that only the 1x3x1 supercell with a Co^{2+} to Co^{3+} ratio of 2:1 is compatible with the experimental data. The SOD code was used to establish the number of inequivalent 1x3x1 supercells based on the aforementioned Co^{2+}/Co^{3+} ratio if 4 of the 12 Li atoms are removed from the structure consistent with a $Li_{2/3}$ stoichiometry. This study attempts to bypass the computationally expensive DFT-based characterization of each of these supercells by using symmetry-based arguments from the interpretation of the ssNMR data to sift incompatible candidates from the set. This allows the reduction of the 32 potential configurations to a more tractable set of six candidate structures. Subsequent DFT calculations are used to calculate the energy of formation and demonstrate that all the $Li_{2/3}CoPO_4$ configurations are thermodynamically stable with respect to the two end member phases, but that the three most stable structures exist within an energy range of 5 meV per formula unit suggesting that more than one structure may be present at room temperature. Indeed it is shown that the structures can interconvert by Li ion hopping to adjacent Li sites thereby suggesting the structure contains a disordered Li sublattice.

Despite the SOD programs ability to reduce the set of configurations that need to be considered, the number can still be substantial enough to make an accurate assessment of each configuration intractable via first-principle routes due to the

computational cost. This situation is generally resolved by employing interatomic potential functions as opposed to *ab initio* electronic structure methods so that computational cost is balanced against a lose of accuracy. For example in Ruiz-Salvador *et al*'s[131] study on the aluminium distribution in the zeolite ZSM-5 the energies of a full set of >1000 configurations evaluated in SOD are successfully assessed using interatomic potentials for unit cells of ~300 atoms. However, this approach only works if good potentials exist for the system of interest. If this is not the case then the generation of new interatomic potentials can make this a more costly approach than the brute-force DFT method for small supercells.

Rather than attempting to reduce the number of supercells that need to be considered to characterize a configurational space the special quasi-random structure (SQS)[17] method selectively populates a supercell such that the short-ranged geometric correlation functions mimic that of a random alloy within a finite cell. As demonstrated by Zunger *et al*[17] when introducing the SQS technique for an fcc symmetry the pair correlation functions for the first two fcc coordination shells for a infinite random alloy can be perfectly reproduced by as little as 8 atoms (with modest errors in subsequent shells). It is additionally shown that for a range of pseudobinary alloy semiconductors a single calculation on a large enough SQS structure reproduces the corresponding results from a full statistical mechanical simulation for mixing enthalpies and band gaps.

Since its introduction there have been a number of independent verifications of the techniques validity in the context of random alloys. Hass *et al*[132] compared the SQS approach to characterize the spectral function A(**k**, E), which represents the probability of finding an electron with zinc blende structure wave vector **k** and energy E, for the zinc-blende type $Al_{0.5}Ga_{0.5}As$ alloy. In this study the author compared the SQS approach to the conventional random alloy coherent-potential approximation[133] and recursion method applied to a randomly occupied supercell (>2000 atoms) and concluded that for an SQS-8 structure the spectral features of the random alloy are reproduced within the accuracy with which these properties are known over a broad range of scattering strengths. Pezold *et al*[134] assessed the accuracy of the SQS method across the entire concentration range of the Al-Ti random alloy for studying elastic properties against a randomly generated impurity distribution within the alloy matrix. Ten random distributions were considered for every impurity concentration and the supercell sizes were systematically increased from 2x2x2 (32 atoms) to 10x10x10 (4000 atoms) to establish a converged set of elastic constants (C_{11}, C_{12}, C_{44}) to compare the SQS results

to. The study concludes that the single SQS structures evaluated at each concentration have accuracy comparable with a statistical sampling of the configurational space of 3x3x3 (108 atoms, C_{44}) and 4x4x4 (256 atoms C_{11}, C_{12}) fcc supercells.

Though Zunger *et al*[117] originally proposed the SQS method to study disorder in random alloys it has now been shown to accurately reproduce the properties of metals[135,136,137], semiconductors[138,139] and oxides[140,141,142]. The branching of the SQS approach into oxides has largely happened through investigations into ferroelectric materials. In a first principles study of the order-disorder transition in $Ba(Zn_xNb_{1-x})O_3$ and of B-site ordering in $Ba(Mg_xTa_{1-x})O_3$ the SQS approach is simply used to corroborate a cluster expansion's ability to approximate the disordered state within the supercell. [143,141]

An *Ab initio* study on the dielectric, piezoelectric and elastic properties of the perovskite-type $BaTiO_3/SrTiO_3$ ferroelectric superlattices employed the SQS method to model the disordered $Ba_{0.5}Sr_{0.5}TiO_3$ solid solution so that the thermodynamic stability, which is characterized by the enthalpy of mixing, could be calculated.[140] The structure of the disordered $Ba_{0.5}Sr_{0.}5TiO_3$ solid solution was simulated with two quasirandom structures SQS-4 with rhombohedral and monoclinic unit cells constructed with the gensqs program of the Alloy Theoretic Automated Toolkit (ATAT)[144] code. The paper compares the enthalpy of mixing with that calculated from DFT calculations on free-standing and substrate-supported superlattices of $m BaTiO_3/n SrTiO_3$ (m/n superlattices) with $m=n$=1-4 showing that the shortest period superlattices have a smaller enthalpy of mixing than the disordered phase suggesting that the $BaTiO_3$-$SrTiO_3$ system is prone to superstructure ordering of the components.

However it has been recognized that in some oxides the occupation of lattice sites is effectively random. Indeed Burton *et al*, showed that the B-site cation of the perovskite-type $Pb(Mg_{1/3}Nb_{2/3})O_3$ material converges to an SQS-type structure by using a cluster expansion Hamiltonian derived from total energy calculations.[145] In this material this phenomenon is thought to arise because the short-range Pb-O interactions are strong enough to compete with the long-range coulomb interactions that generally dictate the ground state structure.

The local structure of $K_{0.5}Na_{0.5}NbO_3$ has been investigated using the SQS approach with DFT methods as the similarities between the Na and K cations mean it falls into this 'random-distribution' category.[142] By comparing the computed pair distribution functions with those from neutron-diffraction data the accuracy of the SQS

structures are shown to capture the local structure patterns derived from a random distribution of K and Na on the perovskite A-site. This study used the ATAT[144] to generate the SQS structures with the 1:1 K:Na ratio where the SQS structure was selected as the one with the minimum root-mean-square deviation from the random pair-wise correlations out to a distance of 6a. Both the room temperature *Pm* and low-temperature *R3c* phase were examined. The SQS method generates supercells based on an ideal perovskite lattice such that the distribution of K:Na atoms on the A-sublattice approaches statistical randomness, therefore an additional post-processing step was undertaken to initialize the structures to their Glazer tilt patterns: $a_+^- a_+^- a_+^-$ for *R3c* and $a_+^0 b_0 c_+^0$ for *Pm*. These temperature dependent phases were optimized using the QUANTUM ESPRESSO[146] software package under the symmetry constraints of the diffraction data.

4

APATITES – A SIMPLE CASE OF PARTIAL DISORDER

4.1 Introduction

The chapter reports a brief case study of the germanium-based apatite $La_{7.5}Ca_{2.5}Ge_6O_{25.75}$ that exhibits partial occupancy type disorder in its rare earth metal crystallographic sites. In such systems, for a given volumetric slice of the crystal structure (e.g. a computational supercell) there are many possible structural realisations commensurate with experimentally measured fractional occupancies. In this work we assume these realisations to be independent of one another, which is an approximation, the severity of which decreases as increasingly large supercells are considered. An ideal treatment of such a system would consider every realisation individually so that the macroscopic bulk NMR properties can be derived via first principle DFT calculations by averaging across the results according to the distribution of these crystal structures in nature.

We initially outline an enumerative approach to the simple partial occupancy disorder exhibited in $La_{7.5}Ca_{2.5}Ge_6O_{25.75}$ where the bulk spectra observed in an NMR experiment is approximated by weighting the contributions of each realization according to the Boltzmann distribution.

However, in the majority of cases such a thorough treatment is prohibited by computational time and is likely to be inefficient. The number of configurations that one needs to consider in such an approach can be significantly reduced if one only considers symmetry-inequivalent crystallographic realisations. The Solid Occupancy Disorder (SOD)[16] program is designed to reduce the configuration space to a subset of inquivalent structures with a corresponding degeneracy by sifting the realisations according to the crystal symmetry of the lattice. This is shown to produce results of equivalent accuracy to the aforementioned enumerative approach for the apatite under investigation.

From a broader perspective this material is one of a suite of Si -and Ge-based apatite compounds that are of interest as a potential oxide-ion electrolytes for use in solid oxide fuel cells (SOFC) that are able operate at intermediate temperatures (500-700°C). Such a development will allow the technology to be utilized in smaller scale applications thereby making this green technology much more accessible.

The design of these apatite materials seeks to promote interstitial ion conduction by incorporating varying levels of oxide-ion excess.[147] Thus these materials are highly disordered, possessing both fractional occupancy of lattice sites and local distortions due oxide-ion interstitials. Consequently understanding the local structural and conduction properties on the atomic scale is a challenge both computationally and experimentally.

4.2 Computational Details

All calculations were at completed using density functional theory (DFT) as implemented in the *ab initio* CASTEP[94] code, which employs the Kohn-Sham DFT methodology using periodic plane-waves, under the ultrasoft pseudopotential approximation[93]. The exchange-correlation energy was estimated using the generalized gradient approximation outlined by Perdew-Burke-Ernzerhof for solids (PBEsol)[79]. A basis set convergence of 0.012mH per atom was achieved by sampling over the Brillouin zone using a 2x2x2 Monkhorst-Pack grid with a cut-off energy of 800eV. Structural optimisations allowed the ionic positions to relax within the symmetry constraints of the crystal lattice, as specified by diffraction, to a force tolerance of 0.05 eV/Å using a maximum ionic displacement of 1×10^{-3} Å and total energy of 2×10^{-5} eV per atom. GIPAW–NMR calculations were completed with identical cut-off and k-point Monkhorst-Pack grids to the structural optimizations. The isotropic chemical shift δ_{iso} for each nucleus was calculated from the isotropic magnetic shielding σ_{iso} generated by GIPAW-CASTEP calculation using the relationship $\delta_{iso} = -[\sigma_{iso} - \sigma_{REF}]$ where σ_{REF} is the reference isotropic shielding against a bare atom. The reference isotropic shielding (σ_{REF} = 188.95 ppm) was calculated using the room temperature phase of $LaAlO_3$ (ISCD – 164506) using the same basis set convergence (0.012mH) as the original calculations in order to minimise the propagation of errors.

Calculations were weighted by the relative total energies using the Boltzmann distribution where the total energy values were considered equal to the enthalpy, under the assumption that the lattice vibrational entropy was not significantly different between

structures and therefore its effects could be neglected (note that the lattice has been allowed to relax so that the internal and external (equal to zero) pressures were the same).

The pNMRsim software was used to simulate the ^{17}O experimental spectrum for each configuration where each ^{17}O crystallographic site was considered independently so that the total lineshape was produced by a summation over the individual lineshapes. The pNMRsim software outputs a free induction decay (FID) that can be processed like the equivalent experimental signal. The simulations do not explicitly account for distributions in the NMR parameters. This was introduced artificially by applying 150 Hz of Gaussian apodization.

4.3 Enumerative Approach

The $La_{7.5}Ca_{2.5}Ge_6O_{25.75}$ structure is shown schematically in **Figure 4.1** where it can be seen to be composed of with La_6O_2 units occupying channels within an $La_4(GeO_4)_6$ framework. The separate bonding motifs can be described by two unique crystallographic environments that are denoted La1 and La2 respectively for the purpose of discussion. According to diffraction-based studies both the La1 and La2 crystallographic sites are partially occupied by calcium cations, though this substitutional disorder is predominantly associated with the La2 site: the La2 site is cited as possessing a fractional occupancy of 0.52 La and 0.48 Ca, while the La1 site is distributed according to 0.92 La and 0.08 Ca.

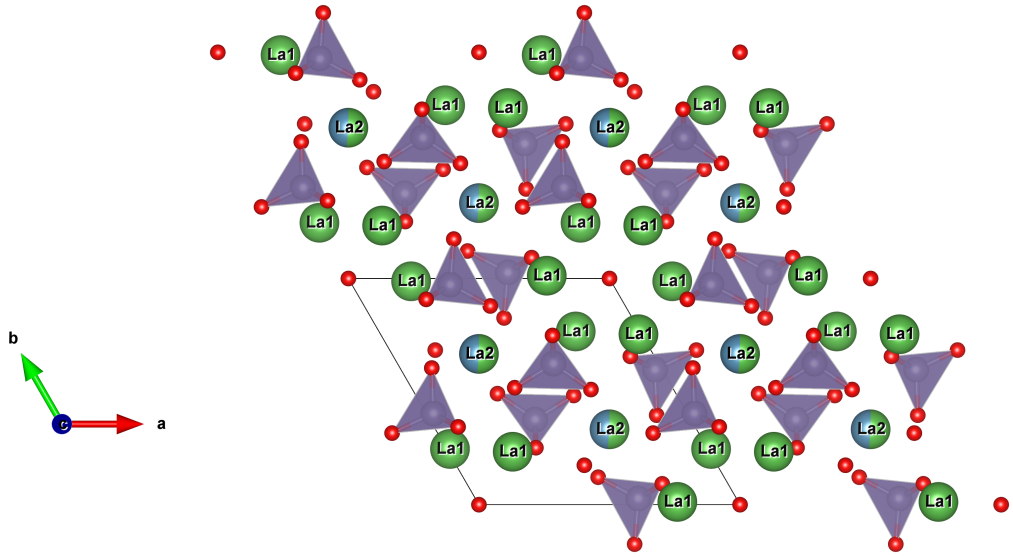

Figure 4.1, structure of $La_{7.5}Ca_{2.5}Ge_6O_{25.75}$ with lanthanum lattice environments denoted as either La1 or La2.

In order to model the $La_{7.5}Ca_{2.5}Ge_6O_{25.75}$ structure approximate fractional occupancies were imposed upon the unit cell of 1.0 La and 0.0 Ca at the La1 lattice position and 0.5 La 0.5 Ca at the La2 lattice site. Within the unit cell there are four La2 lattice sites so that realizations with two Ca^{2+} and two La^{2+} cations distributed across the La2 positions were commensurate with the approximate fractional occupancies. Simple combinatorial considerations show that this means there are six possible realizations $(\frac{4!}{2!2!} = 6)$ of this substitutional disorder within the unit cell.

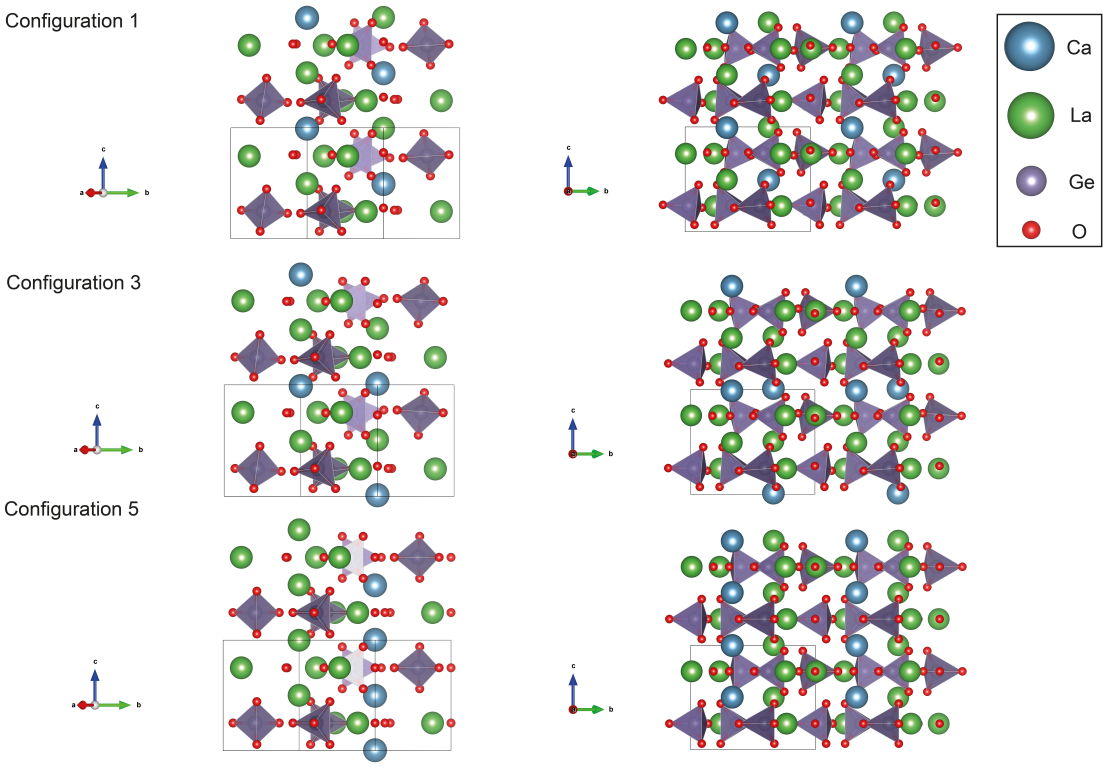

Figure 4.2, structural diagrams for three of the six configurations to show the different permutations of calcium cation distribution across the La2 lattice sites commensurate with the approximate fractional occupancy.

The total energy for each of the six configurations (neglecting zero point energy and lattice vibrational entropy) relative to the lowest energy configuration is listed in Table 4-1. These were used to estimate an associated probability (P_i) for each configuration according to eq. (4.1). [148]

$$\boldsymbol{P_i} = \frac{\boldsymbol{e}^{-\frac{\Delta\varepsilon_i}{kT}}}{\sum_i \boldsymbol{e}^{-\frac{\Delta\varepsilon_i}{kT}}} \tag{4.1}$$

where $\Delta\varepsilon_i$ is the relative energy of a state i occurring at a temperature T.

The energetics suggests that the lattice favours maximal calcium cation separation, which is achieved by configurations 1 and 2. The energetically unfavourable configurations 5 and 6 are arranged such that calcium occupies the next-nearest neighbour bonding sphere of other calcium cations, whereas in all other configurations the calcium is sufficiently dispersed that this bonding arrangement is never realized (see **Figure 4.2**).

Table 4-1 Energy difference (ΔE) between structures relative to configuration 2 and the relative probability **(P)** of configurations calculated from the relative energy at 0K.

Configuration	ΔE/ eV	*P*/ %
1	0.0013	0.423
2	0.0000	0.445
3	0.0491	0.066
4	0.0491	0.066
5	0.6615	0.000
6	0.6615	0.000

The solid-echo experimental ^{17}O MAS NMR data acquired at 14.1 T for $La_{7.5}Ca_{2.5}Ge_6O_{25.75}$ is displayed in **Figure 4.3**. Dr Gregory Rees at the University of Warwick acquired this spectrum. According to the parent lattice there are four inequivalent oxygen sites in the unit cell: three are associated with the GeO_4 tetrahedral framework and one occupying the channel. However, only a single resonance is observed at an apparent (uncorrected) chemical shift of ~ 170 ppm that is consistent with the oxide ions within the GeO_4 unit. The absence of a resonance for the channel oxide ion is attributed to the poor oxide-ion conductivity of $La_{7.5}Ca_{2.5}Ge_6O_{25.75}$ inhibiting the ^{17}O exchange process.

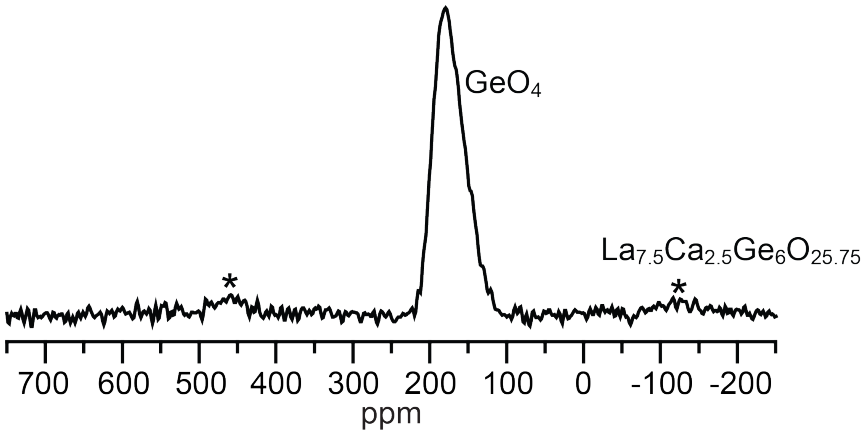

Figure 4.3, *^{17}O MAS NMR data at 14.1 T with peak assignment for $La_{7.5}Ca_{2.5}Ge_6O_{25.75}$*

The corresponding simulations based on the six realizations consistent with the fractional occupancies are shown in **Figure 4.4**. It is evident that there is excellent agreement between the line position and the assignment of the bulk GeO_4 framework species. Moreover the simulated lineshape for configurations 5 and 6 demonstrates that these structures are not well represented in the crystal lattice, which agrees with the less favourable energetics reported for these structures.

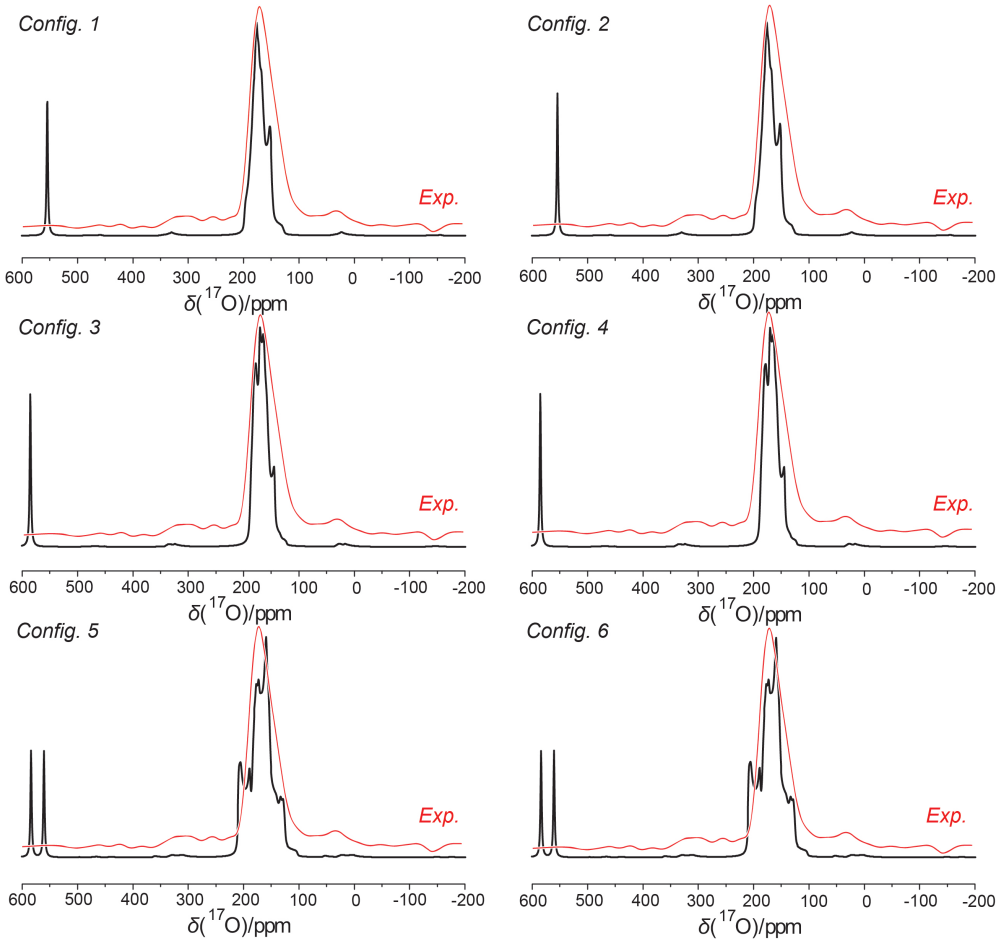

Figure 4.4, Simulated ^{17}O MAS NMR data displayed against the experimental lineshape for each of the six configurations commensurate the partial occupancy of the La2 site of the parent lattice.

4.4 SOD Approach

Additionally the SOD program was used to generate cells under the same fractional occupancy approximations outlined earlier. This showed that there was three inequivalent cells each with a degeneracy of 2. Indeed it can be seen in the relative probabilities reported in Table 4-1 and in the simulations of the six configurations (**Figure 4.4**) that the configurations can be grouped into pairs (1 and 2, 3 and 4, 5 and 6), which corresponds to the equivalence of these structures. The weighted average for the

enumerative approach and the SOD approach are shown in **Figure 4.5**. Here the two approaches can be seen to produce comparable NMR spectra, thereby confirming the validity of the SOD approach in the context of NMR. However, the lineshapes of the isolated configurations shown in **Figure 4.4** display the small shift separation between the different GeO_4 framework environments whereas this fine detail is lost in the experimental spectra that is indicative of a distribution of nuclear environments.

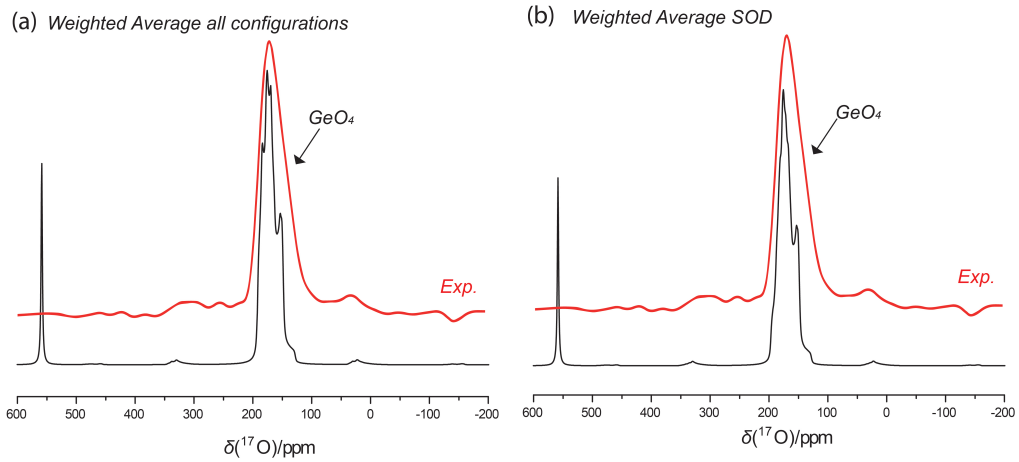

Figure 4.5, ^{17}O MAS NMR simulated spectra derived from a) a weighted average of six configurations from the enumerative approach b) a weighted average from the three inequivalent configurations according to the SOD approach.

The approximation to the bulk NMR spectra by a weighted average across the configurations (shown in **Figure 4.5**) according to their estimated probabilities does not capture this distribution in nuclear sites. It was assumed in the approximation of the fractional occupancies outlined on the parent lattice that the La2 site would dominate the variation seen in the bulk NMR spectra as this offered the greatest opportunity for structural variation. However it appears that the additional partial occupancy at the La1 site and the dilute oxide ion vacancy defect (a single oxygen anion for every four unit cell) that are not considered in these configurations are a necessary in order to fully represent the NMR spectra for $La_{7.5}Ca_{2.5}Ge_6O_{25.75}$.

4.5 Conclusions

This brief case study of $La_{7.5}Ca_{2.5}Ge_6O_{25.75}$ attempted to investigate partial occupancy type problems using the SOD approach in contrast with a more conventional enumerative approach. The SOD approach is shown to reduce the number of configurations that need to be considered without impinging negatively on the NMR spectra. However, it is

shown that even for this comparatively simple Ge-based apatite that considering the partial occupancy at the La2 site alone was insufficient to fully account for the total lineshape observed experimentally and that in order to simulate the full distribution of nuclear sites a more thorough account of the partial occupancy is necessary. Considering the La1 partial occupancy alone would require expanding the configurations to supercells generated from a minimum of five unit cells, which in term would increase the number of configurations necessary to model the La2 partial occupancy to > 9000 inequivalent structures. Thus even for simple problems the scale of the computational task escalates rapidly with multiple cases of site occupation disorder.

Furthermore the correct Boltzmann weighting should be taken in the thermodynamic limit (infinite cell size) and include contribution from both energetic and entropic (number of ways of arranging the defects). These factors act in opposite ways such that both increase with the number of atoms in roughly the same way according to Stirling's approximation for N!.[148] Accordingly taking the Boltzmann weight of a particular cell in the manner outlined in this chapter is an approximation and a further limitation of the methodology.

In summary, when the combinatoric considerations are coupled with the observation that rounding occupancies to convenient numbers removes detail in the lineshape, it can be seen that this approach is only valid for very simple partial occupancy problems where such approximations are unnecessary. However, this suggests that in these cases that it may be possible to vastly reduce the configurational space that needs to be considered by generating the reduced configurational space using SOD and then 'sifting' these structures according to their total energy. This can reduce the configurational space to structures that only make a large contribution to the total simulated spectrum via their Boltzmann weighting.

5

AB INITIO DFT CALCULATIONS ON THE $Na_{1-x}K_xNbO_3$ SYSTEM

5.1 Introduction

Regulations in European communities that push for the creation of sustainable society will mandate the elimination of lead (Pb^{2+}) from consumer items due to their volatility and toxicity in the coming years. High performance piezoelectric materials, in particular lead zirconium titanate (PZT), have been used extensively in electronic devices, actuators and sensors. The current political climate means that there has been a push to find alternative lead-free alternatives where the ferroelectric perovskites (K, Na)NbO_3 have shown to be outstanding candidates.

Owing to the potentially huge commercial implications for lead-free piezoelectric materials there has been extensive work undertaken on characterising these materials so that the structure-function relation can be understood and exploited to achieve the required levels of performance. In parallel to previous investigations on PZT, diffraction based studies have been used to search across the phase-diagram for key structural changes such as the morphotropic phase boundary observed in PZT at x = 0.52[149]. Solid-state NMR is considered an ideal complementary technique to diffraction-based studies due to its sensitivity to short-range order. In contrast to the long-range average atomic information garnered from diffraction, ssNMR provides a direct route to investigate the complex tilting distortions observed in the NbO_6 octahedra where the quadrupolar coupling constant is strongly related to distortions in the nearest neighbour coordination sphere.[150] In this regard the pairing of ssNMR techniques with GIPAW-DFT based studies can hugely enhance links between structure and function.

Indeed the room temperature solid-state NMR spectra reported in this investigation show that for key sodium potassium niobate ($K_xNa_{1-x}NbO_3$) (KNN) compositions across the entire phase diagram, the ssNMR shows well defined tends in ^{23}Na NMR parameters. Sodium-rich compositions exhibit highly correlated ^{23}Na

chemical shifts and quadrupolar parameter behaviour. Moreover there are distinctive increases in ^{93}Nb quadrupolar coupling constants and a movement downfield of isotropic chemical shifts with increasing potassium content.

Existing diffraction based structures for KNN display both atomic and positional disorder. Traditionally expensive supercells need to be constructed in order to accommodate for these factors making the computational requirements for these DFT calculations very large. Efficient alternative methods for the investigation of disorder via GIPAW-DFT are still being validated.

For random alloys there are well-established approaches to treating disorder via first-principle calculations.[151,152,18] For partial occupancy problems in simple oxides it has been shown that chemically similar cations can mimic the distribution of cations in random alloys.[145,142] In this study we have exploited the relative chemical similarities between K and Na in an attempt to model the occupation of the A-site on the perovskite KNN structure as a random structure.

The GIPAW-DFT NMR approach[11] allows for the calculation of NMR parameters for extended periodic solids, although it is impossible to truly represent a random structure using a system with period boundary conditions. The cluster expansion method[106] was first introduced to characterise binary metal alloys exhibiting partial occupancy disorder, but has been extended to a host of chemically diverse materials in recent times. Using special quasi-random Structures (SQS)[17] it has been shown that one can avoid having to complete the highly intensive and computationally expensive cluster expansion method by generating structures that mimic 'randomness'. Having proven to be relatively robust in the calculation of the energetics of an arbitrary disordered set of configurations it has been additionally used to calculate a number of other physical relevant properties like band gaps from a reduced set of calculations.[17,153]

We choose to approximate the cation distribution using the special quasi-random structures (SQS) approach to explore the suitability of these SQS for modelling the complex KNN structure across its phase diagram. In this approach a set of supercells are generated on the basis that their short-ranged geometric correlations approximate that of a random alloy. Our predicted NMR results from these computations are validated against a set of GIPAW-DFT calculations undertaken on a structure derived from existing room temperature diffraction-based experiments at x = 0.3 on the $K_xNa_{1-x}NbO_3$ phase diagram using a conventional supercell approach.

5.2 Glazer notation

Glazer notation[154] is used throughout this chapter to describe the tilt system of the NbO_6 octahedra. In Glazer notation the tilt system is described by rotations of the BX_6 octahedra about three orthogonal Cartesian axes that are coincident with the three axes of the aristotype cubic unit cell. Tilting can be reduced into two categories: *in-phase* where the neighbouring octahedra tilt in the same direction and *out of phase* where the neighbouring octahedra tilt in opposite directions. These motifs are denoted by a negative or positive superscript respectively. A superscript of 0 signifies that no tilting is present about that axis. Additionally the relative magnitude of the rotations about a given axis is denoted by the use of letters *a, b* and *c* so that $a^-a^-a^-$ would denote equal out-of-phase tilts about the x, y and z axes, where as $a^-b^-c^-$ implies unequal tilts about the x, y and z axes. For illustrative purposes **Figure 5.1** demonstrates the Glazer notation for an in-phase and out of phase tilt system along the *c*-axis for a general perovskite.

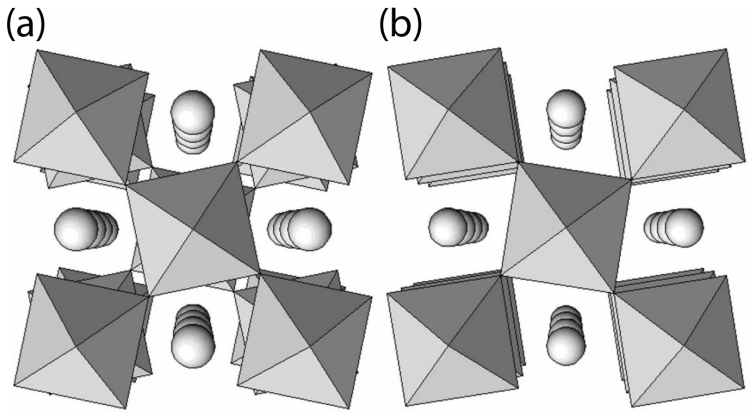

Figure 5.1, pictorial representation of a) out of phase $a^0a^0c^-$ and b) in-phase $a^0a^0c^+$ octahedral tilting along the c-axis. Diagram is adapted from Lufaso et al[155].

5.3 The $K_xNa_{1-x}NbO_3$ Phase diagram

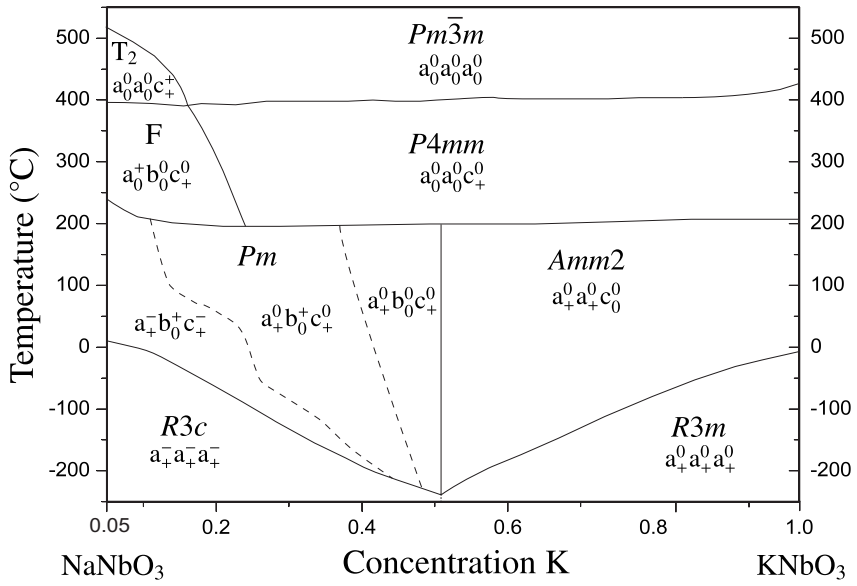

Figure 5.2, Phase diagram for KNN taken from Baker et al[156] where the octahedral tilting oxygen tilting is denoted by Glazer superscripts[157] (subscripts refer to cation displacements[158]) Each phase Dotted lines represent change in tilt system, and phases.

The phase diagram of Sodium Potassium Niobate (KNN) as reported by Baker *et al*[156] is shown in **Figure 5.2**. Moving across the phase diagram at room temperature from the low-potassium to high-potassium side we can observe three major changes in the crystal structure at x = 0.2, x = 0.4 and x = 0.5. Up to x = 0.4 the changes in the oxygen framework are second order in nature and comprise of changes to the tilt system; below x = 0.2 both in-phase and anti-phase tilts (plus and minus in Glazer notation) are observed, in the interval 0.2 < x < 0.4 only in-phase tilts are observed and beyond x = 0.4 the tilting patterns disappear. At x = 0.5 a first-order phase transition with composition is reported from the monoclinic structure with space group *Pm* to an orthorhombic structure with space group *Amm*2.

5.4 Solid-state NMR measurements on the $K_xNa_{1-x}NbO_3$ system

Solid-state NMR measurements were acquired by John Hanna at the University of Warwick under ambient conditions for a set of key compositions across the phase diagram (x= 0.1, 0.18, 0.26, 0.4, 0.5, 0.7 and 0.9). For each composition a ^{23}Na 3Q-MAS experiment was used to characterise the ^{23}Na nuclear environments. A numerical inversion procedure was applied to ^{23}Na 3Q-MAS spectra in order to reconstruct the

distribution $P(\delta_{iso}, C_Q, \eta_Q)$ from the 2D data. As 2D datasets for disordered materials are relatively featureless, an assumption ($\eta_Q = 0.5$) is made about the asymmetry parameter η_Q to facilitate the extraction of $P(\delta_{iso}, C_Q)$. The corresponding MQ-MAS and inversion MQ-MAS NMR datasets for all the investigated samples are shown in **Figure 5.3**.

For the structurally ordered $NaNbO_3$ it can be seen that the 3Q-MAS data produces tightly defined contours that translate into well-defined δ_{iso}/P_Q. In contrast the analogous data for $K_{0.18}Na_{0.82}NbO_3$ yield a comparatively broad, asymmetric resonance with diffuse contours, which is consistent with a disordered system. The corresponding inversion for the $K_{0.18}Na_{0.82}NbO_3$ spectrum provides less clearly defined solutions for δ_{iso}/C_Q and is unable to delineate isolated crystallographic environments. Nonetheless it is useful because it describes the characteristic distribution of EFG and CS parameters.

The orientation of the distribution of δ_{iso}/C_Q environments in the inversion plots indicates whether these parameters are correlated. For the samples investigated with compositions in the concentration range x = 0.18 – 0.4 the δ_{iso}/C_Q parameters are clearly highly correlated, which are coupled with a general trend of decreasing C_Q and an upfield shift in δ_{iso} with increasing x.

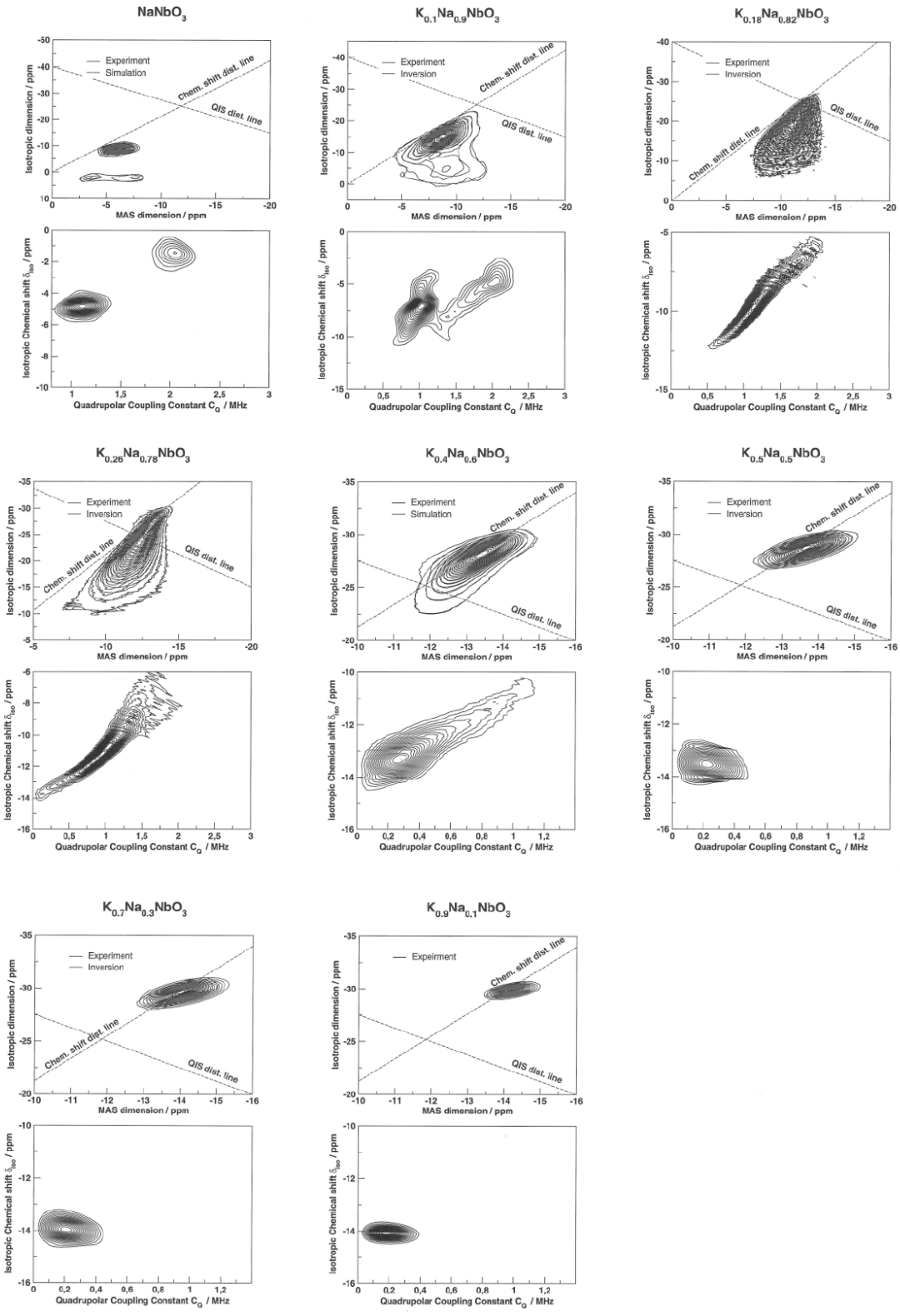

Figure 5.3, 3QMAS data and inversion data for $NaNbO_3$ and various compositions of $K_xNa_{1-x}NbO_3$. The spectra are arranged so that the potassium concentration increases from left to right. For all samples the inversion data is the arrayed below its corresponding 3Q-MAS spectrum.

Thus, the key displacive changes in the tilting patterns with increasing potassium content are being described by the high-correlated inversion data. As the sodium content decreases beyond x = 0.4, δ_{iso}/C_Q distributions are increasingly well defined consistent with the increasing tendency towards an ordered crystalline structure.

Additional ssNMR measurements were undertaken on ^{93}Nb. For the purpose of this investigation only the trends in average isotropic chemical shift $\langle\delta_{iso}\rangle$ and quadrupolar coupling constant $\langle C_Q\rangle$ are displayed (see **Figure 5.4**).

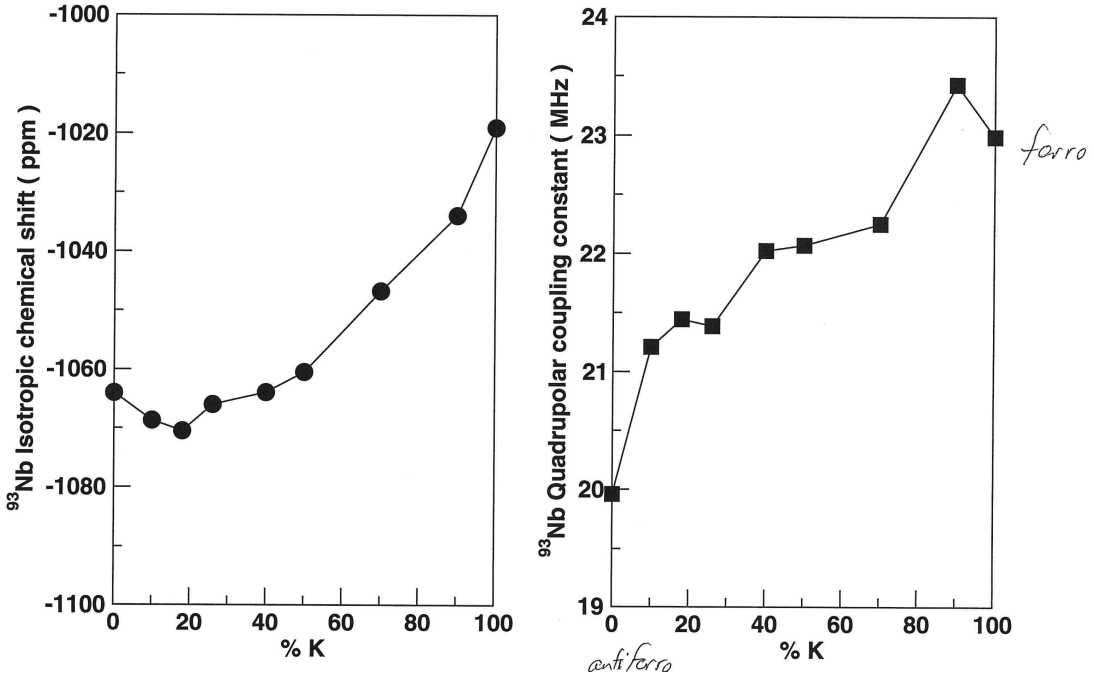

Figure 5.4, ^{93}Nb $\langle\delta_{iso}\rangle$ and $\langle C_Q\rangle$ experimental values for various compositions of $K_xNa_{1-x}NbO_3$.

In the KNN system the ^{93}Nb occupy NbO_6 octahedral bonding arrangements. In an ideal octahedral coordination in which only the nearest coordinating atoms are considered (these generally contributed most significantly to the electric field gradient) there would be no EFG and therefore the no quadrupolar interaction. Therefore deviations from the ideal octahedral arrangement are described by increasingly large quadrupolar coupling constants. The trend in quadrupolar coupling constants shows a general increase with potassium content.

5.5 Preliminary investigations using CASTEP

The SQS method generates structures based on the selective occupation of lattice sites by Na or K atoms that mimic, for a finite number of sites, the correlation functions of an

infinite substitutional random alloy. The template structure used for our study is the ideal ABO_3 perovskite lattice. Therefore detailed nuclei specific information such as bond angles or lengths is absent from such a template statistical description. This system dependent information is introduced by the use of a first principle code (CASTEP[94] in this instance) via geometry optimization. It is therefore vital that the first principles code is able to accurately represent the systems so that the physical properties of the SQS structures are well represented.

As structural parameters are of vital interest to this study a preliminary investigation was undertaken on both the end members of KNN and at the point x = 0.3 within the phase diagram. For all these points of the phase diagram, there exists high quality diffraction data for the room temperature phases. There is little dispute concerning the orthorhombic structure of $KNbO_3$ (space group Amm2)[159]. In contrast $NaNbO_3$ has been the subject to substantial discussion over many years[160,161,162]. At room temperature the orthorhombic unit cell with space group *Pbcm* is generally accepted[160], though some authors have suggested the alternative *Pbma*. Additionally Ashbrook *et al*[102] have shown that a low temperature synthetic route for $NaNbO_3$ produced a mixed phase sample of *Pbcm* and a second polymorph *P*21*ma*. The room temperature structure of $K_{0.3}Na_{0.7}NbO_3$ (space group *P*1*m*1) has been establish in a study by Baker *et al*[156] and shown to possess partial occupancy in both of its two sodium crystallographic sites.

5.5.1 Comparison of the default pseudopotentials in CASTEP

A recent publication by Lejaeghere, et al. [163] provided error estimates for solid-state DFT predictions across numerous codes by evaluating ground-state elemental crystals across the periodic table (in which Na, K, Nb and O were all considered). The spread in predictions from two distinct DFT implementations can be conveniently assessed by the Δ-value that is simply a single number. Formally the Δ-value corresponds to the root-mean-square energy difference between the equations of state of the two codes, averaged over all crystals in a purely elemental benchmark set. The variation in the Δ-value OTFG CASTEP 7 Na, K, Nb and O strings and the equivalent CASTEP 8 strings in the PBE formalism compared to the all-electron WIEN2k code with LAPW/APW+lo basis are summarized in **Table 5-1**.

Table 5-1 Difference in **Δ-values for the CASTEP OTFG Material Studio pseudopotential strings in CASTEP 7 and the default OTFG library in CASTEP 8 as compared to WIEN2k. Values are taken from ref -**

	CASTEP 8	CASTEP 7
	Δ-value/ meV/atom	Δ-value/ meV/atom
Na	0.44	0.32
K	0.12	0.40
Nb	0.30	1.66
O	1.17	9.51

It can be observed that the Δ-values describe a systematic improvement between the two libraries. In section 5.8 the accuracy of the Nb psuedopotential is cited as a possible origin for difference between some of the theoretical and experimental results, therefore the Nb OTF generation string for its CASTEP 7 and CASTEP 8 definitions respectively are listed below with a brief discussion hereafter.

Nb 3|2.2|2.2|1|7.7|8.8|10|40U=-2.145:50U=-0.145:41U=-1.27U=+0.25:42U=-0.1U=+0[]
Nb 3|1.6|8|11|14|40U:50:41:42(qc=6)

Both the pseudopotential strings employ the same definition for the valence electrons for Nb (4s2 4p6 4d4 5s1). The long string corresponding to the CASTEP OTFG Material Studio pseudopotential sets values for the matching radius for the local channel, non-local channels, and augmentation functions, whereas the shorter string uses a single number that is used for the local and non-local channels (the augmentation function radius will be taken as 0.7 multiplied by this value). As the shorter string has a smaller matching radius it is a harder pseudopotential (will need more planewaves). Additionally the longer pseudopotential string explicitly sets the energy of each projector, which is based on the Accelrys' desire to get their OTFG generator to reproduce their legacy pseudopotentials rather than being physically motivated.

5.5.2 Default pseudopotentials in CASTEP 7

As a brief aside it is worth commenting on the initial problems encountered with modelling these niobate systems. The introductory calculations used to characterise the $NaNbO_3$ and $KNbO_3$ systems were performed using density functional theory (DFT) as implemented in CASTEP 7. Previous NMR motivated DFT studies of related niobate

structures suggested that the Perdew-Burke-Ernzerhof (PBE)[78] generalised gradient approximation (GGA) where the core-valence interactions were approximated by default ultrasoft pseudopotentials were sufficient to achieve good agreement between experiment and theoretical results.[103]

This setup was taken as the starting point for the assessment of the accuracy of the DFT approach for predicting NMR parameters. However, structural optimisations under this setup showed limited agreement with experimental values in almost all cases, as emphasised by the relevant NMR parameters displayed in **Table 5.2** and **Table 5.3** for the $NaNbO_3$ structure (ICSD – 89317) calculated with various levels of constraint on the unit cell: '*Fixed lattice'* describes optimisation where the ionic positions are relaxed within constrained lattice parameters under the point symmetry indicated by the diffraction data, '*Unconstrained lattice'* relaxes this lattice constraint, while '*fixed volume'* allows both the lattice and atomic positions to vary within the confines of the crystal point symmetry under the restriction of a fixed unit cell volume and '*full relaxation'* describes unrestricted relaxation.

Table 5-2 Calculated ^{93}Nb NMR parameters for $NaNbO_3$ using various methods of geometry optimization in CASTEP 7 using the default pseudopotentials and the PBE functional in comparison to the experimental values. All δ_{iso} values are referenced according to ref-[164]

Experimental – ^{93}Nb	**$\delta_{iso(MAS)}$**	**C_Q**	**η**
	-1078	19.5	0.7
CASTEP - ^{93}Nb			
Relaxation method	**$\delta_{iso(MAS)}$**	**C_Q**	**η**
Fixed lattice	-987.73	19.40	0.51
Unconstrained lattice	-977.26	37.73	0.71
Fixed Volume	-984.24	22.24	0.82
Full relaxation (no symmetry)	-977.40	25.30	0.95

Table 5-3 Calculated ^{23}Na NMR parameters for $NaNbO_3$ using various methods of geometry optimization in CASTEP 7 using the default pseudopotentials and the PBE functional in comparison to experimental values.

Experimental – ^{23}Na	**Site**	**$\delta_{iso(MAS)}$**	**P_Q**		
	1	-0.6	2.2		
	2	-4.2	1.2		
CASTEP - ^{23}Na					
Relaxation method	**Site**	**δ_{iso}**	**P_Q**	**C_Q**	**η**
Fixed lattice	1	2.49	2.81	2.8	0.15
	2	-2.19	1.13	1.07	0.57
Unconstrained lattice	1	-1.9	2.44	2.43	0.13
	2	-6.1	1.00	0.96	0.49
Fixed Volume	1	3.31	2.93	2.92	0.15
	2	-1.61	1.18	1.11	0.62
Full relaxation (no symmetry)	1	3.31	2.44	2.43	0.13
	2	-1.61	1.00	0.96	0.49

The preliminary NMR-CASTEP results for $NaNbO_3$ show that more degrees of freedom in the relaxation process tend to distort the structure from that observed in nature. Hanna *et al*[103] have observed this non-physical relaxation of niobate structures using CASTEP with early versions Na, Nb and O on-the-fly (OTF) pseudopotentials provided by the Accelrys company. The release of CASTEP 8 with a new suite of pseudopotentials coincided with the identification of this problem. **Figure 5.5** shows that relaxation of the SQS generated structures (to be discussed further later in the chapter) using the default CASTEP 7 pseudopotentials leads to a non-physical expansion of the unit cell in all directions that is reflected in the NMR parameters, whereas the improved ultrasoft Vanderbilt pseudopotentials[93] in CASTEP 8 reproduce the experimental trend to a much higher level of accuracy.

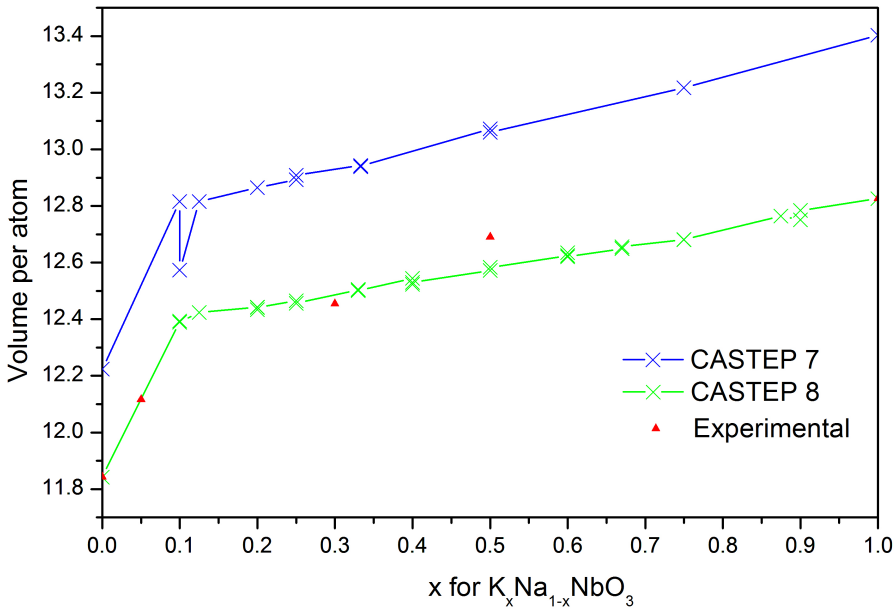

Figure 5.5, volume per atom of the $NaNbO_3$, $KNbO_3$ and SQS supercells relaxed using the default pseudopotentials in CASTEP 7 and CASTEP 8 plotted against the available room temperature experimental values.

5.5.3 Default pseudopotentials in CASTEP 8

For all structures the ionic positions were relaxed using the CASTEP 8 code with an unconstrained lattice in order to assess the robustness of this approach. Structural .cif files were taken from the Inorganic Crystal Structure Database (ICSD) with the relevant collection codes provided in **Table 5-4**.

Table 5-4 The reported niobate structures with ICSD codes and space groups

Structure	ICSD code	Space Group
$NaNbO_3$	247310	*Pbcm*
	247312	*Pbcm*
	247311	*P*21*ma*
	97669	*Pbma*
$KNbO_3$	9533	*Amm*2
$K_{0.3}Na_{0.7}NbO_3$	173740	*P*1*m*1

The default Ultrasoft Vanderbilt[93] CASTEP8 pseudopotentials were employed with the exchange and correlation potentials calculated using the generalized gradient approximation (GGA) in the parameterization of the Perdew-Burke-Ernzerhof functional developed for solids (PBEsol)[79]. All geometry optimization calculations were

performed with a cut-off energy of 700 eV with k-point Monkhorst-Pack grids of 4x3x2 for the *Pbcm* structures, 3x2x4 for *Pbma* and 3x3x4 for *P21ma* to sample the Brillouin zone.

Additionally NMR parameters were calculated within periodic boundary conditions and the pseudopotential approximation using the GIPAW[11] to compute the chemical shielding tensor and PAW[100] methods to compute the EFG tensor. For all NMR calculations the cut-off energy was increased to 800 eV to ensure the accuracy of the all-electron construction.

5.5.4 Calibrating the chemical shifts for ^{23}Na and ^{93}Nb

NMR experiments are referenced according to the known shift of another compound, whereas CASTEP calculations output the chemical shielding compared to a bare nucleus. In order to convert the isotropic shielding (σ_{iso}) to the experimentally observable isotropic chemical shift (δ_{iso}) a reference isotropic shielding (σ_{ref}) is used:

$$\boldsymbol{\delta_{iso} = -(\sigma_{iso} - \sigma_{ref})} \qquad (5.1)$$

The obvious solution would be to run an NMR calculation on the same reference as the experiment at the same level of accuracy of the original calculation(s) to determine σ_{ref}; however there are numerous cases where the shielding-shift correlation plots for GIPAW NMR calculations diverge from the ideal gradient of -1. From a calculation perspective the type of bonding in the system of interest should be reflected in the reference sample in order to achieve an accurate calibration of the isotropic chemical shift. As such σ_{ref} has been calibrated against the different polymorphs of $NaNbO_3$ for both ^{23}Na and ^{93}Nb to produce reference shielding of σ_{ref}(^{23}Na) = 562.35 ppm and σ_{ref}(^{93}Nb) = -642.335 ppm as shown in **Table 5-5** and **Table 5-6**.

Table 5-5. Experimental δ_{iso} values for two different polymorphs of $NaNbO_3$ taken from Johnston et al[165] with calculated σ_{iso} values used to generate $\sigma_{ref}(^{23}Na)$

^{23}Na

Experimental	Site	δ_{iso}(ppm)	CASTEP	σ_{iso}(ppm)	σ_{ref}(ppm)
Pbcm	Na1	−0.5(5)	ICSD - 247312	562.46	561.96
	Na2	−4.2(5)		566.20	562.00
	Na1	−0.5(5)	ICSD - 247310	562.77	562.27
	Na2	−4.2(5)		566.49	562.29
*P*21*ma*	Na1	−1.4(5)	ICSD - 247311	564.02	562.62
	Na2	−5.1(5)		568.04	562.94
				AVERAGE (σ_{ref})	**562.35**

Table 5-6 Experimental δ_{iso} values for Pbcm polymorphs of $NaNbO_3$ taken from Johnston et al[150] with calculated σ_{iso} values used to generate $\sigma_{ref}(^{93}Nb)$ (note P21ma is excluded because no ^{93}Nb ssNMR values have been reported for this structure)

^{93}Nb

Experimental	Site	δ_{iso}(ppm)	CASTEP	σ_{iso}(ppm)	σ_{ref}(ppm)
Pbcm	Nb1	−1078.3(5)	ICSD - 247312	435.47	-642.83
			ICSD - 247310	436.46	-641.84
				AVERAGE (σ_{ref})	**-642.34**

5.6 Validation of the approach

In order to test the suitability of the reference shielding values (σ_{ref}) calculated from the different polymoprhs of $NaNbO_3$ reported in the literature and to assess the expected accuracy of the GIPAW-NMR calculation a further set of calculations were undertaken on $KNbO_3$ and $K_{0.3}Na_{0.7}NbO_3$. The investigation of $K_{0.3}Na_{0.7}NbO_3$ will also act as a direct point of comparison for the accuracy of the SQS structures that are discussed later in this chapter.

5.6.1 $KNbO_3$

For $KNbO_3$ the structure an identical setup was used to the $NaNbO_3$ calculations except that a k-point Monkhorst-Pack grid of 6x4x4 was employed for all calculations. The results of the GIPAW-NMR results after geometry optimization under the constraint of

the diffraction-based point symmetry without lattice restrictions are summarized in **Table 5-7**.

Table 5-7 Experimental δ_{iso} , C_Q , η values for $KNbO_3$ taken from Hanna et al[103] with corresponding CASTEP 8 calculated values. The isotropic chemical shift was calibrated using $\sigma_{ref}(^{93}Nb)$ = -642.34 ppm

$KNbO_3$	$\delta_{iso(MAS)}$	C_Q	η
Experimental	-1019.0	22.99	0.822
CASTEP 8	-1019.7	22.59	0.710

The CASTEP-NMR ^{93}Nb results for $KNbO_3$ fall within the reported experimental error and therefore supports both the calibration of $\sigma_{ref}(^{93}Nb)$ and this DFT approach.

5.1.1.1 $K_{0.3}Na_{0.7}NbO_3$

In order to characterize the NMR parameters for $K_{0.3}Na_{0.7}NbO_3$ a more involved methodology had to be incorporated to accommodate the cation partial occupancy exhibited by the $K_{0.3}Na_{0.7}NbO_3$ structure. The SOD[16] program was employed to create a set of representative 2x5x1 supercell configurations that were compatible with the fractional occupancy reported on the Na1 and Na2 sites. The process produced 64 inequivalent supercells of 100 atoms. These were geometry optimized using relatively cheap constraints (cut-off 600 eV with k-point Monkhorst-Pack grids of 1x1x2) to identify the energetically relevant structures from the configurational space.

Accounting for the degeneracy of configurations as calculated by SOD a relative probability based on the total energies (at 0 K) was assigned to each supercell according to the Boltzmann distribution. This suggested that 8 structures were able to capture ~95% of the probability distribution. This subset of energetically relevant structures underwent higher-accuracy geometry optimizations (700eV with k-point Monkhorst-Pack grids of 2x1x3) where the maximum force on any atom was lowered to 1×10^{-4} eV/Å.

Interestingly all of the low energy structures show a tendency to potassium clustering on the (010) plane. This effect is most prominent in the lowest energy supercell as shown in **Figure 5.6**.

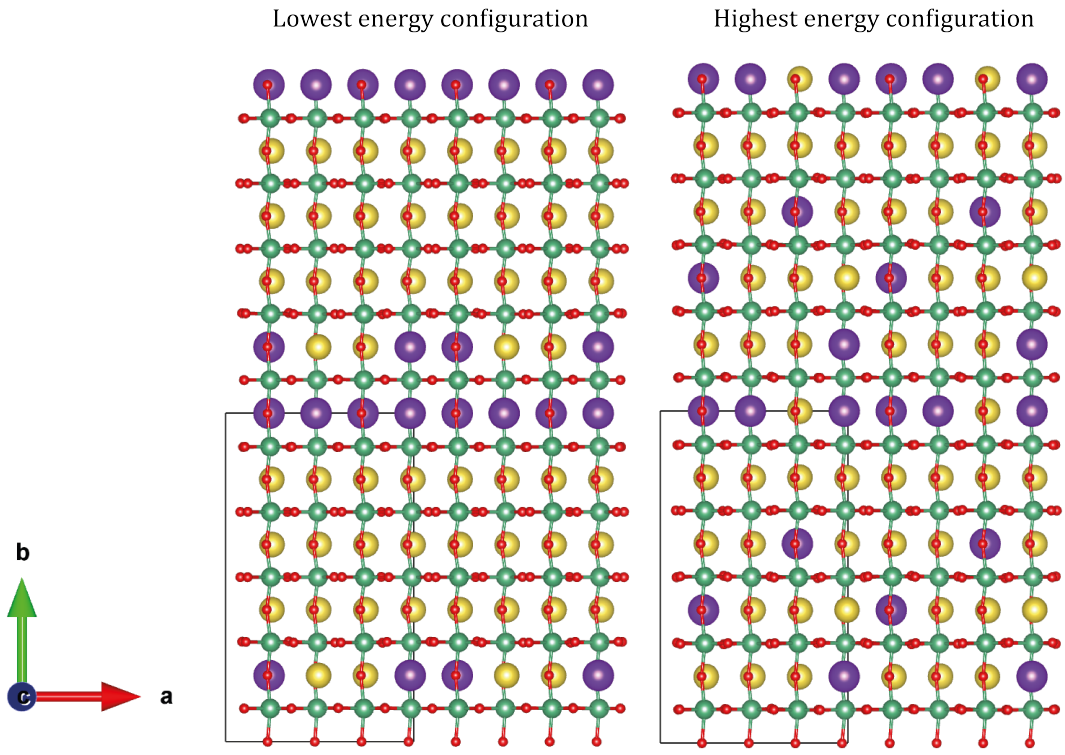

Figure 5.6, the lowest and highest energy supercells of $K_{0.3}Na_{0.7}NbO_3$. Na cations are in yellow, K cations are in purple, niobium cations are in green and oxygen anions are in red. The lower energy structures show a tendency for K cations to order along the (010) plane.

Based on the relative energetics, the lowest energy supercell would be expected to dominate the bulk properties of the $K_{0.3}Na_{0.7}NbO_3$ structure as it represents ~80% of the probability distribution: the relative energy between the two lowest energy structures is approximately 0.087eV, which exceeds the thermal range at room temperature (~ 0.0257eV).

In order to compare these results with the corresponding experimental ^{23}Na NMR data sets, MQMAS-inversion correlation plots of δ_{iso} against C_Q were created for the 8 low-energy structures. These are shown in **Figure 5.7**.

The linear distribution of the data points indicates that all eight of the supercells display highly correlated ^{23}Na chemical shifts and quadrupolar parameter behaviour. It is evident that the dispersion around this correlated behaviour is associated with the distribution of the potassium environments. This is consistent with observations on $K_{0.5}Na_{0.5}NbO_3$ that have shown that the phase and symmetry of are most strongly correlated with the local, nearest-neighbour Na-O interactions as these dictate the polarization direction.[142]

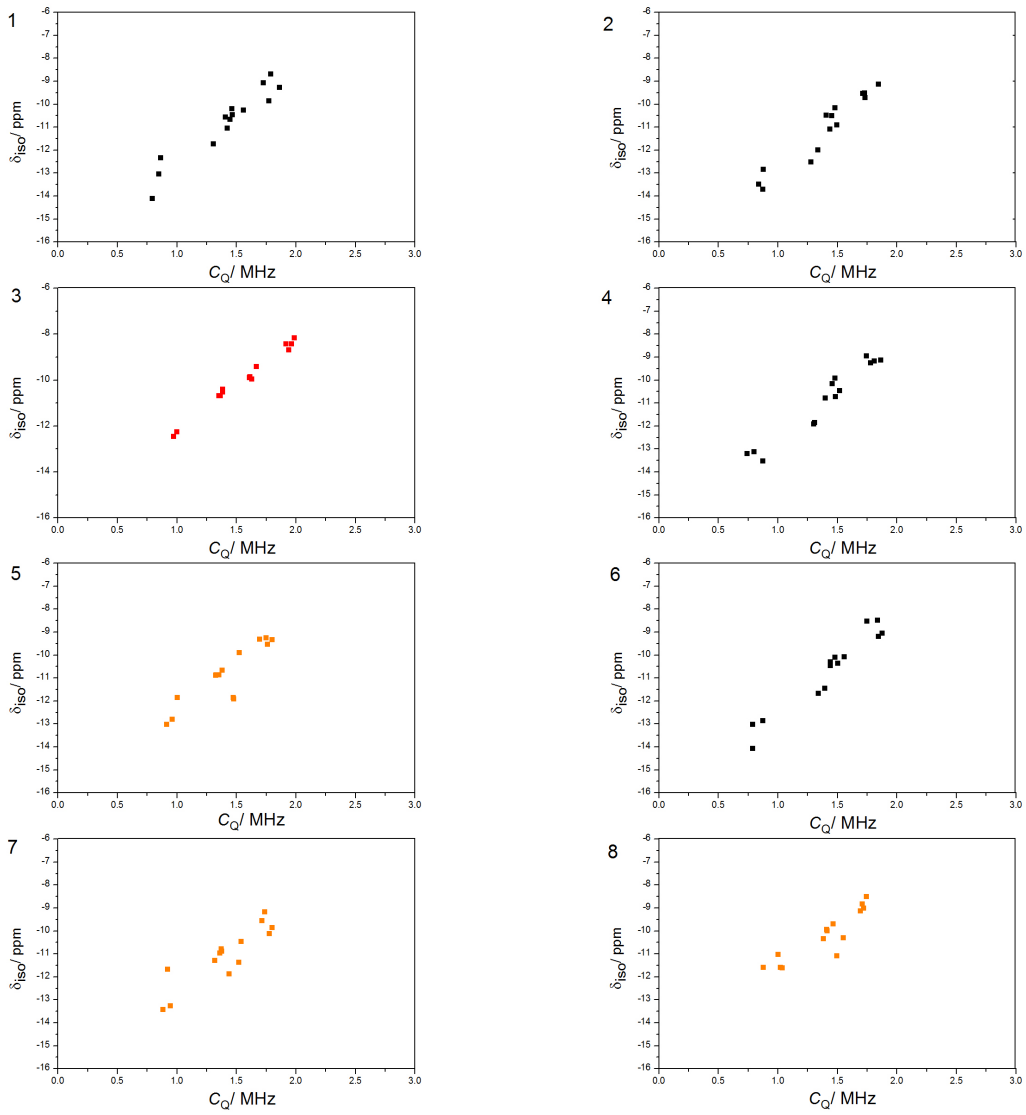

Figure 5.7, ^{23}Na MQMAS-inversion plots of $\boldsymbol{\delta_{iso}}$ against $\boldsymbol{C_Q}$ for the 8 lowest energy supercells of $K_{0.3}Na_{0.7}NbO_3$. The lowest energy configuration is labelled in red, while those labelled in orange of lower energy, but still considered significant.

The lowest energy structures and highest energy structure are overlaid with the experimental data acquired for $K_{0.26}Na_{0.74}NbO_3$, as this was the closest composition to the available diffraction structure (see **Figure 5.8**). According to the phase diagram this composition should have the same structural motifs as $K_{0.3}Na_{0.7}NbO_3$ as the second-order phase changes in the tilting patterns at room temperature are predicted at x = 0.2 and x =0.4.

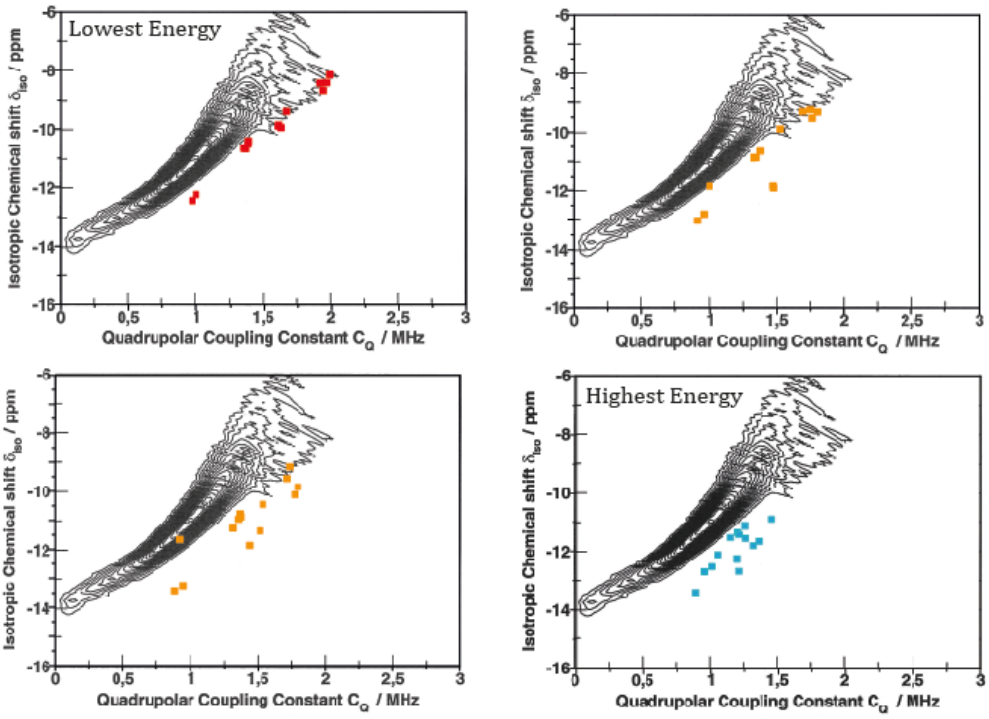

Figure 5.8, ^{23}Na MQMAS-inversion plots of $\boldsymbol{\delta_{iso}}$ against $\boldsymbol{C_Q}$ for the 3 lowest energy supercells and the highest energy configuration of $K_{0.3}Na_{0.7}NbO_3$ overlaid on the $K_{0.26}Na_{0.74}NbO_3$ experimental data. The lowest energy configuration is labelled in red, those that are energetically relevant but not the lowest are in orange and highest energy is in blue.

Whilst a thorough investigation should consider supercells of different lattice dimensions, from this investigation it is clear that CASTEP 8 is able to capture the fine structural detail in these samples. The lattice sites associated with the more deshielded δ_{iso} and larger C_Q parameters can be correlated with ^{23}Na cations surrounded by sodium cations in the next-nearest neighbour bonding sphere, whereas the most shielded δ_{iso} and smaller C_Q parameters are connected with potassium cations in the next-nearest neighbour bonding spheres. Between these two extremes the correlated behaviour originates from changes in the number of Na^+ cations in the next nearest neighbour bonding sphere. Thus, it is only for configurations with clustering of the K^+/Na^+ cations that the full range of δ_{iso} and C_Q values can be realised.

NMR-CASTEP exhibits excellent predictive capabilities for the ^{23}Na δ_{iso} and C_Q parameters, which additionally confirms the suitability of the calibrated reference shift σ_{ref}(^{23}Na). The degree of correlation between the δ_{iso} and C_Q parameters is worst for the highest energy structure (and therefore least likely). In this structure the K cations are more dispersed throughout the lattice. The ionic radius for the K cation is comparatively much larger in comparison to the Na cation. This stepwise change in ionic radii between Na and K means that the structure is less able to accommodate the complex tilting

motifs. Whilst tilting is still a characteristic feature of the high-energy structure it is comparatively weaker due to the limiting influence of the K cations. This structural motif is reflected in the distribution of the δ_{iso} and C_Q parameters that display a much smaller range of variation. In contrast the highest energy KNN structure shows the greatest tendency towards a planar arrangement of K cations. In this configuration the influence of the K cations is minimized, enabling the structure to accommodate more extensive octahedral tilting distortions.

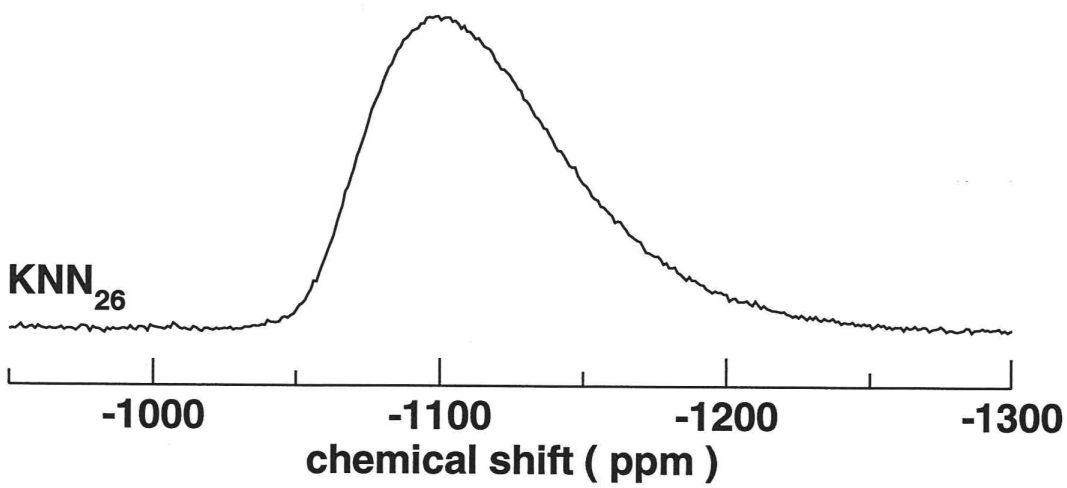

Figure 5.9, ^{93}Nb solid-echo spectrum for $K_{0.26}Na_{0.74}NbO_3$

The ^{93}Nb solid-echo spectrum of the $K_{0.26}Na_{0.74}NbO_3$ sample has an asymmetric lineshape that tails off towards lower frequencies (see **Figure 5.9**). This occurs when a distribution of quadrupolar dominated local environments are convoluted with a powder lineshape. Though this appears a generic lineshape its exact form is dependent on the distribution of the local environments, which is not known a priori and therefore the lineshapes can be difficult to model. In these situations it is common to parameterize the lineshape in terms of an average isotropic chemical shift $\langle\delta_{iso}\rangle$ and quadrupolar coupling constant $\langle C_Q\rangle$. These key experimental values are compared against the computed values for all eight of the low energy supercells in **Table 5-8**.

Table 5-8 Experimental $<\delta_{iso}>$,$<C_Q>$ values for $K_{0.26}Na_{0.74}NbO_3$ (closest experimental composition to $K_{0.3}Na_{0.7}NbO_3$) listed against the corresponding values for the low energy supercells (lowest energy is labelled in red) and the highest energy supercell (blue).

	$<\delta_{iso}>$/ppm	$<C_Q>$/MHz
Experimental	-1066	21.8
Configuration	$<\delta_{iso}>$/ppm	$< C_Q >$/MHz
1	-1016.5	21.8
2	-1017.3	21.5
3	-1016.1	21.8
4	-1016.5	21.1
5	-1016.7	21.2
6	-1016.4	21.5
7	-1017.2	21.2
8	-1016.7	21.8
9	-1017.31	20.3

Particular attention is drawn to the excellent agreement between the computed and measured values of the mean quadrupolar coupling for the low energy structures. The high-energy structure shows the largest error, which would further corroborate the conclusions from the ^{23}Na data.

However there are only modest correlations between the calculated and experimental $\langle\delta_{iso}\rangle$ values where there is a consistent difference of ~ 40 ppm. Hanna *et al*[103] reported DFT approaches for ^{93}Nb NMR parameter calculation. In this study 13 separate niobate systems are investigated using CASTEP. The experimental data is plotted against the calculated parameters to obtain correlation coefficients (R^2). A relatively poor correlation coefficient of R^2 = 0.784 for the chemical shift relationship δ_{iso} is reported and errors of > 40 ppm are observed for around half of the 13 systems under investigation.

It is possible that this represents a systematic deficiency in the description of the heavy ^{93}Nb nucleus. For heavy nuclei it has been shown that relativistic descriptions are required in order to compensate for the all-electronic characteristics at the nucleus where the strong nuclear potential means that the electrons possess a large angular momentum leading to velocities that approach the speed of light. Yates *et al*[166] have demonstrated that the zero-order regular approximation (ZORA) implemented in CASTEP, which is a

scalar relativistic correction for the core electrons, is successful with the pseudopotential approach for many nuclei. However, the deficiencies observed here, and in prior studies, suggest that a fully relativistic description could be required to accurately describe the influence of the ^{93}Nb valence states on the chemical shift.

5.7 Preliminary investigations into characterizing the KNN Phase diagram using special quasi-random structures

With the introduction of the GIPAW method it is now common practice within the field of NMR crystallography to complete a set of electric field gradients and NMR chemical shift calculations from the putative crystal structures to aid the interpretation of experimental datasets. However for disordered structures like KNN modelling the partial occupancy via conventional supercell techniques are prohibitively computationally expensive if numerous points across the phase diagram are to be considered.

The SQS approach is a potential computationally cheaper alternative to the conventional supercell method. In order to assess the suitability of SQS structures for characterising the KNN system, we attempt to reproduce the experimentally observed ssNMR correlations described previously.

Here we attempt approximate the disordered state by the use of special quasi-random structures (SQS). For a given number of crystallographic sites this approach maps the best possible approximation to a disordered state onto a supercell where the quality of the approximation is based on the correspondence of the lattice correlation functions correlations to those of the disordered state.

5.7.1 SQS structure generation

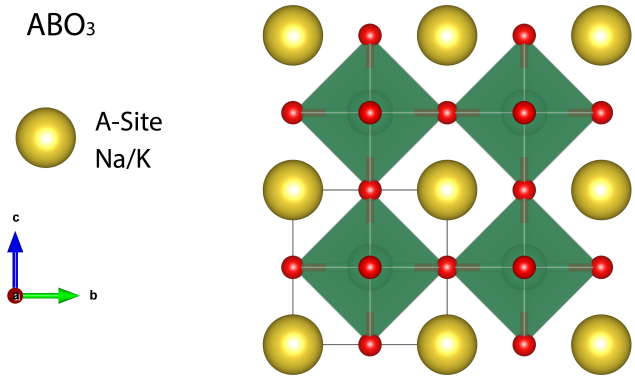

Figure 5.10, ideal ABO_3 perovskite lattice. SQS structures are generated by distributing Na/K on the A-lattice site.

Specifically a custom code written by Dr Zhe Liu was used to distribute Na/K cations for a given concentration across the A-site of an ideal fcc perovskite (see **Figure 5.10**) such that their radial correlation functions mimic those of a random alloy up to the 6-body term. The correlations were generated for a finite number of lattice sites, therefore designing N-atom periodic structures. The finite number of lattice sites required to accurately represent a random structure was increased to minimize the difference in correlation functions for each concentration thereby generating supercells between 60-100 atoms of various unit cell shapes. The maximal errors in the subsequent correlation functions in comparison with an infinite perfectly random alloy are shown in **Table 5-9**.

Particular emphasis was placed on attempting to minimize the most significant first and second neighbour correlation functions. It is only for the x = 0.25, x = 0.33 structures that significant divergence is observed in the second-nearest neighbour term. For these structures it was only for prohibitively large supercells that the second-nearest neighbour correlation could be reduced significantly. In order to sample concentrations over x = 0.5 it is sufficient to use the SQS generated structures except that the potassium and sodium sites are inverted.

Table 5-9 The largest error values of the mth-neighbour pair-correlation functions as obtained in SQS in comparison with a perfectly random alloy $<\Pi_{k,m}>=(2x-1)^k$

		1-Body	2-Body	3-Body	4-Body	5-Body	6-Body
x	Structure code	Error in correlation functions					
0.1	1477390	0	0.093	0.112	0.124	-0.189	0.305
0.1	1632673	0	0.093	-0.121	-0.143	0.144	-0.162
0.125	97635	0	0.063	-0.063	0.125	-0.159	0.280
0.2	1549394	0	0.140	0.149	0.204	0.028	-0.097
0.2	1602847	0	-0.110	0.183	-0.130	0.078	-0.047
0.2	1715711	0	-0.160	-0.217	-0.146	-0.072	-0.097
0.25	80178	0	0.750	0.625	0.188	0.156	-0.266
0.25	80269	0	0.750	0.625	0.438	-0.219	0.234
0.33	620	0	0.593	-0.296	0.395	0.115	-0.224
0.33	639	0	0.889	-0.296	0.395	0.115	-0.224
0.33	653	0	-0.296	-0.296	0.395	0.115	-0.224
0.4	910622	0	-0.440	0.208	0.232	0.200	-0.067
0.4	1067792	0	-0.240	-0.325	0.232	-0.150	0.150
0.4	1709526	0	0.427	0.208	-0.402	0.150	0.150
0.5	84466	0	0.333	0	-0.333	0	0
0.5	92929	0	0.333	0	-0.333	0	0

5.7.2 Optimizing the SQS structures

The generated SQS structures reflect a statistical distribution of K and Na over the A-Site of an undistorted cubic lattice, whereas in reality this symmetry is reduced to orthorhombic and monoclinic depending on the potassium content of the structure.

In order to convert the SQS structures from this non-physical situation to a plausible representation of the KNN structure, geometry optimisations were undertaken on all the structures using CASTEP 8. In order to allow the structures to adopt a structure consistent with the ions present in the supercells the lattice was left unconstrained.

Default parameters for convergence of the geometry relaxation were used (maximum force of 0.05 eV/Angstrom on any atom, maximum stress tensor component of 0.1 Gpa and a maximum change in energy of $2X10^{-5}$eV per optimization step) in both optimization strategies. Under these conditions the supercells converge on a lattice cell volume that looks to be within error of the experimental value (see **Figure 5.11**) for the four experimental data points.

However under such conditions the ideal lattice symmetry remains unbroken (even if the point symmetry is unconstrained during relaxation), that is the characteristic tilting of the sodium-rich side of the phase diagram is ill defined.

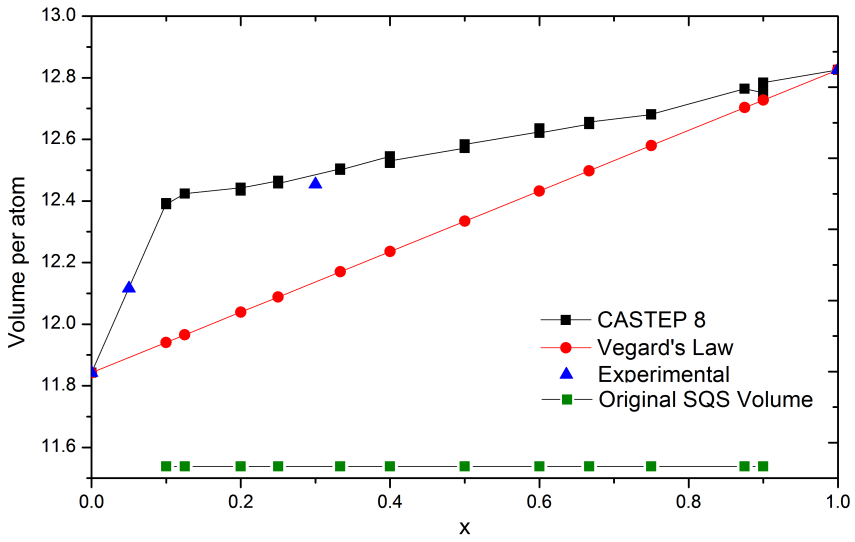

Figure 5.11, SQS supercell volume per atom before and after geometry optimization using CASTEP against reported experimental values and the volume according to Vegard's Law. The volume according to Vegard's Law that states for a randomly distributed continuous substitutional solid solution the unit cell parameters vary linearly with composition.

Therefore after generation and relaxation a further post-processing procedure was required to 'initialize' the structures according to their experimentally reported Glazer tilt patterns. Whilst these patterns could be introduced manually by distorting atomic positions it is difficult to do so systematically across relatively large supercells.

In a number of perovskite systems, mainly the tilting of octahedra controls the unit cell compression.[167,168] This fact is exploited to use cell compression to introduce tilting to the idealized structures. This method was tested on the SQS structure designed to represent the $Na_{0.875}K_{0.125}NbO_3$ composition that falls within a region of complex tilting according to the phase diagram. Cell compression was undertaken by reducing the volume such that the ratio of the relaxed lattice parameters remained equal.

The structure was geometry optimized under the relatively cheap constraints of 500 eV and a single *k*-point using the default CASTEP constrains. Additionally 0.05Å of noise was added onto the atomic positions in order to promote symmetry breaking. **Table 5-10** summarizes the resulting tilting introduced into the $Na_{0.875}K_{0.125}NbO_3$ structure based on geometry optimization under different cell compressions.

Table 5-10 Glazer tilting motifs in the $Na_{0.875}K_{0.125}NbO_3$ structure after various levels of cell compression

Percentage cell compression	Glazer notation according to phase diagram	SQS structures
1%	a(-)b(+)c(-)	a(0)b(0)c(0)
3%	a(-)b(+)c(-)	a(-)b(0)c(0)
5%	a(-)b(+)c(-)	a(-)b(+)c(0)

A subsequent geometry optimization was undertaken on the compressed $Na_{0.875}K_{0.125}NbO_3$ cells with an unconstrained lattice as the original cell volumes predicted by CASTEP that were arrived at under identical conditions replicated the experimental data. For these calculations the structures were initially relaxed using a cut-off energy of 650 eV with a 2x2x1 *k*-point grid before increasing the cut-off energy to 800 eV and the *k*-point grid to 2x2x2 for the last few iterations of the geometry optimization process.

After the corresponding cell expansions the imprint of the tilting patterns induced by the cell compression remained, so a set of subsequent NMR calculations were undertaken to obtain the EFG tensor and chemical shielding tensor on the optimized structures. The ^{23}Na MQ-MAS inversion for $K_{0.1}Na_{0.9}NbO_3$ is compared to the computed values for $K_{0.125}Na_{0.875}NbO_3$ in **Figure 5.12**.

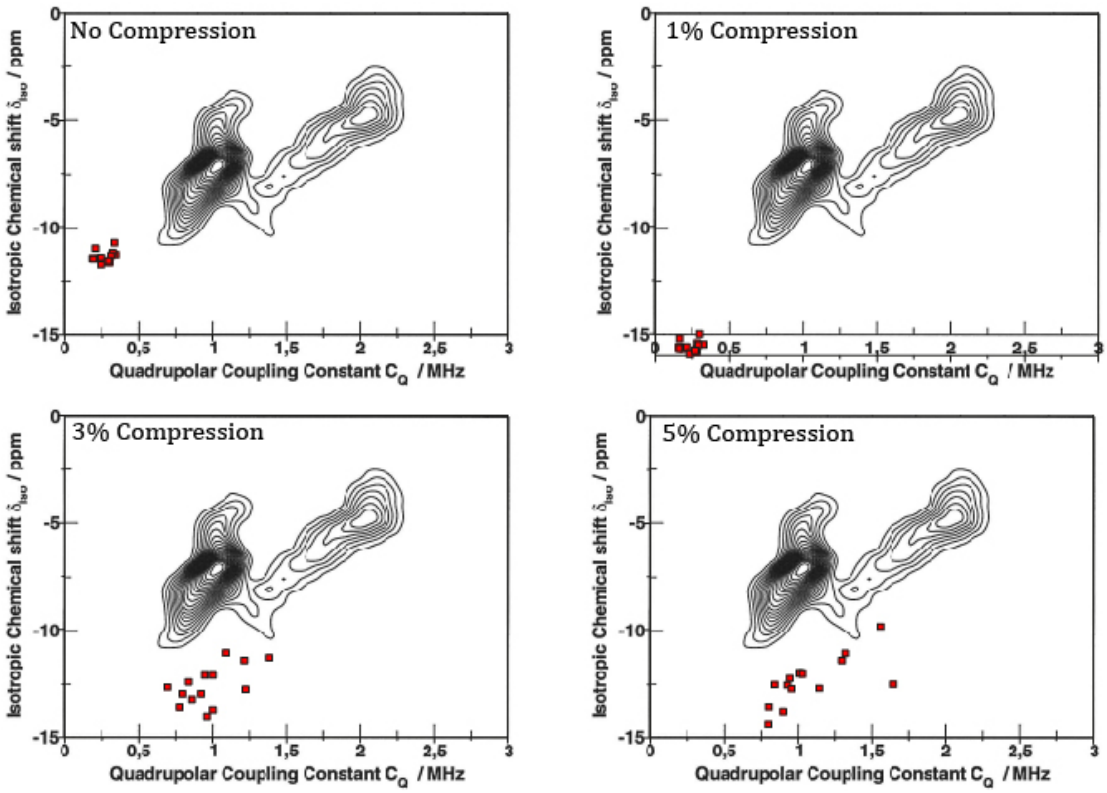

Figure 5.12, Comparison of the ^{23}Na MQ-MAS inversion for $K_{0.1}Na_{0.9}NbO_3$ against the SQS supercells for $K_{0.125}Na_{0.875}NbO_3$ after various levels of compression and subsequent relaxation using CASTEP

The NMR parameters under no compression reflect the non-physical order in the SQS structure by the isolated, tight cluster of the NMR parameters. As tilting patterns are introduced into the system a greater dispersion is observed in the parameters consistent with the trends observed experimentally. The closest agreement between the datasets is observed for a 5% compression of the supercell, which coincides with the closest match to the tilting pattern observed experimentally. For this structure there is a systematic ~ 5 ppm error in δ_{iso}, whereas C_Q seems to be captured accurately. Additionally the dispersion in the NMR parameters shows a propensity towards the two isolated environments observed experimentally.

The average δ_{iso}/C_Q ^{93}Nb parameters for the structures are summarised in **Table 5-11**. It is evident that the introduction of the tilting pattern via a geometry optimization under a 5% compression followed by a geometry optimisation under no lattice constraints sees the ^{23}Nb converge on the experimentally observed values.

Table 5-11 Calculated ^{93}Nb parameters following different levels of supercell compression and relaxation, compared with experimental values.

Cell compression	$<\delta_{iso}>$/ppm	$<C_Q>$/MHz
0%	-1066.4	19.16
1%	-1032.9	19.92
3%	-1035.8	22.69
5%	-1085.2	22.83
Experimental	-1069.0	21.45

The 5% cell compression methodology tested above for the $K_{0.125}Na_{0.875}NbO_3$ SQS supercell was extended to 12 compositions of KNN (x = 0.1, 0.125, 0.2, 0.25, 0.33, 0.4, 0.5, 0.6, 0.66, 0.75, 0.8, 0.9): all structures relating to the aforementioned concentrations were relaxed using CASTEP 8 with the default pseudopotentials and the PBEsol functional, before attempting to introduce tilting to the niobium octahedra by employing a 5% compression of the total volume to the supercells and geometry optimizing the structures under this compression using relatively cheap constraints of 500 eV and a single *k*-point with 0.05Å of noise imposed upon the atomic position. This compression was subsequently released for a further geometry optimization using a larger cut-off energy of 650eV that was increased to 800eV for the last stages of the geometry

optimization process. The resultant tilting patterns introduced onto the structures are described in **Table 5-12**.

Table 5-12 Summary of the tilting patterns introduced onto the perovskite SQS supercells and those observed experimentally in Glazer notation. Note the structure numbers are an arbitrary reference number. Entries in the table where there is agreement with experiment are highlighted in yellow.

x	Chemical formula	Structure number	Glazer notation according to phase diagram	SQS structures
0.1	$Na_{0.9}K_{0.1}NbO_3$	1477390	a(-)b(+)c(-)	a(0)b(0)c(-)
0.1		1632673	a(-)b(+)c(-)	a(-)b(+)c(-)
0.125	$Na_{0.875}K_{0.125}NbO_3$	97635	a(-)b(+)c(-)	a(-)b(+)c(0)
0.2	$Na_{0.8}K_{0.2}NbO_3$	1549394	a(-)b(+)c(-)	a(-)b(+)c(-)
0.2		1602847	a(-)b(+)c(-)	a(-)b(+)c(-)
0.2		1715711	a(-)b(+)c(-)	a(-)b(0)c(-)
0.25	$Na_{0.75}K_{0.25}NbO_3$	80178	a(-)b(+)c(-)/a(0)b(+)c(0)	a(-)b(+)c(-)
0.25		80269	a(-)b(+)c(-)/a(0)b(+)c(0)	a(-)b(-)c(-)
1/3	$Na_{2/3}K_{1/3}NbO_3$	620	a(0)b(+)c(0)	a(-)b(+)c(0)
1/3		639	a(0)b(+)c(0)	a(0)b(0)c(0)
1/3		653	a(0)b(+)c(0)	a(0)b(+)c(-)
0.4	$Na_{0.6}K_{0.4}NbO_3$	1067792	a(0)b(+)c(0)	a(0)b(-)c(0)
0.4		1709526	a(0)b(+)c(0)	a(0)b(0)c(-)
0.4		910622	a(0)b(+)c(0)	a(0)b(0)c(-)
0.5	$Na_{0.5}K_{0.5}NbO_3$	84466	a(0)b(0)c(0)	a(0)b(0)c(0)
0.5		92929	a(0)b(0)c(0)	a(0)b(0)c(-)
0.6	$Na_{0.4}K_{0.6}NbO_3$	1067792	a(0)b(0)c(0)	a(0)b(0)c(0)
2/3	$Na_{1/3}K_{2/3}NbO_3$	620	a(0)b(0)c(0)	a(0)b(0)c(0)
2/3		639	a(0)b(0)c(0)	a(0)b(0)c(0)
2/3		653	a(0)b(0)c(0)	a(0)b(0)c(0)
0.75	$Na_{0.25}K_{0.75}NbO_3$	80178	a(0)b(0)c(0)	a(0)b(0)c(0)
0.75		80269	a(0)b(0)c(0)	a(0)b(0)c(0)
0.875	$Na_{0.125}K_{0.875}NbO_3$	97635	a(0)b(0)c(0)	a(0)b(0)c(0)
0.9	$Na_{0.1}K_{0.9}NbO_3$	1632673	a(0)b(0)c(0)	a(0)b(0)c(0)

The extension of the approach produces modest correlation with the glazer patterns observed experimentally. The effectiveness of this approach is heavily dependent upon the unit cell shapes that are chosen on the basis of their ability to represent the disordered state. For example for the two $K_{0.1}Na_{0.9}NbO_3$ SQS structures where the lattice parameters are a = 8.87481, b = 8.81227 and c = 17.81784 and a = 9.59577, b = 11.78366 and c = 11.76426 where α, β and γ are very similar for structure numbers 1477390 and 1632673 respectively, the system responds to produce extensive distortions to the niobium based octahedra for the 1632673 structure where the lattice parameters are more equal as opposed the elongated unit cell of 1477390. Indeed all the 33 and 40 percent SQS structures adopted distortions incompatible with the experimental Glazer patterns. Thus, this method needs to be refined for future applications.

5.7.3 NMR Calculations on the SQS structures

In spite of these structural variations further NMR-CASTEP calculations were performed on the structures obtained by the compression process using a cut-off energy of 800eV where the tolerance on the convergence of the electronic structure calculation was reduced to 10^{-7}eV/atom (default is 10^{-5}eV/atom) as experience suggests that this is often required to ensure the repeatability of NMR calculations.

The experimental ^{23}Na inversion for $K_{0.1}Na_{0.9}NbO_3$ shows two distinct isolated clusters that are elongated along different directions. SQS structures generated for x = 0.1 and x = 0.125 with compatible tilt distortions are overlaid with the experimental data in **Figure 5.13**. Both structures display discrepancies from the experimental distributions: for the x = 0.1 the ^{23}Na quadrupolar coupling is overestimated by ~ 0.5 MHz, while for the x = 0.125 the isotropic chemical shifts are calculated 5 ppm upfield from the reported experimental shifts.

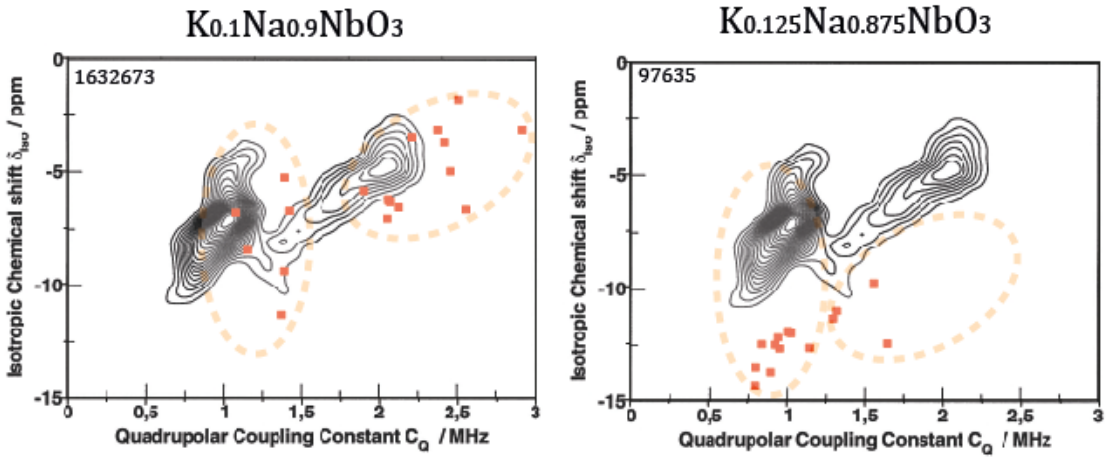

Figure 5.13, Comparison of the ^{23}Na MQ-MAS inversion for $K_{0.1}Na_{0.9}NbO_3$ against the SQS supercells 1632673 and 97635.

Nonetheless, for the $K_{0.1}Na_{0.9}NbO_3$ SQS structure in particular, the calculated data points on the inversion spectrum can be split into two regions that roughly align with the experimental distributions, suggesting that the supercells are capturing some of the structural detail.

Moving from the sodium rich side of the phase diagram towards the potassium rich side the next experimental dataset corresponds to the $K_{0.18}Na_{0.82}NbO_3$ composition. For this sample the ^{23}Na inversion spectrum reveals a distribution of nuclear environments by the elongation of the lineshape across a comparatively wide range of ^{23}Na isotropic chemical shielding and quadrupolar values. The orientation of the dataset reveals that these parameters are strongly correlated for this composition. The SQS structures 1549394 and 1602847 corresponding to KNN compositions of $K_{0.2}Na_{0.8}NbO_3$ are overlaid with the $K_{0.18}Na_{0.82}NbO_3$ data in **Figure 5.14**.

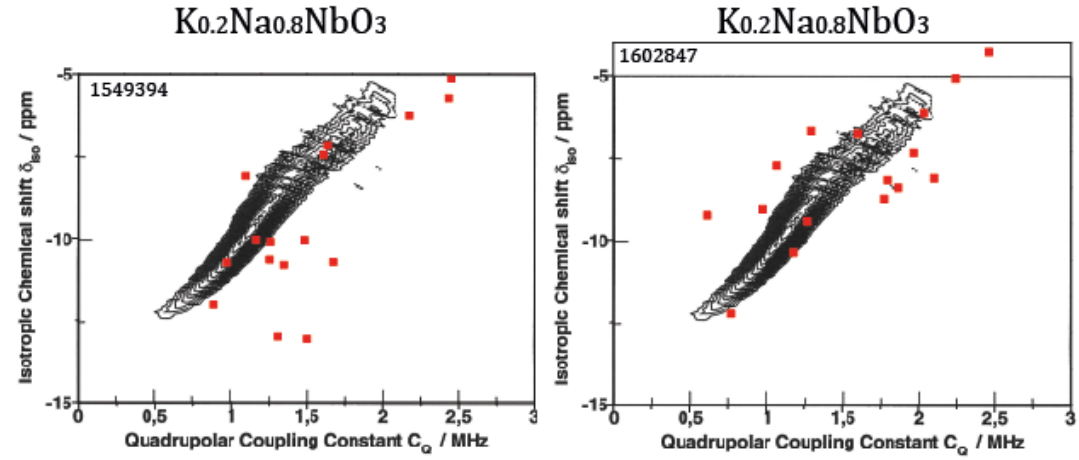

Figure 5.14, Comparison of the ^{23}Na MQ-MAS inversion for $K_{0.18}Na_{0.82}NbO_3$ against the SQS supercells 1549394 and 1602847

The SQS structures display a more diffused scattering of δ_{iso}/C_Q points in comparison to the experimental correlated trend, although the arrangement of the data points for the 1602847 structure does generally follow this development.

The experimental data shows that this correlated behaviour is extended to the $K_{0.26}Na_{0.74}NbO_3$ composition, although there is a significant reduction in the magnitude quadrupolar coupling constants consistent with the predicted second-order phase change in the octahedral tilting. The SQS structure 80178 corresponding to KNN compositions of $K_{0.25}Na_{0.75}NbO_3$ is overlaid with the $K_{0.26}Na_{0.74}NbO_3$ data in **Figure 5.15**.

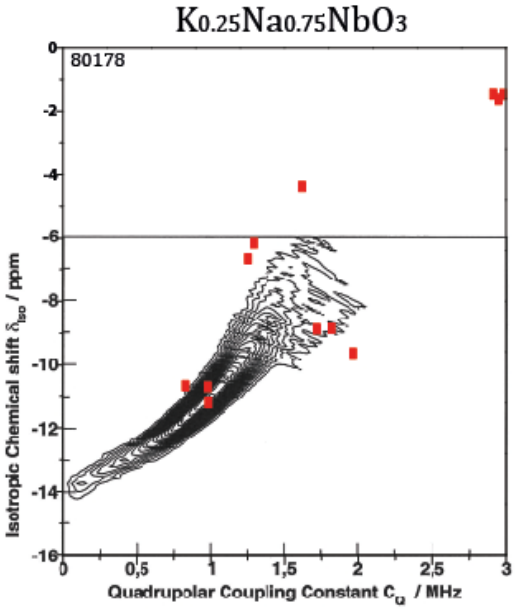

Figure 5.15, Comparison of the ^{23}Na MQ-MAS inversion for $K_{0.26}Na_{0.74}NbO_3$ against the SQS supercell 80178

As has been observed previously the data points are more dispersed than their experimental counterparts. In particular this structure predicts nuclear environments that extend downfield with larger quadrupolar coupling constants, which is at odds with the experimental data.

At x = 0.5 the octahedral tilting has disappeared and the KNN structure is predicted to undergo no further phase changes until the potassium niobate end member. This is reflected in the ^{23}Na inversion plots (see **Figure 5.3**) that display increasingly tight isolated clusters with decreasing sodium content. The SQS structures 84466, 1067792, 653, 80178, 97635 and 1632673 corresponding to x = 0.5, 0.6, 0.6667, 0.75, 0.875 and 0.9 are displayed in **Figure 5.16**.

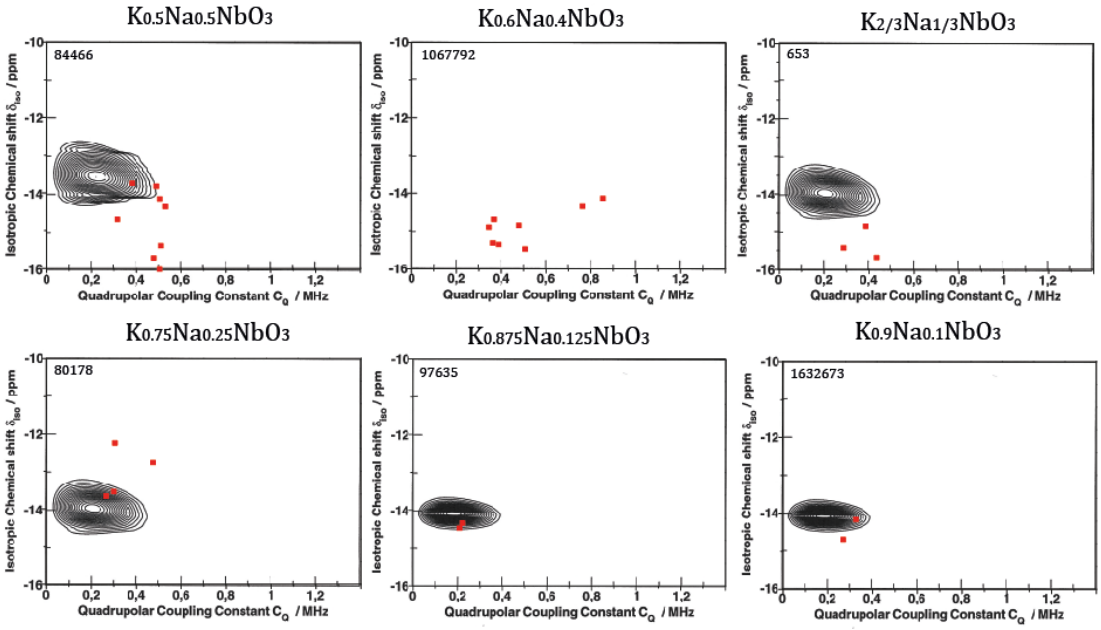

Figure 5.16, Comparison of the ^{23}Na MQ-MAS inversion plots for $K_{05}Na_{0.5}NbO_3$ plotted against SQS supercell 84466, $K_{0.7}Na_{0.3}NbO_3$ against SQS supercells 653 and 80178 and $K_{0.9}Na_{0.1}NbO_3$ against SQS supercells 97635 and 1632673.

The ^{23}Na inversion plots for the SQS structures capture the general trend towards an increasingly well-defined ^{23}Na nuclear environment. Given the lack of structural disorder for the potassium-rich side of the phase diagram these structures are less influenced by the difficulties with reproducing the tilting patterns observed the sodium-rich side of the phase diagram and are therefore a more reliable test for the suitability of SQS structures for representing the KNN system. For the SQS structures designed to represent x = 0.6667, 0.75, 0.875 and x = 0.9 the predicted structure are converging on the experimental error for the plots.

The corresponding ^{93}Nb NMR data for the SQS structure that have just been discussed are shown in **Figure 5.17**. Though caution should be applied when assessing the accuracy of the δ_{iso} values due to the possibility of systematic errors as has been discussed previously, it is clear that the SQS structure possess substantial deviation from the predicted experimental trend. Whilst moving from the sodium rich side to the potassium rich side the SQS structures capture the movement downfield of $\langle\delta_{iso}\rangle$. Within the two $\langle\delta_{iso}\rangle$ regions predicted by the SQS structures there is significant deviation from the experimental trend, the largest of which is recorded for the x = 0.5 SQS structure (~ 30 ppm). Counter intuitively the correlation between the $\langle C_Q\rangle$ datasets is even poorer than that observed for $\langle\delta_{iso}\rangle$. While the experimental trend spans a 3.5 MHz range the SQS structures span a 16 MHz range with composition. Even for the x =

0.67, 0.75, 0.875 and 0.9 structures that appeared good matches for the ^{23}Na experimental data there are major discrepancies.

Johnston *et al*[150] have shown that the ^{93}Nb quadrupolar coupling constant is very sensitive to the $NaNbO_3$ structural environment. Using a complementary CASTEP-DFT approach with experimental ssNMR is it shown that the *Pnma* and *Pbnm* exhibit a large change in C_Q from 25-32 MHz to ~4-5 MHz upon geometry optimization, despite the changes in both long range and local structure being relatively small.

Deviations from the ideal octahedral coordination have been described by the shear strain that denotes distortions from the ideal O-Nb-O bond angle and longitudinal strain that denoted distortions from the ideal Nb-O bond length. For ^{27}Al there are strong linear correlations in the magnitude of the C_Q and the shear strain.[169] However, for ^{93}Nb while it appears that the nearest coordination sphere dominates the EFG, such a simple description is insufficient as both the magnitude of any distortion and the exact direction and nature of any displacement must be accounted for. Thus it is difficult to establish exactly why the SQS structures display such large C_Q values, though it is clear that the distortions in the NbO_6 octahedra are too large to describe the experimentally observed structures.

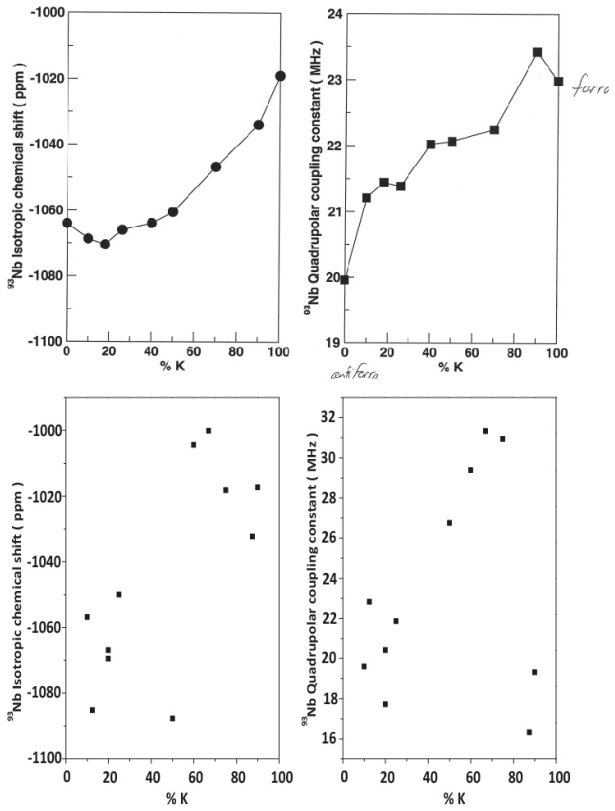

Figure 5.17, Comparison of the extracted $<\delta_{iso}>$ and $<C_Q>$ ^{93}Nb NMR parameters for experiment and for the SQS generated structures with compatible tilting patterns to the established KNN phase diagram.

5.8 Conclusions

Compared to the correlation obtained by the conventional supercell approach applied on the $K_{0.3}Na_{0.7}NbO_3$ structure the ability of the SQS structures, using the method outlined in this chapter, to predict the NMR parameters of KNN is relatively poor. Further work is required to establish an efficient method of introducing the tilting distortion on to these structures in a systematic and controllable manner in order to produce a thorough assessment of the potential for SQS structures to model the KNN system. Although broadly speaking it would be preferable to have a system to test the SQS approach on that does not have the tilting complication and where the pseudopotentials have less history of being suspect.

Though cell compression in the manner outlined in this chapter is able to introduce displacive tilting patterns upon the SQS structures, its dependence on the unit cell dimensions means it is non-transferable from the calibration unit cell. As this process involves the use of random coordinate noise to break symmetry, better results could be achieved if the process is repeated several times for each structure with different random number seeds. After relaxation back to zero compression the lowest energy structures could be taken for further consideration. A more sophisticated approach using cell compression might calculate the elastic modulus tensor in order to normalise the necessary cell compressions for different unit cells. However due to the sensitivity if the niobium octahedra to this process it is perhaps preferable to manipulate the coordinates manually in order to initialise the structures before relaxing them using the appropriate *ab initio* software.

The supercell investigation on $K_{0.3}Na_{0.7}NbO_3$ using the SOD software showed a tendency of the K cations towards occupying (010) planes. Furthermore it was seen that this structural ordering promoted an accentuation of the tilting distortion responsible for the range of δ_{iso} and C_Q observed experimentally. Whilst further investigation should be undertaken with both differently orientated and larger supercells to ensure the consistency of this observation, the ordering observed here is at odds with the disorder assumed in the SQS approach and therefore suggest SQS structures will be unable to represent the $K_{0.3}Na_{0.7}NbO_3$ composition.

6

SOLID STATE NMR STUDY OF VATERITE

6.1 Introduction

As calcium carbonate *(CaCO3)* is the most abundant biogenic mineral its importance in nature is undeniable (Lowenstam et al (1989))[170]. The skeletons of key marine organisms such as coral and some plankton are comprised of calcium carbonate. At least 20% of sedimentary rock is composed of chalk or limestone that is the result of organogenic sedimentation. Geological chalk deposits and the coral reef represent great reservoirs of sequestered carbon dioxide so they have a direct influence on regulating climate (Zeebe et al (2008))[171]. As anthropogenic oceanic acidification due to increasing atmospheric carbon dioxide (CO_2) levels looks to directly inhibit these processes they are of increasing relevance in modern times (Orr et al (2005))[172] Calcium carbonate also constitutes approximately 4% of the Earth's crust and therefore it is perhaps unsurprising that it already has proven to be a vital resource in the production of common materials like paper, rubber, plastics and paint (Xiang et al (2006))[173]

Calcium carbonate exists in three known polymorphs of pure calcium carbonate under biologically relevant temperatures and pressures; calcite, aragonite and vaterite. Vaterite is comparatively rare in geological settings due to its metastability with respect to the other calcium carbonates in the trimorphic series. However, it occurs in many unexpected places in nature where it is often associated with biological functions or as a precursor to carbonate-forming processes (Rodriguez-Navarro et al (2007), Heywood (1994) & Skinner (2005)) [174,175,174a]; as pancreatic stones (Falini et al (1998))[176], in gallstones (Sutor et al (1968))[177], in clogging human heart valves (Kanakis et al (2001))[178], in hamster vaginas[179], in microbial biscuits (Giralt et al (2001))[180] and in the hard tissue of fish otoliths (Falini et al (2005))[181]. Therefore this polymorph is of direct relevance to the study of biomineralization, but also in the wider context of crystal nucleation theory and

growth in general.[176] Recent reports on the stable prenucleation of ion clusters in $CaCO_3$ crystallization have challenged the model of classical nucleation theory that have underpinned the conventional understanding of the formation of $CaCO_3$ (Gebauer et al (2008), Pouget et al (2008) & Gebauer et al (2010))[182 183,184] A major stumbling block to the understanding the atomistic processes involved in the crystallization and stabilization of calcium carbonate is the lack of a recognised crystal structure of vaterite.

The German mineralogist Heinrich Vater synthesized vaterite in the laboratory before it was identified as a natural mineral. Linck (1903) evoked the mineralogical term of vaterite before Gibson et al (1925)[185] used X-ray diffraction on laboratory-synthesized vaterite to confirm its distinction from calcite and aragonite, thereby establishing the trimorphic nature of calcium carbonate. Following this Olshausen (1925)[186] indexed the X-ray diffraction powder pattern for synthetic vaterite based on a hexagonal symmetry, but it took more than a further three decades before the first complete structural model of vaterite (Meyer, 1959)[187] was reported. Following this publications there have been many scientific contributions on the topic of vaterite though there remains controversy surrounding important facets of its structure; indeed there is not consensus on its symmetry, space group, its unit cell parameters or the carbonate orientation and site symmetry. This opens up the question as to why there is such discord as to the fundamental aspects of the vaterite structure.

6.2 Brief literature review

The major publications that have contributed to the structural elucidation of vaterite are reviewed below.

Diffraction based studies on vaterite have been hindered by the inability to grow single crystals of a suitable size. It has now been well established that vaterite exists in nanosized crystallites (10-50nm) (Andreassen (2005))[188] that have been shown to form polycrystalline spherulites. Many of the early (and indeed some modern) attempts to refine the vaterite crystal structure relied on the relatively low-quality diffraction data that permitted a range of different interpretations. Meyer (1959)[187] initially proposed an orthorhombic (*Pbma*) structural solution based on single-crystal X-ray diffraction data of nano-crystalline vaterite that he later revised to the frequently cited (*Pbnm*) (Mayer (1960))[189] orthorhombic model to compensate for the apparent disorder in the carbonate molecules. Kamhi (1963)[21] later interpreted the X-ray diffraction data in terms of a

hexagonal symmetry ($P6_322$, $P6_3/mmc$) sparking debate as to whether vaterite has a hexagonal or orthorhombic crystal system.

Kamhi's hexagonal model posits the existence of partial occupancy in the carbonate positions. Under the assumption of hexagonal symmetry he was unable to index five weak reflections that he subsequently attributed to the existence of a superstructure defined by a 30° rotation of the pseudo-unit cell about the *c*-axis so that the true cell is defined by ($a=\sqrt{3}a'$, $c=2c'$) with an ABAB stacking sequence. Meyer (1969)[190] later suggested an alternative hexagonal based symmetry solution ($P6_3/mmc$) without partial occupancy of the carbonate positions and echoed Kamhi's suggestion that stacking faults were the origin of the spectral features that the model could not account for.

Broadly speaking Kamhi's solution contained two themes that have defined the modern debate over the structure of vaterite: the manifestation of disorder within the carbonate molecules within the unit cell and the possibility of stacking faults.

Two further structural models complete the set of five models defined by X-ray diffraction studies. Lippmann (1973)[191] proposed the space group *$P6_322$* by drawing from the vaterite-type high-temperature phase of $YbBO_3$ before Le Bail *et al* (2011)[192] proposed an orthorhombic fully ordered structural model with space group (*Ama2*) with a microtwinning of three domains rotated by 120° along the orthorhombic *a*-axis generating the apparent hexagonal character.

Numerous spectroscopic techniques have been applied in an attempt to eliminate the disagreement on the structural models of vaterite. Raman and infrared spectroscopy provide a direct method of evaluating the space group and site symmetry of the carbonates . However, the findings of the resultant studies offer a disparate set of conclusions that can largely be attributed to either sample impurity or different interpretations of mode assignments or group theory analysis. (Anderson (1996)[193], Wehrmeister et al (2010)[194])

In summary Behrens *et al*[195] suggested that the hexagonal crystal systems ($P6_3/mmc$ and $P63_22$) are incommensurate with the experimental data, Gabrielli *et al* (2000)[196] analysis of the Raman spectrum agreed with Meyer's hexagonal structure while Anderson's[193] group theory analysis favours Lippmann's ($P6_322$) model without ruling out the validity of Kamhi's model. Furthermore Wehrmeister *et al*[194] showed that their data was inconsistent with all the proposed models at the point of publication, though concludes that any model of vaterite must have at least three independent carbonates by

drawing parallels with the bastnäesite mineral paristie.

Current solid-state NMR spectroscopic studies of vaterite have predominantly focused on ^{43}Ca. (Bryce et al (2008), Burgess & Bryce (2015)) [197,198] As many of the outstanding issues regarding the vaterite structure involve the questions of carbonate orientation and/or disordering of which the ^{43}Ca nuclei is a comparatively poor probe this has done little to advance structural arguments. Nonetheless they identify one crystallographically unique Ca^{2+} site in vaterite with little dispersion in chemical shift or quadrupolar parameters. Though ^{13}C solid-state NMR measurements have been undertaken on vaterite these have been done so in the context of studying tangentially related aspects of calcium carbonates and have placed little emphasis on spectra assignment. The reported ^{13}C spectra for vaterite show two peaks with isotropic chemical shifts of 170.12 ppm and 169.07 ppm (Nebel et al (2008)).[199]

Within the last decade a spate of computation studies have provided important contributions to the structural debate on vaterite. Medeiros *et al* (2007) [200] published the first *ab initio* quantum mechanical calculations at the density functional (DFT) level of theory for vaterite in the local density approximation (LDA) and generalized gradient approximation (GGA). Despite recognizing that there were multiple possible structural models for vaterite they only consider Meyer's orthorhombic (*Pbnm*) cell, concluding through structural relaxation that the lattice parameters are in alignment with experimental observation but that the carbonates deviate from the *ab* plane they define in the original model.

Wang and Becker[201] used quantum mechanical first principles calculation within the DFT framework and molecular-dynamics (MD) simulations to propose an alternative unit cell with the space group $P6_522$ (Wang & Becker (2009)).[201] In doing so they made some important observations that informed subsequent publications; molecular dynamic studies at 300 K showed that the orientations of the CO_3 ions are disordered with an angle of 120° between CO_3 planes consistent with Kamhi's model, but that this fully-disordered arrangement cannot account for the low intensity features (weak reflections and diffuse streaks) in the single-crystal diffraction data. They investigate the existence of superstructure (and therefore CO_3 orientational ordering) by higher temperature MD and show that a fully ordered hexagonal superstructure without stacking faults with an ABC layer stacking sequence can be obtained. They conclude that the degree of CO_3 ion ordering is dependent on sample preparation in thermal history and can account for the large variation in the measured enthalpies of formation from vaterite to calcite (Wolf et al

(2000), Plummer & Busenberg (1982) & Turnbull (1973))[202,203,204]. Importantly this highlighted the possibility of thermally activated CO_3 rotation that has become a pivotal feature of the modern structural models.

Perhaps the most significant advances with regards to the structural elucidation of vaterite have been made in the past five years using first-principle DFT calculations. Demichelis *et al*[205] showed that both the hexagonal (*P6₅22*) and orthorhombic (*Pbnm*) ordered structures are unstable transition states by calculating the vibrational spectra for the candidate structures using the first principle method. (Balan et al (2014))[206] The *Ama2* structure suggested by La Bail *et al*[192] was shown to represent a true minima but was rejected on energetic grounds as it is ~ 16KJmol^{-1} less stable than *Pbnm*. Scanning along the corresponding imaginary modes they determined that the *Pbnm* structure relaxes to a basin with $P2_12_12_1$ symmetry while the hexagonal *P6₅22*-structure relaxes to three minimum energy structures; $P112_1$, $P6_5$, $P3_221$. By considering the energy difference between the unstable *P6₅22*-structure with respect to the distinct energy minima the activation barrier for interconversion are shown to be within thermal energy under ambient conditions. This justified the paradigm shift from describing the 'disorder' in vaterite via a static partial occupancy to a set of structural exchanges by CO_3^{2-} rotations between different distorted minima so that the true structure of vaterite could be a combination of the minimum energy structures.

Mugnaioli *et al* (2012)[207] used a combined *ab initio* and automated electron diffraction experimental approach to study two samples of vaterite prepared by different synthesis routes. On the basis of structural refinements by *ab initio* methods their samples had either monoclinic or triclinic structures with space groups *C2/c* ("2-layer") or $C\bar{1}$ ("6-layer") respectively.

In the subsequent follow-up paper Demichelis *et al* (2013)[22] used the same phonon-based methodology as employed in the evaluation of the *Pbnm* and *P6₅22* structures to show that both the *C2/c* and $C\bar{1}$ monoclinic structures correspond to unstable transition states with corresponding minimum energy structures with space groups of *C2* and *Cc* for the former and to two distinct minimum energy structures with space group *C1* for the latter. Using energetic considerations it is shown that these multiple structures of vaterite also permit structural interconversion at room temperature due to the rotational freedom of the CO_3^{2-}units. Furthermore the hypothesis that different layer stacking in vaterite is a second source of disorder is assessed by constructing all possible permutations of six planes taken from low-energy structure

$P3_221$ along the c-axis. Geometry optimization of the viable structures leads to structures in the *C2* or *$P3_221$* (or its mirror image *$P3_121$*) space groups. From the energetics it follows that vaterite has multiple structure that form three almost isoenergetic basins with hexagonal, 2-layer and 6-layer monoclinic structures thereby validating this as an additional source of disorder. It is noted that some of the possible structures in the hexagonal basin are intrinsically chiral ($P6_5|P6_1$, $P3_221|P3_121$, $P6_522|P6_122$) adding a third possible dimensions of complexity to the vaterite structure.

Kabalah-Amitai *et al* (2013)[208] made a radical breakthrough experimentally by studying biogenic vaterite spicules grown by the *Herdmania momus* (a red-throated ascidian). This animal is a sessile filter feeder that is commonly found attached to rocks from depths of 3 to 50m in temperate and tropical oceans. The vaterite spicules range in size between 100μm and 2.5mm and line the H. momus' tunic, siphons and branchial basket[209] Those in the tunic are thought to provide protection while those in the body are used as mechanical support. These spicules grow larger than typical vaterite single crystals in a perfectly and reproducibly orientated manner allowing for a convenient cutting of specimens along known crystallographic directions. By using high-resolution synchrotron powder diffraction in conjunction with aberration-corrected high-resolution transmission spectroscopy (HRTEM) they concluded that in their biogenic samples of vaterite were actually composed of at least two different crystallographic structures that co-exist within a pseudo-single crystal. The structural components were split into to a dominant hexagonal major matrix into which nanodomains of an undetermined minor structure fitted.

Further evidence for the existence of two or more distinct structures being present within a single sample of vaterite were made by Demichelis et al (2014)[210] using a complementary theoretical and experimental Raman spectroscopy approach. New spectra were recorded from the vaterite spicules of *H. momus* from the Great Barrier Reef, as used to identify two distinct structures by Kabalah-Amitai *et al*[208]. *B*ased on matching the simulated Raman spectra to the experimental measurement all but two of the models can be ruled out; the two lowest energy structures (*$P3_221$* and *C2*). These have indistinguishable simulated Raman spectra that are compatible with the experimental Raman measurements. However the inability to match more than two stable structures to the experimental data brings into question the possibility of intrabasin structural interconversion at room temperature.

This last point highlights that there are still important questions regarding the

structure of vaterite that need to be reconciled. Whilst there is theoretical evidence for structural interconversion, this might be inhibited such that the system becomes kinetically trapped in a subset of stable structures. Indeed there are still questions over how many polytypes of vaterite even exist in reality and whether this varies between different syntheses and biological conditions. The Raman spectroscopy studies by Demichelis *et al* (2014)[210] and Wehrmeister *et al*[194] found no significant difference between samples of biological, geological and synthetic origin. However there is also significant evidence that well-known biomolecules such as aspartic acid (Makai et al (2004))[211], taurine, glutamate, serine, glycine, and glycoprotein (Kitano et al (1965))[212] can alter the potential for vaterite to form and its stability (Wu et al (2004))[213, 176]. It follows that the principles of formation under biogenic conditions may vary the chemical composition. If a direct dependency on the structural crystallographic constituents could be shown with regards to synthesis then we cannot rule out the possibility of a true single crystal existing for vaterite. There are many examples of organisms transferring chirality to crystal surfaces that in turn imprint an asymmetry upon biominerals (the Nautilus shell is perhaps the most famous example). Orme *et al* (2001) [214] showed that aspartic acid (which is chiral) bound to growing calcite crystals (which is are not chiral) lead to macroscopic hillock forms on the crystal surface with shapes that are mirror images of one another depending on which molecular form of aspartic acid was involved in the process. As many of the possible theoretically predicted structures for vaterite are intrinsically chiral (*C2*, *C1, P6$_5$*, *P3$_2$21*, *P6$_5$22*) there remains the possibility that chirality might be a source of structural variation in vaterite crystallites.

For the sake of completeness a full summary of the current models of vaterite is shown schematically in **Figure 6.1** (as adapted from Burgess *et al* (2015)[198])

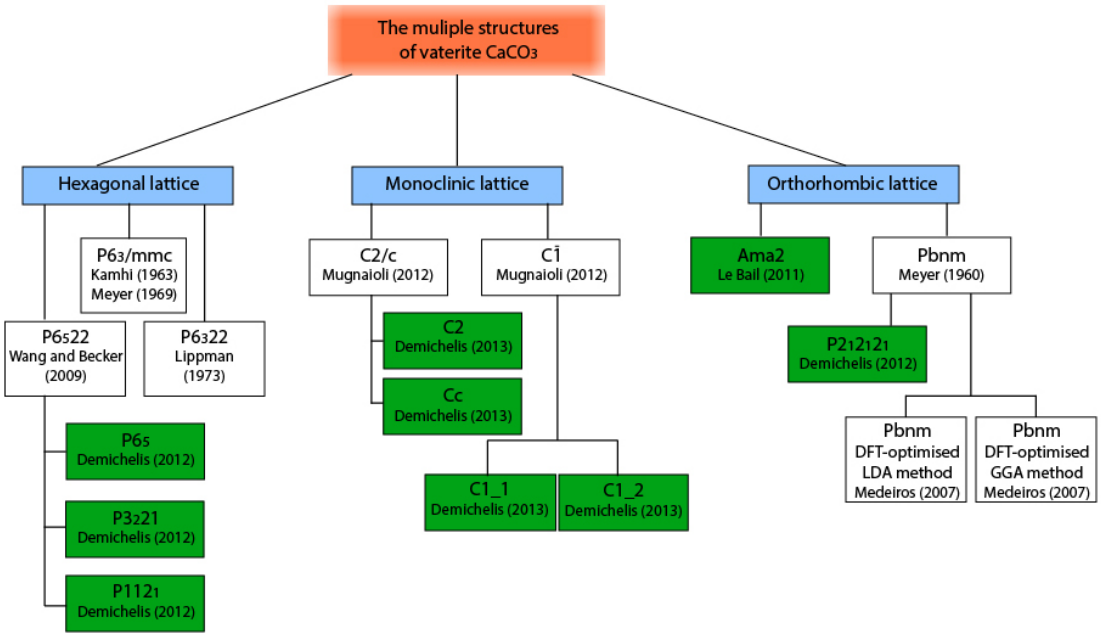

Figure 6.1, Chart summarizing the multiple proposed structures for the vaterite polymorph of CaCO3. Models are based on hexagonal, monoclinic, or orthorhombic lattices. Green labels denote stable structures while white labels denote metastable structures according to Demichelis *et al*[205,22]

6.3 Experimental

6.3.1 Sample preparation

The chemical reagents used in the following syntheses were of analytical grade. The preparation of a ^{13}C and ^{17}O isotopically-enriched sample of vaterite was conducted according to the procedure outlined by Shivkumara et al. (2006)[215]. A Na_2CO_3 solution was prepared by dissolving 0.214 g of 99.9% ^{13}C-enriched Na_2CO_3 (Sigma-Aldrich) in 2 g of 40% ^{17}O-enriched H_2O (Cortecnet) and refluxed at 70°C overnight. The solution was then allowed to cool to room temperature wherein 1.201 g of glycine (Sigma-Aldrich) was dissolved in 12 ml of distilled H_2O before adding a 4 ml 0.5 M solution of the refluxed Na_2CO_3. This solution was stirred for thirty minutes before adding 4ml of 0.5 M $CaCl_2$ (Sigma Aldrich) dropwise over 10 minutes. The solution was then stirred for 30 minutes before the product was filtered and rinsed with distilled water. The precipitate was then dried under vacuum overnight. For the preparation of the other ^{13}C and ^{17}O isotopically-enriched $CaCO_3$ polymorphs the synthesis was adapted from previous literature.[215]

Calcite was prepared by dissolving 0.107g of 99.9% ^{13}C-enriched Na_2CO_3 in 2 g of 40% ^{17}O-enriched H_2O and refluxed at 70°C overnight. The solution was then

allowed to cool to room temperature. The directing agent (glycine) is not needed in the synthesis of calcite so the resulting liquid was used to create a 2ml 0.5 M Na_2CO_3 aqueous solution. Subsequently 0.111 g of $CaCl_2$ was dissolved in 0.5 ml of distilled water to create a 2 M aqueous solution. One drop of 0.1 M HCl was added to the solution such that the pH ~ 2.7 before being heated to 40°C. When a stable temperature had been reached the 0.5 M Na_2CO_3 aqueous solution was rapidly added to the 2 M $CaCl_2$ aqueous solution. The mixture was then refluxed overnight at 40°C. The precipitate was then filtered and rinsed with distilled water before being dried under vacuum overnight.

A mixed aragonite and calcite sample was created by adding 0.535 g of 99.9% ^{13}C-enriched Na_2CO_3 to 2 g of 40% ^{17}O-enriched H_2O and a refluxed at 70°C overnight before being allowed to cool to room temperature. This solution was then used to create a 50 ml 0.1 M Na_2CO_3 aqueous solution, which was stirred at a constant rate for 30 minutes. A 50 ml 0.1M $CaCl_2$ (pH~4) was heated to 80°C before the two solutions were rapidly mixed. The product was immediately filtered after mixing and vacuum dried.

6.3.2 Powder X-ray Diffraction

In all cases the precipitated powders were initially analysed using a Rigaku Ultima IV Diffractometer to verify the phase composition and crystal structures over the 2θ range of 5-75° with increments of 0.02°. Scanning rates of 0.08°/min were employed to acquire the patterns for calcite, the mixed phase aragonite samples and vaterite. The experimental PXRD patterns for the $CaCO_3$ polymorphs are shown in **Figure 6.2**. The vaterite pattern is consistent with PXRD patterns reported for synthetic[215] and natural[216] sources of vaterite. An additional detailed vaterite PXRD experiment was performed using a Panalytical X-Pert Pro MPD Diffractometer with scanning rates of 0.00326°/min at increments of 0.0131303° ~7 months after the original synthesis when all NMR experiments described in this study had been undertaken to check that there had been no transformation to the more stable $CaCO_3$ polymorphs. As there are only minor differences in resolution between the two PXRD powder patterns due to the slower scanning raters and finer scanning increments of the second experiment, this second vaterite PXRD experiment shows that vaterite has remained stable over this period of experimentation. The powder X-ray patterns for the calcite and aragonite powders obtained from the synthesis methods outlined previously match the known PXRD patterns. [215,217]

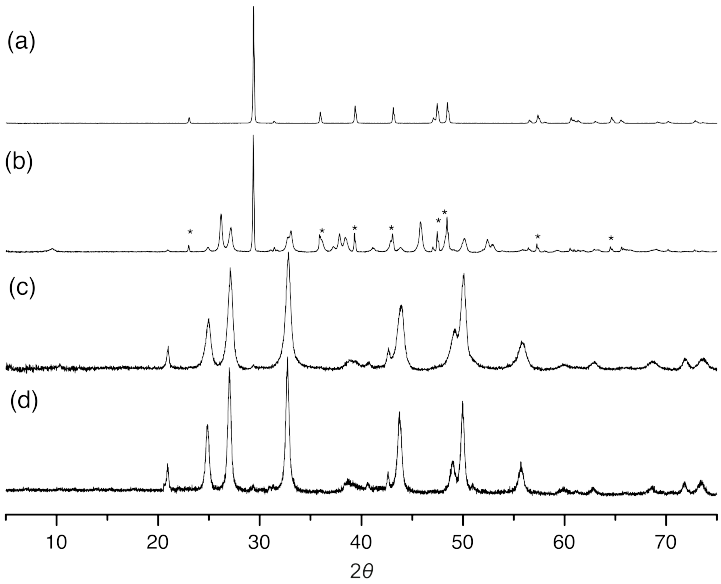

Figure 6.2, powder X-ray diffractograms for ^{13}C-^{17}O isotopically-enriched samples of (a) Calcite (b) Mixed phases aragonite and calcite (c) Vaterite as synthesized (d) Vaterite after ~7 months. No peaks in the vaterite experimental powder patters show peaks that would indicate the presence of calcite or aragonite

6.3.3 ^{17}O solid-state NMR experiments

All ^{17}O spectra in this study were referenced against the primary IUPAC reference of H_2O (δ_{iso} = 0 ppm). Additionally pulse lengths were calibrated against this solution to establish selective and non-selective $\pi/2$ pulse lengths where the 'solid' $\pi/2$ pulse lengths were scaled from the 'solution' values by a factor of 1/(I+1/2)=1/3.For each of the samples the recycle delay was estimated by acquisitions employing a recycle delay up to 30 s informing the use of the following subsequent recycle delays; 15.0 s for vaterite and the mixed phase $CaCO_3$ sample and 6.0 s for calcite. ^{17}O rotor-synchronized solid-echo (υ_R =20 kHz) NMR experiments (θ - τ - θ - τ – acquire) where $\theta = \frac{\pi}{4}$ with a corresponding pulse length of 1.5 μs were undertaken across multiple fields of 21.14T (Bruker AVANCE II, ω(^{17}O)=122.01 MHz), 14.1T (Bruker AVANCE II, ω (^{17}O)=81.26 MHz) and 11.75T (Bruker AVANCE III, ω(^{17}O)= 67.8 MHz) where the spectra were the product of averaging across 1536, 8004 and 8192 transients respectively. For the pure calcite and mixed phase the same pulse lengths and rotor frequency were employed, but spectra were acquired with 720 transients at 21.14 T only.

^{17}O double orientation rotation (DOR)[218] experiments were acquired across magnetic fields of 9.4T (Bruker Avance-400), 11.7T (Bruker Avance III-500), 14.1T (Bruker Avance II-600) and 20.0T (Bruker Avance III-850) using a custom built Samoson DOR probes in conjunction the odd order sideband suppression as outlined

by Samoson et al. (1994)[219]. External rotor spinning frequencies of 1.0-1.6 kHz and internal rotor spinning frequency 5.6-7.6 kHz were employed such that the variation in the outer rotor frequency was used in order to isolate the resonant positions from the spinning sidebands.

A ^{17}O 3QMAS NMR was performed on a Bruker 900 MHz Bruker Avance II NMR spectrometer (21.1 T) for all $CaCO_3$ under investigation. The 3QMAS measurements were performed with a custom 3.2-mm HX probe at rotor speed of 20 kHz and a resonance frequency of 122.01 MHz. The 3-pulse z-filter sequence[57] employed excitation ($\frac{3\pi}{2}$), conversion ($\frac{\pi}{2}$) and selective detection ($\frac{\pi}{2}$) pulses of 5.8 μs, 2.0 μs and 18.0 μs respectively. For vaterite each slice was created by averaging across 612 transients for 48 increments with a recycle delay of 10s. Identical setups were used for calcite and the mixed phase sample except for the former where each slice was the created by averaging across 180 transients for 256 increments with a recycle delay of 3 s, and the latter where each slice was created by averaging across 96 transients for 56 increments with a recycle delay of 10 s. For all 3QMAS experiments purely absorptive 2D peaks were achieved by using the States method.[59]

2D ^{13}C-^{17}O J-HMQC (Heteronuclear Multiple-Quantum Coherence)[220] experiments were performed on a Bruker Avance III spectrometer operating at 19.96T (^{1}H Larmor frequency of 850.2 MHz) using a Bruker 3.2 mm double resonance probe at an MAS frequency of 20 kHz. All experiments were performed at room temperature unless otherwise stated. Detection was carried out on ^{17}O due to the substantially quicker relaxation of the ^{17}O sites within the samples.

Calcite was used as a setup sample as it only possesses one independent carbon and oxygen (and therefore a single well-defined ^{13}C-^{17}O J-coupling). This preliminary J-HMQC was run using 32 co-added transients for each of 64 t1-FIDs in combination with a recycle delay of 8.0 s where the States method[59] was used to achieve sign discrimination in F1. ^{13}C $\frac{\pi}{2}$ of pulse duration 5 μs were used in conjunction with ^{17}O $\frac{\pi}{2}$ and π pulses of 2.25 μs and 5.25 μs duration where the recoupling delay (1/2J) was optimised to 14.9965ms, which is consistent with carbonate J-couplings of approximated ~30 Hz. For vaterite the setup was identical to that of calcite except that 304 transients were co-added for each of 96 t1-FIDs.

6.3.4 ^{13}C solid-state NMR experiments

^{13}C Single-pulse MAS experiments were completed at 150.86 MHz (14.1T) using a HX 3.2 mm Bruker probe at rotor spinning frequencies of 0.8 kHz (Calcite only), 1 kHz and 15 kHz. The spinning sideband manifold simulation was completed using the appropriate solid line analysis function available in DMFit[221]. In order to ensure that the spectra were quantitative the T1 was evaluated for each of the samples using an inversion-recovery experiment; leading to the use of the cautious recycle delay of 3600s for all the ^{13}C-labelled samples.

6.4 The structure of the calcium carbonate ($CaCO_3$) polymorphs

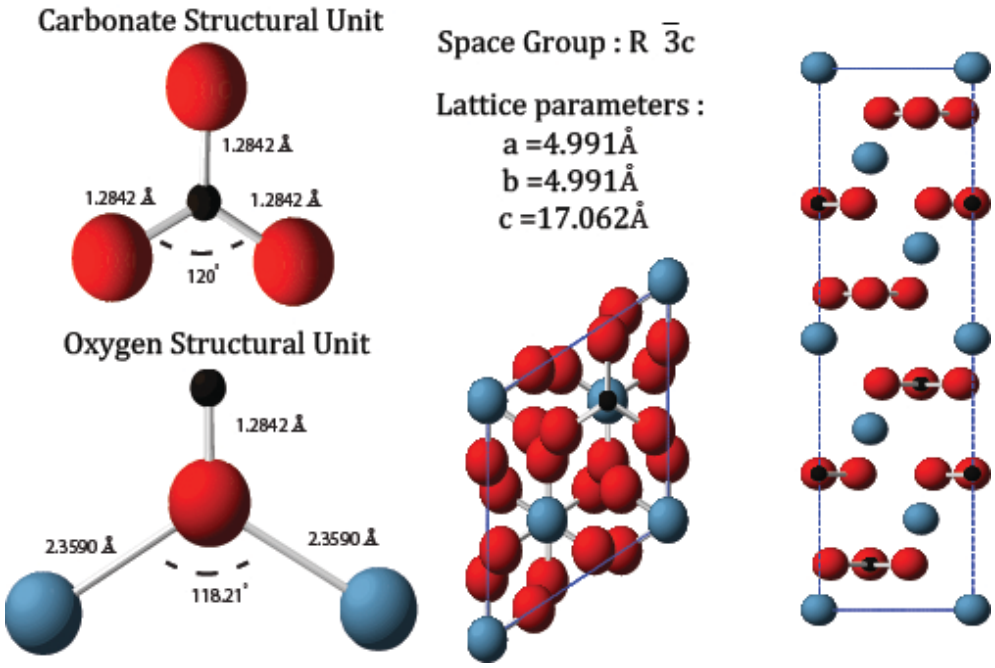

Figure 6.3, the symmetric carbonate structural unit and oxygen structural unit comprising the calcite structure (left). The unit cell of calcite orientated along the c-axis and along a-axis.

Calcite is the most stable polymorph of the trimorphic calcium carbonate series. It is rhombohedral carbonate consisting of CaO_6 octahedra (distorted face centered cubic calcium) with CO_3 trigonal planar units arranged along the *c*-axis as shown schematically in **Figure 6.3**. In crystallographic terms this means that the simple structure can be reduced to a single inequivalent calcium, carbon and oxygen site in the asymmetric unit cell. The single oxygen site is a 3-coordinate with a single covalent bond to carbon and two equal length ionic bonds to calcium ions such that the C-O-Ca_2 unit is planar.[222]

In aragonite the calcium layers are still separated by carbonate groups as in calcite, but these lie along the *c*-axis in two oppositely orientated parallel layers creating an ABAB layer stacking sequence. The trigonal planar symmetry that is distinctive of the carbonate groups in calcite is broken so that in aragonite there are two unique C-O distances (and two unique O-C-O angles) in the CO_3 group. This translates into two crystallographically inequivalent-oxygen sites in the aragonite orthorhombic unit cell as shown schematically in **Figure 6.4**. In aragonite the oxygen environments are always 4-coordinate with a single covalent bond to carbon and three ionic bonds to calcium. These oxygen structural units are distorted tetrahedra where the calcium cations are arranged such that two of the Ca-O bonds are equal and the third Ca-O bond is comparatively shorter.[223]

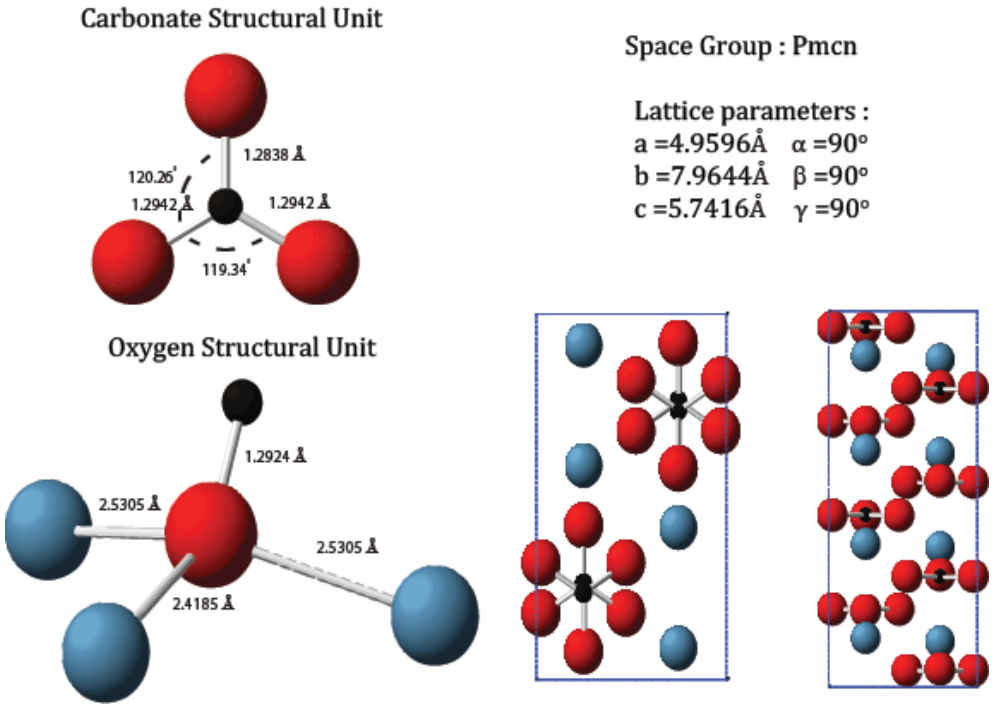

Figure 6.4, the carbonate structural unit and oxygen structural unit comprising aragonite (left). The unit cell of aragonite orientated along the c-axis and along a-axis.

Owing to the ubiquity of calcite and aragonite in nature these polymorphs have been extensively studied such that their respective structures have been successfully refined under numerous external conditions. In juxtaposition with the definitive crystallographic characterization of calcite and aragonite, the structure of the least stable $CaCO_3$ polymorph vaterite is still not well understood. In fact it is disconcerting to note the number and the variation in complexity of the structures proposed by existing literature (and therefore scientific endeavour) as solutions to the make-up of vaterite under ambient conditions.

From an NMR perspective we are interested in solving the structure of vaterite, like any other crystallographic technique, by identifying the number of inequivalent species in the unit cell and how they relate to one another. As this particular study is focusing on the use of ^{17}O and ^{13}C ssNMR for structural elucidation it is worth commenting more specifically on how these species vary in the structures from existing literature.

The oxygen coordinations and the number of inequivalent oxygen and carbon species in the asymmetric unit cell for these structures are summarized in **Table 6-1**. This summary shows that the number of crystallographically unique oxygen environments varies extensively between different proposed structures. Tri-coordinate oxygen is common to all the vaterite structures, though many also contain additional four-coordinate oxygen sites. Raman evidence[194] indicating that vaterite must have at least three independent carbonates does little to help constrain the structural data to a particular model. **Table 6-1** shows that all the energetically stable structures of vaterite possess between 3-18 unique carbonate species making this observation commensurate with any one of them.

Table 6-1 *Number of inequivalent oxygen and carbon crystallographic sites in the proposed structures of vaterite and O coordination number (CN). Note all carbon species are carbonates so CN(C) = 3.*

	Inequivalent oxygen species in unit cell	**CN(O)**	**Inequivalent carbon species in the unit cell**
Orthorhombic			
$P2_12_12_1$	3	3,4	1
Ama2	2	3	1
Pbnm	2	3,4	1
Hexagonal			
$P3_221$	10	3,4	4
$P3_121$	10	3,4	4
$P112_1$	27	3,4	9
$P6_5$	9	3,4	3
$P6_522$	5	3	2
$P6_3/mmc$	2	3	1
Monoclinic			
C2	10	3,4	4
C2c	5	3	2
Cc	9	3,4	3
C1_1	54	3, 4	18
C1_2	54	3,4	18
$C\bar{1}$	27	3	9

The situation is further complicated if this fact is coupled with the possibility of vaterite having different constituent domains as observed by Kabalah-Amitai (2013)[208] then this constraint cannot even eliminate the comparatively simple orthorhombic models from consideration.

6.5 ^{17}O – A brief prologue on the oxygen bonding environment

To the authors knowledge there has been few prior ^{17}O solid-state NMR (ssNMR) studies of ternary oxides like calcium carbonate. The single existing ^{17}O ssNMR study of calcite reports a relatively large C_Q ~ 7MHz and an asymmetry parameter η_Q ~1 for the single tricoordinate oxygen (C-O-Ca_2) site.[224] In crystalline ionic solids interpretation of ^{17}O ssNMR spectra can be informed by the observation that in such systems the ^{17}O nucleus becomes more shielded with increasing coordination number (generally between 1-5).[225,225b,226,227] However, in the $CaCO_3$ system the oxygen is involved in both strong covalent bonding within the CO_3^{2-} units and bonding to the metal Ca^{2+} cations that has more ionic character. How the interplay of the two types of chemical bonding affects such well-defined trends in the context of $CaCO_3$ is unclear.

Traditional chemical shift theory suggests that the dominant paramagnetic shielding term for the isotropic chemical shift increases with the occupation of excited states.[40] As the internal covalent C-O bonds will have the greatest effect on the electronic excited states it is tempting to propose this as the dominant effect on $\delta_{iso}(^{17}O)$. However, in aluminosilicates the partially covalent nature of the Ca-O bond has a large effect on the ^{17}O chemical shifts. This is particularly well demonstrated by the deshielding effect on the ^{17}O chemical shift observed between Ca oxides and aluminosilicates and the corresponding Mg compounds. The ^{17}O chemical shifts of non-bridging oxygen in Mg aluminosilicates is ~40 ppm[228,229] while in Ca aluminosilicates it is ~ 105 ppm[230] and this difference is further amplified for the purely ionic MgO ($\delta_{iso}(^{17}O)$=47ppm[231]) system in relation to its CaO counterpart ($\delta_{iso}(^{17}O)$=294ppm[232]).

As an exercise to investigate the importance of the bivalent Ca^{2+} cation to the ^{17}O NMR parameters in the calcite and aragonite calcium carbonate systems an Mg^{2+} and an Sr^{2+} cation were independently inserted in the place of a single Ca^{2+} cation of fully relaxed structures described in section 6.4 NMR calculations were subsequently performed on the modified structures using CASTEP 8 with parameters as outlined in section 7.1.1. The corresponding changes to the NMR parameters of the nearest ^{17}O nuclei and the ^{13}C

nucleus of the related carbonate unit to the substituted Mg^{2+} and Sr^{2+} cations are shown in **Table 6-2**.

Table 6-2 ^{13}C and ^{17}O NMR parameters for calcite and aragonite calculated with and without an additional Mg^{2+} or Sr^{2+} cation inserted into the $CaCO_3$ system in place of a Ca^{2+} using CASTEP8 with the PBEsol functional

		Unaltered	**Single Ca replaced by Mg**	***% diff***
Calcite	$\delta_{iso}(^{13}C)$/ppm	168.101	169.111	0.6
Aragonite	$\delta_{iso}(^{13}C)$/ppm	170.141	171.491	0.79
		Unaltered	**Single Ca replaced by Sr**	**% diff**
Calcite	$\delta_{iso}(^{13}C)$/ppm	168.101	166.701	-0.83
Aragonite	$\delta_{iso}(^{13}C)$/ppm	170.141	169.331	-0.48
		Unaltered	**Single Ca replaced by Mg**	***% diff***
Calcite	σ(O1)/ppm	31	58.33	88.16
	C_Q(O1)/MHz	-7.029	-7.05	0.3
Aragonite	σ(O1)/ppm	34.61	33.62	-2.86
	σ(O2)/ppm	39.54	59.9	51.49
	C_Q (O1)/MHz	-6.514	-6.409	-1.61
	C_Q (O2)/MHz	6.71	7.141	6.42
		Unaltered	**Single Ca replaced by Sr**	**% diff**
Calcite	σ(O1)/ppm	31	21.84	-29.55
	C_Q(O1)/MHz	-7.029	-7.042	0.18
Aragonite	σ(O1)/ppm	34.61	31.78	-8.18
	σ(O2)/ppm	39.54	31.79	-19.6
	C_Q (O1)/MHz	-6.514	-6.627	1.73
	C_Q (O2)/MHz	6.71	6.492	-3.25

As has been observed before for ^{13}C ssNMR studies of biogenic and synthetic carbonates[233] the carbon is relatively insensitive to the changes in the alkali cation; the change in δ_{iso} when substituting Mg^{2+} into the calcite and aragonite structures is on the same order as that observed between calcite and aragonite.

For the oxygen species in direct coordination with the Mg^{2+} cation the change is more dramatic than that observed for the ^{13}C nuclei where the magnetic shielding (σ_{iso}) is seen to become more deshielded by ~27 ppm and ~20 ppm in calcite and aragonite respectively consistent with more ionocovalent character in the calcium.

In spite of the larger ionic radii of the Sr^{2+} cation it maintains the same coordination as the Ca^{2+} but the ^{17}O chemical shift is increasingly deshielded with respect to the calcium. This change is consistent with an increase in the paramagentic response due to virtual transitions involving the Sr 4d orbitals where the 2p orbitals of the oxygen hybridize with with unoccupied 4d state of the Sr.[234] Whereas there was a large stepwise change in the ^{17}O chemical shift for the substitution of the Ca^{2+} for a Mg^{2+} species this change is much less significant between the Ca^{2+} and Sr^{2+} consistent with the onset of this dominant unoccupied d-orbital effect on the chemical shift that is absent from the Mg system.

Although these observations are by no means definitive they certainly suggest that the calcium has some covalent character in the $CaCO_3$ system. By examining the possible vaterite structures it is evident that thought the C-O bond length varies little (1.28-1.31Å), the Ca-O bonds can vary between 2.27-2.79Å. Moreover the number of nearest neighbour Ca^{2+} cations in the oxygen coordination sphere is seen to vary between 3 and 4 for $CaCO_3$ structures.

In conclusion, though it is tempting at first glance to simply consider the Ca-O bonds as mostly ionic so that the ^{17}O ssNMR spectra can be rationalized in terms of the C-O bonds of the carbonate units alone, when one couples the fact that the Ca-O bonds do have significant covalent contributions with a comparatively wide range of Ca bonding environments it is clear that it is necessary to include both the carbonate unit and the Ca bonding arrangement in the assignment of any oxygen crystallographic site.

6.6 ^{17}O MAS solid-state NMR

Conventional ^{17}O MAS NMR spectra for synthetic calcite, a mixed phase sample of aragonite and calcite and vaterite are shown in **Figure 6.5**. The calcite spectrum shows a distinctive second-order quadrupolar powder pattern consistent with a single crystallographically distinct ^{17}O site. The small peak on the downfield side of the powder pattern corresponds to the centreband of the first satellite transitions. The (+1/2 <-> -1/2) transition centreband was fitted in DMFit[221] (see **Figure 6.5**) allowing the extraction of the NMR interaction parameters recorded in **Table 6-3**.

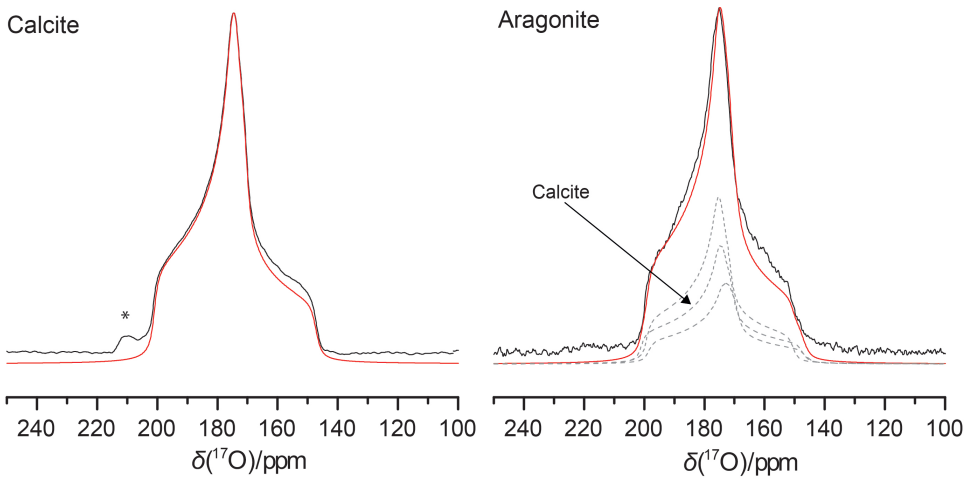

Figure 6.5, deconvolution of the 20kHz MAS spin-echo experiments acquired at 21.1 T for synthetic calcite, a mixed phased synthetic sample of aragonite/calcite (black corresponds to the experimental lineshape and red to the deconvolution)

Table 6-3 NMR parameters from deconvolution of the 20kHz MAS spin-echo experiments acquired at 21.1 T for synthetic calcite and a mixed phased synthetic sample of aragonite/calcite

^{17}O NMR – MAS Spin-Echo Experiment

System	Site	$\delta_{iso(MAS)}$ ppm/±1.75	C_Q MHz/±0.15	η ±0.03
Calcite	1	201.05	6.85	0.95
Aragonite	1	199.2	6.5	0.96
	2	198.6	6.8	0.92

The equivalent ^{17}O MAS NMR spectrum for the mixed phase sample, with contributions from both calcite and aragonite, has a lineshape that mirrors the shape of the pure calcite spectrum except that the singularity and edges are broadened consistent with the presence of three very similar overlapping second-order quadrupolar powder patterns. For the mixed phase lineshape fitting the pure calcite deconvolution was used such that only its intensity was allowed to iterate while for the aragonite contributions the relative intensity and NMR parameters were allowed to iterate and uncertainties in the NMR parameters were estimated by repeating lineshape fittings from various initial conditions.

It is significant that for both calcite and aragonite where the oxygen coordination is seen to vary from a C-O-Ca_2 tri-coordinate position to a C-O-Ca_3 quad-coordinate position that the quadrupolar asymmetry parameter (η) remains close to 1 and the

isotropic chemical shift only varies by ~ 2 ppm. Thus this mixed phase sample is particularly illustrative of the difficulty in resolving crystallographically-inequivalent carbonate oxygen sites by conventional ^{17}O MAS NMR: where it would be impossible to conclude *a priori* that there were three crystallographically-distinct oxygens as predicted by the crystal structures from this experimental result alone.

For vaterite the complication of its corresponding ^{17}O MAS NMR spectrum escalates further from that of the mixed phase sample where the signal intensity is split into a narrow downfield component and a broader upfield component. The visible shoulder of the narrow downfield component looks to follow the general shape of a second-order quadrupolar powder pattern where quadrupolar asymmetry parameters is ~1 as is the case for the pure calcite and mixed phase samples. However few conclusions can be drawn as to the number and environments of the crystallographically-distinct oxygens in the vaterite sample from this spectrum alone.

Due to the interdependence of the ^{17}O NMR parameters on the chemical bonding with respect to both the Ca^{2+} cations and covalent C-O bonds any deconvolution model must include reference to both these structural components.

As calcite and aragonite have distinctive oxygen bonding arrangements that incorporate the oxygen-environment alkali metal cation and carbonate duality they are a useful reference points in the discussion of the vaterite structure. Then the stable structures of vaterite as proposed by Demichelis et al[22] can be reduced into both three and four-coordinated oxygen sites with a mixture of calcite-distorted oxygen environments and aragonite-distorted oxygen environments: in calcite the carbonate unit is rotated about the axis of the C-O bond where the oxygen is ionically bonded to the calcium such that it is neither coincident with the plane of the Ca-O-Ca or completely perpendicular to it as demonstrated in **Figure 6.6**.

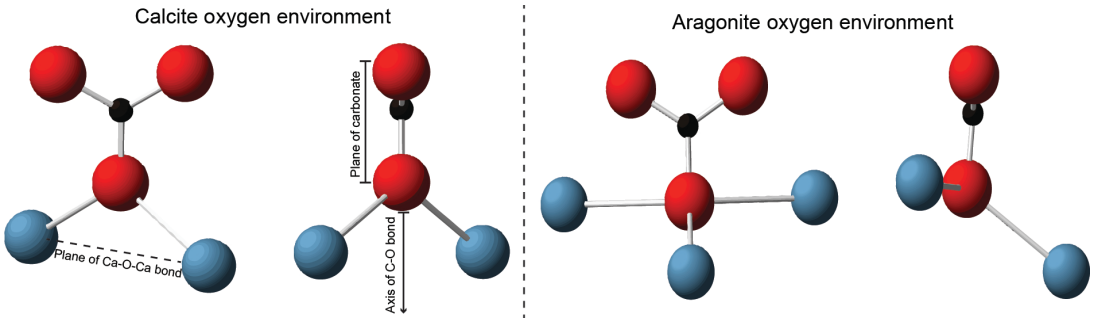

Figure 6.6, Calcite and aragonite oxygen environment as a structural unit that includes both the ionic and covalent components.

In aragonite there are two unique four coordinate crystallographic oxygen sites. One of the oxygen sites is shown in **Figure 6.6** as a representative environment in the aragonite structure. In aragonite the two longer Ca-O bonds are of equal length and the carbonate unit is not aligned along any one of the C-O bonds.

In vaterite there are both tri and quad-coordinated oxygen environments that are divided into structural subsets in **Figure 6.7**. Moreover to emphasise how this reasoning translates to the experimental spectra the ^{17}O MAS NMR vaterite spectrum is shown in **Figure 6.7** with different oxygen resonances arrayed beneath corresponding to each of the subsets of the vaterite system based on the proposed structural models.

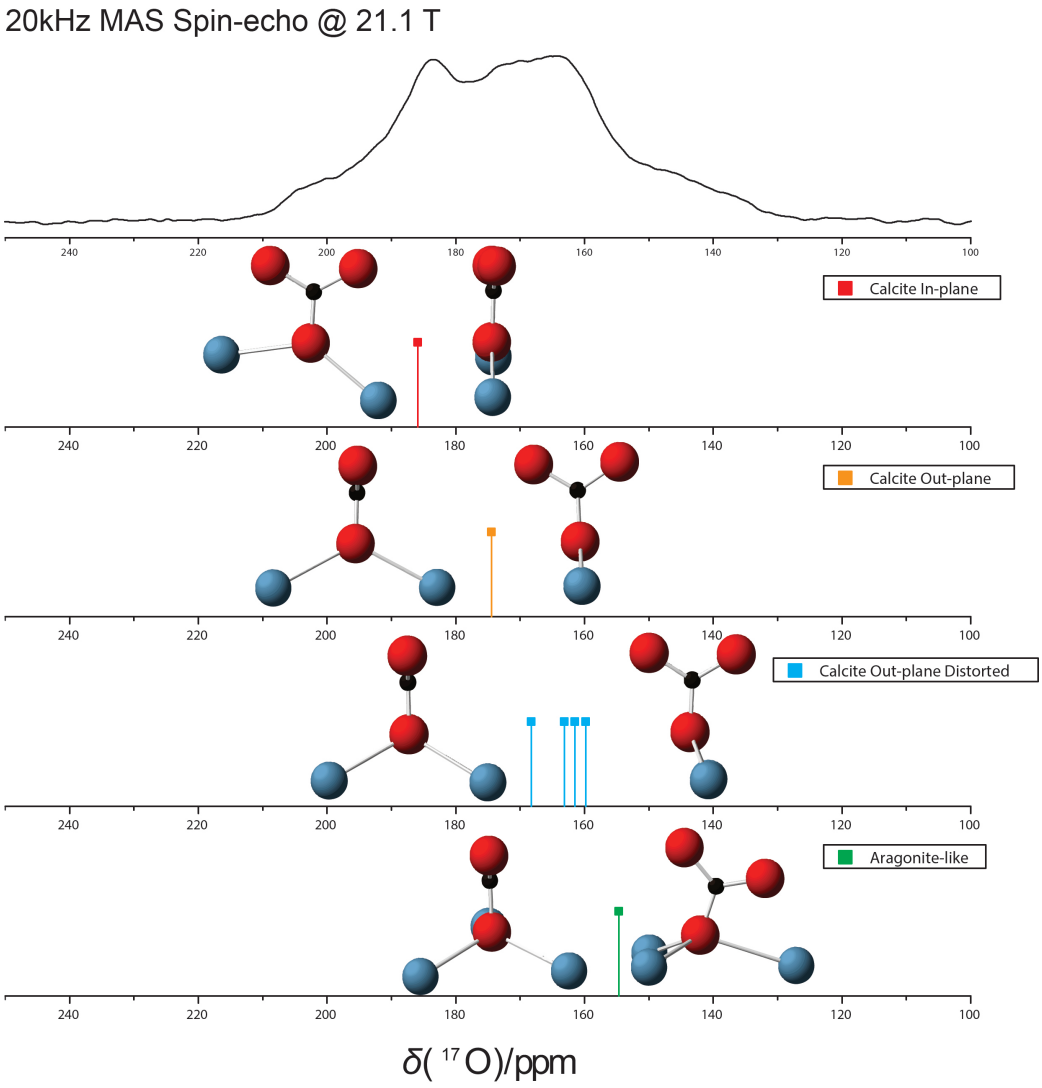

Figure 6.7, centre of gravity for major structural units proposed for the deconvolution of the experimental ^{17}O NMR data for vaterite. An example of a resonance position for each of the structural subsets is shown below the 20kHz MAS spin-echo experiments acquired at 21.1 T

The tri-coordinated oxygen bonding regimes differ from calcite in that the carbonate unit is always orientated such that the Ca-O-Ca unit is in the plane of the CO_3^{2-} unit or perpendicular to the Ca-O-Ca plane. This is shown schematically in **Figure 6.7** (calcite in-plane and calcite out-plane) with a corresponding representative centre of gravity position for such a group at 21.1T. The calcite out-plane motif has a more distorted twin whereby the Ca^{2+} cations are rotated so that if looking down a plane defined by the direction of the C-O bond the Ca-O-Ca unit is lifted from this plane (calcite out-plane distorted in **Figure 6.7**).

This distortion is present in varying degrees where the extreme point corresponds to the oxygen being able to accommodate another Ca^{2+} cation such that the species can be considered 4-coordinate (aragonite-like in figure 5). Whereas in aragonite there are two longer bonds (and they're of equal length) the four coordinate environments in vaterite are all unequal with two comparatively shorter Ca-O bonds. The carbonate unit is always orientated as observed in the 'calcite out-plane' structural motif.

By the outlined model for the deconvolution of vaterite the more deshielded oxygen environments can be associated with the tri-coordinated oxygen environments and the most shielded with the distorted tetrahedral oxygen environments. Then the oxygen environments recorded between these two 'extremes' can be considered as distorted intermediate arrangements of tri-coordinated oxygen.

6.7 Two-dimensional ^{17}O Multiple-Quantum MAS NMR

The inhomogeneous quadrupolar broadening that is compromising the resolution of the MAS NMR spectra can be removed by using the 2D-MQMAS technique[55] that correlates the symmetric (m_I<->-m_I) multiple quantum transitions with the central transition, for 3QMAS this means that the triple quantum coherence (-3/2, +3/2) is correlated to the single quantum coherence (-1/2, +1/2). **Figure 6.8**a shows the triple quantum ^{17}O MAS NMR spectra for a pure calcite and a mixed phase calcite and aragonite sample after a shear transformation has been applied to the raw data.

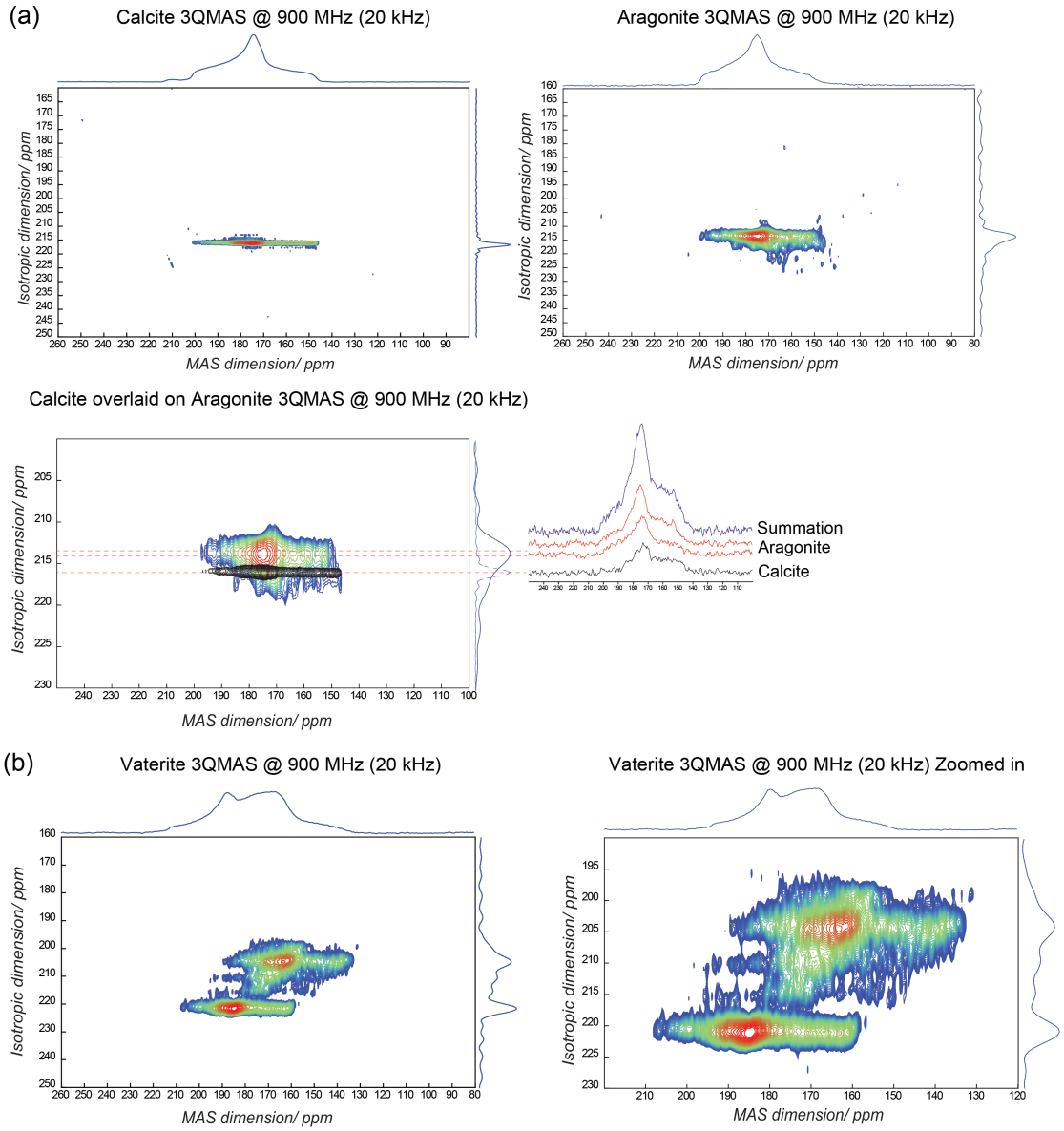

Figure 6.8, (a) ^{17}O 3Q-MAS NMR spectra acquired at 21.1 T for synthetic calcite and a mixed phase (calcite/aragonite) sample. The calcite 3QMAS is overlaid with the zoomed in version (bottom). Additionally rows corresponding to each of the inequivalent oxygen environments are displayed to the right of the 3QMAS (red –aragonite, black- calcite). The extracted slices are summed to produce the blue spectrum that is a good approximation to the spin-echo spectra shown earlier. (b) ^{17}O 3Q-MAS NMR spectra acquired at 21.1 T for a synthetic vaterite sample at two levels of detail.

The indirect F_1 dimension is described as the isotopic dimension as projections of the signal along the F_1 axis are free from the anisotropic quadrupolar broadening. The narrow ridge shaped lineshapes that are orientated parallel to the F_2 (direct) axis in the calcite is consistent with a well-resolved crystalline ^{17}O environment with little chemical

shift dispersion. The projection of the calcite peak onto the F_1 axis shows a narrow peak consistent with a single oxygen species as predicted from the crystal structure.

For the mixed phase sample the broader lineshape is also orientated parallel to the F_2 axis consistent with insignificant chemical shift dispersion, but the individual inequivalent oxygen sites are not fully resolved. The position of the peak along F1 is shifted from its isotropic position due to a modulation effect of the quadrupolar interaction allowing different sites to be resolved according to the size of their C_Q. If the isotropic chemical shifts and C_Q parameters are very similar then the peaks overlap as in the case for the mixed phase sample. Here the broadness is due to the contribution of the single calcite ^{17}O peak and the two ^{17}O aragonite peaks. However, the triple quantum spectrum allows one to separate quadrupolar parameters C_Q and η by fitting extracted second-order lineshapes from the cross-sections of the ridge lineshapes parallel to the F_2 axis. This is a useful form of data validation against the direct measurements reported in **Table 6-3**. The cross sections parallel to the F_2 axis of the 3Q MAS mixed phase spectra are shown in **Figure 6.8**a. NMR interaction parameters obtained by fitting the relevant rows of the 3Q-MAS spectra for calcite and the mixed phase same are summarized in **Table 6-4**.

Table 6-4 ^{17}O NMR parameters obtained by fitting row extractions from the 3Q-MAS experiment acquired at 21.1 T for synthetic calcite and mixed phase (calcite/aragonite) sample.

^{17}O NMR – 3QMAS Experiment

System	Site	$\delta_{iso(MAS)}$ ppm/±1.75	C_Q MHz/±0.15	η ±0.03
Calcite	1	201.1	6.9	0.97
Aragonite	1	199.3	6.63	0.95
	2	198.8	6.75	0.9

For vaterite the peak complexity in the 2D 3Q-MAS spectra increases in a manner akin to the increase observed between the pure calcite and mixed phase spectra (see **Figure 6.8**b); the number of ridged lineshapes parallel to the F_2 axis is seen to increase, but this does not correlate with a large increase in positional disorder. It follows that the 'disorder' in vaterite is based on a number of ordered oxygen environments with well-defined bond lengths and bond angles as opposed to a disorder based around structural distortions of similar environments. The resolution afforded by the 3QMAS technique allows us to identify a minimum of six inequivalent oxygen species by the

closely spaced ridges of the lineshape in the synthetic vaterite sample despite the considerable overlap of the intensity of the inequivalent sites.

The spectrum-inversion approach[62] is a post-processing technique used to extract information from MQ-MAS NMR spectra in disordered materials to reconstruct the underlying two-dimensional distribution of isotropic chemical shift (δ_{iso}) with respect to the quadrupolar interaction (ν_Q), which can in turn be correlated with local structural information.[63] The procedure is approached as an inverse problem so that the underlying distribution is reconstructed from the measured data. In the present work the singular value decomposition (SVD) approach is used as outlined by Zwanziger (1994). [62]

This approach is employed here for two reasons; 1) It is clear that the 'disorder' present in vaterite is not that typical of a disordered solid with an approximately continuous distribution of environments. Vaterite looks to be a roughly crystalline solid with a relatively small set of bond angles and lengths. This will be emphasized by the spectrum-inversion approach where the little chemical shift dispersion results in isolated sections of intensity defined by the unique δ_{iso} and C_Q values for each inequivalent site. 2) This process relies on generating model data to complete the inversion procedure so that the efficiency of the coherence transfers involved in the MQ-MAS experiment as dictated by the sample rotation, RF field strength (finite pulse widths) and pulse offsets are accounted for in the fitting process.[235,236] Then the corresponding extracted cross sections parallel to the F_2 axis used to model the data were corrected for pulse sequence distortions leading to higher quality NMR parameters (see **Figure 6.9**).

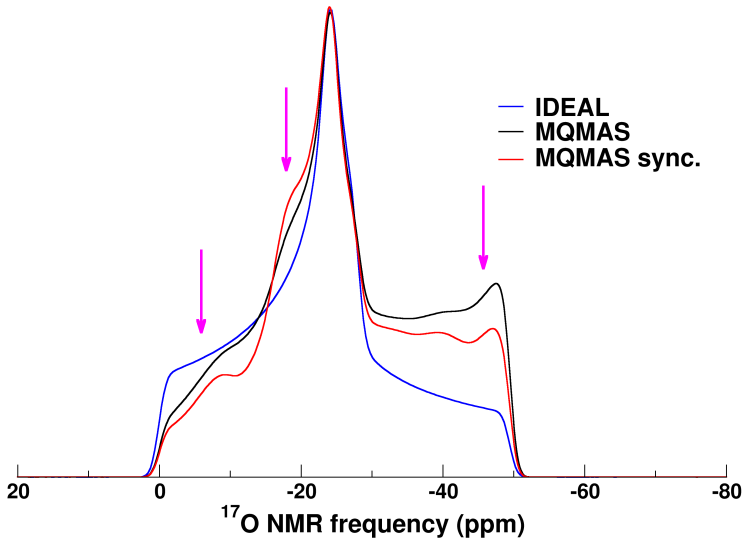

Figure 6.9, example of a simulated distortion to a η=0.9 lineshape extracted from a 3Q-MAS spectra

As suspected the inversion (see **Figure 6.10**) emphasizes the site breakdown of the larger subset of oxygen environments that was identified earlier from the ridge-like peaks of intensity parallel to the F_2 axis in the MQ-MAS. The corresponding NMR-parameters for each inequivalent oxygen site are presented in **Table 6-5**. The slice extraction of rows parallel to F_2 shows that the individual sites are all high η (~0.9-1.0).

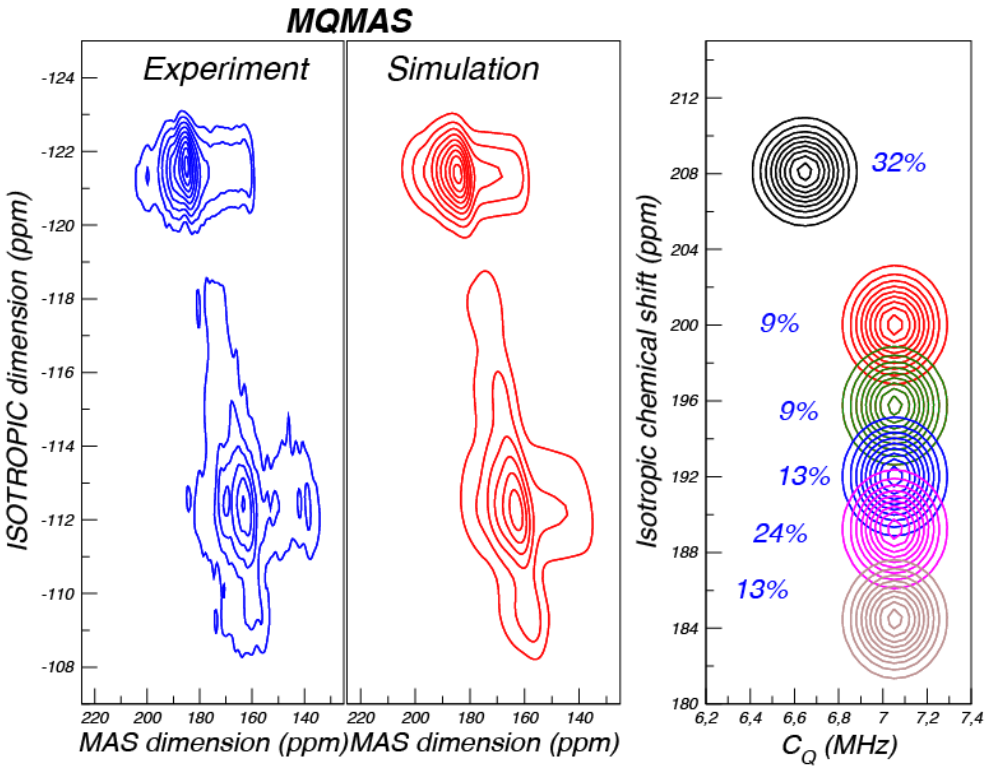

Figure 6.10, ^{17}O 3Q-MAS Inversion for the synthetic vaterite sample

The extracted NMR parameters for vaterite show that the quadrupolar parameters vary within the range observed for aragonite and calcite. It appears that these parameters are relatively insensitive to the changes in the oxygen environments for the synthetic vaterite sample; based on the C_Q the oxygen species can only be split into two major subsets centered around 6.60 MHz and 7.07 MHz . In contrast the isotropic shift varies over a relatively large range $\Delta\delta_{iso}$ ~ 208-184 ppm implying that this parameter is a better gauge of short-range differences in the ^{17}O nuclear environments.

Table 6-5 ^{17}O NMR parameters obtained by fitting row extractions from the 3Q-MAS experiment acquired at 21.1 T for synthetic vaterite

Site	$\delta_{iso}(^{17}O)$/ppm	C_Q/MHz	η	Population
1	208	6.600	0.92	32%
2	200	7.013	0.92	9%
3	196	7.049	0.92	9%
4	192	7.111	0.92	13%
5	189	7.131	0.92	24%
6	184	7.100	0.92	13%

A comparison of the isotropic chemical shifts with those roughly predicted for the vaterite deconvolution motifs based on GIPAW-DFT calculations in CASTEP means that we can begin to assign the resonances in the synthetic vaterite sample under investigation as shown schematically in Figure 6.11.

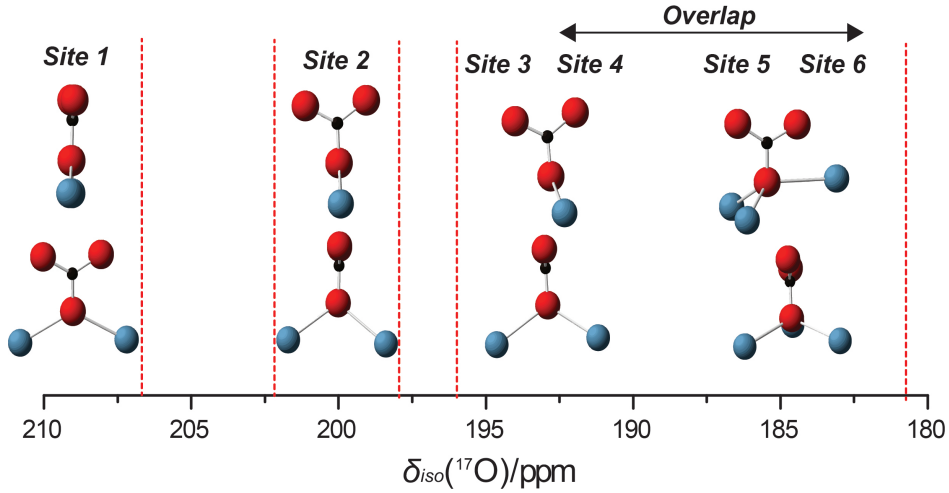

Figure 6.11, major structural units proposed for the deconvolution of the experimental ^{17}O NMR data for vaterite. An example of a resonance position for each of the structural subsets is shown below the 20kHz MAS spin-echo experiments acquired at 21.1 T

Downfield shifts were diagnostic of oxygen-environments that the author has labelled as 'calcite in-plane'. The orientation of this structural assemblage allows for relatively short Ca-O bonds, which can account for the deshielding of the oxygen nucleus and the movement of the resonance downfield.

It is also interesting to note that the population of this site by MQ-MAS inversion is 32%. This offers compelling evidence that the ^{17}O lineshape is split in a 1:2 ratio of the narrow feature to the broader downfield component, which reflects the

carbonate chemistry. Unfortunately this feature is common to all carbonates units in the proposed structures so cannot be used as a criterion to sift the proposed models.

The second peak undergoes a step in both the isotropic chemical shift and the C_Q in comparison to site 1. Such a step is likely to be indicative of a movement between oxygen bonding motifs and from **Figure 6.7** we can see that this corresponds to the most symmetric form of what the author has labelled as the calcite out-plane bonding arrangement. It is perhaps worth noting that the parameters for this fit only vary in the η parameter in comparison with calcite, however the bonding environments from a configurational point of view is quite different highlighting the complexity of interpreting these species.

The minor changes to quadrupolar coupling parameters in moving further down the sites corroborate our suggesting that the bonding motif undergoes no further major changes, but involves alterations in bond angles and orientation of the Ca-O-Ca bonds relative to the carbonate. The change in isotropic chemical shift between sites 2 and 3 correlates with the onset of a change of the 'calcite out-plane' environment to the 'calcite out-plane distorted' environment where the planar C-O-Ca_2 arrangement is broken such that the Ca-O-Ca bonding formation begins to be lifted out of the plane.

Site 4 and site 5 correlate with an oxygen nuclear environment that has a more extreme distortion to that observed for site 3. However the distinction between site 4 and 5 is that in site 5 the distortion is such that the oxygen can begin to accommodate another calcium in its coordination sphere. The subset of structures described by sites 2-6 has populations of ~10% except for site 5, which looks to be roughly double this. This is suggestive that this is actually indicative of two overlapping structural motifs. The fact this region is where we predict the 'calcite out-plane distorted' site to begin to accommodate another Ca^{2+} to form the 'aragonite-like' 4-coordinate speciation suggests that both of these types of nuclear environment appear under this resonance. Given the estimated population reflects that of the other sites involving a single structural motif and that the most upfield shifts are indicative of 4-coorindated oxygen nuclear environments we can assign site 6 to purely 'aragonite-like' environments.

It should be emphasized that isolating the exact structural alterations to the change in isotropic chemical shifts becomes increasingly difficult for the distorted sites of site 4, 5 and 6 because they do not correlate with the change of any one single characteristic but are caused by the aggregation of minor structural alterations. These minor structural alterations can accumulate in different permutations to create the same

isotropic chemical shift parameters so in fact represent crystallographically unique oxygen environments, however the resolution of the ssNMR experimental data does not allow one to account for this. Then the deconvolution of the spectra into six (or possibly seven) subsets as proposed in the 3QMAS spectral assignment (see **Figure 6.10**) do not necessarily represent isolated crystallographic environments, but groups of oxygen nuclear environments who's unique configurations combine to produce similar NMR parameters.

As such the 3QMAS offers insufficient resolution to count the exact number of isolated crystallographic species, however does offer important clarification on a number of issues. Firstly any model of vaterite must incorporate 4-coordinated oxygen species. These are absent from the 'transition' state structures C2c, $P6_522$ and $C\bar{1}$ so these structures can only be incorporated as part of more complex multi-structure vaterite model. Additionally the population of the sites in the broad component looks to be approximately equally distributed (~10%) assuming site 5 is actually two components. Some of the most outstanding candidates based on energetically considerations such as the C2 symmetry based model cannot account for this distribution of oxygen isotropic chemical shifts observed experimentally. These observations substantiate the domain-based model that postulates that vaterite is actually composed of two or more unique crystallographic forms.

6.8 Double Orientation Rotation ^{17}O NMR

Double Orientation Rotation (DOR)[218] is an alternate technique to the MQ-MAS experiment for removing the influence of the anisotropic quadrupolar interaction from NMR spectra. It extends the concept of magic angle spinning by using a double rotor that is able to spin at both the magic angle and an angle of 30.56° thereby the second and fourth-rank anisotropic broadening can be simultaneously removed to produce an isotropic spectrum. The ^{17}O DOR spectra for calcite across multiple fields of 20.0 T, 14.1 T, 11.75 T and 9.4 T are shown in **Figure 6.12**a.

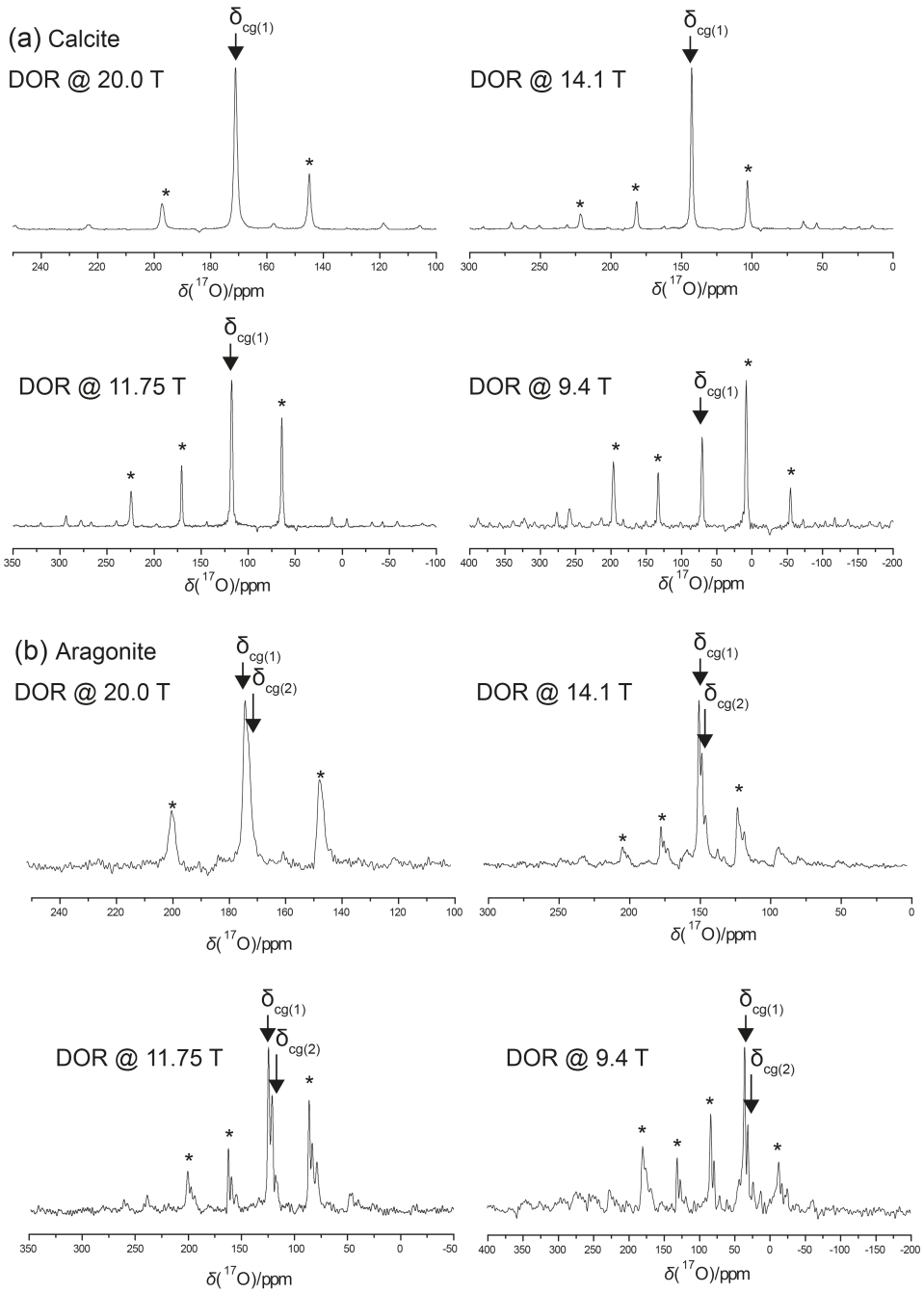

Figure 6.12, a) ^{17}O DOR spectra of synthetic calcite and b) synthetic mixed phase (calcite/aragonite) taken across fields of 20.0T, 14.T, 11.75T and 9.4T.

The calcite sample exemplifies the resolution enhancement that is achievable by successfully utilizing the DOR technique. In these 'isotropic' spectra the calcite ^{17}O lineshape is reduced to a single centre of gravity (FWHM ~ 123.5 Hz, 1.53 ppm) and a spinning sideband manifold. The narrow resonance demonstrates the lack of chemical shift dispersion thereby confirming the high crystallinity of the calcite sample. A corresponding set of ^{17}O DOR spectra for the mixed phase calcite and aragonite sample

are shown in **Figure 6.12**b. Here the resolution enhancement bestowed by the DOR technique allows for the two inequivalent oxygen positions of aragonite and the calcite resonance to be differentiated.

The isotropic chemical shifts were extracted by exploiting the field dependence of the centre of gravity according to the relation shown in eq.(6.1[70], which shows that the isotropic chemical shift is essentially the centre of gravity at an infinity external magnetic field.

$$\delta_{cg}(ppm) = \delta_{iso}(ppm) - \frac{3}{500}\frac{{P_Q}^2}{{\nu_o}^2}\times 10^6 \qquad (6.1)$$

This analytic expression was used to fit the corresponding data as shown in **Figure 6.13**.

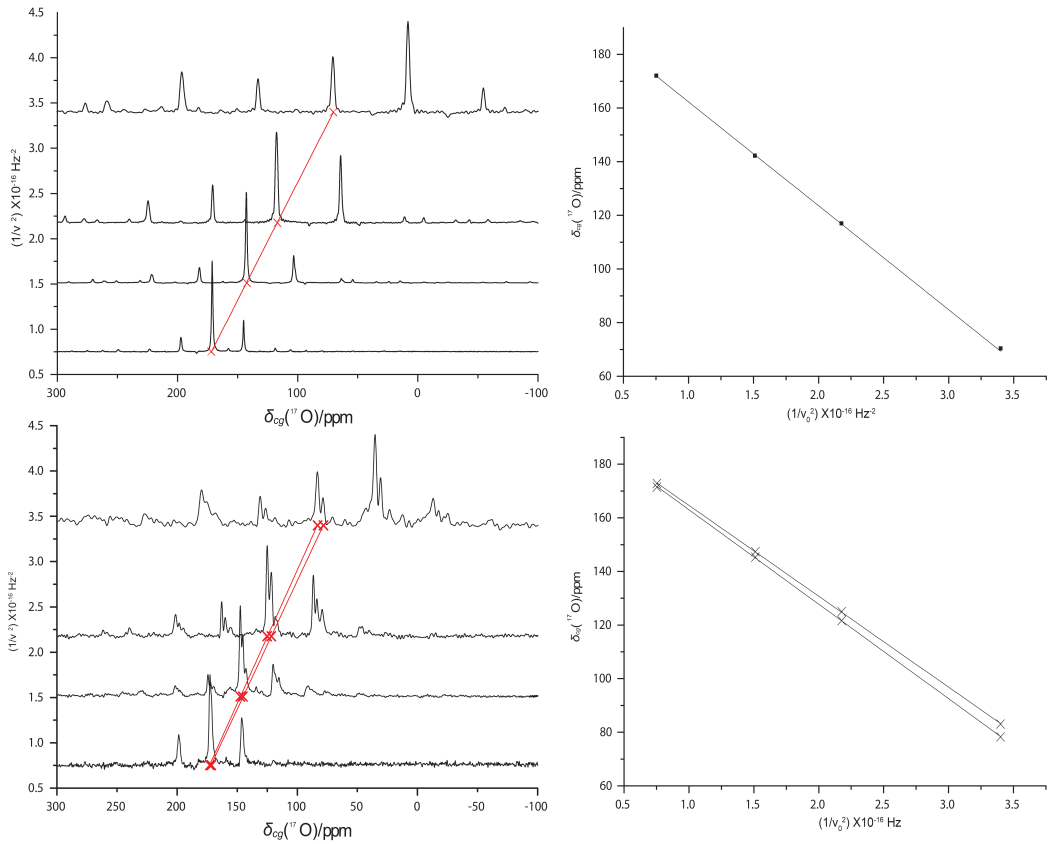

Figure 6.13, following the centre of gravity for each inequivalent oxygen environment across the 4 acquisition fields for calcite (top left) and aragonite (bottom left) and the accompanying quadrupole coupling parameter and isotropic shift plots for synthetic calcite (top right) and aragonite (bottom right)

The corresponding NMR parameters extracted from the DOR data for both the pure calcite and mixed phase sample are summarized in **Table 6-6**.

Table 6-6 ^{17}O NMR parameters obtained from the 20 kHz MAS spin-echo acquired at 21.1 T against those extracted from the DOR experiments for synthetic calcite and the mixed phase (calcite/aragonite) sample.

		^{17}O MAS NMR			^{17}O DOR NMR		^{17}O DOR Simulation		
System	Site	$\delta_{iso(MAS)}$ ppm/±	C_Q MHz/±	η ±	$\delta_{iso(PQ)}$ ppm/±0.7 5	P_Q MHz/ ±	δ_{iso}	C_Q	η
Calcite	1	201.05	6.85	0.95	200.55	8.04	201.250	7.00	0.98
Aragonite	1	199.20	6.50	0.96	198.54	7.52	198.600	6.60	0.96
	2	198.60	6.80	0.92	198.26	7.66	198.220	6.77	0.92

For the synthetic vaterite the DOR data reveals the complexity of this sample (see **Figure 6.14**). Given that the MQMAS suggests that the oxygen occupies well-defined crystallographic positions with little chemical shift dispersion the majority of this lineshape is the product of overlapping inequivalent oxygen environments. Initially the lineshape was fitted according to six Gaussian peaks consistent with the observations of the 3Q-MAS data.

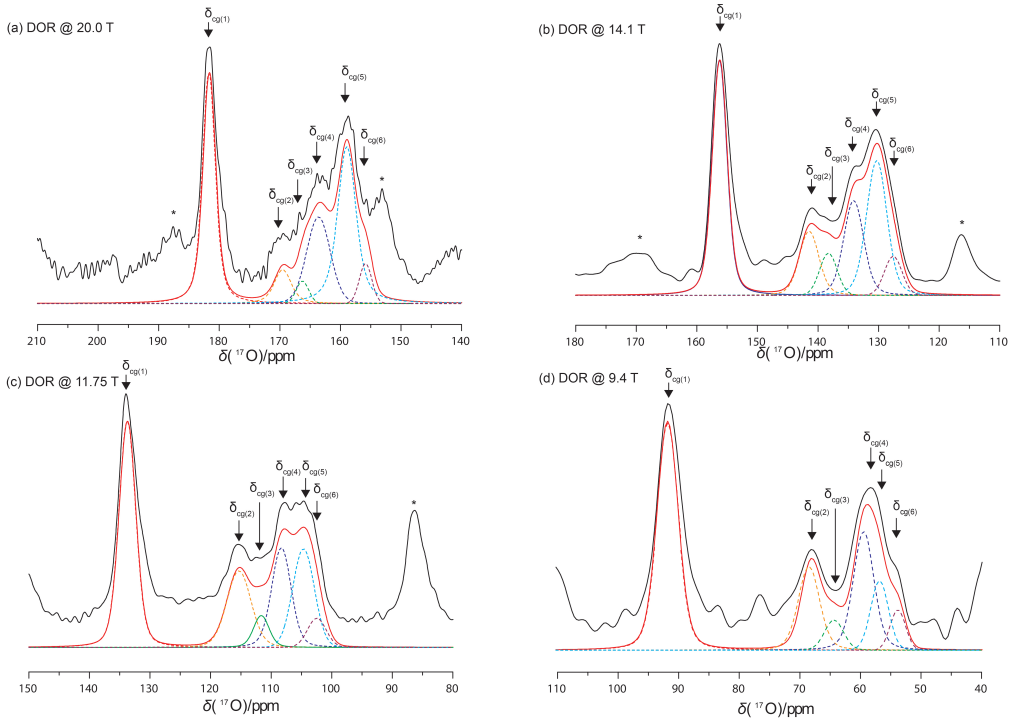

Figure 6.14, ^{17}O DOR spectra of synthetic vaterite sample taken across fields of 20.0T, 14.T, 11.75T and 9.4T.

At each field six peaks are sufficient to closely fit the major features of the spectral intensity, which corroborates the 3Q-MAS experimental findings. The individual integrated intensities of the peaks are not quantitative under DOR as the comparatively low spinning speeds mean that the signal is distributed amongst a spinning sideband manifold. The shape of the spinning sideband manifold is dictated by the field-dependent interplay between the CSA and the quadrupolar interactions, therefore the ratio of the centre of gravity peaks is seen to vary with field. The centre of gravity peak selections across the multiple fields used to extract the corresponding isotropic chemical shift and the P_Q is shown in **Figure 6.15**.

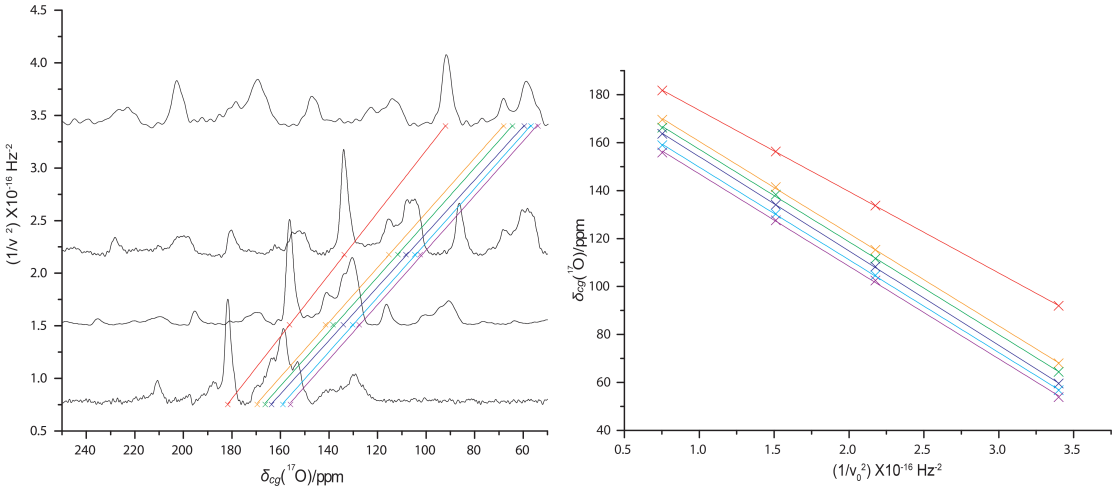

Figure 6.15, following the centre of gravity for each inequivalent oxygen environment across the 4 acquisition fields and the accompanying quadrupole coupling parameter and isotropic shift plots for synthetic vaterite

These isotropic chemical shifts and quadrupolar parameters extracted from this procedure are shown in **Table 6-7**. The NMR parameters isolated from the DOR experiments were used as an experimental constraint in order to simulate the MAS spin-echo experiments undertaken across the multiple fields in order to assess the populations of the oxygen speciation in the synthetic vaterite sample. Due to the field dependence of the individual lineshapes only a faithful representation of the relative intensities allows for the reproduction of the experimental MAS spin-echo lineshape across the multiple externally applied magnetic fields. The results of this exercise are shown schematically in **Figure 6.16** and the relative populations of each site are reported in **Table 6-7**.

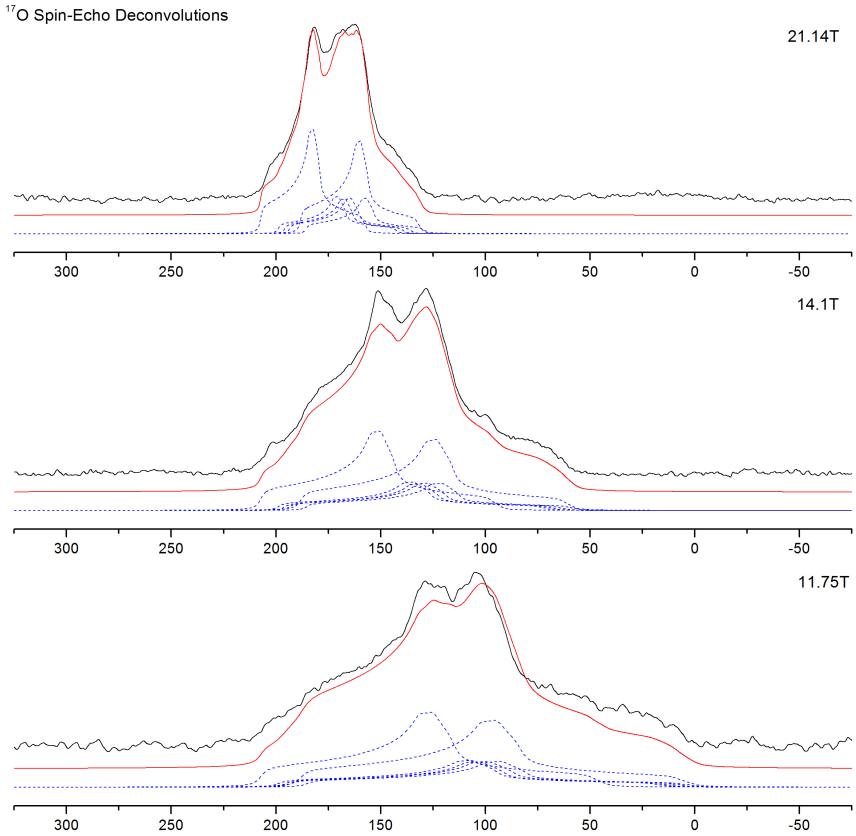

Figure 6.16, deconvolution of the spin-echo vaterite lineshape across 3 acquisition fields (21.14T, 14.1T and 11.75T) using the quadrupole coupling parameter and isotropic shift obtained from the DOR experiments on synthetic vaterite

Table 6-7 ^{17}O NMR parameters used for deconvolution of the ^{17}O 20 kHz MAS spin-echo experiment across multiple fields for synthetic vaterite and corresponding site populations in comparison with those extracted by the 3QMAS inversion fitting process.

	^{17}O DOR (Experimental)			Populations	
Site	δ_{iso} (P_Q) ppm/±2.2	P_Q MHz/±0.25	C_Q (Assuming η = 0.92)	MAS	MQMAS
1	207.4	7.52	6.64	31	32
2	199.0	8.01	7.07	11	9
3	195.8	8.02	7.08	10	9
4	193.5	8.10	7.15	10	13
5	188.4	8.03	7.09	27	24
6	185.5	8.02	7.08	10	13

The multi-field MAS spin-echo deconvolution outlined in **Figure 6.16** shows that the DOR NMR parameters can accurately reproduce independently acquired experimental data affording further confidence in the extracted NMR parameters. The MAS spin-echo experimental measurements are fully quantitative. The fact that the deconvolution follows the lineshape across the external magnetic field offers another level of verification of the individual site populations. The population of the individual sites according to both the MAS and MQMAS-inversion methods are compared in table 8 and there is good agreement between the two datasets. Note that in this case the MQMAS can be considered a good approximation to being quantitative as the C_Q's are very similar.

As can be seen in **Figure 6.16** six independent sites are sufficient to account for the majority of the experimental intensity. This fitting corresponds to employing the principle of Occam's razor - that is the minimum number of assumptions has been employed so that only the well-defined spectral-detail has been simulated. However further examination of the spectra show that the high level of resolution provided by the DOR technique reveals further fine detail. At 20.0 T the spectral intensity is split between two main resonances, but that distinction is lost in the lower fields (14.1 T, 11.75 and 9.4 T) where there is low-level signal intensity between these two major spectral features. The detail of this low-level signal intensity is ill resolved until 9.4 T where the quadrupolar interaction has an increasingly strong effect so that larger quadrupolar coupling constants lead to a correspondingly larger movement of the centre of gravities. Thus differences in individual quadrupolar parameters for each inequivalent site are exaggerated and fine detail becomes more visible.

While the DOR data is not quantitative the fact that these peaks are consistently low intensity across the fields in which they are visible and that they have similarly low-level contributions in the spinning side-band manifold suggest that these environments represent inequivalent oxygen environments that are infrequent crystalline motifs in comparison to the six main features. Such behaviour would be consistent with a domain-based model as observed by Kabalah-Amitai et al (2013)[208] where there is an unequal representation of one or more crystallographically unique form of vaterite, though this observation alone cannot directly confirm this.

The breadth of these low level peaks reveals the crystallinity of the oxygen environments they represent and their low-levels suggested they could be considered a representation of a roughly isolated crystalline oxygen environment. If this level of

crystallinity and therefore individual peak breadth can be applied across the entire spectral intensity then the line shape breaks down into many inequivalent oxygen environments that could easily exceed twenty. Apart from the comparatively large C1-symmetry based models for vaterite structures proposed by Mugnaioli et al[207] (revised by Demichelis et al[22]) this would require the presence of more than one unique crystallographic structure thereby offering further support to the domain based model.

6.9 ^{13}C CSA Experiments

Routine ^{13}C single pulse MAS NMR spectroscopy was undertaken on all the synthetic inorganic calcium carbonate polymorphs. The range of ^{13}C chemical shifts for different inorganic carbonates is relatively small (~3.6 ppm)[233] as it is largely governed by small differences in the C-O bonding.

As ^{13}C has a nuclear spin I=1/2 it does not suffer quadrupolar effects, therefore obstacles to meaningful acquisition are governed by the low natural abundance of the NMR active ^{13}C nucleus (~1.1%) and the long T_1 relaxation times (see **Figure 6.17**)

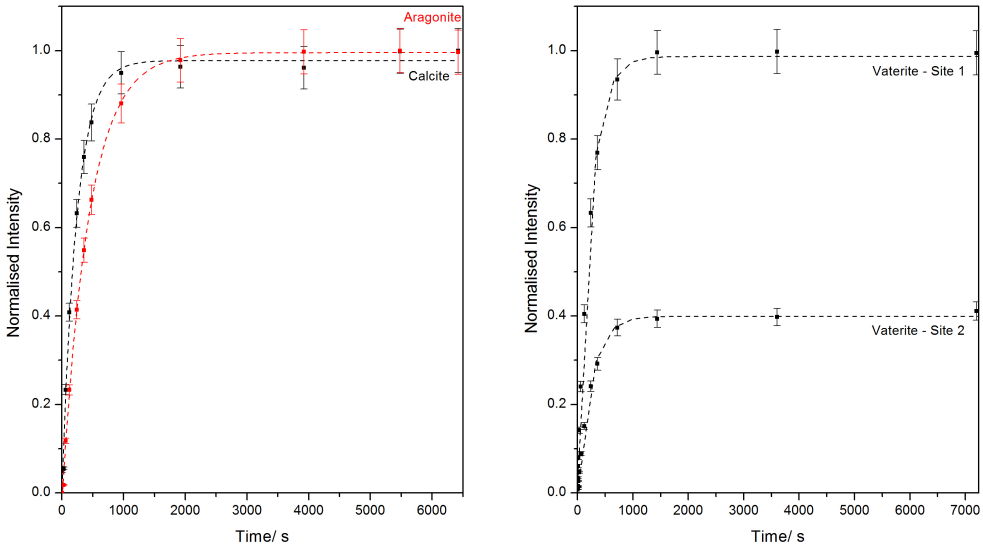

Figure 6.17, ^{13}C inversion recovery measurements on synthetic calcite and aragonite (left) and the two ^{13}C sites in synthetic vaterite (right)

The issues are both compensated for by the use of 100%-^{13}C isotopic enrichment in the samples. In **Figure 6.18** is the MAS single-pulse spectrum of calcite. Calcite has a single carbon site in the asymmetric unit cell, therefore it is surprising to note that the synthetic calcite spectrum actually shows three peaks, the largest is observed at 168.14 ppm with another positioned ~90 Hz downfield and the final peak ~60 Hz upfield from this centre peak.

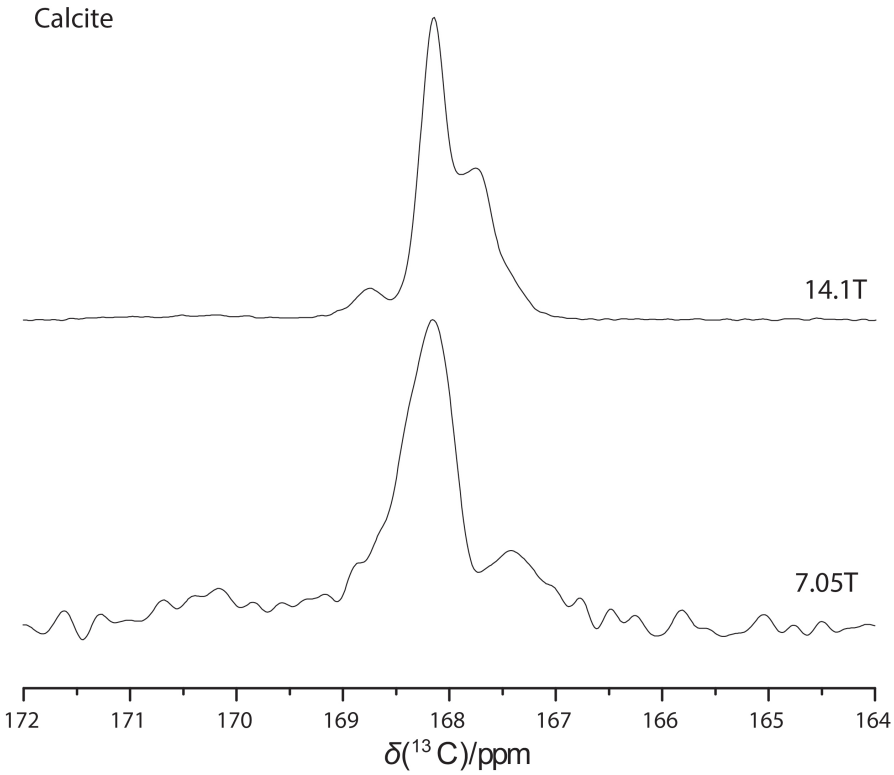

Figure 6.18, ^{13}C 15kHz MAS measurements acquired at 14.1T and 7.05T on synthetic calcite. Note the field dependence of the lineshape.

This extra definition is absent from previous reports of ^{13}C MAS NMR data for calcite where only a single peak is reported. [233,199] Only one of the studies has a full width at half maximum comparable with our lineshape (~0.5 ppm). In this study the single peak of calcite is asymmetric such that its tails upfield, a feature that could be mimicked in the spectrum reported in this study if line broadening were used in the spectral processing. As the powder PXRD shows no impurity this explanation can be eliminated. There are then two possible mechanisms by which such a splitting of the lineshape may occur: it is either a quadrupolar-modulated *J*-coupling between the ^{17}O and the ^{13}C or is it is a manifestation of an isotopomer effect due to the incomplete oxygen-17 enrichment of the carbonate units as observed in the ^{1}H NMR of naturally occurring TMS where the proton isotropic chemical shift is dependent on the isotopes of carbon and silicon in the molecule.

Due to the field dependence of the former interaction acquiring an identical spectra at another field provides a simple test for this hypothesis. A ^{13}C spectrum acquired at 7.05 T is arrayed with the spectra acquired at 14.1 T in **Figure 6.18**. The deviation of the lower field lineshape from that acquired at 14.1 T confirms a field dependence and therefore confirms the former *J*-coupling based hypothesis. *J*-couplings

of the observed ^{13}C to the ^{17}O should yield a splitting of 6 resonances. If the lineshape splitting is simply due to the different spin states of the quadrupolar nucleus then these lines should be of identical intensity and equally spaced by the magnitude of the ^{13}C-^{17}O *J*-coupling (for calcite we know this is ~ 30 Hz). However, the *J*-multiplet can undergo asymmetric broadening and shifts to the different components if there is a significant dipolar/quadrupolar cross-term. This second-order effect sees the re-introduction of the quadrupolar interaction through the dipolar interaction and accounts for the field dependence of the lineshape. To summarise, the calcite spectra does not consist of six equally spaced lines, however the resolved lines are separated by multiples of ~ 30Hz. This is consistent with a *J*-coupling between a ^{17}O quadrupolar nucleus (Q=5/2) and a ^{13}C dipolar nucleus (I=1/2) in the presence of a significant dipolar contribution in addition to the large quadrupolar interaction. In order to fully characterise the interaction a sample that is only ^{13}C enriched should be prepared in order to establish the true ^{13}C calcite lineshape and its isotropic chemical shift.

Figure 6.19 shows representative spectra of the ^{13}C MAS NMR (15 kHz) undertaken at 14.1 T. For the mixed phase sample two resonances are observed; the peak at 170.337 ppm corresponding to aragonite and the peak at 168.101 ppm to calcite. As the FWHM of these peaks is ~140 Hz the phenomena outlined above would be masked if similar peak separations are involved (previously the FWHM was ~60 Hz)

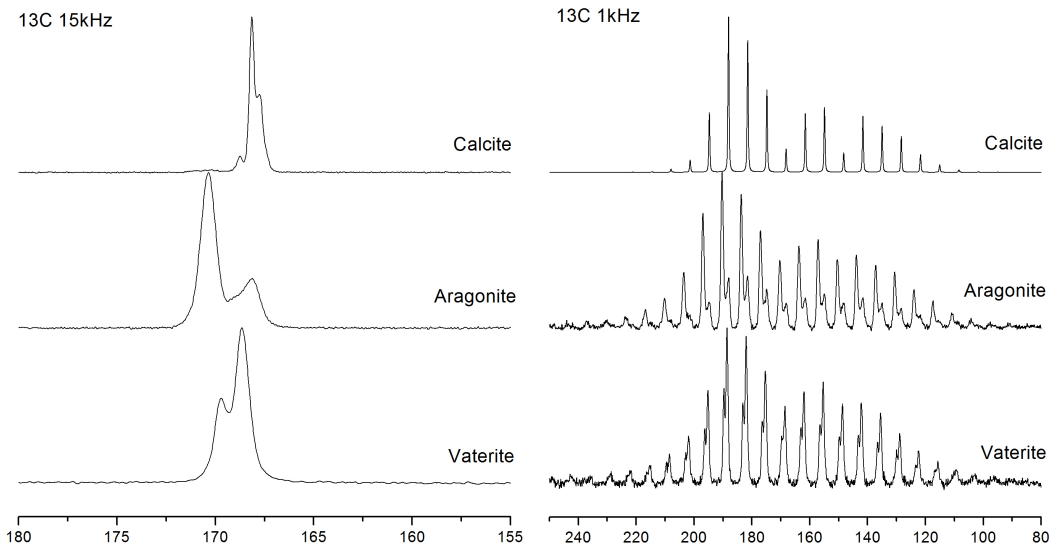

Figure 6.19, ^{13}C MAS measurements on synthetic calcite, aragonite and vaterite at 15kHz (left) and 1kHz (right)

For vaterite two ^{13}C resonances are observed (168.638 and 169.693 ppm) that are positioned between the calcite and aragonite peaks. The metastable C2/c and $P6_522$ structures both have two types of carbonates, however the requirement of vaterite to possess 4 coordinate oxygen species that are absent from these structures would discredit this assignment. Furthermore it is worth re-iterating at this point that the Raman study[194] reported that the vaterite structure must possess at least three independent carbonates. Given that the integrated intensity of the peaks are in a ratio of 2:1 it is plausible that the third site is hidden beneath the upfield peak.

Unlike the ^{17}O NMR parameters, the C-O bonds dominate the ^{13}C isotropic chemical shift parameters. In calcite the carbonate units are symmetric such that the C-O bonds and O-C-O angles are equal. In vaterite a distorted form of the calcite CO_3 group exists where none of the C-O bonds are equal and there are small distortions in the O-C-O bonds. The other general type is analogous to aragonite where there are two C-O types with site populations in a ratio of 2:1. The observation of two peaks in the NMR spectra corroborates the rationalization of the chemical composition based on two carbonate motifs.

The metastable structures possess two independent carbonates that fall into these two groupings, while the stable structures can possess multiple carbonate units that fall within either these carbonate motifs (the stable forms of vaterite have between 3-18 carbonates). Differentiating between the structures is impossible given the resolution in the ^{13}C spectrum. Then the only useful conclusions with implications for vaterite models are the peak positions and that the ratio of distorted-calcite environments to distorted-aragonite carbon environments is 2:1.

Additional low rotor frequency measurements were undertaken in order to try and estimate the chemical shift tensorial components of the ^{13}C environments. The corresponding spectra for the three synthetic calcium carbonate samples under investigation are shown in **Figure 6.19**.

The powder patterns for the carbonate environments show the ^{13}C environments are all near axial symmetry ($\sigma_{11} = \sigma_{22}$). The chemical shift anisotropy parameters for each calcium carbonate polymorph were extracted by spectral simulation in DMFit[221] and are summarized in **Table 6-8**. Calcite is axially symmetric to within experimental error that reflects the trigonal planar symmetry of the carbonate species. Thus the carbon experiences maximum shielding when the carbonate unit is orientated parallel to the

external magnetic field and maximum deshielding when the unit is perpendicular to the external magnetic field.

Table 6-8 ^{13}C NMR parameters extracted by fitting the CSA powder patterns of synthetic calcite, aragonite and vaterite using DMFit.

Type of $CaCO_3$ polymorph	δ/ppm	Δδ/ppm	η	δ_{11}/ppm	δ_{22}/ppm	δ_{33}/ppm
Calcite	168.1	-48.75	0.01	192.72	192.23	119.35
Aragonite	170.34	-52.25	0.2	201.69	191.24	118.09
Vaterite	168.64	-49.5	0.25	199.58	187.20	119.14
	169.69	-49.25	0.15	198.01	190.62	120.44

In aragonite the three-fold symmetry of its carbonates are broken and this is reflected in the deviation from axial symmetry for aragonite η = 0.2. In vaterite the distorted-calcite environment (δ_{iso}=168.64 ppm) is seen to vary most from axial symmetry where η = 0.25. Yet the modest overall changes in the CSA parameters show that the carbonates remain close to a planar configuration in all three polymorphs.

6.9.1 Possible future experiments

6.9.2 J-HMQC

The 2D ^{13}C-^{17}O *J*-HMQC (Heteronuclear Multiple-Quantum Coherence)[220] experiment presents an opportunity to use through-bond couplings to investigate ^{13}C-^{17}O connectivities. In **Figure 6.20** the correlation experiment was undertaken with a reconversion time selective to CO connectivties with *J*-couplings of ~33.33 Hz. There is some imprecision in this value as both scalar coupling and residual dipolar splitting contributions determine *J*.

The peaks in the *J*-HMQC represent one-bond ^{13}C-^{17}O couplings. It is evident that there are carbonate species with similar *J*-couplings common to both major oxygen resonances, however the resolution in the ^{13}C dimension is insufficient to identify distinct correlations between the different carbon sites. The *J*-HMQC experiment used to acquire the spectrum shown in **Figure 6.20** took 2-3 days using 92 t1-FIDs. To achieve the resolution of ~150 Hz in the ^{13}C dimension the number of increments would need to be increased to 256 t1-FIDs, which would need to be accompanied by an increase in the number of scans per increment as the signal had died away by 92 increments. This

potentially more than triples the experimental time making it impractical on the basis of magnet availability. A higher level of ^{17}O-enrichment would partially compensate for this issue (the estimated the enrichment is ~20% for the synthetic vaterite sample under investigation).

As *J*-couplings should correlate with C-O bond lengths structurally this means there are common bond lengths to carbonates associated with both the major oxygen resonances and both the ^{13}C carbonate resonances. Additional *J*-HMQC experiments were attempted where the recoupling period was increased to make the experiment sensitive to smaller *J*-couplings (~20Hz). However this form of spectral editing for longer bond lengths showed little difference (apart from signal to noise) from that acquired earlier suggesting that the carbonates cannot be differentiated via this methodology.

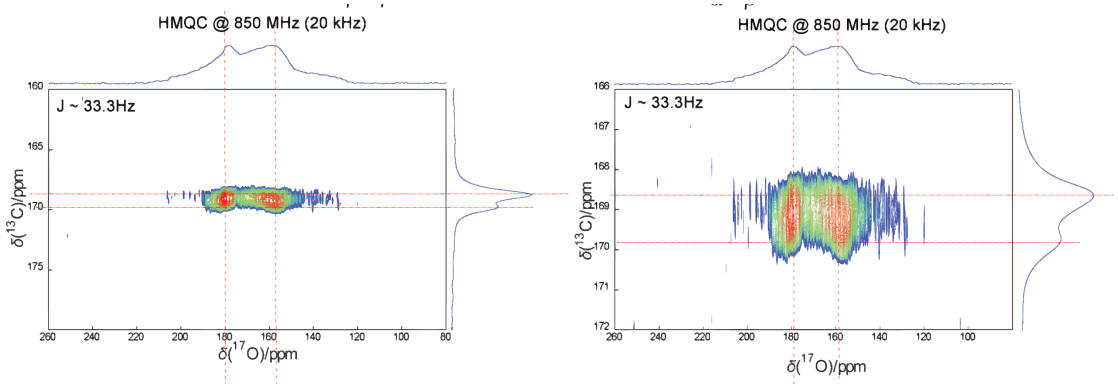

Figure 6.20, ^{17}O J-HMQC (850 MHz, 20kHz) spectrum recorded for synthetic vaterite sample

7

AB INITO DFT CALCULATIONS OF THE VATERITE SYSTEM

7.1 Computational details

Ab initio DFT calculations were performed using CASTEP 8[94] using the Perdew-Burke-Ernzerhof exchange-correlation functional intended for use with the solid state (PBEsol).[79]

In the following study the default, unmodified Vanderbilt Ultrasoft pseudopotentials were used as generated on-the-fly (OTF) in CASTEP-8 in all cases except for calculations of ^{17}O isotropic chemical shifts. As outlined by Profeta et al. (2004)[237] in a study of Ca oxides the unmodified CASTEP pseudopotentials overestimate the Ca-O covalency when used in conjunction with the PBE functional and suggest that it is possible to correct for the PBE-DFT deficiency by introducing an energy penalty for occupation of d orbitals in the calcium pseudopotential.[2] Hence an alternative based on a +3.2eV shift in the Ca 3d orbital was employed in all ^{17}O isotropic chemical shift calculations.

The modified OTF generation string and the resulting shift in the mulliken atomic population description of the Ca species in calcite with respect to the default string are shown below.

Ca 3|2.0|10|15|20|30U:40:31:32U@0.118U@0.118

Atomic Populations (Mulliken)							
Species	Ion	s	p	d	f	Total	Charge/e
$Ca_{(default)}$	1	2.12	6	0.5	0	8.62	1.38
$Ca_{(modified)}$	1	2.16	6.12	0	0	8.28	1.72

7.1.1 Convergence and Testing – Calcite and Aragonite

Tests of convergence and an appraisal of the computational methodology's ability to capture structural and NMR properties of these systems were performed on the two stable polymorphs of calcium carbonate ($CaCO_3$); calcite and aragonite. Crystal structures for calcite and aragonite at room temperature and atmospheric pressure were taken directly from the Inorganic Chemical Structure Database (ICSD), entry codes 73446, 190072 respectively. Like all natural carbonates, calcium carbonate phases have isolated CO_3^{2+} groups and no bridging oxygens. It follows that for a family of polymorphs where the sequence of next nearest neighbours is identical only changes in structure can account for changes in the NMR parameters. Thus convergence tests were undertaken for structural parameters in addition to the NMR parameters. As calcite is a rhombohedral carbonate possessing 6-coordinated Ca and 3-coordinated oxygen[222] while aragonite is orthorhombic with 9-coordinated Ca and 4-coordinated oxygen[223] the structural differences in their putative crystal structures provide and excellent way to calibrate the accuracy of the DFT approach for vaterite.

The basis set convergence was calibrated (see **Figure 7.1**a) with respect to the basis-set size and Brillouin k-point sampling to achieve a minimum basis set convergences of 0.13 mH per atom. It is pertinent to note that convergence of the electronic total-energy does not allow one to infer the convergence of the forces as the numerical errors for the total energy are of second order; whilst for the forces they're of first order. Given that the NMR parameters are sensitive to local changes in geometry additional convergence testing was explicitly undertaken against plane wave basis set and k-point sampling for the cell parameters and bond lengths (**Figure 7.1**b).

Finally to minimize the error due to finite k-point sampling and basis set truncation the NMR parameters were converged as outlined earlier. The displayed convergence trends focus on the computed ^{17}O NMR parameters; the convergence of the ^{17}O isotropic magnetic shielding and quadrupolar coupling constants for calcite and aragonite are displayed in **Figure 7.1**c and with respect to k-points for aragonite in **Table 7-1**. Yet, as convergence of a calculation scales with both the number of electrons and the 'hardness' of the respective pseudopotentials the convergence of the ^{13}C NMR parameters were independently checked in the same manner as for the ^{17}O NMR parameters. In **Table 7-1** the "number" of k-points refers to the symmetry reduced subset of the k-points grid listed in the second column.

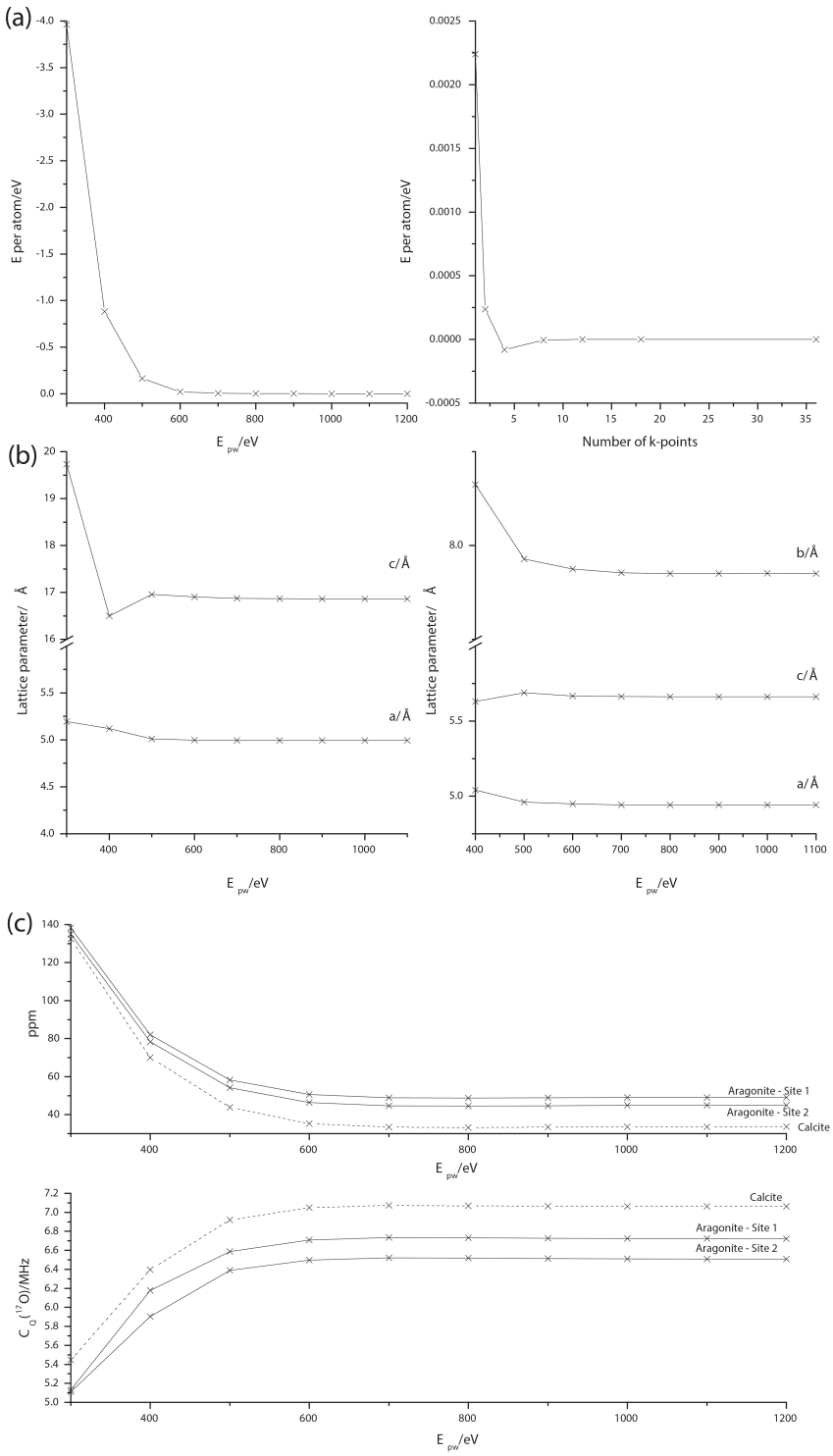

Figure 7.1, Figure 1, a) convergence of the electronic energy per atom relative to the electronic energy calculated at 1200 eV for aragonite with respect to plane wave cut-off energy (left) and the convergence of the electronic energy per atom relative to the electronic energy calculated using 36 kpoints with respect to the number of k-points (right) b) convergence of the cell parameters for calcite (left) and aragonite (right) with respect to plane wave cut-off energy c) convergence of the computed isotropic magnetic shielding (top) and quadrupolar coupling constants (bottom) for the oxygen sites in calcite and aragonite as a function of plane wave cut-off energy at k-point grids of 5x5x2 & 5x3x4 and a fine grid scale of 2.0. In each case the structure used was that obtained from a geometry optimization with the same basis set.

Table 7-1 Convergence of the isotropic magnetic shielding and quadrupolar coupling constants for the oxygen sites in aragonite as a function of the k-point grid used to sample the 1st Brillouin Zone

Number of k-points	k-point grid	σ_{iso}(O1) /ppm	C_Q (O1) /MHz	σ_{iso}(O2) /ppm	C_Q (O2) /MHz
2	2x2x1	31.54	6.525	6.74	-6.667
3	3x3x1	41.56	6.731	37.25	-6.511
6	4x4x1	40.43	6.729	36.10	-6.514
7	5x5x2	40.61	6.728	36.10	-6.514
21	6x6x2	40.61	6.728	36.10	-6.514
36	8x8x2	40.62	6.728	36.10	-6.514
120	12x12x3	40.60	6.728	36.10	-6.514

7.1.2 Accuracy assessment of PBEsol-DFT calculations on calcite and aragonite

Calcite and aragonite calculations were considered to assess the expected accuracy of this PBEsol-DFT based approach and to inform the appropriate level of constraint to be applied to the relaxation of the suite of vaterite structures. Accordingly NMR calculations were performed on the unoptimised crystallographic structures and on structures generated by symmetry constrained optimisations with and without the unit cell parameters constrained at their experimentally determined values. Finally the structures were optimised without any symmetry or cell constraints to establish whether CASTEP maintains the configuration observed in nature as any major deviation would indicate that lower symmetry structures might suffer inaccurate structural changes.

Default tolerances for convergence of the geometry relaxation were employed (maximum force 0.05eV/Angstrom on any atom, maximum stress tensor component of 0.1 GPa and a maximum change in energy of $2x10^{-5}$eV per optimization step). In order to ensure that the precision of the wavefunction was suitable for the NMR calculation the tolerance criteria of convergence of the electronic structure calculation were reduced to 10^{-7} eV per atom and the maximum force change was set to be less than 10^{-4} eV per Angstrom.

Experimental NMR for powdered solids (or solution) reports a field-independent chemical shift δ as opposed to the isotropic part of the magnetic shielding tensor.

Accordingly comparing calculated magnetic shielding and observed chemical shift requires scaling the calculated values to relate them to the chemical shift scale. In this work the shift values (σ_{ref}) for ^{17}O are determined by comparing the magnetic shield and observed experimental chemical shift for calcite. This value is then applied to aragonite in order to assess its suitability. Earlier allusion was made to a complication in the calculation of ^{17}O chemical shifts at the GGA PBE level of theory, which incorrectly hybridises the Ca 3d unoccupied states with the O 2p states. However it was unclear in the paper whether the empirical adjustment of the Ca 3d levels via the pseudopotential should be used in all calculations or only for NMR calculations. Additionally it is also notable that the author suggests the empirical fix has negligible effect on the other NMR parameters.

An identical set of structural optimizations and NMR calculations were undertaken using the modified Ca pseudopotential to investigate these issues. The changes in structural parameters with respect to the use of the default CASTEP 8 pseudopotentials in conjunction with the PBEsol functional are displayed in the appendix. The corresponding ^{17}O NMR parameters for the two-optimization strategies are shown in **Table 7-2**.

The differences between the two sets of structural parameters for geometry relaxation using the default CASTEP 8 pseudopotentials with the PBEsol functional and the employment of the modified Ca pseudopotential in conjunction with the PBE functional recorded in table 3 are slight; in fact the percentage changes show that the methods are identical except for calcite where changes on the order of ~3-4% in lattice parameters and bond lengths from their experimental values are recorded for the latter method in contrast to the ~1% change in the former.

Table 7-2 ^{17}O NMR parameters obtained upon relaxing the positions of all ions to their minimum energy configuration with the unit cell parameters constrained to their experimental values and unconstrained whilst employing the CASTEP8 default pseudopotentials in conjunction with the PBEsol functional and the modified-Ca pseudopotential in conjunction with the PBE functional. The absent calcite values are because these are zero by definition in the referencing scheme employed.

		Exp	*CASTEP*		
Functional-PBEsol Pseudopotentials– CASTEP 8 defaults			Unoptimised	PBEsol lattice fixed	PBEsol lattice vary
NMR parameter	$CaCO_3$ polymorph		CASTEP8 defaults	CASTEP8 defaults	CASTEP8 defaults
δ/ ppm	Calcite	201.05	-	-	-
	Aragonite	198.6	189.44	191.68	191.98
		199.2	194.61	196.2	196.91
C_Q/ MHz	Calcite	6.85	6.91	-7.03	-7.03
	Aragonite	6.8	6.64	6.73	6.71
		6.5	-6.37	-6.51	-6.51
η	Calcite	0.95	0.99	0.98	0.98
	Aragonite	0.92	0.88	0.92	0.92
		0.96	0.97	0.95	0.95

		Exp	*CASTEP*		
Functional-PBE Pseudopotentials – modified Ca, CASTEP 8 defaults (C, O)			Unoptimised	PBE lattice fixed	PBE lattice vary
NMR parameter	$CaCO_3$ polymorph		CASTEP8 defaults (O, C), Shifted-Ca	CASTEP8 defaults (O, C), Shifted-Ca	CASTEP8 defaults (O, C), Shifted-Ca
δ/ ppm	Calcite	201.05	-	-	-
	Aragonite	198.6	198.32	202.13	202.67
		199.2	200.25	204.7	202.93
C_Q/ MHz	Calcite	6.85	-7.207	-7.279	-7.399
	Aragonite	6.8	6.97	7.02	7.04
		6.5	-6.79	-6.92	-7.00
η	Calcite	0.95	0.99	0.98	0.96
	Aragonite	0.92	0.91	0.96	0.96
		0.96	0.96	0.94	0.91

The close agreement of the structural parameters with experiment for both optimization strategies suggests both are valid candidates to capture these physical details. Nonetheless on inspection of the NMR parameters calculated by identical setups to the aforementioned geometry optimizations the agreement between the datasets and experiment is less consistent. Whilst the results in **Table 7-2** confirm that the modified pseudopotential improves the calculated isotropic chemical shifts with respect to those calculated by the default Ca-pseudopotential, it also highlights that there is in fact an unwanted secondary effect on the C_Q that is not negligible. This parameter is consistently overestimated by the modified Ca-pseudopotential for both calcite and aragonite. Given that the configurations after structural relaxation were identical to within computational noise for aragonite this difference cannot be solely attributed to variation in geometry, but must partially be an artefact of the calculation. It would be an interesting exercise to refit the +3.2eV shift in the Ca 3d orbital for the current setup as opposed to using the setup optimised on CaO to establish how transferable this modification is across inorganic calcium systems and whether this is the origin of this difference although this is not done here.

Nonetheless in the context of this investigation these observations clarify the ambiguous aspect of the modified Ca pseudopotentials use; that the most representative calculated NMR data is achieved if the shifted pseudopotential is only used to compute the shielding parameters - given that this modification is an empirical adjustment to fix a DFT issue relevant to the shielding it would not seem unreasonable to use the PBEsol geometries and only compute the shielding using the shifted potential. Another NMR calculation with the default CASTEP 8 pseudopotentials with the PBEsol functional will be used to estimate the quadrupolar parameters. A summary of the NMR parameters for calcite and aragonite calculated in accordance with this methodology are reported in **Table 7-3**, whilst the corresponding deconvolution of the experimental ^{17}O solid-echo pulse spectra are shown in **Figure 7.2**.

Table 7-3 ^{17}O NMR parameters obtained from unoptimised experimental geometry, upon relaxing the positions of all ions to their minimum energy configuration with the unit cell parameters constrained to their experimental values and unconstrained whilst employing the CASTEP8 default pseudopotentials in conjunction with the PBEsol functional. Chemical shift parameters are calculated with the modified-Ca pseudopotential, whilst quadrupolar parameters are calculated using the CASTEP8 defaults.

		Expt	*CASTEP*		
			Unoptimised	PBEsol lattice fixed (CASTEP 8 pseudopotentials)	PBEsol lattice vary (CASTEP 8 pseudopotenitals)
NMR parameter	CaCO3 polymorph		CASTEP8 defaults (O, C), Shifted-Ca	CASTEP8 defaults (O, C), Shifted-Ca	CASTEP8 defaults (O, C), Shifted-Ca
δ/ ppm	Calcite	201.05	-	-	-
	Aragonite	198.6	198.32	200.45	200.91
		199.2	200.25	201.87	202.83
C_Q/ MHz	Calcite	6.85	6.91	-7.03	-7.03
	Aragonite	6.8	6.64	6.73	6.71
		6.5	-6.37	-6.51	-6.51
η	Calcite	0.95	0.99	0.98	0.98
	Aragonite	0.92	0.88	0.92	0.92
		0.96	0.97	0.95	0.95

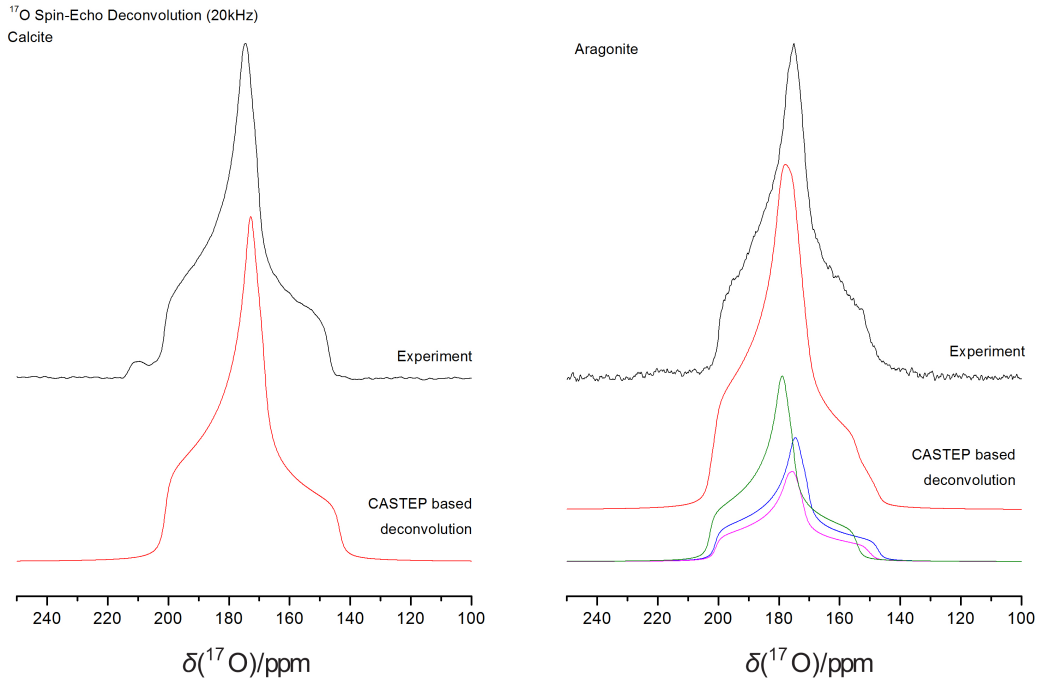

Figure 7.2, deconvolution of the ^{17}O solid-echo spectra for calcite (left) and a mixed phase calcite/aragonite sample (right) acquired at 21.14T based on chemical shift NMR parameters calculated using the modified Ca-pseudopotential and quadrupolar parameters calculated using the default CASTEP8 pseudopotentials.

7.1.3 Simulation of experimental DOR spectra

DOR is a technique capable of providing isotropic 1D spectra for quadrupolar nuclei in real time, making it a powerful tool in terms of characterizing quadrupolar nuclei. It has been outlined by Hung et al (2007)[72] that the anisotropic NMR parameters for half-integer quadrupolar nuclei can be established by spectral simulation of the DOR spinning sideband intensities using a computer program written with the GAMMA spin-simulation libraries. This spectral fitting approach is particularly viable for well-resolved quadrupolar lineshapes, but becomes increasingly intractable for multiple overlapping sites. Deconvolution in the manner can be bypassed if computed input values are accurate. Then for structures like vaterite where the experimental lineshape comprises of multiple sites, but structural models have not been able to be verified, the technique can be elevated to a predictive tool for structural elucidation.

Again calcite and aragonite were used as proof of principle of the proposed approach where NMR parameter inputs were calculated from CASTEP8 derived in the manner outlined previously. These structures are ideal case studies because under DOR the calcite and aragonite spectra become simple enough such that they can be deconvoluted without computational input, while their structures have been well characterized and thus the quality of the structural data is unlikely to contribute any significant errors to the simulations via the theoretical NMR parameters. As such the accuracy of the DOR simulation was almost exclusively dependent on the ability of CASTEP to capture the experimental NMR inputs. The numerical density-matrix simulations were performed using spinning side-band (ssb) suppression[219] across four fields (9.4 T, 11.7 T, 14.1 T, 20 T) using the experimental inputs for ν_{OR} and ν_{IR}/ν_{OR}. The simulations were completed in the time-domain and apodized with an exponential decay function corresponding 75 Hz of line broadening prior to Fourier transformation.

The conditions of DOR are engineered such that if the rotor frequencies are sufficient to partially average the quadrupolar interaction then the spin system becomes pseudo-spin-1/2. Generally due to the relatively low limits of the outer rotor spinning frequency (~ 2kHz) the intensity of the NMR interactions is forced into a (ssb) manifold analogous to a CSA ssb manifold observed for a spin-1/2 systems in the slow spinning regime. The exact shape and relative intensities for the peaks of this manifold can be influenced by quadrupolar (QI), chemical shift (CS), dipolar and j-coupling interactions. The influence of any one of these interactions on the ssb manifold is related to the

relative sizes and orientations of the respective tensors of the interactions so while the most accurate simulation would include all four interactions this is often unnecessary due to the large differences in the strengths of the interactions.

A top-down approach was employed to establish the level of appropriate detail for the simulations whereby the single largest contributing interaction is initially included and tested for adequacy against the experimental lineshape. If this is deemed an inadequate fit of the experimental spectrum then a combination of the largest and next largest interaction is included in combination and the process is repeated until the lineshape did not change significantly upon adding further interactions.

Accordingly the initial preliminary testing only included the calculated EFG parameters where the implicit assumption is that the quadrupolar interaction dwarfs the chemical shift interaction such that the latters effect on the lineshape can be ignored. This regime is preferable because it makes deconvolution of the DOR experimental ssb manifold much simpler. The simulations in the absence of CSA for calcite and aragonite are shown in **Figure 7.3** & **Figure 7.4** and it is clear from these results that this first order approximation is insufficient.

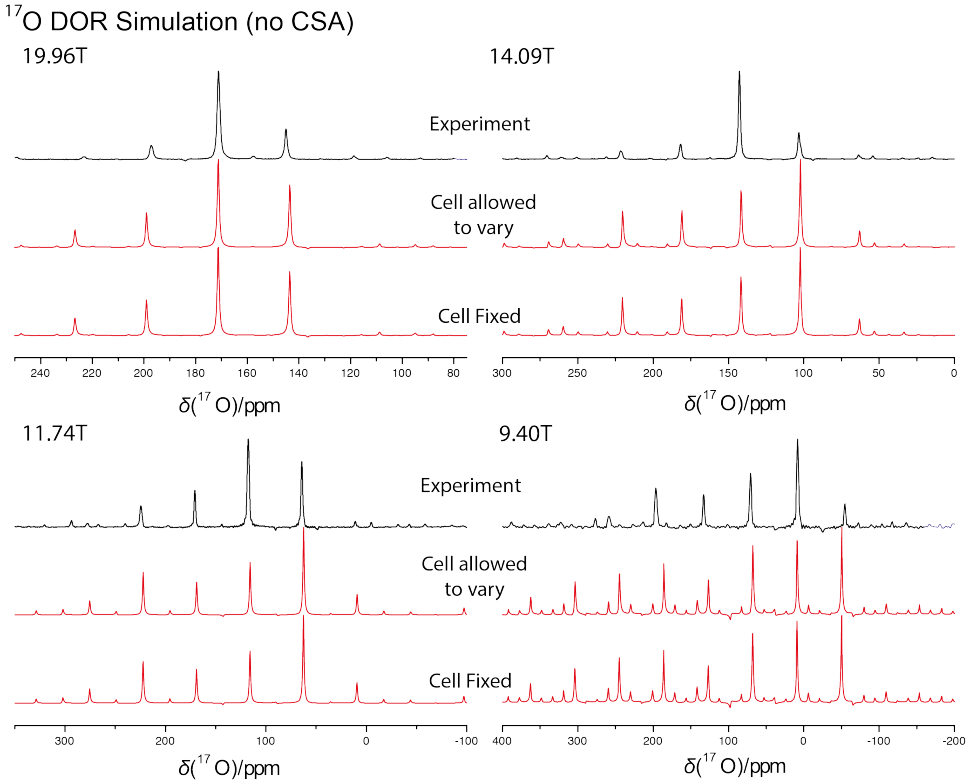

Figure 7.3, comparison of ^{17}O DOR simulations across multiple fields (19.96T(top left), 14.1T(top right), 11.75T(bottom left), 9.4T (bottom right)) for calcite against experiment (black spectra) based on the inclusion of the quadrupolar interaction only for CASTEP data derive from structures optimized with the lattice fixed at the experimental value and whilst allowing the lattice to vary (red spectra)

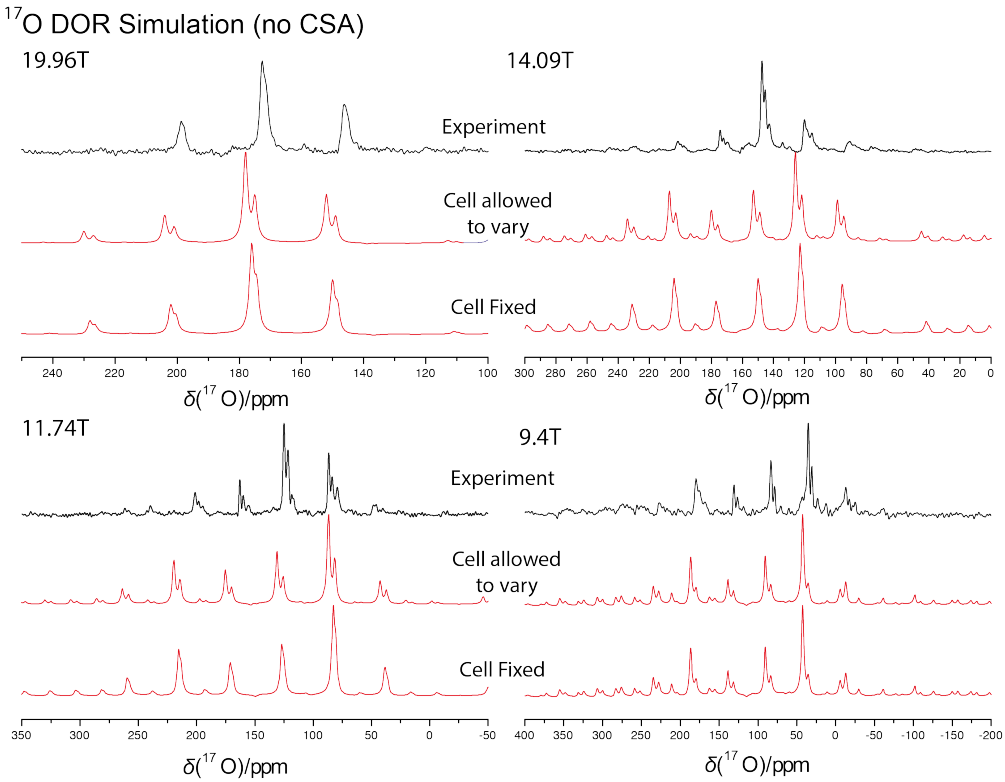

Figure 7.4, comparison of ^{17}O DOR simulations across multiple fields (19.96T(top left), 14.1T(top right), 11.75T(bottom left), 9.4T (bottom right)) for aragonite against experiment (black spectra) based on the inclusion of the quadrupolar interaction only for CASTEP data derive from structures optimized with the lattice fixed at the experimental value and whilst allowing the lattice to vary (red spectra)

The next simulation approach included a combination of QI and CS. To correctly model the interplay between these two interactions requires the inclusion of the relative orientation of the ^{17}O EFG and CS tensors. This is denoted by three Euler angles $(\alpha_{CE}, \beta_{CE}, \gamma_{CE})$ that describe the co-ordinate frame transformation that makes the EFG principal axis frame (PAF) and the CS PAF coincide. For this work the specification of the orientation between the magnetic shielding tensor and the EFG tensor was done as specified by Gervais *et al.* (2005)[238]. The simulations corresponding to the combined effect of CSA and QI for calcite and aragonite are displayed in **Figure 7.5** and **Figure 7.6**.

At this level of detail the accuracy of the lineshape fitting is in very good agreement with the experimental data and of an equivalent standard to the best fit of the parameters arrived at independently of the computed values. **Table 7-4** offers a full comparison of the ^{17}O NMR parameters for calcite and aragonite obtained by fitting the DOR ssb intensities with the quantum mechanical calculated values.

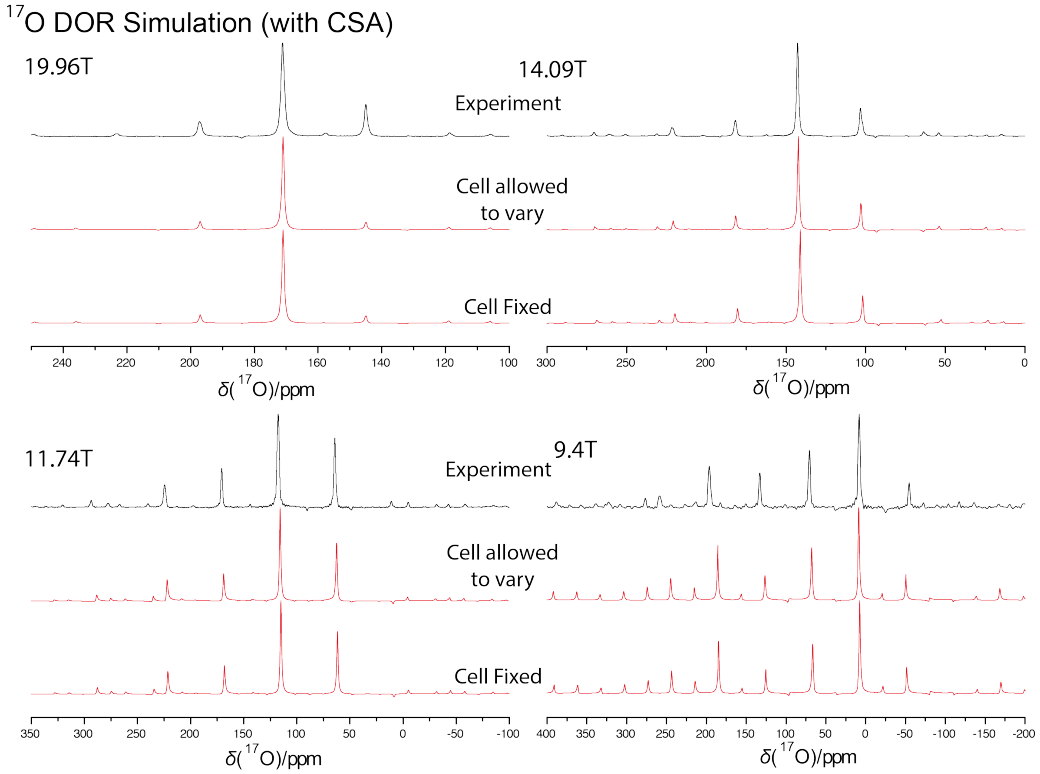

Figure 7.5, comparison of ^{17}O DOR simulations across multiple fields (19.96T(top left), 14.1T(top right), 11.75T(bottom left), 9.4T (bottom right)) for calcite against experiment (black spectra) based on the inclusion of the quadrupolar and CSA interactions for CASTEP data derive from structures optimized with the lattice fixed at the experimental value and whilst allowing the lattice to vary (red spectra)

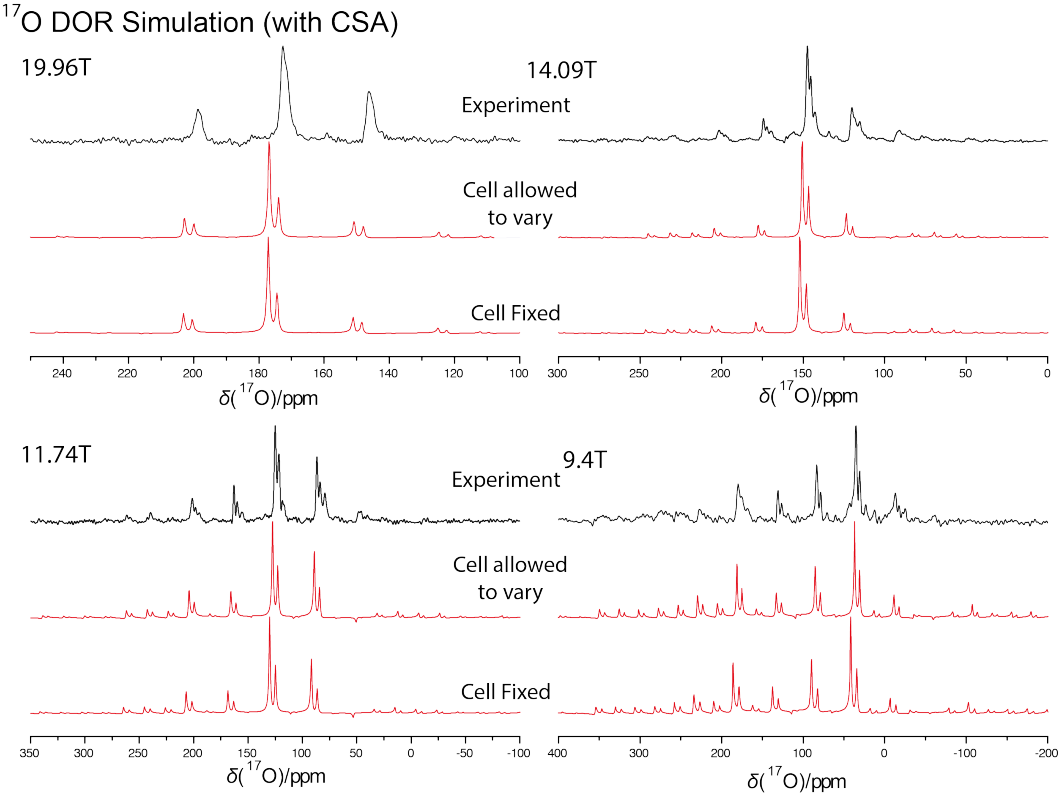

Figure 7.6, Comparison of ^{17}O DOR simulations across multiple fields (19.96T(top left), 14.1T(top right), 11.75T(bottom left), 9.4T (bottom right)) for aragonite against experiment (black spectra) based on the inclusion of the quadrupolar and CSA interactions for CASTEP data derive from structures optimized with the lattice fixed at the experimental value and whilst allowing the lattice to vary (red spectra)

Table 7-4, ^{17}O NMR parameters used for the DOR spectral simulation obtained by relaxing the positions of all ions to their minimum energy configuration with the unit cell parameters constrained to their experimental values and unconstrained whilst employing the CASTEP8 default pseudopotentials in conjunction with the PBEsol functional. Chemical shift parameters are calculated with the modified-Ca pseudopotential, whilst quadrupolar parameters are calculated using the CASTEP8 defaults.

Anisotropic ^{17}O NMR parameters for Calcite and Aragonite

	Calcite		Aragonite O1		Aragonite O2	
	Calculation		Calculation		Calculation	
	Fixed lattice	Unconstrained lattice	Fixed lattice	Unconstrained lattice	Fixed lattice	Unconstrained lattice
C_Q / MHz	7.03	7.03	6.73	6.71	6.62	6.51
η_Q	0.98	0.98	0.92	0.92	0.97	0.95
δ_{iso} / ppm	200.60	200.60	200.50	200.90	201.90	202.80
$\Delta\delta$/ ppm	163.63	164.17	211.92	215.26	184.86	188.58
η	0.84	0.83	0.73	0.72	0.83	0.81
$\alpha_{(CE)}(°)$	0.00	0.00	90.00	90.00	0.00	0.00
$\beta_{(CE)}(°)$	90.00	90.00	90.00	90.00	90.00	90.00
$\gamma_{(CE)}(°)$	90.00	90.00	270.00	270.00	270.00	270.00

7.1.4 Assessment of ^{13}C CASTEP data – Calcite and Aragonite Simulation

Although the total ^{13}C chemical shift range is ~250 ppm the ^{13}C chemical shift range of carbonates is relatively small ~6.5 ppm. This highlights the insensitivity of the ^{13}C centre of the carbonate group to variation in its external next nearest neighbour, therefore emphasizing the importance of an accurate local description of the electronic carbonate environment for GIPAW-DFT based calculations in reproducing the ^{13}C chemical shift. A systematic study Johnston et al. (2009)[239] into the feasible accuracy of GIPAW calculated ^{13}C chemical shift tensors for organic systems outlined the best computational strategies for a faithful representation of a crystallographic structures NMR fingerprint. In general one must be careful when comparing organic and mineral systems where large thermal motion typically makes organic structural data less accurate, however this particular study uses high quality neutron data from 14 organic single crystals with fully

characterised ^{13}C chemical shift tensors as the basis for its investigation and addresses the effect of dynamics on the ^{13}C chemical shift tensor within the paper.

The study compared the calculated shifts for both unoptimised neutron diffraction data for the structures and geometry-optimized versions of the structures. The analysis concludes that structural optmisation is vital (even for high quality neutron diffraction data) for NMR crystallography considerations and emphasized the importance of removing systematic flaws when converting shielding values to the chemical shift scale; showing that the ^{13}C shielding-shift correlation plots for the GIPAW PBE method diverge from an ideal gradient of -1. In fact they go on to show that the divergent trend lines are dependent on the type of bonding, which needs to be calibrated for if theory is to accurately predict the isotropic chemical shift. The authors report that after proper calibration the GIPAW method can accurately predict the ^{13}C isotropic shifts to 1 ppm.

The difference in ^{13}C chemical shift between calcite and aragonite has been reported to be ~1.5 ppm[233] and thus provides an ideal test for the GIPAW method in calcium carbonate systems. Moreover given the reported divergence of the trend line from the ideal case the scaling value (σ_{ref}) for ^{13}C, this value was calculated by comparing the magnetic shielding and observed experimental chemical shift for calcite and then the calibration value tested on aragonite.

A comparison of the experimental and calculated ^{13}C data for calcite and aragonite is shown in **Table 7-5**. Calibrating the isotropic magnetic shielding for aragonite using (σ_{ref}) as calculated from the isotropic magnetic shielding value for calcite is shown to produce good agreement with experiment. Furthermore there is excellent agreement with the individual chemical shift tensor components (~2 ppm) stressing the fact that the GIPAW method is able to faithfully capture the nuances in the NMR parameters due to fine structural changes of the $CaCO_3$ systems.

Table 7-5 ^{13}C NMR parameters obtained from unrealxed experimental structures, by relaxing the positions of all ions to their minimum energy configuration with the unit cell parameters constrained to their experimental values and unconstrained whilst employing the CASTEP8 default pseudopotentials in conjunction with the PBEsol functional. The calcite magnetic shielding was used to calibrate the aragonite chemical shifts.

			Exp	**CASTEP**		
NMR parameter				Optimisation Strategy		
	Type of $CaCO_3$ polymorph	ICSD Code		Unopt	PBEsol lattice fixed	PBEsol lattice vary
δ/ppm	Calcite	73446	168.10	-	-	-
	Aragonite	190072	170.34	170.06	170.53	170.16
Δδ/ppm	Calcite	73446	-48.75	-47.01	-46.38	-46.40
	Aragonite	190072	-52.25	-50.09	-50.52	-50.53
η	Calcite	73446	0.01	0.00	0.00	0.00
	Aragonite	190072	0.20	0.18	0.17	0.17
δ_{11}/ppm	Calcite	73446	192.72	192.81	191.30	191.30
	Aragonite	190072	201.69	199.70	200.17	199.66
δ_{22}/ppm	Calcite	73446	192.23	192.81	191.29	191.30
	Aragonite	190072	191.24	190.52	191.42	191.19
δ_{33}/ppm	Calcite	73446	119.35	122.30	121.72	121.70
	Aragonite	190072	118.09	119.97	120.01	119.63

7.2 DFT calculations in support of an NMR study on vaterite

7.2.1 Computational details

The optimisation strategy for the existing ordered structures proposed for vaterite were relaxed in accordance with the findings for calcite and aragonite; the PBEsol functional was employed with default CASTEP 8 pseudopotentials. Given that the majority of ordered configurations of vaterite were proposed by a mixture of experimental and theoretical studies using a variety of *ab-initio* quantum mechanical codes it was decided that in all cases structural relaxation should be undertaken with both the lattice fixed and unconstrained, but that the relaxation should always be completed such that the space group symmetry was always constrained. Thereby our geometry optimisations simply act as a procedure to allow the ionic positions to establish their energy minima within the confines of the proposed structures rather than potentially distorting the structures to lower symmetry. The calculations were completed with a cautious choice of planewave

basis set cut-off energy (800eV) in combination with a k-point grids of 3x3x1 for ordered structures with symmetries $P6_5$, $P3_221$, $P3_121$, $P112_1$, 4x4x1 for $P6_522$ and 4x4x2 for the lowest energy realisation of $P6_3/mmc$, 2x3x3 for structures C2, C2/c Ama2, 2x4x3 for Cc, 2x4x1 for $C\bar{1}$, 2x3x1 for C1_1 and C1_2, 5x4x3 for $P2_12_12_1$ and 5x4x3 for Pbnm. The choice of k-point grid for each structure was informed by the study on calcite and aragonite described earlier and is consistent with a k-point density necessary for the convergence of the relevant parameters.

NMR parameters are typically more sensitive to basis set truncation error than total energies and forces. However the over-converged basis-set defined for the geometry-optimization will compensate for this and an identical plane-wave basis set and k-point sampling of the 1st Brillouin zone are suitable for the NMR calculations.

The NMR calculations were completed twice; once with the PBE functional and modified Ca pseudopotential for the ^{17}O chemical shift parameters and once with the PBEsol functional and default CASTEP 8 pseudopotentials for the quadrupolar parameters. The default CASTEP tolerance on the convergence of the electronic structure calculation was reduced to 10^{-7}eV/atom to ensure a accurate ground state density.

In order to calculate absolute isotropic chemical shifts $\delta_{iso} = -[\sigma_{iso} - \sigma_{ref}]$, where is the isotropic shielding σ_{iso} and σ_{ref} is the isotropic chemical shifts of the same nuclei in a reference frame calcite is used in an identical fashion to that outlined earlier; the independent GIPAW-DFT calculations lead to σ_{ref} values of $\sigma_{ref}(^{17}O)$ =252.55 ppm and $\sigma_{ref}(^{13}C)$ =172.211 ppm when the calcite lattice is constrained to its experimental values and $\sigma_{ref}(^{17}O)$ =251.93 ppm and $\sigma_{ref}(^{13}C)$ =172.501 ppm when a full structural relaxation was undertaken.

7.2.2 Energetics

Major theoretical insights into the possible structural models for vaterite have come from publications by Demichelis et al.(2012, 2013)[205],[22] where the quantum-mechanical *ab initio* all-electron CRYSTAL09 program[240] was employed with the PBEsol functional in order to assess the relative stabilities of the ordered structures for vaterite. One of many insights from these publications is that the energy difference between metastable states and minimum energy structures are within the accessible thermal energy at room temperature, a finding that is central to the proposed stacking models of interest in this

study. These stacking models comprise of ordered vaterite structures that are able to interconvert such that the true vaterite structure observed would be a Boltzmann-weighted average structure of these individual components.

The relative calculated energies for these structures become vital for an accurate weighting of the individual contributions of each system to the NMR spectra. As such a comparison of the energetic ordering according to total energy calculation relative to the unstable transition *Pbnm*-structure studied by Medeiros et al[200] (as reported by Demichelis et al (2012)[205]) were undertaken in CASTEP (with plane-wave pseudopotential density functional theory at the level of the generalized gradient approximation) to check that these findings could be reproduced at this level of theory. The results are summarized in **Table 7-6**.

Table 7-6 Energy differences between structures relative to the unstable Pbnm configuration. [a]Demichelis (2012)[10]

Geometry Optimisation Strategy	Cell Fixed	Cell allowed to vary	
	ΔE (kJ/mol)	ΔE (kJ/mol)	ΔE (kJ/mol)[a]
Ama2	12.76	15.16	15.09
$P2_12_12_1$	-4.03	-1.68	-2.27
Pbnm	0.00	0.00	0
$P3_221$	-6.29	-3.89	-3.5
$P3_121$	-6.28	-3.88	-3.5
$P112_1$	-5.79	-3.39	-3.01
$P6_522$	-3.63	-3.36	-2.04
$P6_5$	-5.51	-3.10	-2.58

For all the possible ordered structures of vaterite the trend in relative energies is reproduced by both optimization strategies (see **Figure 7.6a**). The discrepancy in the results where the lattice is constrained is systematic and relates to the total energy calculation for *Pbnm*. This systematic problem is removed from the datasets if the structures are optimized such that the lattice is unconstrained in the structural relaxation and unambiguously shows that the data can be reproduced at this level of theory.

The stacking models alluded to previously comprise of three almost isoenergtic basins where the absolute minimum energy structures for each basin have $P3_221$, C2 and C1 symmetry. The three basins (hexagonal, 2-layer and 6-layer monoclinic) differ by the stacking sequence of carbonate layers. The energy landscape of the basins for the relevant ordered structures of vaterite according to my own total energy quantum-mechanical calculations on configurations that have been relaxed with both the lattice constrained and unconstrained (0K) are shown in **Figure 7.6b**.

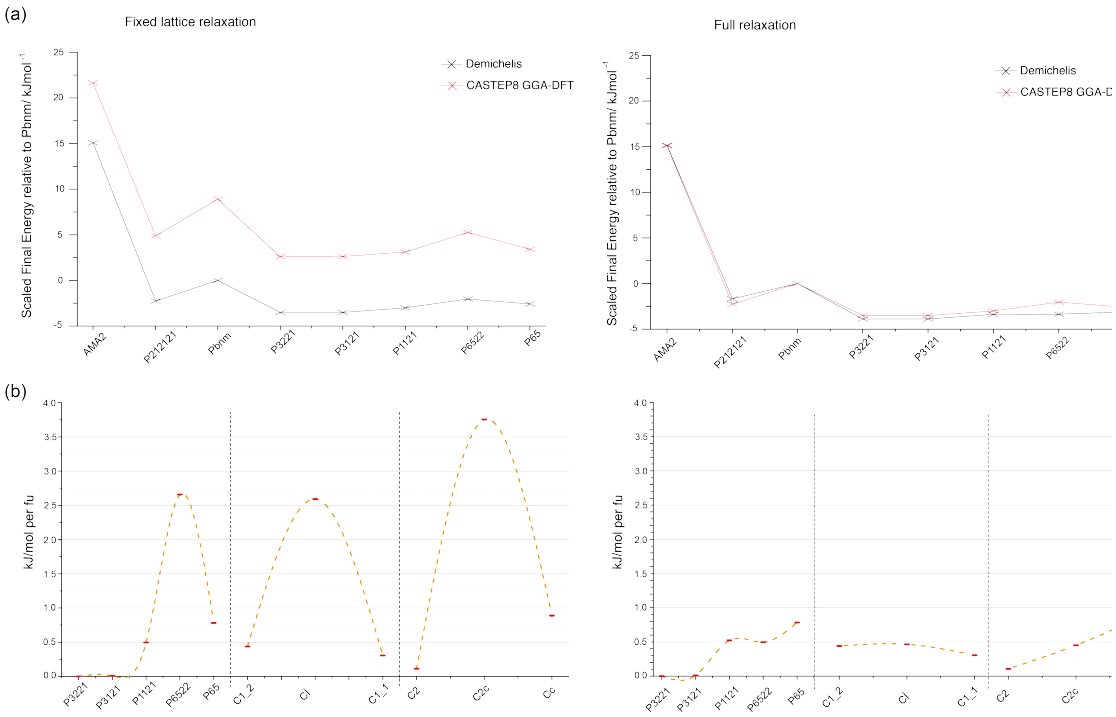

Figure 7.6, a) energy differences between structures relative to the unstable Pbnm configuration for structures geometry optimized with the lattice constrained (left) and unconstrained (right) b) energy landscape of the three basins for vaterite relative to the $P3_221$ configuration for structures geometry optimized with the lattice constrained (left) and unconstrained (right)

Figure 7.6b emphasises that it is only when the lattice is allowed to vary that the energetics become comparable with the findings of Demichelis et al 2013.[9] Here the trends deviate from the findings of Demichelis et al for the hexagonal and 2-layer monoclinic stacking models. In these stacking models the $P6_522$ and C2/c transition states are recorded as being lower energy configurations than their $P6_5$ and Cc respective minima (~0.43 kJ/mol per formula unit for C2/c with respect to Cc and ~0.287 kJ/mol per formula unit for $P6_522$ with respect to $P6_5$). Nonetheless these difference are small and well within thermal energy at room temperature. For the purposes of this study the relative energies are used to calculate a probability based on these energetic

considerations that will comprise our construction of a Boltzmann weighted average structure. As such these difference in energetics translate into very small changes in relative population of the configurations (~1%) and therefore their contribution to the bulk NMR spectra is likely to be within the experimental accuracy. The relative populations of the configurations in each isolated stacking model as calculated at 0 K are summarised in **Table 7-7**. Note that the population (p) in this context denotes the probability that a single carbonate unit at equilibrium, which is free to explore all the local crystal environments listed, will occupy one of those environments.

Table 7-7 Relative population of configurations (p) calculated from relative energy at 0K.

		Cell Fixed	Cell allowed to vary
Stacking Model		*p*	*p*
2-layer monoclinic	C2	0.372	0.343
	C2/c	0.278	0.334
	Cc	0.350	0.323
6-layer monoclinic	C1_2	0.351	0.332
	$C\bar{1}$	0.295	0.332
	C1_1	0.354	0.336
Hexagonal	$P3_221$	0.212	0.206
	$P3_121$	0.212	0.206
	$P112_1$	0.204	0.198
	$P6_522$	0.172	0.197
	$P6_5$	0.200	0.193

7.2.3 Spectral simulation of ordered vaterite structures (Spin-Echo)

Vaterite is assessed initially as unique crystallographic structure. Whilst experimental and computational data seem to suggest that a single ordered form of vaterite is insufficient to describe its structural complexity there are recent publications that highlight some configurations as likely importance realisations of the structural disorder.[197],[198]

The CASTEP data was initially used to simulate the solid-echo MAS powder experiment acquired at 21.1 T at 20kHz. Given that there is negligible signal lost into ssbs in the experimental lineshape due to chemical shift anisotropy (CSA) the centre band is considered to be largely independent of CSA effects. Thus the simulations assume that the MAS NMR spectra are devoid of any CSA effects. The simulations were completed using SIMPSON.[241] As there is no explicit treatment for a distribution of the

NMR parameters, which will broaden spectral features, 125 Hz apodization was applied to the simulated free induction decays (FID) to mimic this effect. The corresponding simulations are shown in **Figure 7.7**.

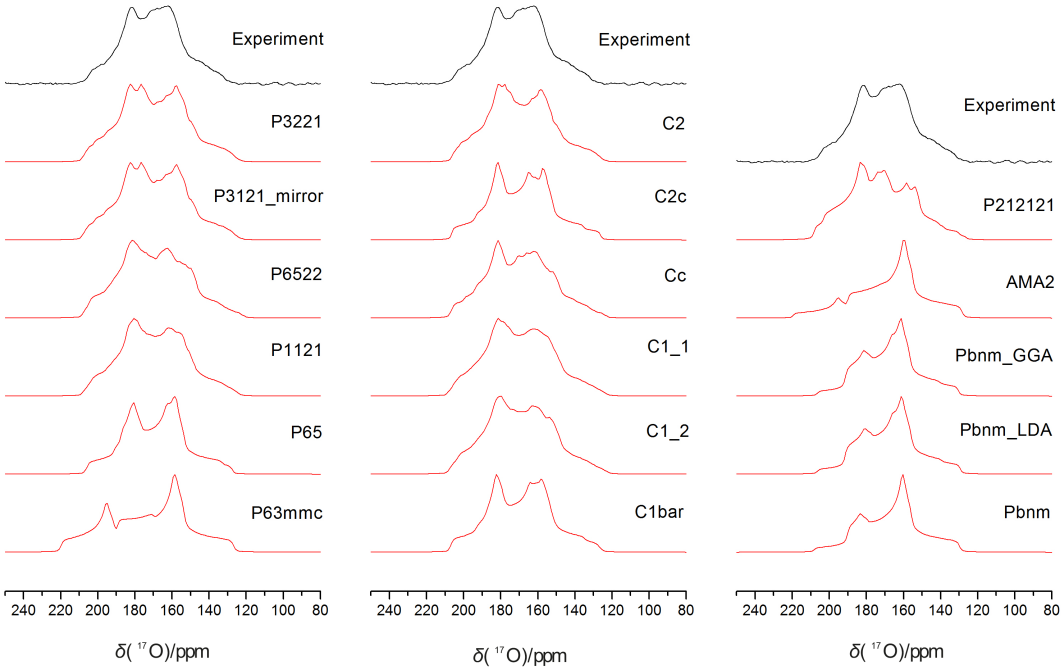

Figure 7.7, Solid-echo simulations of the calculated NMR parameters for each of the ordered vaterite structures. The simulations are grouped according their lattice family; hexagonal (left), monoclinic (centre) and orthorhombic (right)

The salient observation to be taken from these simulations is that none of the individual lineshapes can fully account for the experimental data, thus substantiating the arguments for more complex models of vaterite. It follows that if the proposed models are correct then the vaterite lineshape should either be reproducible via a stacking model or via a combination of structures consistent with the model of vaterite as domains of two or more ordered configurations. A random or more complex stacking model would combine elements from the three different families, however disorder resulting in realization of several elements within a family is also possible.

The orthorhombic structures have generally been rejected on energetic grounds, but are included here in part for completion. Individually these structures represent the worst fits to the experimental data along with the $P6_3/mmc$ hexagonal structure proposed by Kamhi (1963).[21] The orthorhombic *Ama2* and $P2_12_12_1$ configuration represent the two stable minima for the transition state *Pbnm*. No combination of the orthorhombic family structures comes to a satisfactory reproduction of the experimental

lineshape. Whilst the $P2_12_12_1$ could be energetically relevant to a domain model the breadth of its predicted lineshape means it can be excluded from further consideration.

It is worth noting that the structure with $P3_221$ symmetry, which is the outstanding candidate based on energetic considerations, does not represent the best fit to the experimental lineshape. In addition to the breadth of the experimental lineshape the narrow downfield feature represents a strong criterion against which to identify possible structural candidates. For both the $P3_221$ and its mirror image $P3_121$ the spin-echo simulations show that this narrow downfield feature is shown to be too broad. This characteristic will remain in the construction of a Boltzmann weighted average structure containing these ordered models and this suggests that at least for this sample of vaterite they are not major constituents. Of the hexagonal structures only the $P112_1$, $P6_522$ and $P6_5$ structures seem viable components of a more complex vaterite model. Conversely, based on the spin-echo simulations all of the monoclinic structures could plausibly represent ordered components of vaterite.

The broad upfield component of the resonance is less diagnostic in terms of eliminating possible configurations, but it is significant to note that its maximum intensity is approximately equal to that of the narrow downfield component. It is interesting to note that for all of the monoclinic models, except for the transition $C2/c$ and $C\bar{1}$ structures, the narrow feature is of greater maximum intensity so that unless these transition states are major constituents then this feature will always be under represented in a Boltzmann-weighted average structure of exclusively monoclinic structural models. As we have suggested that the $P3_221$ and $P3_121$ structures look to fail in other respects and can therefore be eliminated from further considerations, only $P6_5$ (that we identify as higher energy than the hexagonal transition state $P6_522$) of the hexagonal series of structures has this requisite characteristic. This suggests that any constructed component model according these simulations will under-represent the relatively broad upfield resonance of the experimental lineshape unless it is dominated by the structures with corresponding symmetries $P65$, $C2/c$ or $C\bar{1}$.

7.2.4 Spectral simulation of ordered vaterite structures (DOR)

In spite of these useful observations the spin-echo spectra offers poor resolution in comparison to that recorded by the experimental DOR technique that removes the dominant quadrupolar based broadening from the lineshape thereby making the isotropic spectral features of the inequivalent ^{17}O environments observable.

As a first-approximation numerical density-matrix simulations were performed using ssb suppression at 14.1 T using the experimental inputs for ν_{OR} and ν_{IR}/ν_{OR}. As our previous investigation into the NMR parameters suggested that the quadrupolar parameters will suffer the largest computational errors and taking into consideration that the positions of the resonances on the chemical shift axis in the DOR experiment remains modulated by the quadrupolar interaction ideally we would have simulated the acquisition at our largest acquisition field (20T) where this modulation is smallest. However at this field the experimental spectrum was partially blemished by the inability to completely separate the foremost upfield resonance from a spinning sideband. At 14.1 T such resolution issues did not hinder the experimental DOR data rendering it a more representative experimental constraint.

The simulations were completed in the time-domain and apodized with an exponential decay function corresponding to 150 Hz of line broadening prior to Fourier transformation. The corresponding DOR simulations for the individual structural models are shown in **Figure 7.8**. These spectral simulations corroborate the conclusion based on the equivalent spin-echo simulations that no single ordered vaterite structure fulfils the experimental lineshape.

It is important to observe that for almost all of the individual vaterite models the span of the theoretical resonances looks to just exceed the total area covered by the experimental intensity on the upfield side of the signal. The modulation of the resonance positions by the quadrupolar interaction make it very sensitive to the calculated quadrupolar coupling constants for each unique crystallographic form. Given that a spread of the signal in this direction correlates with a larger quadrupolar interaction then the size of the quadrupolar coupling constants looks to be slightly larger than that observed experimentally consistent with the findings reported earlier for the C_Q of calcite.

The quadrupolar-induced shift is directly proportional to the magnitude of the quadrupolar interaction via the square of the quadrupolar-coupling constant. Based on the study of aragonite and calcite the expected accuracy of the quadrupolar coupling constant is ± 0.15 MHz. Thus the DOR simulation will exaggerate small errors by stretching the spectra upfield if the C_Q is consistently overestimated. Assuming the experimental C_Q is between ~6.5 -7.15 MHz then the error can vary between ~2.25-2.50 ppm at 14.1 T. This error is on a scale consistent with that observed in the simulations. As all of the oxygen environments are carbonates and we are characterising relatively fine chemical differences it is not unreasonable to assume that the error in C_Q will be

relatively constant and therefore the DOR spectra will be slightly stretched in the manner outlined above.

The DOR simulations show how the inequivalent downfield oxygen environments observed before, as the 'narrow' feature in the spin-echo simulations, is manifest as numerous isolated resonances for the *P3₂21* and *P3₁21*. The oxygen environments contribution to the narrow spin-echo feature can been seen to split into three isolated resonances that span a region that extends beyond the isolated downfield resonance observed in the experimental DOR spectra. Of these isolated models the *C1_1* and *C1_2* structures look like a strong basis for a more complex vaterite model, but is should be emphasised that none of the monoclinic structures can be eliminated completely from further consideration at this point based on them being components that would combine to reproduce the experimental lineshape. The comparative simplicity of the metastable structures *C2/c*, *P6₅22* and $C\bar{1}$ (all contain only two independent carbonates as opposed to the minimum of three independent carbonates for the stable structural minima) is emphasised by their simple DOR spectra. Whilst the $C\bar{1}$ seemed to be a strong candidate based on its spin-echo simulation the position of its downfield resonance would discredit it from being a major constituent of the synthetic vaterite sample under investigation.

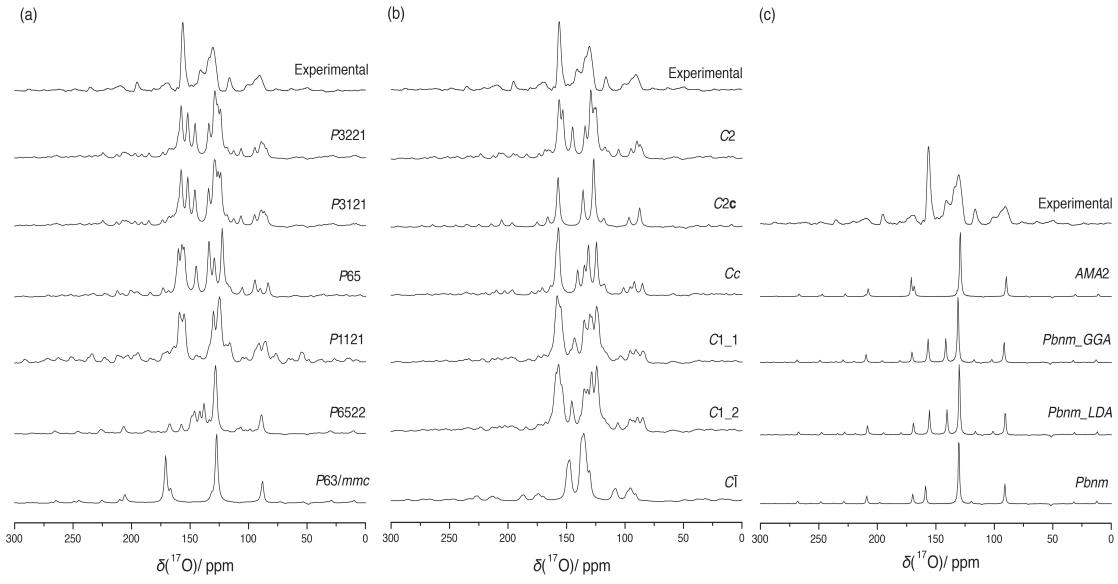

Figure 7.8, DOR simulations of the calculated NMR parameters for each of the ordered vaterite structures. The simulations are grouped according their lattice family; (a) hexagonal, (b) monoclinic and (c) orthorhombic

7.2.5 Spectral simulation of a domain based model

Kabalah-Amitai et al.'s[208] study on biogenic vaterite crystals was the experimental precursor to the idea of structural vaterite as a domain based structure: suggesting that vaterite consisted of a minimum of two co-existing structures of which one exhibits hexagonal symmetry and the other component(s) were unable to be assigned.[12] Thus vaterite looks to possess interspersed crystals that exist in domains, though the exact form of these domains are unclear.

In this context the motifs for the more complex models of vaterite can be defined: whether vaterite simply involves the co-existence of at least two or more distinct stable crystallographic forms in domains that co-exist within a pseudo-single crystal[208] or whether these domains actually involve higher order superstructure involving energetically favourable stacking of the carbonate layers where the stacking is defined by combinations of vaterite structures that fall within any one of three approximately isoenergetic basins respectively.[22]

Under ambient conditions the narrow energetic window has shown that a coexistence of different structures is plausible. The relative populations of all the relevant energetic minima for the hexagonal and monoclinic structures have been previously calculated from the free energy at room temperature (including electronic, vibrational and configurational entropy contributions)[22] and are reported in **Table 7-8**.

Table 7-8 Relative population of configurations (p) calculated from the free energy at 298K taken from ref - [205].Electronic energy (E), enthalpy (H), free energy (G) and entropy (S).

	ΔE kJ/mol	ΔH kJ/mol	ΔS J/(mol K)	ΔG kJ/mol	p
$P3_221(P3_121)$	3.1	3.3	0.8	3.1	0.132
$P6_5(P6_1)$	3.8	3.8	-1.1	4.1	0.088
$P112_1$	3.6	3.9	1.2	3.6	0.11
Cc	4	4	-0.5	4.2	0.086
C2	3.2	3.2	-1	3.5	0.113
C1_1	3.5	3.7	1.7	3.2	0.127
C1_1	3.6	3.9	2	3.3	0.123
Average		3.6	0.4	3.5	
Exp		3.6	1.3	3.21	

Such a model is a good representation of a non-biased domain-based model where a wide variety of structures with minor structural (and energetic) differences co-exist. This model ignores interfaces, which is a good approximation if there are is no interfacial structure (so that the disorder is simply due to different carbonate disorders within the stacking) or if the domains are large such as might be expected for domains of different stacking.

These domains will then be observed experimentally by a weighting to the bulk NMR signal according to the size (or population) of each domain of ordered structure (density is roughly equal across all ordered structures). A Boltzmann-weighed averaging across the spin-echo and DOR simulations for the relevant structures based on their energetics mimics this here. The corresponding spin-echo and DOR simulations based on a Boltzmann-weighted average structure using these calculated probabilities is shown in **Figure 7.9a**.

The discussion of the spin-echo simulations for the isolated structures highlighted that many of these structures fail to capture the downfield narrow feature or intensity and breadth of the broader upfield resonance of the experimental lineshape for the spin-echo experiment, an effect that is inherited by these Boltzmann-weighted simulations. As such it is clear that the set of ^{17}O carbonate environments present in the minimum energy structures do not completely describe the set of carbonate environments in the synthetic sample of vaterite under investigation.

Not only is co-existence of different ordered vaterite structures a possibility at room temperature, but also interconversion between these ordered structures is energetically possible.[205] The timescale of these potential transitions is key to the reproduction of the experimental spectral sampling of the vaterite configurations. It might be that these interconversions are more rapid or at least on the timescale of the NMR experiment such that experiment is capturing a large proportion of configurations in transition states rather than at the stable energetic minima. Certainly the transition states $C2/c$ and $C\bar{1}$ have more in common with the spin-echo experimental lineshape than many of the stable vaterite structures.

A Boltzmann-weighted reproduction of the spin-echo and DOR experimental spectra for a combination of these metastable transition states are shown in **Figure 7.9b**. It has already been suggested that it is unlikely that the $C\bar{1}$ structure could contribute to a vaterite structural model based on its corresponding DOR simulation the lineshape

produced by a combination of the hexagonal $P6_522$ and monoclinic $C2/c$ metastable structures without the $C\bar{1}$ component is also shown in **Figure 7.9c**.

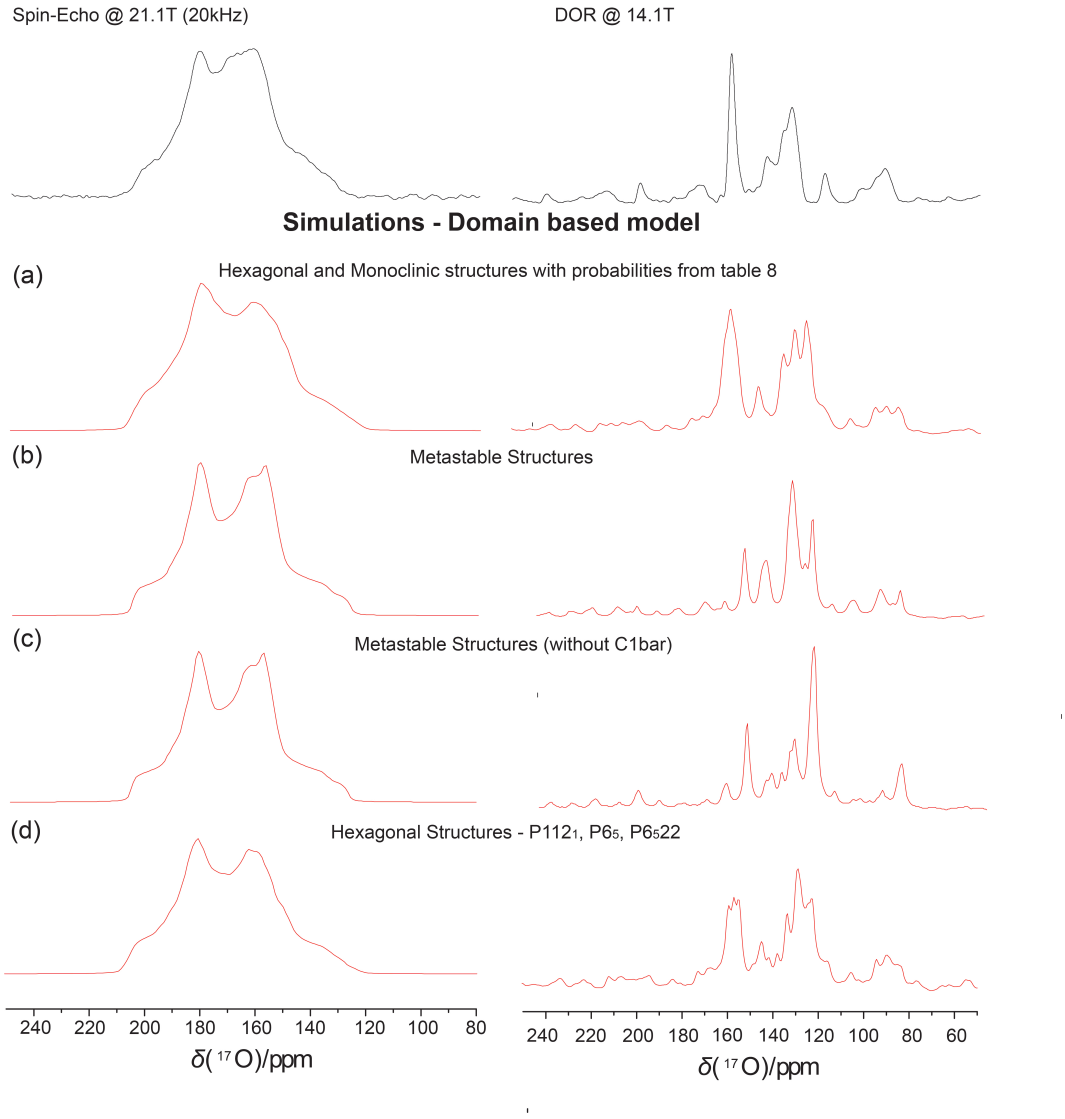

Figure 7.9, a) Spin-echo (left) and DOR (right) simulations for a Boltzmann-weighted average structure using the probabilities reported in table 8. b) Model of all the metastable structures (top) and only the P6522, C2/c structures (bottom) based on Boltzmann-weighted averaging across the unique crystallographic forms. c) Model of the hexagonal structures P112$_1$, P6$_5$, P6$_5$22 based on Boltzmann-weighted averaging across the unique crystallographic forms.

It is clear that of the metastable structures only the $C2/c$ and $P6_522$ structures of vaterite are feasible components the synthetic vaterite structure under investigation, but that these structures can only contribute to a model mixed with stable structures as their structural complexity is not sufficient to represent the full extent of the experimental lineshape (all transition states only possess 2 independent carbonates as opposed to the 3-18 independent carbonates represented by the stable structures), which is well illustrated by the DOR simulation.

In light of Kabalah-Amitai et al.'s study on biogenic vaterite crystals[12] that confirmed a hexagonal component to the structure it is worth considering a hexagonal model in which the low-energy *P3₂21* and *P3₁21* structures that have incompatible spectral signatures are excluded. A Boltzmann-weighted average simulation based on a combination of the hexagonal *P112₁*, *P6₅*, and *P6₅22* structures is displayed in **Figure 7.9d**. Though the simulation displayed in **Figure 7.9d** is not without deficiencies it is the best representation of the experimental lineshape reproduced thus far and could plausibly represent a hexagonal domain in the synthetic vaterite sample under consideration if combined with at least one structure or set of structures that describe another independent domain.

Based on the independent experimental signatures of the monoclinic structures *C2*, *C2/c*, *Cc* are the best candidates for this additional potential domain (the *C1_1* and *C1_2* structures being excluded based on their DOR spectra). However, these individual components constitute the 2-layer monoclinic basin that is considered in the next section so further discussion is deferred until after these models have been evaluated.

7.2.6 Spectral simulation of stacking models

It is noted that there are distinct energy basins corresponding to different crystal symmetries, yet there are remarkable similarities between the hexagonal and 2-layer monoclinic structures such that one could be converted into the other by exchanging certain molecular planes suggesting that there could exist stacking disorder of the CO_3^{2-} planes. Demichelis et al. (2013)[22] investigated possible stacking sequences by considering all possible permutations of 6 planes along the *c*-axis starting from the *P3₂21* structure leading to stacking sequences made exclusively from structures relating to the *C2* and *P3₂21* (or *P3₁21*) symmetries. The second monoclinic model (with *C1* symmetry) proposed by Mugnaioli et al[242] corresponds to structures with a 6-layer stacking sequence in their own right. Key to the analysis was the finding that there is multiple hexagonal and monoclinic stacking sequences that are energetically equivalent (three hexagonal, two 2-layer monoclinic and three 6-layer monoclinic) validating this as a potential source of disorder in the vaterite structure.

The conclusion is that vaterite could interconvert between different structures in their respective energy basins and that there could also be differences in its structure due to the order of these structures. It should also be noted that contributions to the free energy due to configurational entropy are relatively small thus we should still be able to

represent a stacking model to a good approximation by Boltzmann-weighted average according to the relative electronic energies.

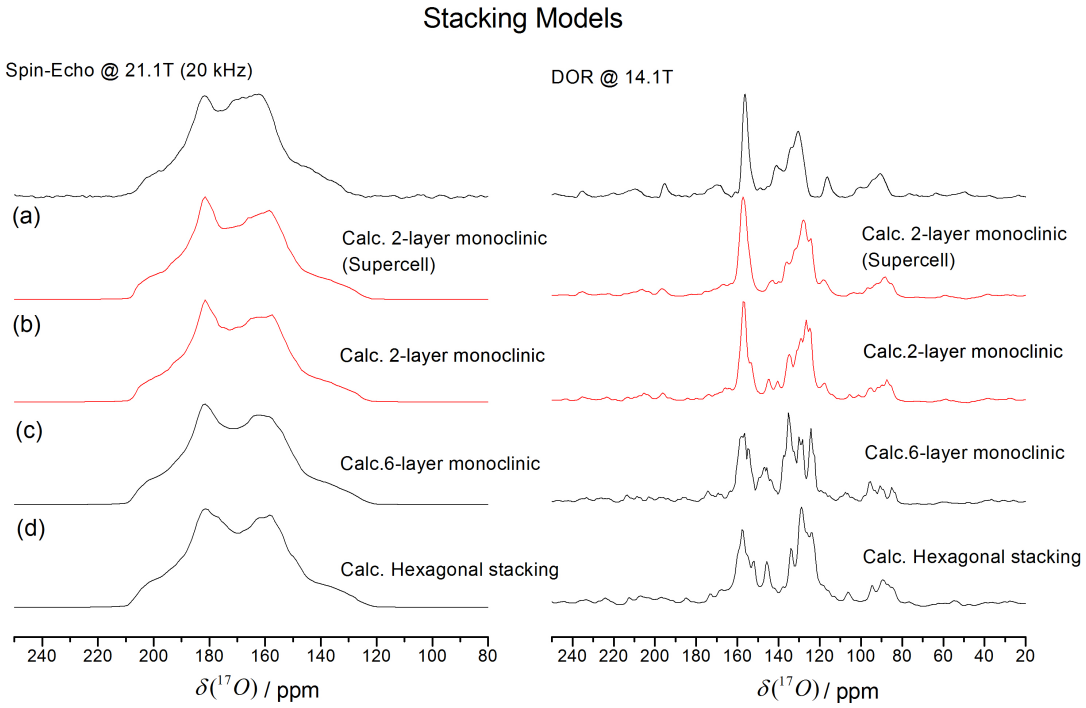

Figure 7.10, Spin-echo (left) and DOR (right) simulations for each of the stacking models a) 2-layer monoclinic based on supercell b) 2-layer monoclinic Boltzmann-weighted averaging across unique crystallographic forms c) 6-layer monoclinic Boltzmann-weighted averaging across unique crystallographic forms d) Hexagonal Boltzmann-weighted averaging across unique crystallographic forms

Thus spectra for the three possible stacking sequences were simulated according to the Boltzmann-weighted average of the spectra within the same basin, where the probabilities for the respective stacking models are displayed in **Table 7-7**. In **Figure 7.10b**, **Figure 7.10c**, **Figure 7.10d** are the corresponding stacking model simulations calculated in the method outlined previously for the DOR and spin-echo experiments.

Both of the monoclinic models capture the narrow downfield peak feature of the experimental spectra, but both fail to fully account for the larger upfield intensity; the 2-layer monoclinic stacking model is a better reproduction of the overall spin-echo experimental lineshape. The hexagonal stacking model is the least representative fit to the experimental lineshape in both respects.

The resolution afforded by the DOR experiment here proves invaluable. Whilst the simulation of the 6-layer monoclinic and hexagonal models proves relatively unconvincing the 2-layer monoclinic captures the experimental lineshape very well, although it is slightly stretched due to small errors in the quadrupolar parameters as

discussed previously. In order to assess whether this was a real correlation for the 2-layer monoclinic model to the experimental data the model was reconstructed at another lower field (9.4T) and a summary of the simulations can be seen in **Figure 7.11**.

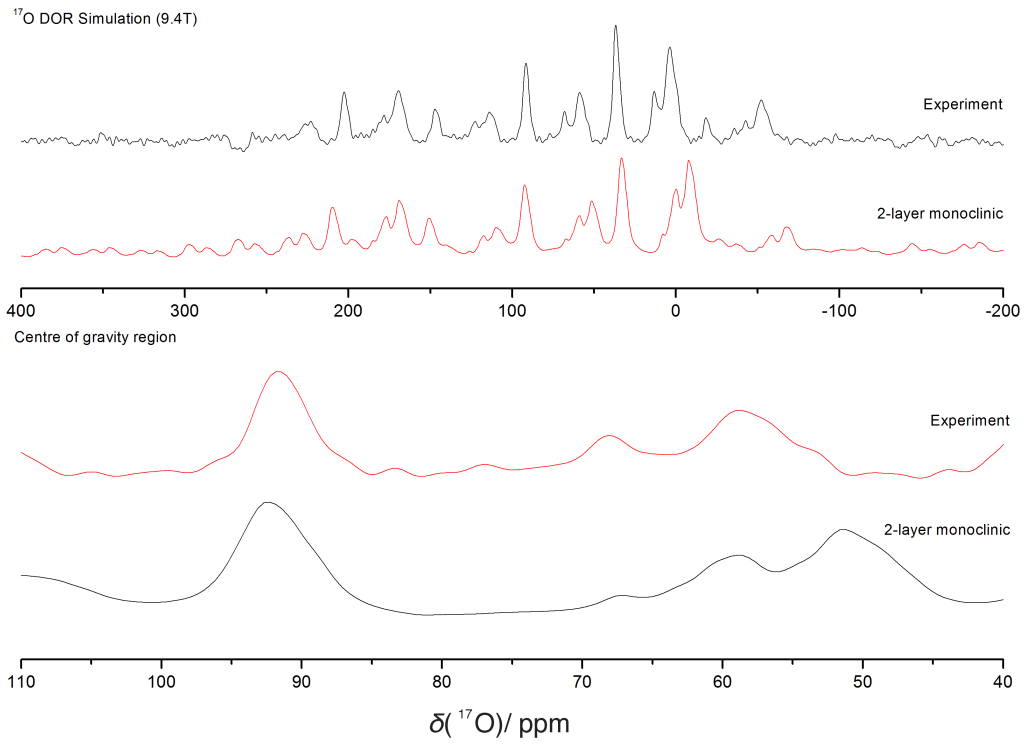

Figure 7.11, ^{17}O DOR simulation for each of the 2-layer monoclinic stacking model at 9.4 T based on Boltzmann-weighted averaging across the unique crystallographic forms. The top simulation shows the entire spinning sideband manifold while the bottom only displays the region of the spectra corresponding to the centre of gravity peaks for the oxygen environments.

Again the simulated DOR lineshape captures the important experimental spectral features. The stretching effect of the spectra due to the accuracy of the calculations will be more pronounced at lower field as the effect of the C_Q is magnified. Nonetheless the dominant features of the simulation at 9.4 T have all the principal resonances in similar ratios of intensity to the experimental lineshape. Accordingly the strong correlation at 14.1 T seen for the 2-layer monoclinic stacking model is not coincidental and represents an important result in the structural elucidation of synthetic vaterite.

In the previous results the spectra were recreated from a Boltzmann-weighted average of the individual models. In reality the structures are layered to form a superstructure. Demichelis et al[22] have discussed the possibility of these superstructures and the three proposed models from this study are shown schematically in **Figure 7.12**.

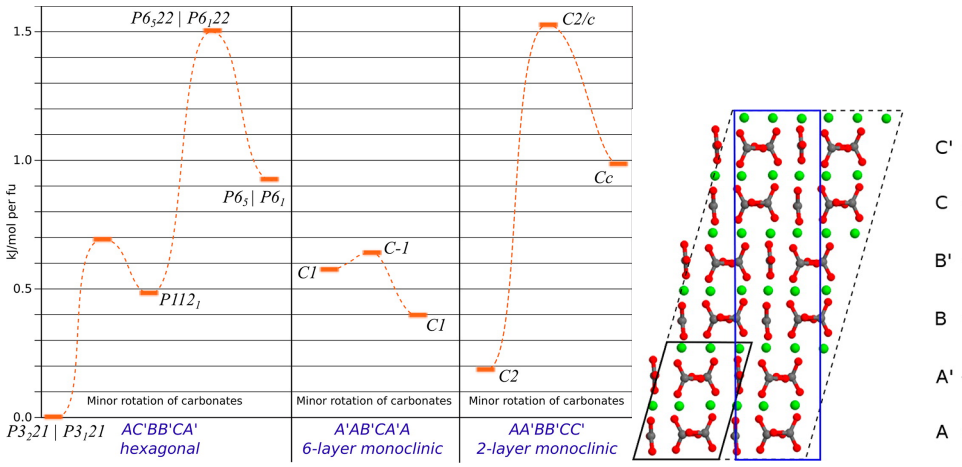

Figure 7.12, energy landscape of the three basins for vaterite relative to the $P3_221$ configuration according to Demichelis et al (left) The stacking layers (A, A', B, B', C, C') used to generate the hexagonal, 6-layer monoclinic and 2-layer monoclinic superstructures in the same publication.[22]

Such a superstructure may be able to access lower energy configurations via the re-orientation of ionic positions around the interfaces between different layers. This cannot be accounted for via the structural optimisation of individual configurations, which are optimised against the constraints of their own image in all directions. To investigate this effect a superstructure was created according to the low energy stacking sequence that constitutes the 2-layer monoclinic basin (AA'BB'CC').

The superstructure was geometry optimised and the relaxed configurations were used to calculate the NMR parameters. All computational steps were completed in a manner consistent with the method outlined earlier. The corresponding spin-echo and DOR simulations are displayed against the Boltzmann-weighted and experimental spectra in **Figure 7.10a**.

The differences between the Boltzmann-weighted spectra and that of the constructed supercell are small. The broad upfield component is slightly better characterised by the supercell as opposed to the weighted spectra, whilst there is little to interpret from the fine level difference in the DOR spectra for the two methods.

From this result we can state within a particular superbasin corresponding to a single stacking at least that interface effects cannot account for the missing intensity in the broad upfield component of the spectra. Moreover the agreement between the two methodologies justifies the legitimacy of our Boltzmann-weighting across the basin components to reproduce their corresponding spectral simulations.

7.2.7 PXRD Simulation

To further consolidate the 2-layer monoclinic stacking model a X-ray diffraction pattern was calculated using the Mercury software (version 3.1) available from the Cambridge Crystallographic Data Centre assuming a wavelength of 0.15406 nm (Cu*K*α), Lorentzian peaks and crystal sizes of 50nm which is consistent with the nanosized crystallites observed for vaterite.[188] (shown in **Figure 7.13**)

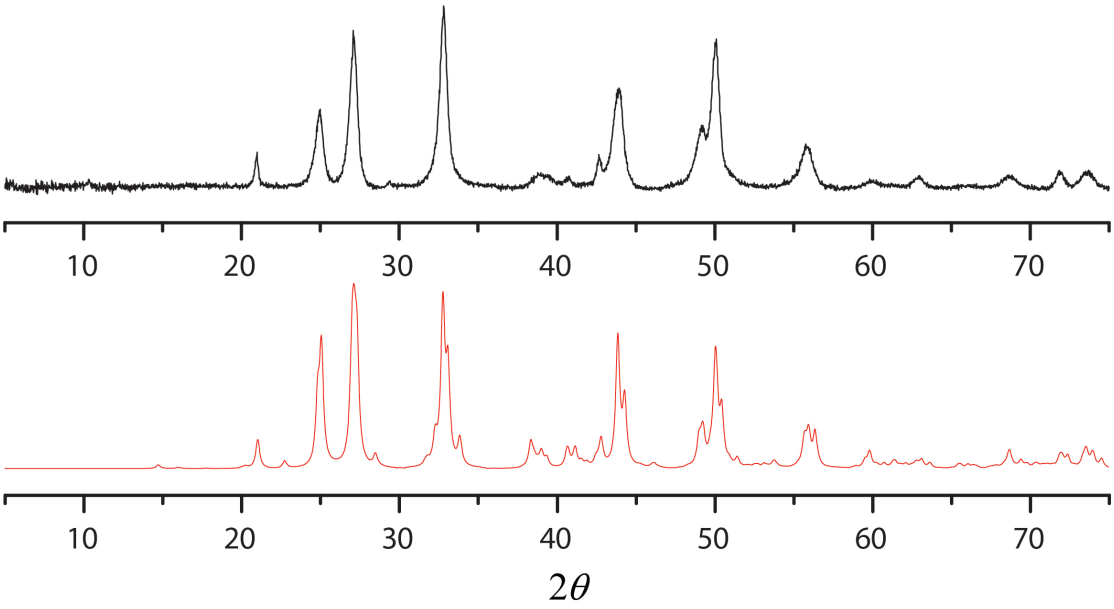

Figure 7.13, calculated (red) and experimental vaterite (black) X-ray diffraction pattern. The simulations is based on the 2-layer monoclinic stacking model based on a first-principles optimized constructed supercell and was generated using the Mercury software.

The calculated and experimental XRD patterns have very similar peaks positions, though the peaks in the experimental PXRD powder pattern are relatively broad when compared to the major peak reflections in the generated pattern. There are additional weak reflections in the 2-layer monoclinic simulation with 2θ near 23°, 28°, 42°. Wang and Becker[201] showed that these small peaks become more visible when CO_3 ions are more ordered and postulated that these peaks can serve as an order-disorder indicator. Then it follows that the simulated spectra represents a more ordered manifestation of the synthetic vaterite sample. The supercell represents and an average snapshot of the vaterite structure for the 2-layer monoclinic superstructure. Then it is not unreasonable to postulate that the discrepancy in the X-ray diffraction patterns is due to differences the effective sampling in the two experimental techniques. The experimental ^{17}O NMR spectra for the synthetic vaterite is typically produced by adding across > 1000 transients. For the pxrd each sampling point is the average of approximately two orders of

magnitude less than the NMR experiment. If structural interconversion is occurring within the 2-layer monoclinic superbasin then the pxrd will be more sensitive to intermediate configurations, which is equivalent to sampling a range of carbonate positions.

7.2.8 Possible combination of 2-layer monoclinic model and the P1121/P65/P6522 model

Earlier a combination of hexagonal structures (*P112$_1$*, *P6$_5$* and *P6$_5$22*) proved to be a viable candidate as a domain that could co-exist with one or more other domains. The 2-layer monoclinic simulation can convincingly account for almost all of the experimental lineshape, however the hexagonal model was combined with it in varying proportions to investigate whether this fit could be improved.

The corresponding simulations based on varying the contributing proportions of either model in comparison to their independent simulation and the experimental data are shown in **Figure 7.14**.

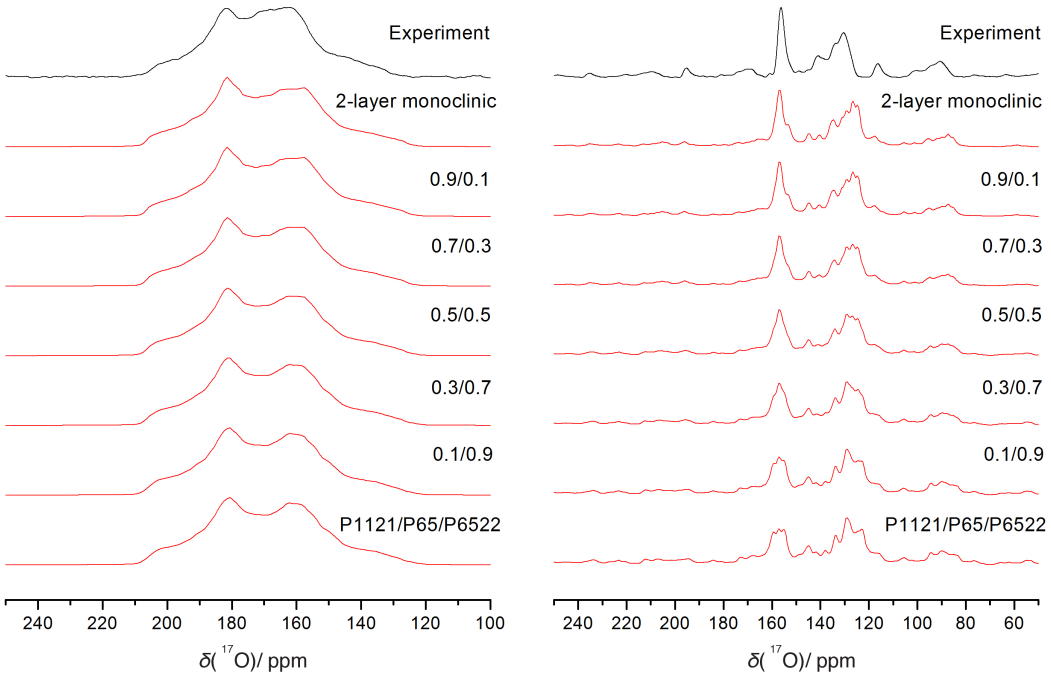

Figure 7.14, Spin-echo (left) and DOR (right) simulations for a model of varying proportions of 2-layer monoclinic and a hexagonal structures ($P6_522$, $P6_5$, $P112_1$)

In the regime where the proportion of the hexagonal structure is small (≤10%) the spin-echo and DOR simulated lineshapes can plausibly incorporate this hexagonal model without being distorted showing that this synthetic sample could have multiple domains, though clearly the 2-layer monoclinic basin dominates.

7.2.9 Exclusion of metastable components

It is postulated that interconversion can occur between structures in their respective basins via the rotational freedom of the CO_3^{2-} units as the activation barrier to such transitions are within thermal energy at room temperature. The inclusion of the metastable transition state *C2/c* in the 2-layer monoclinic stacking model represents a transition state in the interconverison between minimum energy structures. As the NMR experiment records signal across configurational snapshots it would sample these postulated interconversions such that the bulk average total spectra would require the contribution of a metastable component to reproduce the overall experimental lineshape. A comparison to the line shape with and without the transition state *C*2/*c* structure is displayed in **Figure 7.15**.

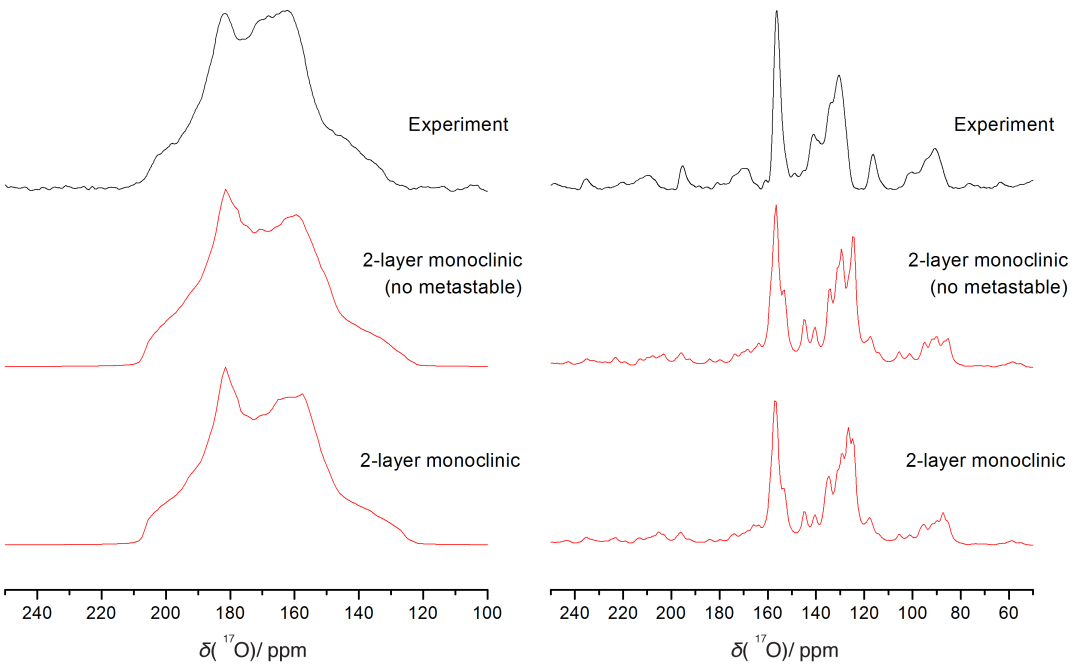

Figure 7.15, Spin-echo (left) and DOR (right) simulations for a model of the 2-layer monoclinic model with (bottom) and without the C2/c structure based on Boltzmann-weighted averaging across the unique crystallographic forms.

For the spin-echo simulation the metastable component contributes most significantly to the broad upfield component of the experimental spectra and to the most prominent peak in the upfield resonance of the DOR spectra. In order for the spectral simulations to be convincing the inclusions of this 'distorted' structure is vital. This means that on the timescale of the NMR experiment this is consistently a significant component to the structure and so the timescale of interconversion between structures within a superbasin is small. In fact a larger contribution than that dictated by the calculated probability based on relative electronic energies might improve the agreement between the spin-echo simulation and experiment. This emphasises the view of vaterite as a dynamic structure and not a disordered system in the conventional sense; vaterite looks to be a family of ordered structures connected by differences in their carbonate stacking layer sequences.

7.2.10 Lineshape Deconvolution

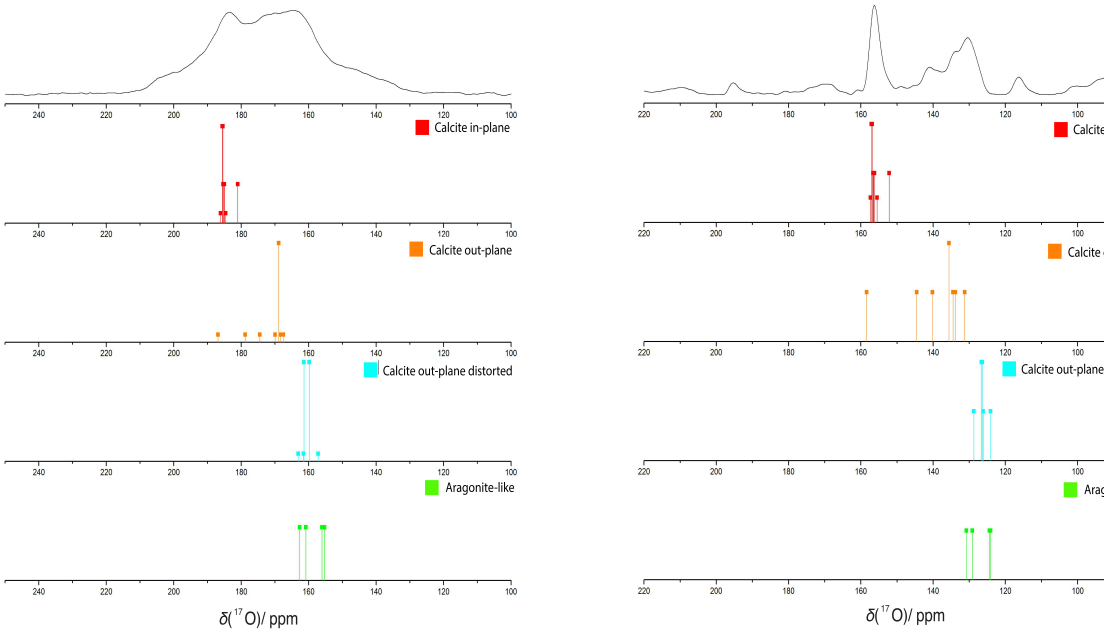

Figure 7.16, ^{17}O Spin-echo spectrum for synthetic vaterite with the peak positions for the 2-layer monoclinic model plotted below based on the three structural groups used for the lineshape deconvolution

The peak positions of the 2-layer monoclinic model are displayed below the spin-echo experimental and DOR lineshape in **Figure 7.16**. The peaks are split into the four major structural groups used for the lineshape deconvolution as described in the experimental chapter. This schematic representation shows the 'calcite in-plane' component to be most downfield and the 'aragonite like' to describe the most upfield

oxygen-17 nuclear environments. However, there is overlap of the structural units; in its most symmetric form the 'calcite out-plane' can appear as upfield as the 'calcite in-plane' environment. The calcite out-plane peak position is seen to move upfield as the planar Ca_2-O-C arrangement is increasingly distorted and is seen to strongly overlap with the 4-coordinate aragonite-like environments, which correlates with the oxygen environments becoming so distorted that they are effectively 4 co-ordinate.

Using the isotropic shifts of the DOR experimental data to categorise the isotropic shift positions of the CASTEP data into 6 groups consistent with resolving six peak positions in the experimental data the estimated populations of the respective oxygen environments according to the 2-layer monoclinic structural model were calculated. The populations according to the CASTEP data with respect to the MAS and MQMAS data are shown in **Table 7-9**. The agreement between the three datasets offers further compelling evidence that the model is a good representation of the experimental data.

Table 7-9 ^{17}O site populations for deconvolution of the MAS spin-echo experiment across multiple fields for synthetic vaterite (column 1), those extracted by the 3QMAS inversion fitting process and the site populations predicted by CASTEP

Site Populations

MAS	**MQMAS**	**CASTEP**
%	**%**	**%**
31	32	33
11	9	8.3
10	9	8.3
10	13	8.3
27	24	29.17
10	13	12.5

7.2.11 ^{13}C Vaterite Simulations

^{13}C simulations were undertaken as outlined earlier for calcite and aragonite with NMR parameters calculated in CASTEP8 to the same levels of precision for each of the ordered vaterite structures. Analogous to the protocol employed for the ^{17}O DOR and spin-echo simulations the calculated NMR parameters for the individual ordered vaterite structures were simulated in SIMPSON except that the focus here was on the ^{13}C data as

opposed to ^{17}O. Then the more complex vaterite models were considered by combining these individual simulations according to a Boltzmann-weighted average that can approximate the existence of stacking models for each of the three almost isoenergetic basins for vaterite. For brevity only the ^{13}C simulations of the stacking models are evaluated here (shown in **Figure 7.17**)

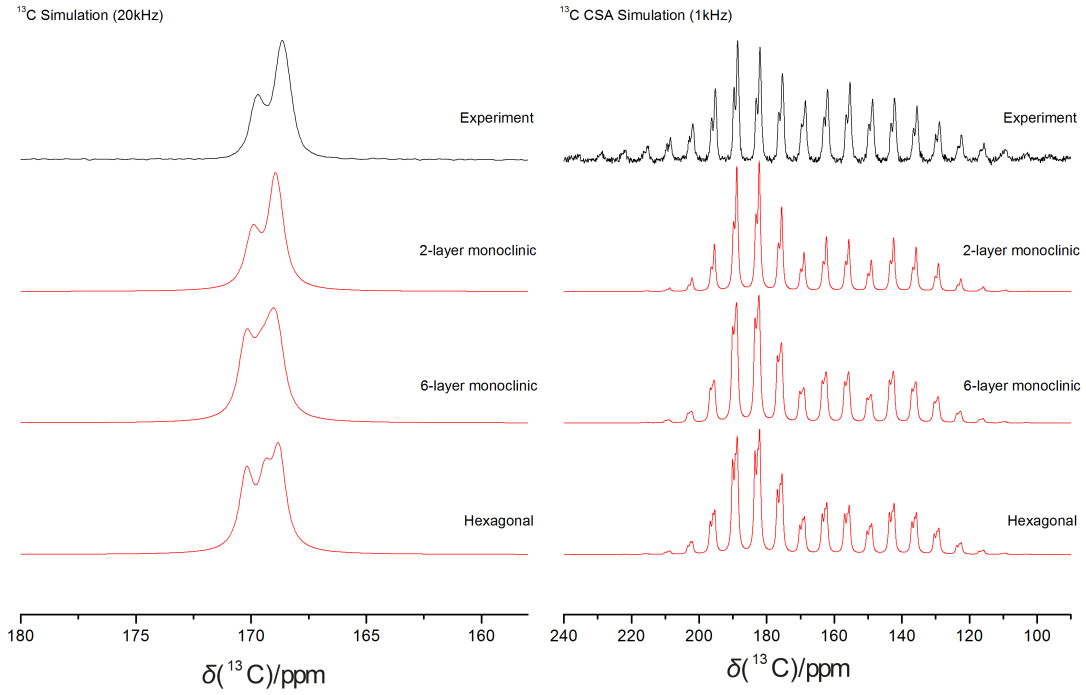

Figure 7.17, Spin-pulse simulations for ^{13}C experimental spectra acquired at 20 kHz (top left) and 1 kHz (top right) for the respective 2-layer, 6-layer and hexagonal basins

The ^{13}C 20 kHz experimental data acquired under a rotor frequency of 20 kHz is quantitative and purely based on the distribution of isotropic chemical shifts present in the 2-layer monoclinic structure. Thus the excellent correlation between the 2-layer monoclinic simulation and the vaterite experimental data means that the type and quantity of carbonate environments in this model must describe the synthetic vaterite structure.

Irrespective of the differences in the distribution of the isotropic peaks for the stacking models, the shape of the spinning sideband manifold as dictated by the anisotropy and asymmetry parameters is very consistent. The average anisotropy and asymmetry parameters for the two peaks of vaterite against the experimental fit are displayed in **Table 7-10**.

Table 7-10 Comparison of ^{13}C experimental NMR parameters against the theoretical NMR parameters calculated for the Boltzmann-weighted 2-layer monoclinic model and 2-layer monoclinic supercell

^{13}C NMR - Experimental

NMR parameter	Experiment	Boltzmann-weighted 2-layer monoclinic	2-layer monoclinic supercell
δ/ppm	168.64	168.96	169.02
	169.69	169.95	169.89
Δδ/ppm	-49.5	-47.58	-47.32
	-49.25	-46.57	-46.86
η	0.25	0.19	0.18
	0.15	0.14	0.13
δ_{11}/ppm	199.58	197.27	196.87
	198.01	196.53	196.25
δ_{22}/ppm	187.2	188.23	188.49
	190.62	189.93	190.39
δ_{33}/ppm	119.14	121.38	121.70
	120.44	123.37	123.04

For completion the ^{13}C simulations of the 2-layer monoclinic supercell-stacking model are included in **Figure 7.18** with a summary of the corresponding NMR parameters in **Table 7-10**.

Full relaxation of the structure leads to a spectrum that shares the common features of the Boltzmann-weighted averaged simulation except that there is a small variation in the ratio of the two resonances. As this spectrum is fully quantitative and acquired on a 100%-^{13}C labelled sample it is fully representative of the ^{13}C environments in the sample.

In the supercell the contribution of each structure in the 2-layer monoclinic basin is equal, which in the context of Boltzmann-weighting is equivalent to weighting each simulation by a third (the number of ^{13}C species is identical in each structure). Initially this was considered the major source of this error as in the broader context of a bulk crystal the statistical distribution of vaterite structures would deviate from this according to the energetic landscape. However as the probabilities calculated from the relative electronic energies used to create the Boltzmann-weighted average simulation show (see

Table 7-7) this deviation is on the scale of ~1% translating into a maximum net change in ratio of 2%.

Then the origin of this difference must derive from the relaxation of the structure in CASTEP. For the individual structures the point symmetry can be easily constrained, but the number of these constrains will be reduced for the supercell. As relaxation is considered at 0K this is likely to be the source of the variation in shielding.

Nevertheless the agreement between the 2-layer monoclinic model and experiment is excellent and the ^{13}C simulations corroborate the previous conclusion based on the ^{17}O simulations: that the 2-layer monoclinic basin of structures dominates the synthetic vaterite sample under investigation.

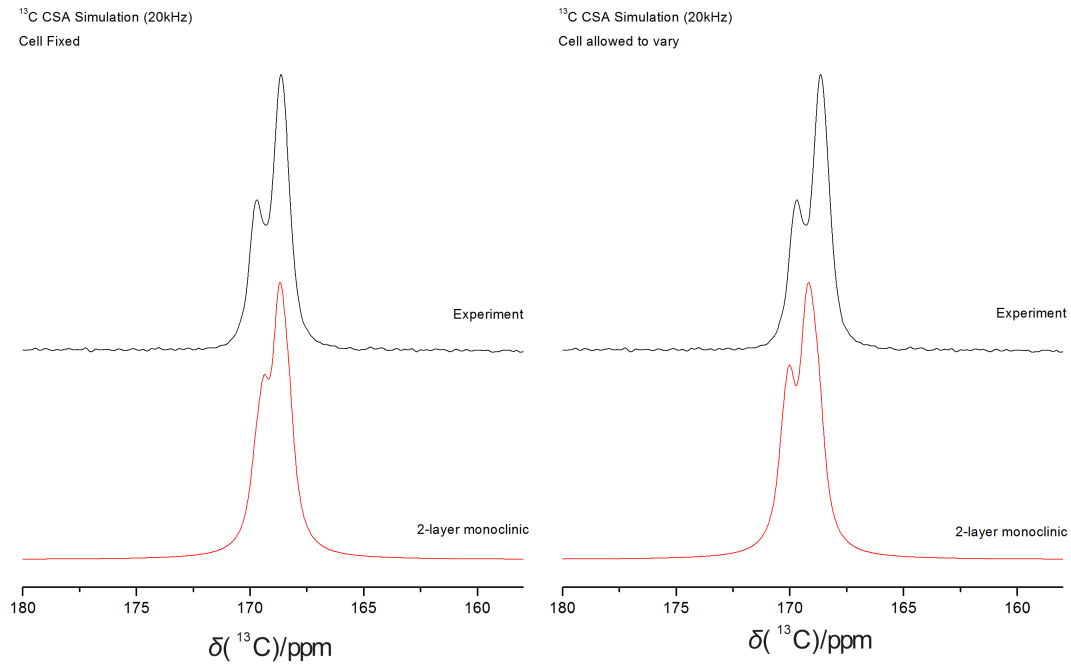

Figure 7.18, Spin-pulse simulations for ^{13}C experimental spectra acquired at 20 kHz (top) for the 2-layer monoclinic supercell optimized with the cell fixed (bottom left) and unconstrained

7.2.12 Lineshape Deconvolution

The break down of the ^{13}C experimental spectrum into peaks positions as calculated by CASTEP is shown in **Figure 7.19**. These peak positions are broken into the calcite-distorted and aragonite-like environments described in the experimental chapter. The distinct subset of peaks for each component unambiguously confirms the experimental assignment. The one overlapping peak for the calcite-distorted subset represents a carbonate unit where two of the bonds are very close to being equal (~0.003Å) and therefore the carbon environment is very close to being considered aragonite-like. Only carbonate units with exactly two equal bonds were categorised as aragonite-like, therefore this peak is still consistent with the deconvolution.

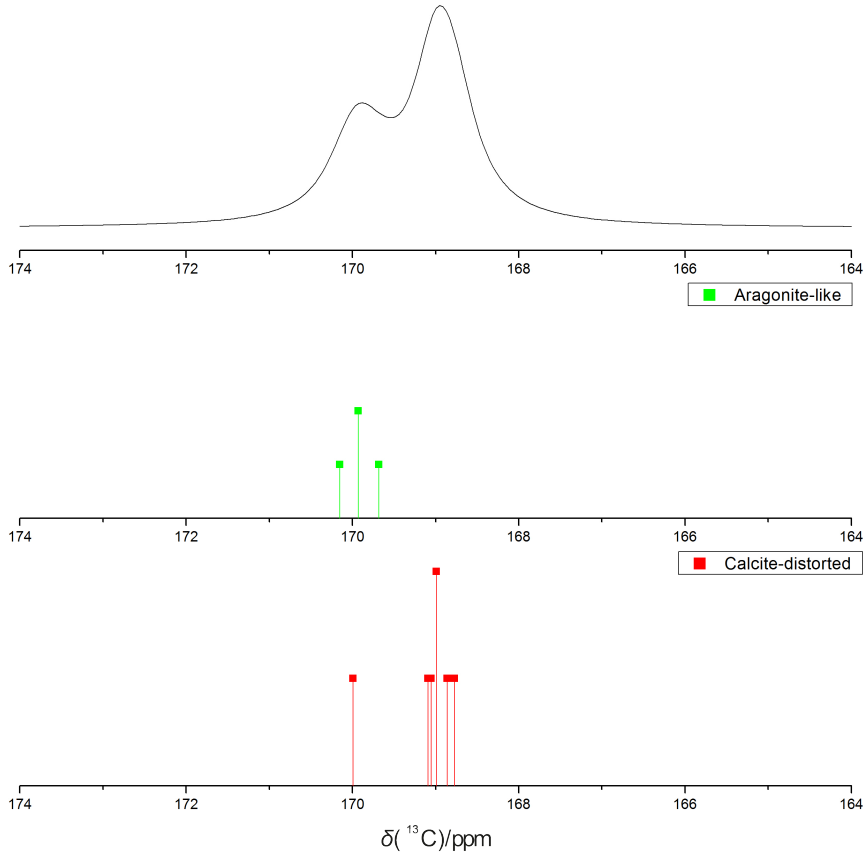

Figure 7.19, ^{13}C MAS NMR spectrum for synthetic vaterite with the peak positions for the 2-layer monoclinic model plotted below based on the three structural groups used for the lineshape deconvolution

7.3 Conclusions

This study has shown that the synthetic vaterite sample under investigation is well characterised by the 2-layer monoclinic isoenergetic basin with absolute minimum energy

structure C2. Unlike Kabalah-Amitai et al.'s experimental observation of a major hexagonal component to their biogenic vaterite crystals via electron transmission spectroscopy[208] we do not find any major hexagonal component in this sample of synthetic vaterite. The ^{17}O studies showed that if another domain of the most plausible hexagonal structures exists it couldn't exceed 10% of the synthetic vaterite sample. The excellent agreement between the fully quantitative ^{13}C experimental data and the Boltzmann-weighted average simulation for the 2-layer monoclinic basin suggests that this model could account for the entirety of the ^{13}C signal suggesting that this contribution is in fact negligible and that the synthetic sample can in fact be described completely be the 2-layer monoclinic model.

Then discrepancy of the spin-echo simulation from the experimental lineshape for the 2-layer monoclinic sample could be perhaps assigned to extended defects related stacking faults or the sampling of different points in the transition state between the energy minima. The importance of the transition C2/c structure, in which the carbonates occupy a rotational state between the two minimum energy structures C2 and Cc, to the faithful reproduction of the experimental lineshapes suggests that the rotational freedom of the carbonate units at room temperature are causing structural interconversion within each basin and emphasis that vaterite is a dynamic system under ambient conditions.

It has been postulated from the conversion of ikaite to vaterite[243] and the formation of vaterite from supersaturated[244] and from ACC nanoparticles[183] that vaterite crystallites with different structures could grow in the same solution. Hence on the basis of the findings in this study we can conclude in a broader sense that the vaterite structure must depend on the environmental conditions in which it is grown. The use of glycine as a nucleation buffer under ambient conditions at a roughly neutral pH must promote the formation of the 2-layer monoclinic basin of structures, whereas as the environmental conditions for the biogenic crystals used in Kabalah-Amitai et al.'s study[208] must have favoured the formation of the hexagonal layer stacking without excluding the formation of other structures.

Additionally we have shown that the short range information provided by solid state NMR in conjunction with complementary GIPAW-DFT based calculations provides sufficient information to distinguish between these basins to elucidate the average nature of the vaterite structure on larger length scales. By this combined approach, other vaterite samples should be able to be fully characterised in accordance with the low energy superbasins.

8

SUMMARY OF CONCLUSIONS

One of the major impetuses behind the work reported in this thesis was to investigate computationally tractable methods of incorporating partial occupancy disorder in *ab initio* Density Functional Theory (DFT) calculations for the nuclear magnetic resonance (NMR) parameters with the aim of establishing a protocol for routinely tackling this category of problem. In chapter 4 a simple DFT investigation into the Ge-based apatite $La_{7.5}Ca_{2.5}Ge_6O_{25.75}$ was reported where the partial occupancy disorder was modelled using a wholly enumerative approach where every realisation commensurate with the fractional occupancy of the lattice sites was generated and optimized by conventional DFT geometry optimization. GIPAW NMR calculation methods were then applied to each realisation. This approach is compared to the site occupancy disorder (SOD)[16] approach, used to reduce the configurational space one needs to consider by eliminating configurations which are identical by symmetry. Those that can be related in such a manner are considered equivalent and attributed a corresponding degeneracy. For the particular apatite system under consideration it is shown that the SOD approach can be used to halve the number of configurations one needs to consider for an equivalent level of accuracy. However, it is shown that the approximations to the fractional occupancies described in the unit cell that are necessary to be commensurate with the number of lattice sites in a unit cell restrict the configurational space such that it can never fully characterize the true extent of the positional disorder in these samples. A more faithful reproduction of the fractional occupancies can be obtained by considering the distribution of cations within a supercell, however even when this approach is undertaken with SOD the configurational space is seen to grow prohibitively large very quickly. In spite of this limitation for the simple approximation to the fractional occupancy considered the major structural motifs of the experimental NMR spectrum can be modelled by this route.

It can be additionally observed that the highest energy realisations correlate with simulated NMR spectra that have a negligible contribution to the bulk NMR spectrum. Thus, neglecting these high-energy structures could further reduce the configurational space. Thus for partial occupancy problems we propose that the configurational space should be generated using SOD and further sifted by 'cheaply' geometry optimising the structures. Then the total energies of the geometry-optimised structures can be used to establish a subset of relevant structures that should be extensively characterized.

This method is applied to the $K_{0.3}Na_{0.7}NbO_3$ structure (icsd – 173740) described in chapter 5. In this case it was implemented as an accuracy calibration for a GIPAW-DFT CASTEP[11] approach to the KNN system. The SOD program was employed to create a set of representative supercell configurations that were compatible with the fractional occupancy for the A-sublattice cation environments. The total energy of each realization was then combined with the degeneracy of each structure as output by SOD to calculate a probability for each of the structures. From this information we could sift the complete SOD configurational space for structures with a significant contribution to the NMR spectra: this process suggested that a subset of eight configurations was necessary to capture ~95% of the probability distribution.

The low energy structures for the $K_{0.3}Na_{0.7}NbO_3$ system showed a tendency towards potassium clustering on the (010) plane. This physical phenomenon was necessary to obtain the full extent of the strong linear correlation between δ_{iso} and C_Q for ^{23}Na recorded experimentally as the presence of potassium in the next-nearest neighbour coordination sphere inhibits the tilting in the Nb octahedral units. Accordingly this is evidence of short-range ordering for at least one point within the KNN phase diagram at room temperature.

Chapter 5 is an attempt to assess the suitability of the Special Quasi Random (SQS) approach to modelling partial structural disorder in the context of sodium potassium niobate (KNN). This approach assumes that that there is an approximately random distribution of K/Na on the A sublattice of the ABO_3 perovskite structure. Based on the previous information it appears that this is invalid for at least one point in the KNN phase diagram under ambient conditions. Nonetheless the SQS approach was investigated for its potential to predict spectra of this functional material across the phase diagram at room temperature as it represents a much cheaper alternative to more conventional supercell approaches. A workflow was developed that uses the tools to

generate SQS[17] input structures for the calculation of NMR parameters from first principle quantum mechanical calculations.

Though a substantial series of exemplar calculations were performed a number of issues were illustrated that have questioned the applicability of the method to the KNN system. These additional difficulties were associated with the complex tilting patterns present in these materials at the sodium-rich side of the phase diagram, to which the NMR parameters are highly sensitive.

Consequently, while some of the general trends of the NMR spectra over the phase diagram were reproduced, systematic errors that were attributed to these tilting patterns have prevented a true assessment of the validity of the SQS method and further work is needed before the suitability of this method can be unequivocally appraised.

The final chapter was on the structural elucidation of vaterite that is the least stable crystalline polymorph of anhydrous $CaCO_3$. Though vaterite was identified as a unique form of calcium carbonate over a century ago and has undergone extensive research in the past half-century, at the point of investigation there was no consensus on vaterite's space group, unit cell parameters or carbonate orientations. A large number of possible structures have been proposed in the literature (see section 6.2) that could be split into three lattice families; hexagonal, monoclinic and orthorhombic.

In the past few years the paradigm that vaterite was a single crystal had been brought into question.[208] Indeed theoretical studies have shown that not only are there many possible stable structures for vaterite at room temperature, but that many of these structures are within thermal energy of one another leading Demichelis *et al* [205] to postulate that the structures are able to interconvert at room temperature via carbonate rotations. Subsequent studies by Demichelis *et al*[22] identified stacking faults as an additional source of disorder within the vaterite crystal. Three possible near-isoenergetic stacking models were identified that describe a superbasin containing subbasins corresponding to structures from a particular lattice family that are able to interconvert at room temperature via carbonate rotations. However, there had been no experimental evidence for such processes occurring at room temperature and indeed De La Pierre *et al*'s[245] theoretical Raman investigation and Burgess *et al*'s[198] ^{43}Ca ssNMR studies found that only the *P*3221 and *C*2 structures were consistent with the experimental data, which directly contradicts the room temperature intrabasin structural interconversion suggested by Demichelis *et al*[22].

Given the ability of solid-state NMR to probe short-range nuclear environments it was considered appropriate to study the disorder in the vaterite system in the hope of finally offering experimental verification for the current models of vaterite. A ^{17}O isotopically enriched synthetic vaterite sample was made as outlined in Shivkumara et al. (2006).[215]

Due to the anisotropic nature of the NMR interactions that leads to spectral broadening a number of different techniques were employed to study the synthetic vaterite sample. For quadrupolar nuclei (I>1/2) like ^{17}O the resolution under MAS is limited by quadrupolar broadening. The two-dimensional 3Q-MAS experimental technique was employed in order to remove this inhomogeneous quadrupolar broadening allowing the identification of six different oxygen environments. A post-processing technique called MQ-MAS inversion[62] was employed to extract estimates for the site populations as described by the 3Q-MAS experiment. This can be considered a reliable exercise in this case as the quadrupolar coupling constants for the inequivalent oxygen environments have a narrow window of variation and the inversion technique is able to compensate for erroneous distortions in the spectrum due to inefficiency in the coherence transfers involved in the 3Q-MAS experiment.

DOR[70] is an alternative technique that can be used to remove the influence of anisotropic quadrupolar interaction from the NMR spectrum with the additional advantage that, if the resolution is sufficient across multiple field acquisitions, it allows for the extraction of the isotropic chemical shift and quadrupolar product. This confirmed that the six sites identified via the 3Q-MAS were the minimum number of oxygen environments needed to faithfully represent the experimental spectral intensity. For the current models of vaterite the number of inequivalent oxygen environments in the unit cell varies between 3-54 and no two structures can be combined to give six inequivalent oxygen environments. Thus it appears that the level of detail needed to unambiguously assign the complete set of inequivalent oxygen environments in the vaterite unit cell is beyond the spectroscopic limit.

In order to bypass this limitation the experimental data was instead used as a constraint for a simulation of the solid-state NMR spectra using the *ab initio* DFT code CASTEP[94]. NMR parameters were generated for the theoretical structures proposed in the literature. In particular the NMR signature of each unique crystallographic form was used to simulate its corresponding DOR spectrum. A parallel application of this process to both calcite and aragonite (lower energy polymorphs of $CaCO_3$) showed that by

including both the chemical shift anisotropy and the quadrupolar interaction in the simulation of the data the experimental lineshape could be reproduced to a very high standard of accuracy. Using this method it was shown that no single unique crystallographic form of vaterite as proposed in the literature satisfied the ^{17}O experimental DOR spectra.

The room temperature intrabasin structural interconversion model proposed by Demichelis et al[22] means that on the basis of a CO_3^{2-} rotation mechanism we would expect different domains to be present in the same crystal so that peaks from all structures would contribute to the bulk spectrum. To establish the validity of such stacking models their ^{17}O signals were simulated via a Boltzmann weighted superposition of the individual spectra. It was shown that the synthetic vaterite sample under investigation is well characterized by the 2-layer monoclinic isoenergetic basin with absolute minimum energy structure with C2 symmetry space group. Additionally the oxygen environments in the 2-layer monoclinic model for vaterite can be split into groups according to the six resonances observed experimentally. This exercise shows that there is strong correlation between the theoretical and experimental (MAS, 3Q-MAS) populations for each of these six sites. Comparing ^{13}C ssNMR data with spectral simulations further corroborates this finding. Note that this is in contrast to high profile publications on a biogenic sample of vaterite that was assigned to a predominantly hexagonal structure interspersed with an unknown second structure.[208] This raises the intriguing prospect that the structural form of vaterite is highly dependent on the experimental conditions in which it is formed.

Notably modelling the stacking model via the Boltzmann weighted average requires the inclusion of the *C*2/*c* metastable structure that represents a transition structure between the two stable structures (*C*2 and *Cc*) in the 2-layer monoclinic stacking model and therefore represents the first experimental evidence for structural transition within the basin.

Earlier in this chapter two independent studies were referred to that have separately simulated Raman and ^{43}Ca ssNMR data for vaterite. [245,198] Both of these studies highlighted that the *P*3221 and *C*2 structures are the only structures that are compatible with the observed spectra, though neither are able to discriminate as to whether the first, the second or both structures are present in the experimental sample. The simulated spectra for these structures would also be reasonable, but incompletely match the experimental data. Nonetheless they would appear to suggest that the systems

could become kinetically trapped in subsets of possible stable structures as opposed to the dynamic system Demichelis *et al* have proposed at room temperature. While the study on synthetic vaterite described in this thesis requires a contribution from the *C*2 structure it has enough resolution to prove the additional importance of the *C*2/*c* and *Cc* structures to the vaterite system. However, the dynamic aspect of the vaterite system merits further experimental investigation to understand this process in more detail. Indeed if the vaterite system is dynamic then variable temperature experiments should be completed to determine whether the observed lineshape is impacted by any slow exchange processes due to the interconversion between structures within the basins. Recent studies have shown the possible applicability of two-dimensional chemical exchange spectra for powders containing half-integer quadrupolar nuclei that evolve under the second-order quadrupolar interaction.[246] Such two-dimensional exchange powder spectra are a standard technique for analysing molecular dynamics in a wide range of solids [247,248] using spin-1/2 and spin-1 probe nuclei. Two-dimensional chemical exchange experiments follow the general pulse sequence $\frac{\pi}{2} - t_1 - \frac{\pi}{2} - t_{mixing} - \frac{\pi}{2} - t_2$ such that when a sufficiently large mixing time (t_{mixing}) is employed, off-diagonal intensities in the 2D contour plots indicate the occurrence of exchange processes.

A major advantage of using this experiment on ^{17}O is that the T1s are relatively large, thus a relatively large mixing time up to several seconds could be exploited. If no exchange occurs then all of the spectra intensity will be focused along the diagonal of the spectrum, however if exchange occurs then off-diagonal peaks will appear with features that will be related to the symmetry of the motions due to the change of the quadrupolar tensor from one local geometry to another that will alter the precession frequency ω. While such peaks could appear due to magnetization exchange between the sites with a controlled level of enrichment (such that the ^{17}O are sufficiently dilute analogous to the use of ^{6}Li in the Lithium Zirconate sample studied in ref - 249) then this can be mitigated against. Application of this technique to vaterite is deferred to future work.

APPENDIX

SUPPLEMENTARY INFORMATION FOR STRUCTURAL SSNMR STUDIES

A.1 Supplementary Tables for Chapter 7

Table A.1 Selected structural parameters obtained upon relaxing the positions of all ions to their minimum energy configuration with the unit cell parameters constrained to their experimental values and unconstrained whilst employing the CASTEP8 default pseudopotentials in conjunction with the PBEsol functional and the modified-Ca pseudopotential in conjunction with the PBE functional.

Functional - PBEsol

Pseudopotentials - CASTEP8

Calcite	*Expt.*	*Calc.(constrained lattice)*	*%diff*	*Calc.(unconstrained lattice)*	*%diff*
a/Å	4.9910	-	-	4.9910	0.0
c/ Å	17.062	-	-	16.895	1.0
C-O/ Å	1.2842	1.2917	-0.6	1.2912	-0.5
Ca-O/ Å	2.3590	2.3551	0.2	2.3470	0.5
Aragonite	*Expt.*	*Calc.(constrained lattice)*	*%diff*	*Calc.(unconstrained lattice)*	*%diff*
a/ Å	4.9596	-	-	4.942	0.4
b/ Å	7.9644	-	-	7.932	0.4
c/ Å	5.7416	-	-	5.658	1.5
C-O1/ Å	1.2741	1.2850	-0.9	1.2839	-0.8
C-O2/ Å	1.2855	1.2937	-0.6	1.2924	-0.5
$Ca\text{-}O_{min}$/ Å	2.4165	2.4040	0.3	2.3803	1.5
$Ca\text{-}O_{max}$/ Å	2.6527	2.6532	0.0	2.6399	0.5
$Ca\text{-}O_{av}$/ Å	2.5121	2.5097	0.1	2.4908	0.8

Functional - PBE

Pseudopotentials - Ca-shifted pseudopotential, CASTEP8 (C, O)

Calcite	*Expt.*	*Calc.(constrained lattice)*	*%diff*	*Calc.(unconstrained lattice)*	*%diff*
a/ Å	4.9910	-	-	5.1340	-2.9
c/ Å	17.0620	-	-	17.7020	-3.8
C-O/ Å	1.2842	1.2880	-0.3	1.2965	-1.0
Ca-O/ Å	2.3590	2.3570	0.1	2.4468	-3.7
Aragonite	*Expt.*	*Calc.(constrained lattice)*	*%diff*	*Calc.(unconstrained lattice)*	*%diff*
a/ Å	4.9596	-	-	4.9420	0.4
b/ Å	7.9644	-	-	7.9320	0.4
c/ Å	5.7416	-	-	5.6580	1.5
C-O1/ Å	1.2741	1.2850	-0.9	1.2839	-0.8
C-O2/ Å	1.2855	1.2937	-0.6	1.2924	-0.5
$Ca\text{-}O_{min}$/ Å	2.4165	2.4099	0.3	2.3803	1.5
$Ca\text{-}O_{max}$/ Å	2.6527	2.6532	0.0	2.6399	0.5

BIBLIOGRAPHY

1. Harris, R. K.; Wasylishen, R. E.; Duer, M. J., *NMR Crystallography*. 2009.
2. Balimann, G. E.; Groombridge, C. J.; Harris, R. K.; Packer, K. J.; Say, B. J.; Tanner, S. F., CHEMICAL APPLICATIONS OF HIGH-RESOLUTION C-13 NMR-SPECTRA FOR SOLIDS. *Philosophical Transactions of the Royal Society a-Mathematical Physical and Engineering Sciences* **1981,** *299* (1452), 643-663.
3. Gaudin, E.; Boucher, F.; Evain, M.; Taulelle, F., NMR selection of space groups in structural analysis of Ag7PSe6. *Chemistry of Materials* **2000,** *12* (6), 1715-1720.
4. Fyfe, C. A.; Gies, H.; Kokotailo, G. T.; Marler, B.; Cox, D. E., CRYSTAL-STRUCTURE OF SILICA-ZSM-12 BY THE COMBINED USE OF HIGH-RESOLUTION SOLID-STATE MAS NMR-SPECTROSCOPY AND SYNCHROTRON X-RAY-POWDER DIFFRACTION. *Journal of Physical Chemistry* **1990,** *94* (9), 3718-3721.
5. Harper, J. K.; Grant, D. M.; Zhang, Y. G.; Lee, P. L.; Von Dreele, R., Characterizing challenging microcrystalline solids with solid-state NMR shift tensor and synchrotron X-ray powder diffraction data: Structural analysis of ambuic acid. *Journal of the American Chemical Society* **2006,** *128* (5), 1547-1552.
6. Harper, J. K.; Doebbler, J. A.; Jacques, E.; Grant, D. M.; Von Dreele, R. B., A Combined Solid-State NMR and Synchrotron X-ray Diffraction Powder Study on the Structure of the Antioxidant (+)-Catechin 4.5-hydrate. *Journal of the American Chemical Society* **2010,** *132* (9), 2928-2937.
7. Brouwer, D. H.; Moudrakovski, I. L.; Darton, R. J.; Morris, R. E., Comparing quantum-chemical calculation methods for structural investigation of zeolite crystal structures by solid-state NMR spectroscopy. *Magnetic Resonance in Chemistry* **2010,** *48*, S113-S121.
8. Ramsey, N. F., The Internal Diamagnetic Field Correction in Measurements of the Proton Magnetic Moment. *Physical Review* **1950,** *77* (4), 567-567.
9. Ramsey, N. F., Magnetic Shielding of Nuclei in Molecules. *Physical Review* **1950,** *78* (6), 699-703.
10. Ramsey, N. F., Electron Coupled Interactions between Nuclear Spins in Molecules. *Physical Review* **1953,** *91* (2), 303-307.
11. Pickard, C. J.; Mauri, F., All-electron magnetic response with pseudopotentials: NMR chemical shifts. *Physical Review B* **2001,** *63* (24).
12. Dutour, J.; Guillou, N.; Huguenard, C.; Taulelle, F.; Mellot-Draznieks, C.; Ferey, G., Chiolite, a case study for combining NMR crystallography, diffraction and structural simulation. *Solid State Sciences* **2004,** *6* (10), 1059-1067.
13. Brouwer, D. H.; Darton, R. J.; Morris, R. E.; Levitt, M. H., A solid-state NMR method for solution of zeolite crystal structures. *Journal of the American Chemical Society* **2005,** *127* (29), 10365-10370.
14. Laws, D. D.; Bitter, H. M. L.; Jerschow, A., Solid-state NMR spectroscopic methods in chemistry. *Angewandte Chemie-International Edition* **2002,** *41* (17), 3096-3129.
15. Bonhomme, C.; Gervais, C.; Babonneau, F.; Coelho, C.; Pourpoint, F.; Azais, T.; Ashbrook, S. E.; Griffin, J. M.; Yates, J. R.; Mauri, F.; Pickard, C. J., First-Principles Calculation of NMR Parameters Using the Gauge Including Projector Augmented Wave Method: A Chemist's Point of View. *Chemical Reviews* **2012,** *112* (11), 5733-5779.
16. Grau-Crespo, R.; Hamad, S.; Catlow, C. R. A.; de Leeuw, N. H., Symmetry-adapted configurational modelling of fractional site occupancy in solids. *Journal of Physics-Condensed Matter* **2007,** *19* (25), 16.
17. Zunger, A.; Wei, S. H.; Ferreira, L.; Bernard, J., Special quasirandom structures. *Physical Review Letters* **1990,** *65* (3), 353-356.
18. Sanchez, J. M.; Ducastelle, F.; Gratias, D., GENERALIZED CLUSTER DESCRIPTION OF MULTICOMPONENT SYSTEMS. *Physica A* **1984,** *128* (1-2), 334-350.
19. deFontaine, D., Cluster approach to order-disorder transformations in alloys. *Solid State Physics - Advances in Research and Applications, Vol 47* **1994,** *47*, 33-176.

20. Zunger, A., First-Principles Statistical Mechanics of Semiconductor Alloys and Intermetallic Compounds. In *Statics and Dynamics of Alloy Phase Transformations*, Turchi, P. A.; Gonis, A., Eds. Springer US: 1994; Vol. 319, pp 361-419.
21. Kamhi, S. R., On the Structure of CaCO3. *Acta Cryst.* **1963,** *16*, 770-772.
22. Demichelis, R.; Raiteri, P.; Gale, J. D.; Dovesi, R., The Multiple Structures of Vaterite. *Crystal Growth & Design* **2013,** *13* (6), 2247-2251.
23. Bloch, F.; Hansen, W. W.; Packard, M., Nuclear Induction. *Physical Review* **1946,** *69* (3-4), 127-127.
24. Purcell, E. M.; Torrey, H. C.; Pound, R. V., Resonance Absorption by Nuclear Magnetic Moments in a Solid. *Physical Review* **1946,** *69* (1-2), 37-38.
25. Virlet, J., Line Narrowing Methods in Solids. In *eMagRes*, John Wiley & Sons, Ltd: 2007.
26. Lesage, A., Recent advances in solid-state NMR spectroscopy of spin I = 1/2 nuclei. *Physical Chemistry Chemical Physics* **2009,** *11* (32), 6876-6891.
27. Duer, M. J., *Solid-State NMR Spectroscopy: Principles and Applications*. Blackwell Science: 2002.
28. Ashbrook, S. E., Recent advances in solid-state NMR spectroscopy of quadrupolar nuclei. *Physical Chemistry Chemical Physics* **2009,** *11* (32), 6892-6905.
29. Mehring, M., *Principles of high resolution NMR in solids*. Springer: Berlin, 1983.
30. Slichter, C. P., *Principles of magnetic resonance*. Springer: Berlin, 1990.
31. Smith, M. E.; Eck, E. R. H. v., Recent advances in experimental solid state NMR methodology for half-integer spin quadrupolar nuclei. *Progress in Nuclear Magnetic Resonance Spectroscopy* **1999,** *34*, 159-201.
32. Vega, A. J., Quadrupolar Nuclei in Solids. In *eMagRes*, John Wiley & Sons, Ltd: 2007.
33. Jerschow, A., From nuclear structure to the quadrupolar NMR interaction and high-resolution spectroscopy. *Progress in Nuclear Magnetic Resonance Spectroscopy* **2005,** *46* (1), 63-78.
34. Dybowski, C., Zeeman Interaction in Nuclear Magnetic Resonance. **2006**.
35. Facelli, J. C.; Orendt, A. M., Magnetic Shielding and Chemical Shifts: Basics. In *eMagRes*, John Wiley & Sons, Ltd: 2007.
36. Front Matter. In *High Resolution Nmr in Solids Selective Averaging*, Haeberlen, U., Ed. Academic Press: 1976; p iii.
37. Harris, R. K.; Becker, E. D.; De Menezes, S. M. C.; Goodfellow, R.; Granger, P., NMR nomenclature. Nuclear spin properties and conventions for chemical shifts - (IUPAC recommendations 2001). *Pure and Applied Chemistry* **2001,** *73* (11), 1795-1818.
38. Harris, R. K.; Becker, E. D.; De Menezes, S. M. C.; Granger, P.; Hoffman, R. E.; Zilm, K. W., Further conventions for NMR shielding and chemical shifts (IUPAC recommendations 2008). *Pure and Applied Chemistry* **2008,** *80* (1), 59-84.
39. Tossell, J. A., Correlation of 29SiNuclear Magnetic Resonance Chemical Shifts in Silicates with Orbital Energy Differences Obtained from X-ray Spectra. *Physical Chemisty Minerals* **1984,** *10*, 137-141.
40. Kirkpatrick, R. J., MAS NMR-SPECTROSCOPY OF MINERALS AND GLASSES. *Reviews in Mineralogy* **1988,** *18*, 341-403.
41. Carroll, D. L. A Multi-Analytical Investigation into Glass Dopant Incorporation Warwick, 2008.
42. Man, P. P., Quadrupolar Interactions. In *eMagRes*, John Wiley & Sons, Ltd: 2007.
43. Ashbrook, S. E.; Wimperis, S., Quadrupolar Coupling: An Introduction and Crystallographic Aspects. In *eMagRes*, John Wiley & Sons, Ltd: 2007.
44. Harris, R. K., *Nuclear magnetic resonance spectroscopy*. 1986; p Medium: X; Size: Pages: 272.
45. Andrew, E. R.; Bradbury, A.; Eades, R. G., Nuclear Magnetic Resonance Spectra from a Crystal rotated at High Speed. *Nature* **1958,** *182* (4650), 1659-1659.
46. Tzalmona, A.; Andrew, E. R., *Magnetic Resonance and Related Phenomena*. North-Holland, Amsterdam, 1975.
47. Ackerman, J. L.; Eckman, R.; Pines, A., EXPERIMENTAL RESULTS ON DEUTERIUM NMR IN THE SOLID-STATE BY MAGIC ANGLE SAMPLE SPINNING. *Chemical Physics* **1979,** *42* (3), 423-428.

48. Goldbourt, A.; Madhu, P. K., Multiple-quantum magic-angle spinning: High-resolution solid state NMR Spectroscopy of half-integer quadrupolar nuclei. *Monatshefte Fur Chemie* **2002,** *133* (12), 1497-1534.
49. Brown, S. P.; Wimperis, S., Two-dimensional multiple-quantum MAS NMR of quadrupolar nuclei: A comparison of methods. *Journal of Magnetic Resonance* **1997,** *128* (1), 42-61.
50. Ashbrook, S. E. New NMR Techniques for the Study of Quadrupolar Nuclei. Oxford, 2000.
51. Lamley, J. M. Methods for the Determination of the Structures and Dynamics of Proteins by Solid-State NMR Spectroscopy. Warwick, 2015.
52. Solomon, I., Multiple Echoes in Solids. *Physical Review* **1958,** *110* (1), 61-65.
53. Man, P. P., Excitation conditions for quantitative determination of quadrupolar spins with one pulse or spin-echo sequences in solid-state NMR. *Applied Magnetic Resonance* **1993,** *4*, 65-87.
54. Haase, J.; Oldfield, E., Excitation conditions for quantitative determination of quadrupolar spins with one pulse or spin-echo sequences in solid-state NMR. *Journal of Magnetic Resonance* **1993,** *104*, 1-9.
55. Frydman, L.; Harwood, J. S., ISOTROPIC SPECTRA OF HALF-INTEGER QUADRUPOLAR SPINS FROM BIDIMENSIONAL MAGIC-ANGLE-SPINNING NMR. *Journal of the American Chemical Society* **1995,** *117* (19), 5367-5368.
56. Amoureux, J.-P.; Pruski, M., MQMASNMR: Experimental Strategies and Applications. In *eMagRes*, John Wiley & Sons, Ltd: 2007.
57. Amoureux, J. P.; Fernandez, C.; Steuernagel, S., Z filtering in MQMAS NMR. *Journal of Magnetic Resonance Series A* **1996,** *123* (1), 116-118.
58. Marion, D.; Wuthrich, K., APPLICATION OF PHASE SENSITIVE TWO-DIMENSIONAL CORRELATED SPECTROSCOPY (COSY) FOR MEASUREMENTS OF H-1-H-1 SPIN-SPIN COUPLING-CONSTANTS IN PROTEINS. *Biochemical and Biophysical Research Communications* **1983,** *113* (3), 967-974.
59. States, D. J.; Haberkorn, R. A.; Ruben, D. J., A TWO-DIMENSIONAL NUCLEAR OVERHAUSER EXPERIMENT WITH PURE ABSORPTION PHASE IN 4 QUADRANTS. *Journal of Magnetic Resonance* **1982,** *48* (2), 286-292.
60. Bax, A.; Mehlkopf, A. F.; Smidt, J., Absorption spectra from phase-modulated spin echoes. *Journal of Magnetic Resonance (1969)* **1979,** *35* (3), 373-377.
61. Massiot, D.; Touzo, B.; Trumeau, D.; Coutures, J. P.; Virlet, J.; Florian, P.; Grandinetti, P. J., Two-dimensional magic-angle spinning isotropic reconstruction sequences for quadrupolar nuclei. *Solid State Nuclear Magnetic Resonance* **1996,** *6* (1), 73-83.
62. Zwanziger, J. W., INTERPRETING NUCLEAR-MAGNETIC-RESONANCE SPECTRA OF DISORDERED MATERIALS - DIRECT INVERSION OF POWDER PATTERNS. *Solid State Nuclear Magnetic Resonance* **1994,** *3* (4), 219-229.
63. Angeli, F.; Charpentier, T.; Faucon, P.; Petit, J. C., Structural characterization of glass from the inversion of Na-23 and Al-27 3Q-MAS NMR spectra. *Journal of Physical Chemistry B* **1999,** *103* (47), 10356-10364.
64. Angeli, F.; Delaye, J. M.; Charpentier, T.; Petit, J. C.; Ghaleb, D.; Faucon, P., Influence of glass chemical composition on the Na-O bond distance: a (23)Na 3Q-MAS NMR and molecular dynamics study. *Journal of Non-Crystalline Solids* **2000,** *276* (1-3), 132-144.
65. Pedone, A.; Charpentier, T.; Malavasi, G.; Menziani, M. C., New Insights into the Atomic Structure of 45S5 Bioglass by Means of Solid-State NMR Spectroscopy and Accurate First-Principles Simulations. *Chemistry of Materials* **2010,** *22* (19), 5644-5652.
66. Angeli, F.; Delaye, J. M.; Charpentier, T.; Petit, J. C.; Ghaleb, D.; Faucon, P., Investigation of A1-O-Si bond angle in glass by Al-27 3Q-MAS NMR and molecular dynamics. *Chemical Physics Letters* **2000,** *320* (5-6), 681-687.
67. Llor, A.; Virlet, J., TOWARDS HIGH-RESOLUTION NMR OF MORE NUCLEI IN SOLIDS - SAMPLE SPINNING WITH TIME-DEPENDENT SPINNER AXIS ANGLE. *Chemical Physics Letters* **1988,** *152* (2-3), 248-253.
68. Samoson, A.; Lippmaa, E.; Pines, A., HIGH-RESOLUTION SOLID-STATE NMR AVERAGING OF 2ND-ORDER EFFECTS BY MEANS OF A DOUBLE-ROTOR. *Molecular Physics* **1988,** *65* (4), 1013-1018.

69. Samoson, A.; Lippmaa, E., SYNCHRONIZED DOUBLE-ROTATION NMR-SPECTROSCOPY. *Journal of Magnetic Resonance* **1989,** *84* (2), 410-416.
70. Dupree, R., Double Rotation NMR. *John Wiley & Sons, Ltd* **2007**.
71. MacDonald, J. F. Multinuclear Solid State NMR Studies of α-Tricalcium Phosphate and Silicon Substituted α-Tricalcium Phosphate. Warwick, 2012.
72. Hung, I.; Wong, A.; Howes, A. P.; Anupold, T.; Past, J.; Samoson, A.; Mo, X.; Wu, G.; Smith, M. E.; Brown, S. P.; Dupree, R., Determination of NMR interaction parameters from double rotation NMR. *Journal of Magnetic Resonance* **2007,** *188* (2), 246-259.
73. Martin, R. M., *Electronic Structure: Basic Theory and Practical Methods*. Cambridge University Press: 2004.
74. Bellaiche, L.; Vanderbilt, D., Virtual crystal approximation revisited: Application to dielectric and piezoelectric properties of perovskites. *Physical Review B* **2000,** *61* (12), 7877-7882.
75. Kohn, W.; Sham, L. J., Self-Consistent Equations Including Exchange and Correlation Effects. *Physical Review* **1965,** *140*.
76. van de Walle, A.; Ceder, G., Correcting overbinding in local-density-approximation calculations. *Physical Review B* **1999,** *59* (23), 14992-15001.
77. Koch, W.; Holthausen, M. C., *A chemist's guide to density functional theory*. Wiley-VCH: 2000.
78. Perdew, J. P.; Burke, K.; Ernzerhof, M., Generalized gradient approximation made simple. *Physical Review Letters* **1996,** *77* (18), 3865-3868.
79. Perdew, J. P.; Ruzsinszky, A.; Csonka, G. I.; Vydrov, O. A.; Scuseria, G. E.; Constantin, L. A.; Zhou, X. L.; Burke, K., Restoring the density-gradient expansion for exchange in solids and surfaces. *Physical Review Letters* **2008,** *100* (13), 4.
80. Chadi, D. J.; Cohen, M. L., Special Points in the Brillouin Zone. *Physical Review B* **1973,** *8*, 5747.
81. Monkhorst, H. J.; Pack, J. D., Special points for Brillouin-zone integrations. *Physical Review B* **1976,** *13*, 5188.
82. Methfessel, M.; Paxton, A. T., HIGH-PRECISION SAMPLING FOR BRILLOUIN-ZONE INTEGRATION IN METALS. *Physical Review B* **1989,** *40* (6), 3616-3621.
83. Jensen, F., *Introduction to Computational Chemistry*. Wiley: 2007.
84. Ashcroft, N. W.; Mermin, N. D., *Solid state physics*. Holt, Rinehart and Winston: New York, 1976.
85. Payne, M. C.; Teter, M. P.; Allan, D. C.; Arias, T. A.; Joannopoulos, J. D., ITERATIVE MINIMIZATION TECHNIQUES FOR ABINITIO TOTAL-ENERGY CALCULATIONS - MOLECULAR-DYNAMICS AND CONJUGATE GRADIENTS. *Reviews of Modern Physics* **1992,** *64* (4), 1045-1097.
86. Kohanoff, J., *Electronic Structure Calculations for Solids and Molecules: Theory and Computational Methods*. Cambridge University Press: 2006.
87. Gregor, T.; Mauri, F.; Car, R., A comparison of methods for the calculation of NMR chemical shifts. *Journal of Chemical Physics* **1999,** *111* (5), 1815-1822.
88. Truflandier, L.; Paris, M.; Boucher, F., Density functional theory investigation of 3d transition metal NMR shielding tensors in diamagnetic systems using the gauge-including projector augmented-wave method. *Physical Review B* **2007,** *76* (3), 17.
89. Pickard, C. J.; Needs, R. J., Dense Low-Coordination Phases of Lithium. *Physical Review Letters* **2009,** *102* (14), 4.
90. Hamann, D. R.; Schluter, M.; Chiang, C., NORM-CONSERVING PSEUDOPOTENTIALS. *Physical Review Letters* **1979,** *43* (20), 1494-1497.
91. Bachelet, G. B.; Hamann, D. R.; Schluter, M., PSEUDOPOTENTIALS THAT WORK - FROM H TO PU. *Physical Review B* **1982,** *26* (8), 4199-4228.
92. Kleinman, L.; Bylander, D. M., EFFICACIOUS FORM FOR MODEL PSEUDOPOTENTIALS. *Physical Review Letters* **1982,** *48* (20), 1425-1428.
93. Vanderbilt, D., SOFT SELF-CONSISTENT PSEUDOPOTENTIALS IN A GENERALIZED EIGENVALUE FORMALISM. *Physical Review B* **1990,** *41* (11), 7892-7895.
94. Clark, S. J.; Segall, M. D.; Pickard, C. J.; Hasnip, P. J.; Probert, M. J.; Refson, K.; Payne, M. C., First principles methods using CASTEP. *Zeitschrift Fur Kristallographie* **2005,** *220* (5-6), 567-570.

95. Van De Walle, C. G.; Blochl, P. E., 1ST-PRINCIPLES CALCULATIONS OF HYPERFINE PARAMETERS. *Physical Review B* **1993,** *47* (8), 4244-4255.
96. Snyman, J., *Practical Mathematical Optimization: An Introduction to Basic Optimization Theory and Classical and New Gradient-Based Algorithms*. Springer: 2005.
97. Nocedal, J.; Wright, S., *Numerical Optimization*. Springer New York: 2006.
98. Probert, M. I. J., Improved algorithm for geometry optimisation using damped molecular dynamics. *Journal of Computational Physics* **2003,** *191* (1), 130-146.
99. Dumez, J.-N.; Pickard, C. J., Calculation of NMR chemical shifts in organic solids: Accounting for motional effects. *Journal of Chemical Physics* **2009,** *130* (10).
100. Profeta, M.; Mauri, F.; Pickard, C. J., Accurate first principles prediction of O-17 NMR parameters in SiO2: Assignment of the zeolite ferrierite spectrum. *Journal of the American Chemical Society* **2003,** *125* (2), 541-548.
101. Laskowski, R.; Blaha, P., Calculations of NMR chemical shifts with APW-based methods. *Physical Review B* **2012,** *85* (3), 12.
102. Ashbrook, S. E.; Le Polles, L.; Gautier, R.; Pickard, C. J.; Walton, R. I., Na-23 multiple-quantum MAS NMR of the perovskites NaNbO3 and NaTaO3. *Physical Chemistry Chemical Physics* **2006,** *8* (29), 3423-3431.
103. Hanna, J. V.; Pike, K. J.; Charpentier, T.; Kemp, T. F.; Smith, M. E.; Lucier, B. E. G.; Schurko, R. W.; Cahill, L. S., A Nb-93 Solid-State NMR and Density Functional Theory Study of Four- and Six-Coordinate Niobate Systems. *Chemistry-a European Journal* **2010,** *16* (10), 3222-3239.
104. Mauri, F.; Pfrommer, B. G.; Louie, S. G., Ab initio theory of NMR chemical shifts in solids and liquids. *Physical Review Letters* **1996,** *77* (26), 5300-5303.
105. Giacovazzo, C., *Fundamentals of crystallography*. Oxford University Press: 2002.
106. Sanchez, J. M., Cluster expansion and the configurational theory of alloys. *Physical Review B* **2010,** *81* (22), 13.
107. Cadars, S.; Lesage, A.; Pickard, C. J.; Sautet, P.; Emsley, L., Characterizing Slight Structural Disorder in Solids by Combined Solid-State NMR and First Principles Calculations. *Journal of Physical Chemistry A* **2009,** *113* (5), 902-911.
108. Charpentier, T.; Kroll, P.; Mauri, F., First-Principles Nuclear Magnetic Resonance Structural Analysis of Vitreous Silica. *Journal of Physical Chemistry C* **2009,** *113* (18), 7917-7929.
109. Charpentier, T.; Ispas, S.; Profeta, M.; Mauri, F.; Pickard, C. J., First-principles calculation of O-17, Si-29, and Na-23 NMR spectra of sodium silicate crystals and glasses. *Journal of Physical Chemistry B* **2004,** *108* (13), 4147-4161.
110. Ashbrook, S. E.; Dawson, D. M., Exploiting periodic first-principles calculations in NMR spectroscopy of disordered solids. *Accounts of chemical research* **2013,** *46* (9), 1964-74.
111. Neugebauer, J.; Hickel, T., Density functional theory in materials science. *Wiley Interdisciplinary Reviews-Computational Molecular Science* **2013,** *3* (5), 438-448.
112. Makov, G.; Payne, M. C., PERIODIC BOUNDARY-CONDITIONS IN AB-INITIO CALCULATIONS. *Physical Review B* **1995,** *51* (7), 4014-4022.
113. Lany, S.; Zunger, A., Assessment of correction methods for the band-gap problem and for finite-size effects in supercell defect calculations: Case studies for ZnO and GaAs. *Physical Review B* **2008,** *78* (23), 25.
114. Freysoldt, C.; Neugebauer, J.; Van de Walle, C. G., Fully Ab Initio Finite-Size Corrections for Charged-Defect Supercell Calculations. *Physical Review Letters* **2009,** *102* (1), 4.
115. Yates, J. R.; Dobbins, S. E.; Pickard, C. J.; Mauri, F.; Ghi, P. Y.; Harris, R. K., A combined first principles computational and solid-state NMR study of a molecular crystal: flurbiprofen. *Physical Chemistry Chemical Physics* **2005,** *7* (7), 1402-1407.
116. Robinson, M.; Haynes, P. D., Dynamical effects in ab initio NMR calculations: Classical force fields fitted to quantum forces. *Journal of Chemical Physics* **2010,** *133* (8), 9.
117. Pruneda, J. M.; le Polles, L.; Farnan, I.; Trachenko, K.; Dove, M. T.; Artacho, E., Calculation of the effect of intrinsic point defects and volume swelling in the nuclear magnetic resonance spectra of ZrSiO4. *Molecular Simulation* **2005,** *31* (5), 349-354.
118. Lavrentiev, M. Y.; Purton, J. A.; Allan, N. L., Ordering in spinels - A Monte Carlo study. *American Mineralogist* **2003,** *88* (10), 1522-1531.
119. Todorov, I. T.; Allan, N. L.; Lavrentiev, M. Y.; Freeman, C. L.; Mohn, C. E.; Purton, J. A., Simulation of mineral solid solutions at zero and high pressure using lattice statics, lattice

dynamics and Monte Carlo methods. *Journal of Physics-Condensed Matter* **2004,** *16* (27), S2751-S2770.
120. Purton, J. A.; Lavrentiev, M. Y.; Allan, N. L., Monte Carlo simulation of GaN/InN mixtures. *Journal of Materials Chemistry* **2005,** *15* (7), 785-790.
121. Metropolis, N.; Rosenbluth, A. W.; Rosenbluth, M. N.; Teller, A. H.; Teller, E., Equation of State Calculations by Fast Computing Machines. *The Journal of chemical physics* **1953,** *21* (6), 1087-1092.
122. Benny, S.; Grau-Crespo, R.; de Leeuw, N. H., A theoretical investigation of [small alpha]-Fe2O3-Cr2O3 solid solutions. *Physical Chemistry Chemical Physics* **2009,** *11* (5), 808-815.
123. Haider, S.; Grau-Crespo, R.; Devey, A. J.; de Leeuw, N. H., Cation distribution and mixing thermodynamics in Fe/Ni thiospinels. *Geochimica Et Cosmochimica Acta* **2012,** *88*, 275-282.
124. Wang, Q.; Grau-Crespo, R.; de Leeuw, N. H., Mixing Thermodynamics of the Calcite-Structured (Mn,Ca)CO3 Solid Solution: A Computer Simulation Study. *Journal of Physical Chemistry B* **2011,** *115* (47), 13854-13861.
125. Grau-Crespo, R.; Smith, K. C.; Fisher, T. S.; de Leeuw, N. H.; Waghmare, U. V., Thermodynamics of hydrogen vacancies in MgH2 from first-principles calculations and grand-canonical statistical mechanics. *Physical Review B* **2009,** *80* (17).
126. Laurencin, D.; Almora-Barrios, N.; de Leeuw, N. H.; Gervais, C.; Bonhomme, C.; Mauri, F.; Chrzanowski, W.; Knowles, J. C.; Newport, R. J.; Wong, A.; Gan, Z. H.; Smith, M. E., Magnesium incorporation into hydroxyapatite. *Biomaterials* **2011,** *32* (7), 1826-1837.
127. Gale, J. D., GULP: Capabilities and prospects. *Zeitschrift Fur Kristallographie* **2005,** *220* (5-6), 552-554.
128. Enciso-Maldonado, L.; Dyer, M. S.; Jones, M. D.; Li, M.; Payne, J. L.; Pitcher, M. J.; Omir, M. K.; Claridge, J. B.; Blanc, F.; Rosseinsky, M. J., Computational Identification and Experimental Realization of Lithium Vacancy Introduction into the Olivine LiMgPO4. *Chemistry of Materials* **2015,** *27* (6), 2074-2091.
129. Kresse, G.; Furthmuller, J., Efficient iterative schemes for ab initio total-energy calculations using a plane-wave basis set. *Physical Review B* **1996,** *54* (16), 11169-11186.
130. Strobridge, F. C.; Clement, R. J.; Leskes, M.; Middlemiss, D. S.; Borkiewicz, O. J.; Wiaderek, K. M.; Chapman, K. W.; Chupas, P. J.; Grey, C. P., Identifying the Structure of the Intermediate, Li2/3CoPO4, Formed during Electrochemical Cycling of LiCoPO4. *Chemistry of Materials* **2014,** *26* (21), 6193-6205.
131. Ruiz-Salvador, A. R.; Grau-Crespo, R.; Gray, A. E.; Lewis, D. W., Aluminium distribution in ZSM-5 revisited: The role of Al-Al interactions. *Journal of Solid State Chemistry* **2013,** *198*, 330-336.
132. Hass, K. C.; Davis, L. C.; Zunger, A., Electronic structure of random ${\mathrm{Al}}_{0.5}$${\mathrm{Ga}}_{0.5}$As alloys: Test of the ``special-quasirandom-structures" description. *Physical Review B* **1990,** *42* (6), 3757-3760.
133. Ehrenreich H.; M., S. L., *Solid State Physics*. Academic: New York, 1976; Vol. 31.
134. von Pezold, J.; Dick, A.; Friak, M.; Neugebauer, J., Generation and performance of special quasirandom structures for studying the elastic properties of random alloys: Application to Al-Ti. *Physical Review B* **2010,** *81* (9).
135. Jiang, C.; Wolverton, C.; Sofo, J.; Chen, L.-Q.; Liu, Z.-K., First-principles study of binary bcc alloys using special quasirandom structures. *Physical Review B* **2004,** *69* (21), 214202.
136. Ozolins, V.; Wolverton, C.; Zunger, A., Cu-Au, Ag-Au, Cu-Ag, and Ni-Au intermetallics: First-principles study of temperature-composition phase diagrams and structures. *Physical Review B* **1998,** *57* (11), 6427-6443.
137. Ruban, A. V.; Simak, S. I.; Shallcross, S.; Skriver, H. L., Local lattice relaxations in random metallic alloys: Effective tetrahedron model and supercell approach. *Physical Review B* **2003,** *67* (21), 214302.
138. Wei, S. H.; Zunger, A., Giant and composition-dependent optical bowing coefficient in GaAsN alloys. *Physical Review Letters* **1996,** *76* (4), 664-667.
139. Wei, S. H.; Ferreira, L. G.; Bernard, J. E.; Zunger, A., Electronic properties of random alloys: Special quasirandom structures. *Physical Review B* **1990,** *42* (15), 9622-9649.
140. Lebedev, A. I., Ab initio studies of dielectric, piezoelectric, and elastic properties of BaTiO3/SrTiO3 ferroelectric superlattices. *Physics of the Solid State* **2009,** *51* (11), 2324-2333.

141. Takahashi, T.; Wu, E. J.; Ceder, G., First-principles estimate of the order-disorder transition in Ba(ZnxNb1-x)O-3 microwave dielectrics. *Journal of Materials Research* **2000,** *15* (10), 2061-2064.
142. Voas, B. K.; Usher, T. M.; Liu, X. M.; Li, S.; Jones, J. L.; Tan, X. L.; Cooper, V. R.; Beckman, S. P., Special quasirandom structures to study the (K0.5Na0.5)NbO3 random alloy. *Physical Review B* **2014,** *90* (2), 6.
143. Takahashi, T.; Wu, E. J.; Van der Ven, A.; Ceder, G., First-principles investigation of B-site ordering in Ba(MgxTa1-x)O-3 microwave dielectrics with the complex perovskite structure. *Japanese Journal of Applied Physics Part 1-Regular Papers Short Notes & Review Papers* **2000,** *39* (3A), 1241-1248.
144. van de Walle, A.; Asta, M.; Ceder, G., The alloy theoretic automated toolkit: A user guide. *Calphad* **2002,** *26* (4), 539-553.
145. Burton, B. P.; Cockayne, E., Unexpected ground state structures in relaxor ferroelectrics. *Ferroelectrics* **2002,** *270*, 1359-1364.
146. Giannozzi, P.; Baroni, S.; Bonini, N.; Calandra, M.; Car, R.; Cavazzoni, C.; Ceresoli, D.; Chiarotti, G. L.; Cococcioni, M.; Dabo, I.; Dal Corso, A.; de Gironcoli, S.; Fabris, S.; Fratesi, G.; Gebauer, R.; Gerstmann, U.; Gougoussis, C.; Kokalj, A.; Lazzeri, M.; Martin-Samos, L.; Marzari, N.; Mauri, F.; Mazzarello, R.; Paolini, S.; Pasquarello, A.; Paulatto, L.; Sbraccia, C.; Scandolo, S.; Sclauzero, G.; Seitsonen, A. P.; Smogunov, A.; Umari, P.; Wentzcovitch, R. M., QUANTUM ESPRESSO: a modular and open-source software project for quantum simulations of materials. *Journal of Physics-Condensed Matter* **2009,** *21* (39), 19.
147. Kendrick, E.; Islam, M. S.; Slater, P. R., Developing apatites for solid oxide fuel cells: insight into structural, transport and doping properties. *Journal of Materials Chemistry* **2007,** *17* (30), 3104-3111.
148. Widom, B., *Statistical Mechanics: A Concise Introduction for Chemists*. Cambridge University Press: 2002.
149. Rouquette, J.; Haines, J.; Bornand, V.; Pintard, M.; Papet, P.; Bousquet, C.; Konczewicz, L.; Gorelli, F. A.; Hull, S., Pressure tuning of the morphotropic phase boundary in piezoelectric lead zirconate titanate. *Physical Review B* **2004,** *70* (1), 4.
150. Johnston, K. E.; Griffin, J. M.; Walton, R. I.; Dawson, D. M.; Lightfoot, P.; Ashbrook, S. E., Nb-93 NMR and DFT investigation of the polymorphs of NaNbO3. *Physical Chemistry Chemical Physics* **2011,** *13* (16), 7565-7576.
151. Jaros, M., ELECTRONIC-PROPERTIES OF SEMICONDUCTOR ALLOY SYSTEMS. *Reports on Progress in Physics* **1985,** *48* (8), 1091-&.
152. Binder, K., ORDERING OF THE FACE-CENTERED-CUBIC LATTICE WITH NEAREST-NEIGHBOR INTERACTION. *Physical Review Letters* **1980,** *45* (10), 811-814.
153. Hass, K. C.; Davis, L. C.; Zunger, A., ELECTRONIC-STRUCTURE OF RANDOM AL0.5GA0.5AS ALLOYS - TEST OF THE SPECIAL-QUASIRANDOM-STRUCTURES DESCRIPTION. *Physical Review B* **1990,** *42* (6), 3757-3760.
154. Glazer, A. M., The classification of tilted octahedra in perovskites. *Acta Cryst.* **1972,** *28*, 3384-3392.
155. Lufaso, M. W.; Woodward, P. M. Prediction of the Crystal Structure of Perovskites Using the Software Program SPuDS *Chemistry Faculty Publications.* [Online], 2001.
156. Baker, D. W.; Thomas, P. A.; Zhang, N.; Glazer, A. M., A comprehensive study of the phase diagram of KxNa1-xNbO3. *Applied Physics Letters* **2009,** *95* (9).
157. Glazer, A. M.; Ahtee, M.; Megaw, H. D., HIGH-TEMPERATURE PHASE-TRANSITIONS IN SODIUM NIOBATE AND USE OF TILTING SCHEMES IN SOLUTIONS OF PEROVSKITE STRUCTURES. *Acta Crystallographica Section A* **1972,** *28*, S179-S179.
158. Stokes, H. T.; Kisi, E. H.; Hatch, D. M.; Howard, C. J., Group-theoretical analysis of octahedral tilting in ferroelectric perovskites. *Acta Crystallographica Section B* **2002,** *58* (938).
159. Shuvaeva, V. A.; Antipin, M. Y., STRUCTURAL DISORDER IN KNBO3 CRYSTAL FROM X-RAY-DIFFRACTION AND EXAFS SPECTROSCOPY. *Kristallografiya* **1995,** *40* (3), 511-516.

160. Sakowski-Cowley, A. C.; Lukaszewicz, K.; Megaw, H. D., The structure of sodium niobate at room temperature, and the problem of reliability in pseudosymmetric structures. *Acta Crystallographica Section B* **1969,** *25* (5), 851-865.
161. Hewat, A. W., NEUTRON POWDER PROFILE REFINEMENT OF FERROELECTRIC AND ANTIFERROELECTRIC CRYSTAL-STRUCTURES - SODIUM NIOBATE AT 22 DEGREES C. *Ferroelectrics* **1974,** *7* (1-4), 83-85.
162. Shuvaeva, V. A.; Antipin, M. Y.; Lindeman, R. S. V.; Fesenko, O. E.; Smotrakov, V. G.; Struchkov, Y. T., Crystal structure of the electric-fieldinduced ferroelectric phase of NaNbO3. *Ferroelectrics* **1993,** *141* (1), 307-311.
163. Lejaeghere, K.; Van Speybroeck, V.; Van Oost, G.; Cottenier, S., Error Estimates for Solid-State Density-Functional Theory Predictions: An Overview by Means of the Ground-State Elemental Crystals. *Critical Reviews in Solid State and Materials Sciences* **2014,** *39* (1), 1-24.
164. Papulovskiy, E.; Shubin, A. A.; Terskikh, V. V.; Pickard, C. J.; Lapina, O. B., Theoretical and experimental insights into applicability of solid-state 93Nb NMR in catalysis. *Physical Chemistry Chemical Physics* **2013,** *15* (14), 5115-5131.
165. Johnston, K. E.; Tang, C. C.; Parker, J. E.; Knight, K. S.; Lightfoot, P.; Ashbrook, S. E., The Polar Phase of NaNbO3: A Combined Study by Powder Diffraction, Solid-State NMR, and First-Principles Calculations. *Journal of the American Chemical Society* **2010,** *132* (25), 8732-8746.
166. Yates, J. R.; Pickard, C. J.; Payne, M. C.; Mauri, F., Relativistic nuclear magnetic resonance chemical shifts of heavy nuclei with pseudopotentials and the zeroth-order regular approximation. *Journal of Chemical Physics* **2003,** *118* (13), 5746-5753.
167. Kudoh, Y.; Ito, E.; Takeda, H., EFFECT OF PRESSURE ON THE CRYSTAL-STRUCTURE OF PEROVSKITE-TYPE MGSIO3. *Physics and Chemistry of Minerals* **1987,** *14* (4), 350-354.
168. Zhao, J.; Angel, R. J.; Ross, N. L., The structural variation of rhombohedral LaAlO3 perovskite under non-hydrostatic stress fields in a diamond-anvil cell. *Journal of Physics-Condensed Matter* **2011,** *23* (17), 11.
169. Ghose, S.; Tsang, T., Structural dependence of quadrupole coupling constant e2qQ/h for 27Al and crystal field parameter D for Fe3+ in aluminosilicates. *American Mineralogist* **1973,** *58*, 748.
170. Lowenstam, H. A.; Weiner, S., On Biomineralization. *Oxford University Press, New York* **1989**.
171. Zeebe, R. E.; Zachos, J. C.; Caldeira, K.; Tyrrell, T., Oceans - Carbon emissions and acidification. *Science* **2008,** *321* (5885), 51-52.
172. Orr, J. C.; Fabry, V. J.; Aumont, O.; Bopp, L.; Doney, S. C.; Feely, R. A.; Gnanadesikan, A.; Gruber, N.; Ishida, A.; Joos, F.; Key, R. M.; Lindsay, K.; Maier-Reimer, E.; Matear, R.; Monfray, P.; Mouchet, A.; Najjar, R. G.; Plattner, G. K.; Rodgers, K. B.; Sabine, C. L.; Sarmiento, J. L.; Schlitzer, R.; Slater, R. D.; Totterdell, I. J.; Weirig, M. F.; Yamanaka, Y.; Yool, A., Anthropogenic ocean acidification over the twenty-first century and its impact on calcifying organisms. *Nature* **2005,** *437* (7059), 681-686.
173. Xiang, L.; Wen, Y.; Wang, Q.; Jin, Y., Synthesis of dispersive CaCO3 in the presence of MgO2. *Materials Chemistry and Physics* **2006,** *98* (2-3), 236-240.
174. (a) Rodriguez-Navarro, C.; Jimenez-Lopez, C.; Rodriguez-Navarro, A.; Gonzalez-Munoz, M. T.; Rodriguez-Gallego, M., Bacterially mediated mineralization of vaterite. *Geochimica Et Cosmochimica Acta* **2007,** *71* (5), 1197-1213; (b) Heywood, B. R., BIOMINERALIZATION - NEW DIRECTIONS IN CRYSTAL SCIENCE. *Microscopy Research and Technique* **1994,** *27* (5), 376-388.
175. Skinner, H. C. W., Biominerals. *Mineralogical Magazine* **2005,** *69* (5), 621-641.
176. Falini, G.; Fermani, S.; Gazzano, M.; Ripamonti, A., Oriented crystallization of vaterite in collagenous matrices. *Chemistry-a European Journal* **1998,** *4* (6), 1048-1052.
177. Sutor, D. J.; Wooley, S. E., Gallstone of unusual composition: calcite, aragonite, and vaterite. *Science (New York, N.Y.)* **1968,** *159* (3819), 1113-4.
178. Kanakis, J.; Malkaj, P.; Petroheilos, J.; Dalas, E., The crystallization of calcium carbonate on porcine and human cardiac valves and the antimineralization effect of sodium alginate. *Journal of Crystal Growth* **2001,** *223* (4), 557-564.

179. Alleva, J. J.; Alleva, F. R.; Fry, B. E.; Eanes, E. D., CALCIUM CARBONATE CONCRETIONS - CYCLIC OCCURRENCE IN HAMSTER VAGINA. *Science* **1971,** *174* (4009), 600-&.
180. Giralt, S.; Julia, R.; Klerkx, J., Microbial biscuits of vaterite in Lake Issyk-Kul (Republic of Kyrgyzstan). *Journal of Sedimentary Research* **2001,** *71* (3), 430-435.
181. Falini, G.; Fermani, S.; Vanzo, S.; Miletic, M.; Zaffino, G., Influence on the formation of aragonite or vaterite by otolith macromolecules. *European Journal of Inorganic Chemistry* **2005,** (1), 162-167.
182. Gebauer, D.; Volkel, A.; Colfen, H., Stable Prenucleation Calcium Carbonate Clusters. *Science* **2008,** *322* (5909), 1819-1822.
183. Pouget, E. M.; Bomans, P. H. H.; Goos, J. A. C. M.; Frederik, P. M.; de With, G.; Sommerdijk, N. A. J. M., The Initial Stages of Template-Controlled CaCO3 Formation Revealed by Cryo-TEM. *Science* **2009,** *323* (5920), 1455-1458.
184. Gebauer, D.; Gunawidjaja, P. N.; Ko, J. Y. P.; Bacsik, Z.; Aziz, B.; Liu, L. J.; Hu, Y. F.; Bergstrom, L.; Tai, C. W.; Sham, T. K.; Eden, M.; Hedin, N., Proto-Calcite and Proto-Vaterite in Amorphous Calcium Carbonates. *Angewandte Chemie-International Edition* **2010,** *49* (47), 8889-8891.
185. Gibson, R. E.; Wyckoff, R. W. G.; Merwin, H. E., Vaterite and μ-calcium carbonate. *American Journal of Science* **1925,** *10*, 325-33.
186. Olshausen, S. v., Strukturuntersuchungen nach der Debye-Scherrer-Methode. *Z. Kristallogr* **1925,** *61*, 463–514.
187. Meyer, H. J., Uber Vaterit und seine Struktur. *Angewandte Chemie-International Edition* **1959,** *71*, 678-679.
188. Andreassen, J. P., Formation mechanism and morphology in precipitation of vaterite - nano aggregation or crystal growth? *Journal of Crystal Growth* **2005,** *274* (1-2), 256-264.
189. Meyer, H. J., *Fortsch. Mineral.* **1960,** *38*, 186.
190. Andersen, F. A.; Brecevic, L., INFRARED-SPECTRA OF AMORPHOUS AND CRYSTALLINE CALCIUM-CARBONATE. *Acta Chemica Scandinavica* **1991,** *45* (10), 1018-1024.
191. Lippmann, F., Sedimentary Carbonate Materials. *Springer, New York* **1973**.
192. Le Bail, A.; Ouhenia, S.; Chateigner, D., Microtwinning hypothesis for a more ordered vaterite model. *Powder Diffraction* **2011,** *26* (1), 16-21.
193. Anderson, A., Group theoretical analysis of the nu(1)(CO32-) vibration in crystalline calcium carbonate. *Spectroscopy Letters* **1996,** *29* (5), 819-825.
194. Wehrmeister, U.; Soldati, A. L.; Jacob, D. E.; Haeger, T.; Hofmeister, W., Raman spectroscopy of synthetic, geological and biological vaterite: a Raman spectroscopic study. *Journal of Raman Spectroscopy* **2010,** *41* (2), 193-201.
195. Behrens, G.; Kuhn, L. T.; Ubic, R.; Heuer, A. H., RAMAN-SPECTRA OF VATERITIC CALCIUM-CARBONATE. *Spectroscopy Letters* **1995,** *28* (6), 983-995.
196. Gabrielli, C.; Jaouhari, R.; Joiret, S.; Maurin, G., In situ Raman spectroscopy applied to electrochemical scaling. Determination of the structure of vaterite. *Journal of Raman Spectroscopy* **2000,** *31* (6), 497-501.
197. Bryce, D. L.; Bultz, E. B.; Aebi, D., Calcium-43 chemical shift tensors as probes of calcium binding environments. Insight into the structure of the vaterite CaCO(3) polymorph by (43)Ca solid-state NMR spectroscopy. *Journal of the American Chemical Society* **2008,** *130* (29), 9282-9292.
198. Burgess, K. M.; Bryce, D. L., On the crystal structure of the vaterite polymorph of CaCO3: A calcium-43 solid-state NMR and computational assessment. *Solid State Nucl Magn Reson* **2015,** *65*, 75-83.
199. Nebel, H.; Neumann, M.; Mayer, C.; Epple, M., On the structure of amorphous calcium carbonate - A detailed study by solid-state NMR spectroscopy. *Inorganic Chemistry* **2008,** *47* (17), 7874-7879.
200. Medeiros, S. K.; Albuquerque, E. L.; Maia, F. F., Jr.; Caetano, E. W. S.; Freire, V. N., First-principles calculations of structural, electronic, and optical absorption properties of CaCO3 Vaterite. *Chemical Physics Letters* **2007,** *435* (1-3), 59-64.
201. Wang, J. W.; Becker, U., Structure and carbonate orientation of vaterite (CaCO3). *American Mineralogist* **2009,** *94* (2-3), 380-386.

202. Wolf, G.; Konigsberger, E.; Schmidt, H. G.; Konigsberger, L. C.; Gamsjager, H., Thermodynamic aspects of the vaterite-calcite phase transition. *Journal of Thermal Analysis and Calorimetry* **2000,** *60* (2), 463-472.
203. Plummer, L. N.; Busenberg, E., The solubilities of calcite, aragonite and vaterite in CO2-H2O solutions between 0 and 90°C, and an evaluation of the aqueous model for the system CaCO3-CO2-H2O. *Geochimica Et Cosmochimica Acta* **1982,** *46*, 1011-1040.
204. Turnbull, A. G., A thermochemical study of vaterite. *Geochimica Et Cosmochimica Acta* **1973,** *37*, 1593-1601.
205. Demichelis, R.; Raiteri, P.; Gale, J. D.; Dovesi, R., A new structural model for disorder in vaterite from first-principles calculations. *Crystengcomm* **2012,** *14* (1), 44-47.
206. Balan, E.; Blanchard, M.; Pinilla, C.; Lazzeri, M., First-principles modeling of sulfate incorporation and S-34/S-32 isotopic fractionation in different calcium carbonates. *Chemical Geology* **2014,** *374*, 84-91.
207. Mugnaioli, E.; Andrusenko, I.; Schuler, T.; Loges, N.; Dinnebier, R. E.; Panthofer, M.; Tremel, W.; Kolb, U., Ab Initio Structure Determination of Vaterite by Automated Electron Diffraction. *Angewandte Chemie-International Edition* **2012,** *51* (28), 7041-7045.
208. Kabalah-Amitai, L.; Mayzel, B.; Kauffmann, Y.; Fitch, A. N.; Bloch, L.; Gilbert, P.; Pokroy, B., Vaterite Crystals Contain Two Interspersed Crystal Structures. *Science* **2013,** *340* (6131), 454-457.
209. Lambert, G.; Lambert, C. C., SPICULE FORMATION IN THE SOLITARY ASCIDIAN, HERDMANIA-MOMUS. *Journal of Morphology* **1987,** *192* (2), 145-159.
210. Demichelis, R.; Raiteri, P.; Gale, J. D., Structure of hydrated calcium carbonates: A first-principles study. *Journal of Crystal Growth* **2014,** *401*, 33-37.
211. (a) <Solid-State 17O NMR Investigation of the Carbonyl Oxygen Electric-Field-Gradient Tensor and Chemical Shielding Tensor in Amides.pdf>; (b) Malkaj, P.; Kanakis, J.; Dalas, E., The effect of leucine on the crystal growth of calcium carbonate. *Journal of Crystal Growth* **2004,** *266* (4), 533-538.
212. Kitano, Y.; Hood, D. W., The influence of organic material on the polymorphic crystallization of calcium carbonate. *Geochimica Et Cosmochimica Acta* **1965,** *29*, 29-41.
213. Wu, Q. S.; Sun, D. M.; Liu, H. J.; Ding, Y. P., Abnormal polymorph conversion of calcium carbonate and nano-self-assembly of vaterite by a supported liquid membrane system. *Crystal Growth & Design* **2004,** *4* (4), 717-720.
214. Orme, C. A.; Noy, A.; Wierzbicki, A.; McBride, M. T.; Grantham, M.; Teng, H. H.; Dove, P. M.; DeYoreo, J. J., Formation of chiral morphologies through selective binding of amino acids to calcite surface steps. *Nature* **2001,** *411* (6839), 775-779.
215. Shivkumara, C.; Singh, P.; Gupta, A.; Hegde, M. S., Synthesis of vaterite CaCO3 by direct precipitation using glycine and L-alanine as directing agents. *Materials Research Bulletin* **2006,** *41* (8), 1455-1460.
216. Spann, N.; Harper, E. M.; Aldridge, D. C., The unusual mineral vaterite in shells of the freshwater bivalve Corbicula fluminea from the UK. *Naturwissenschaften* **2010,** *97* (8), 743-751.
217. Wang, W. Z.; Wang, G. H.; Liu, Y. K.; Zheng, C. L.; Zhan, Y. J., Synthesis and characterization of aragonite whiskers by a novel and simple route. *Journal of Materials Chemistry* **2001,** *11* (6), 1752-1754.
218. Samoson, A., Introduction to DOR NMR. *Nuclear Magnetic Resonance in Modern Technology* **1994,** *447*, 525-546.
219. Samoson, A.; Tegenfeldt, J., SUPPRESSION OF DOR SIDE-BAND. *Journal of Magnetic Resonance Series A* **1994,** *110* (2), 238-244.
220. Lesage, A.; Sakellariou, D.; Steuernagel, S.; Emsley, L., Carbon-proton chemical shift correlation in solid-state NMR by through-bond multiple-quantum spectroscopy. *Journal of the American Chemical Society* **1998,** *120* (50), 13194-13201.
221. Massiot, D.; Fayon, F.; Capron, M.; King, I.; Le Calve, S.; Alonso, B.; Durand, J. O.; Bujoli, B.; Gan, Z. H.; Hoatson, G., Modelling one- and two-dimensional solid-state NMR spectra. *Magnetic Resonance in Chemistry* **2002,** *40* (1), 70-76.
222. Maslen, E. N.; Streltsov, V. A.; Streltsova, N. R., X-RAY STUDY OF THE ELECTRON-DENSITY IN CALCITE, CACO3. *Acta Crystallographica Section B-Structural Science* **1993,** *49*, 636-641.

223. Ye, Y.; Smyth, J. R.; Boni, P., Crystal structure and thermal expansion of aragonite-group carbonates by single-crystal X-ray diffraction. *American Mineralogist* **2012,** *97* (4), 707-712.
224. Smith, M. E.; Steuernagel, S.; Whitfield, H. J., O-17 MAGIC-ANGLE-SPINNING NUCLEAR-MAGNETIC-RESONANCE OF CACO3. *Solid State Nuclear Magnetic Resonance* **1995,** *4* (5), 313-316.
225. (a) Bastow, T. J.; Stuart, S. N., O-17 NMR IN SIMPLE OXIDES. *Chemical Physics* **1990,** *143* (3), 459-467; (b) Bastow, T. J.; Moodie, A. F.; Smith, M. E.; Whitfield, H. J., CHARACTERIZATION OF TITANIA GELS BY O-17 NUCLEAR-MAGNETIC-RESONANCE AND ELECTRON-DIFFRACTION. *Journal of Materials Chemistry* **1993,** *3* (7), 697-702.
226. Yang, S. T.; Shore, J.; Oldfield, E., O-17 NUCLEAR-MAGNETIC-RESONANCE SPECTROSCOPIC STUDY OF THE LANTHANIDE OXIDES. *Journal of Magnetic Resonance* **1992,** *99* (2), 408-412.
227. Chadwick, A. V.; Poplett, I. J. F.; Maitland, D. T. S.; Smith, M. E., Oxygen speciation in nanophase MgO from solid-state O-17 NMR. *Chemistry of Materials* **1998,** *10* (3), 864-870.
228. Timken, H. K. C.; Schramm, S. E.; Kirkpatrick, R. J.; Oldfield, E., SOLID-STATE O-17 NUCLEAR-MAGNETIC-RESONANCE SPECTROSCOPIC STUDIES OF ALKALINE-EARTH METASILICATES. *Journal of Physical Chemistry* **1987,** *91* (5), 1054-1058.
229. Mueller, K. T.; Wu, Y.; F., C.; Stebbins, J. F.; Pines, A., High-Resolution Oxygen-17 NMR of Solid Silicates. *Journal of American Chemical Society* **1991,** *113*, 32-38.
230. Mueller, K. T.; Baltisberger, J. H.; Wooten, E. W.; Pines, A., ISOTROPIC CHEMICAL-SHIFTS AND QUADRUPOLAR PARAMETERS FOR O-17 USING DYNAMIC-ANGLE SPINNING NMR. *Journal of Physical Chemistry* **1992,** *96* (17), 7001-7004.
231. Fiske, P. S.; Stebbins, J. F.; Farnan, I., BONDING AND DYNAMICAL PHENOMENA IN MGO - A HIGH-TEMPERATURE O-17 AND MG-25 NMR-STUDY. *Physics and Chemistry of Minerals* **1994,** *20* (8), 587-593.
232. Turner, G. L.; Chung, S. E.; Oldfield, E., SOLID-STATE O-17 NUCLEAR MAGNETIC-RESONANCE SPECTROSCOPIC STUDY OF THE GROUP-II OXIDES. *Journal of Magnetic Resonance* **1985,** *64* (2), 316-324.
233. Hans W. Papenguth, R. J. K., Ben Montez, Philip A. Sandberg, 13C MAS NMR spectroscopy of inorganic and biogenic carbonates. *American Mineralogist* **1989,** *74*, 1152-1158.
234. Tossell, J. A., Calculation of 17 O NMR shieldings in molecular models for crystalline MO, M=Mg, Ca, Sr, and in models for alkaline earth silicates. *Physics and Chemistry of Minerals* **2004,** *31* (1), 41-44.
235. Charpentier, T.; Fermon, C.; Virlet, J., Efficient time propagation technique for MAS NMR simulation: Application to quadrupolar nuclei. *Journal of Magnetic Resonance* **1998,** *132* (2), 181-190.
236. Charpentier, T.; Fermon, C.; Virlet, J., Numerical and theoretical analysis of multiquantum magic-angle spinning experiments. *Journal of Chemical Physics* **1998,** *109* (8), 3116-3130.
237. Profeta, M.; Benoit, M.; Mauri, F.; Pickard, C. J., First-principles calculation of the O-17 NMR parameters in Ca oxide and Ca aluminosilicates: the partially covalent nature of the Ca-O bond, a challenge for density functional theory. *Journal of the American Chemical Society* **2004,** *126* (39), 12628-12635.
238. Gervais, C.; Dupree, R.; Pike, K. J.; Bonhomme, C.; Profeta, M.; Pickard, C. J.; Mauri, F., Combined first-principles computational and experimental multinuclear solid-state NMR investigation of amino acids. *Journal of Physical Chemistry A* **2005,** *109* (31), 6960-6969.
239. Johnston, J. C.; Iuliucci, R. J.; Facelli, J. C.; Fitzgerald, G.; Mueller, K. T., Intermolecular shielding contributions studied by modeling the C-13 chemical-shift tensors of organic single crystals with plane waves. *Journal of Chemical Physics* **2009,** *131* (14).
240. Dovesi, R.; Orlando, R.; Civalleri, B.; Roetti, C.; Saunders, V. R.; Zicovich-Wilson, C. M., CRYSTAL: a computational tool for the ab initio study of the electronic properties of crystals. *Zeitschrift Fur Kristallographie* **2005,** *220* (5-6), 571-573.
241. Bak, M.; Rasmussen, J. T.; Nielsen, N. C., SIMPSON: A general simulation program for solid-state NMR spectroscopy. *Journal of Magnetic Resonance* **2000,** *147* (2), 296-330.

242. Mugnaioli, E.; Andrusenko, I.; Schueler, T.; Loges, N.; Dinnebier, R. E.; Panthoefer, M.; Tremel, W.; Kolb, U., Ab Initio Structure Determination of Vaterite by Automated Electron Diffraction. *Angewandte Chemie-International Edition* **2012,** *51* (28), 7041-7045.
243. Tang, C. C.; Thompson, S. P.; Parker, J. E.; Lennie, A. R.; Azough, F.; Kato, K., The ikaite-to-vaterite transformation: new evidence from diffraction and imaging. *Journal of Applied Crystallography* **2009,** *42*, 225-233.
244. Hu, Q.; Zhang, J.; Teng, H.; Becker, U., Growth process and crystallographic properties of ammonia-induced vaterite. *American Mineralogist* **2012,** *97* (8-9), 1437-1445.
245. De La Pierre, M.; Demichelis, R.; Wehrmeister, U.; Jacob, D. E.; Raiteri, P.; Gale, J. D.; Orlando, R., Probing the Multiple Structures of Vaterite through Combined Computational and Experimental Raman Spectroscopy. *The Journal of Physical Chemistry C* **2014,** *118* (47), 27493-27501.
246. Adjei-Acheamfour, M.; Storek, M.; Beerwerth, J.; Bohmer, R., Two-dimensional second-order quadrupolar exchange powder spectra for nuclei with half-integer spins. Calculations and an experimental example using oxygen NMR. *Solid State Nuclear Magnetic Resonance* **2015,** *71*, 96-107.
247. Schmidt-Rohr, K.; Spiess, H. W., *Multidimensional Solid-State NMR and Polymers*. Academic Press: London, 1994.
248. Schaefer, D. J.; Favre, D. E.; Wilhelm, M.; Weigel, S. J.; Chmelka, B. F., Site-hopping dynamics of benzene adsorbed on Ca-LSX zeolite studied by solid-state exchange C-13 NMR. *Journal of the American Chemical Society* **1997,** *119* (39), 9252-9267.
249. Bottke, P.; Freude, D.; Wilkening, M., Ultraslow Li Exchange Processes in Diamagnetic Li2ZrO3 As Monitored by EXSY NMR. *Journal of Physical Chemistry C* **2013,** *117* (16), 8114-8119.